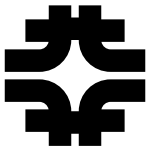

Fermi National Accelerator Laboratory

FERMILAB-Pub-96/024

The Pierre Auger Project Design Report

The Auger Collaboration

Fermi National Accelerator Laboratory
P.O. Box 500, Batavia, Illinois 60510

January 1996

Operated by Universities Research Association Inc. under Contract No. DE-AC02-76CHO3000 with the United States Department of Energy

Disclaimer

19

31

32

32

33

PIERRE AUGER PROJECT
DESIGN REPORT

The Auger Collaboration

October 31st 1995

Contents

Acknowledgements

We gratefully acknowledge support from the following Institutions, who made possible the preparation of this Design Report:

The University of Chicago
Fermi National Accelerator Laboratory
The Grainger Foundation
UNESCO
The National Science Foundation

Chapter 1

Executive Summary

In 1962 a cosmic ray was observed with an energy about 10^{20} eV. This was a demonstration that a macroscopic energy of 16 joules could somehow be acquired by a single atomic nucleus, some 10^8 times more than in a proton extracted from the highest energy terrestial accelerator. The cosmic ray produced an extensive shower of particles through its interactions in the atmosphere. The shower consisted of about 10^{11} charged particles, principally electrons and positrons, spread over a diameter of 5 km at an elevation of 1500 m. The electrons were accompanied by about 10 times as many photons and a tenth as many muons.

The shower was sampled by a number of widely spaced scintillation detectors, and the energy was estimated from the density of charged particles in the scintillators. In the subsequent 30 years some 8 showers in excess of 10^{20} eV have been observed by detectors of ever increasing size and sophistication. The flux is very low, being less than 0.5 per km^2 per century per steradian so that only detectors of immense size will be able to observe a significant number of these extraordinary cosmic rays. In this report we present a conceptual design and cost estimate for two 3000 km^2 detectors to be placed respectively in the Northern and Southern Hemispheres.

Cosmic rays with energy in excess of 10^{20} eV are in a special class because they must have a very short (on a cosmological scale) mean free path in the 2.7K cosmic background radiation. Protons lose energy by photo-pion production, nuclei are photodisintegrated by the giant dipole resonance and photons produce electron-positron pairs. Only neutrinos are relatively freely propagated. A cosmic ray of energy 3×10^{20} eV energy must have had its source less than 50 Mpc (150 million light years) from the Earth, and is so magnetically rigid that it is likely to point back to its source. Credible schemes for the acceleration of protons or nuclei to these extreme energies above 10^{19} do not exist and very few sufficiently energetic astrophysical sources are known within a radius of 50 Mpc from the Earth. In short, the existence of these extraordinary cosmic rays represents a scientific mystery which, if understood, will lead to new discoveries in either fundamental physics or astrophysics.

The purpose of the Auger Observatories is to solve this mystery. The directions and the energies of cosmic rays, together with a measurement of the muon content, can be used

to separate the cosmic rays into samples enriched in either light ($A \leq 16$) or heavy ($A \geq 16$) primaries. Correlations can reveal various possible components contributing to the cosmic ray spectrum. The heavy primaries, which are easier to accelerate because of their larger Z, may have directions correlated with the material in our galaxy. This galactic component, unaffected by the cosmic background radiation, will have the energy spectrum produced directly by the galactic accelerators. The lighter sample (including protons) may be isotropic and exhibit a cut-off due to the cosmic background radiation. These cosmic rays would come from a universal extragalactic component. The cosmic rays with energy $\geq 10^{20}$ are the most incomprehensible component. Although we are now sure of their existence, we have no idea what type of particles they are, how they acquired such high energy, or where their sources are. Their origins must be nearby, within about 50Mpc, and they may cluster about presently visible or invisible sources. Their distribution in energy may be more characteristic of a "top down" source, being created in the decay of topological defects from the early universe, than of an accelerator. An isotropic distribution with no correlation with nearby objects would imply a new class of astrophysical objects observable only by their emission of the highest energy cosmic rays.

New technologies, commonly used in the commercial sector, permit the possibility of constructing cosmic ray observatories consisting of many thousand detectors spread over some 3000-4000 km^2. The detectors will be powered by solar panels and will communicate by modern wireless techniques. The detectors will be correlated in time with a precision of 10ns by means of the Global Positioning Satellite system (GPS),so that the direction of the incoming particle can be dertermined. No physical connections will be required between the detector stations. The use of solar power demands low power electronics. A conservative design is presented that consumes less than 10 watts per station. The architecture for the communications has two alternatives. The condition for recording data can be generated locally to small groups of detectors, or data from the whole array can be passed to a central station. In the latter case the condition for which data are recorded is more flexible. Unusual and unexpected configurations of struck stations can be recognized and recorded.

On clear moonless nights (with about 10% duty cycle) the shower will also be observed by optical detectors, measuring the fluorescence light it produces. This light is detected by arrays of photomultipliers each focused on a patch of the sky. The information from this fluorescence detector, when combined with that of the surface array, allows a more precise measurement of the trajectory of the cosmic ray, as well as the longitudinal development and lateral distribution of the shower. It also provides an independent and absolute energy measurement of the cosmic ray.

A number of options for the surface detectors were explored during the six month design study. The performance of various detectors was calculated using showers generated by Monte Carlo techniques. Extensive care was taken to ensure that the results of the calculations agreed with experimental data available from existing cosmic ray detectors. Variations in the models for the first few interactions, which occur at energies well beyond the range of accelerator measurements, do not affect the shower properties relevant to detector design. The preferred surface detector is a water tank of 10 m^2 area and depth of 1.2 m with an efficient diffusely-reflecting lining. The Čerenkov light produced by the shower particles

is viewed by several photomultipliers. By comparison with scintillation detectors, the water tanks are simple and cheap, require little electronics, and have better sensitivity to showers at large zenith angles. Water tanks have been used in the Haverah Park array for more than twenty years with little maintenance and data from that instrument provide important checks on the design work.

We propose to place the tanks on a triangular grid with a 1.5 km separation. Because of the large separation, it is the properties of the shower particles more than 1 km from the core that are most relevent for the detector design. The electromagnetic particles (electrons, positrons and photons) are some 100 times more numerous than the muons. However their mean energy is 10 MeV while the mean energy of the muons is 1 GeV. The shower particles are detected by the Čerenkov light produced in the water. The particles in the shower front arrive over a time span of several microseconds. The electromagnetic particles produce a large number of small overlapping pulses whereas the muons produce a small number of large pulses during the several μs passage of the shower front. Analysis of a Flash-ADC output of the water tank permits a reasonable separation of the energy carried by the muonic component of the shower particles from that of the electromagnetic part of the shower. This ratio is related to the nature of the primary that initiated the cosmic ray.

A single fluorescence detector of proven design will be placed at the center of the array. It measures the longitudinal development of the shower. The integrated amount of light seen by the fluorescence detector can be related absolutely to the energy dissipated by ionization in the atmosphere, from which the energy of the primary cosmic ray can be deduced. The atmospheric depth at which the maximum number of particles occurs is also related to the primary type.

The surface array as planned is fully efficient for cosmic rays with energy above 10^{19}eV, when a shower is detected simultaneously in five detectors. The energy of the primary can be measured with a precision of 20% and its direction to $\sim 1.5^{\circ}$. For the 10% of the events where full information from both the surface array and the fluorescence detector is available there will two independent energy measurements and the direction can be found with a precision of 0.3°. Showers can be effectively reconstructed when the fluorescence detector is correlated with two or more surface stations. In this case cosmic rays can be detected efficiently down to 10^{18} eV with only longitudinal development information.

The uncertainty in the model for the first few interactions leads to a 30% uncertainty in the relation between the primary type and the measured ratio of muon energy deposition to electromagnetic energy deposition in the water tank. While the absolute value of this ratio cannot identify the specific primary with certainty, the spread in its value and its correlation with the depth of shower maximum in the atmosphere can indicate whether the primaries are a single species or a range of species. For a range of species the events can be divided into two classes of primary, enriched in either protons and light nuclei or heavy nuclei. These classes can then be correlated with the energy and direction measurements.

A survey team has visited sites in the Southern Hemisphere. These are Argentina, South Africa, and Australia. Each of these countries has a reasonable site from the standpoints of optical clarity and the flatness required for line-of-site communications. A decision on

the southern site will come at the end of 1995 with the criteria to be taken into account including the scientific and infrastructure support that can be provided. Surveys of possible northern sites are under way and a decision will be made early in 1996.

A cost estimate is given for the two observatories. A decision was made that the total cost should not exceed US$100 M. The present conservative design will limit the size of each observatory to approximately 3000 km^2.

Chapter 2

Introduction

Pierre Auger first observed [1] extensive air showers caused by the interactions of very high energy cosmic rays in the atmosphere.

The Pierre Auger project is a broadly based international effort to make a detailed study of cosmic rays at the highest energies. Two air shower detectors are proposed, one to be placed in the Northern Hemisphere and one in the Southern Hemisphere. Each installation will consist of an array of 1600 particle detectors spread over 3000 km^2 with a solid angle acceptance of 2 sr for cosmic ray air showers. Each installation will also have an atmospheric fluorescence detector viewing the volume above the surface array. These two air shower detector techniques working together form a powerful instrument for the proposed research. The objectives of the Pierre Auger project are to measure the arrival direction, energy, and mass composition of 60 events per year above an energy of 10^{20} eV and 6000 events per year above 10^{19} eV.

The Auger project had its conception in a series of workshops in Paris (1992), Adelaide (1993), Tokyo (1993), and finally at Fermilab in 1995. The Design Group for the Pierre Auger Project, hosted by Fermilab, met from January 30 through July 31, 1995. More than 140 scientists from 17 counties attended one or more of the conferences and topical workshops. The objective of the Design Group was to produce a design report containing a reference design and a cost estimate for the proposed detector.

This design report is organized as follows: Chapter 3 presents the scientific motivation together with a program of observations that would illuminate the theoretical picture. Chapter 4 contains the historical background of air shower studies, current and expected results, and the role of the Auger project. Chapter 5 describes how the parameters of high energy cosmic ray air showers are measured and interpreted. Chapter 6 details the Auger detector and its expected performance. Chapters 7 through 9 describe the reference design for the detectors, communication, and data acquisition system. Chapter 10 describes the survey of candidate sites. The central station is treated in Chapter 11. The organization, cost, and schedule are outlined in Chapter 12.

Some appendices follow describing detectors that are not now included in the reference

design. Appendices A and B contain a description of two additional measurement techniques, air Čerenkov detectors and radio pulse detectors that may, after suitable development, be low cost but very valuable additions to the measurement capability of the detector. These two detector options are not included in the reference design or cost estimates. Appendix C describes work that was done on a number of particle detector approaches during the early part of the Design Group. Although the water Čerenkov detector was finally chosen for the surface array reference design, the detector alternatives serve as back-up designs.

A list of people who have participated in the workshops or in other ways contributed to this Design Report is given in Appendix D.

Chapter 3

Science

One of the fundamental discoveries of the twentieth century is the cosmic background radiation that fills the Universe with a sea of photons. Characterized by a blackbody temperature of 2.7K, this is the cold remnant of the fireball that accompanied the origin of the Universe some 10 to 20 billion years ago. Its study today is of profound importance for cosmology and astrophysics.

Soon after the discovery by Penzias and Wilson [2] of the background radiation, Greisen [3] and Zatsepin and Kuz'min [4] independently pointed out that this radiation would make the Universe opaque to cosmic rays of sufficiently high energy. This occurs, for example, for protons when they have enough energy to be above the threshold for production of a π-meson in an encounter with a photon of the universal microwave background. This process degrades the energy of the proton with a characteristic length of less than 50 megaparsecs[1] when the energy of the proton[2] is greater than 10^{20} electron volts (eV). This is a small fraction of the size of the Universe and has two implications:

1. If the highest energy cosmic rays are universal in origin, then the energy spectrum should not extend, except at greatly reduced intensity, beyond about $5 \times 10^{19}\ eV$, a phenomenon known as the Greisen-Zatsepin-Kuz'min (GZK) cut-off.

2. Particles with energy above the cut-off must come from nearby — cosmologically speaking. In addition, charged particles of such high energy would traverse cosmic magnetic fields with little deviation; their observed trajectories would thus indicate the direction to their sources. It may therefore be possible to identify the sources of these particles with previously known astrophysical objects, or else to establish the existence of new sources which are not visible in other forms of radiation. Such identification of sources requires sufficient sensitivity that many cosmic ray events are detected from each source.

[1] 50 megaparsecs is the distance light travels in 150 million years. The center of the Virgo cluster of galaxies is approximately 20 megaparsecs away.

[2] A similar phenomenon of degradation also occurs for nuclei over a similar distance scale due to processes of photodisintegration.

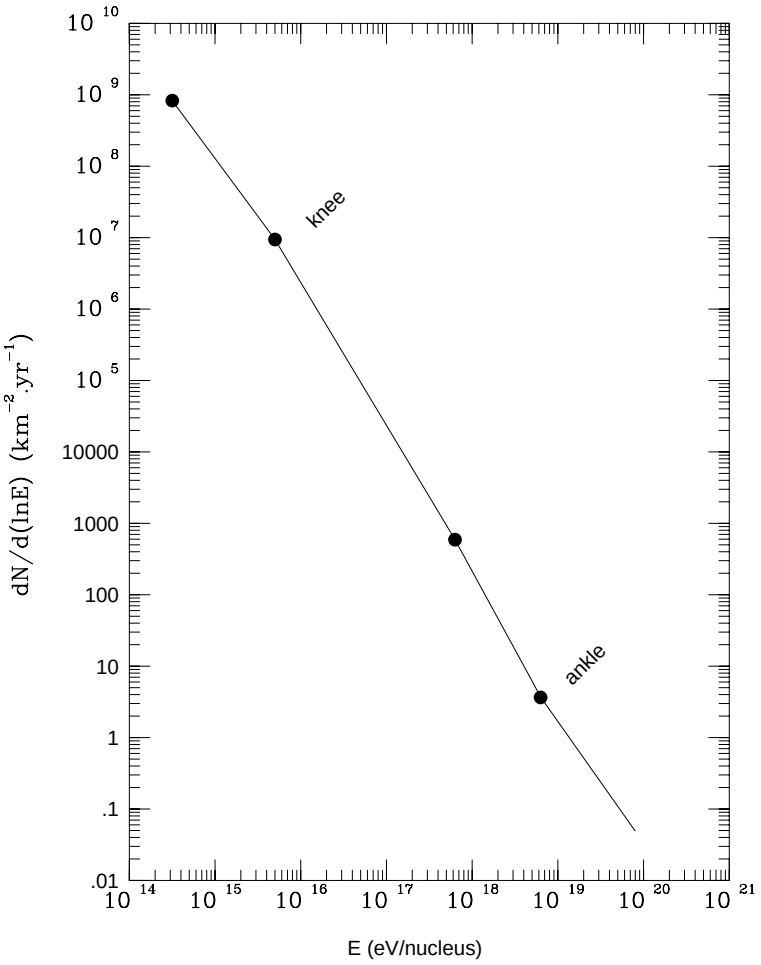

Figure 3.1: A schematic picture of the intensity of cosmic rays as measured by the Akeno air shower experiment [5]. The values are for showers with zenith angles from 0° to 45°.

To study cosmic radiation in the energy region above 10^{19} eV requires extremely large detectors because such particles are extremely rare. This is illustrated in Figure 3.1, which shows the measured energy spectrum in units of events per year per logarithmic interval of energy that strike an area of one square kilometer within an angle of 45° or less from the vertical. In the interval around 10^{19} eV the rate is about 2 events per year per km^2, and it decreases roughly by a factor of 100 when the energy increases by a factor of 10.

Such large areas are at present only possible on the ground with air shower detectors. Present experiments with areas of order 100 km^2 begin to be limited in the number of events they can collect in the decade of energy above 10^{19} eV, just in the crucial energy region. Thus, while present results hint at several interesting and important phenomena, there is not sufficient data to answer some fundamental questions. For example, there are fewer events with $E > 5 \times 10^{19}$ eV than would be expected by a simple power law extrapolation from lower energy. This will be discussed in section 4.2. Could this be the GZK cut off? On the other hand, there are a few events with $E > 10^{20}$ eV, which must be from relatively nearby. What are their sources?

To explore the cosmic-ray spectrum above 10^{20} eV with good statistics is the principal purpose of the proposed Auger Project.

Much new theoretical work has already been stimulated by the recent discovery of two events with energies estimated as $E \geq 2 \times 10^{20}$ eV [6, 7] and also by the series of workshops on the Auger Project, which aims to explore the highest energies with much better collecting power. None of the proposed theories so far accounts for all the facts in a really satisfactory way. We therefore begin this introductory section by describing the questions of great importance for astrophysics and cosmology raised by the present data. Next we review the recent theoretical work, which illustrates the exciting scientific questions we are addressing and at the same time highlights the difficulty of accounting for all the observations with present ideas. This raises the possibility that exploration of the energy region around 10^{20} eV and above with a pair of giant air shower detectors in the Northern and Southern Hemispheres will lead to discoveries which are not conceivable today. We conclude the introduction by describing the capabilities required of the detectors to make possible a full understanding of the most energetic cosmic radiation.

3.1 Astrophysics and cosmology of the highest energy cosmic radiation

Perhaps the most obvious questions about the highest energy cosmic rays are how and where they are accelerated to such high energies. The highest energy particle detected to date, presumably a single proton or a nucleus, had a macroscopic energy of 50 joules — roughly the kinetic energy of a tennis ball at 100 mph! Its energy, 3×10^{20} eV, is more than eight orders of magnitude higher than can be achieved by the most powerful man-made accelerator. Over the years several events with energies near 10^{20} eV have been recorded. More recently two events have been observed with energies well above the GZK cut-off and have, as a result, attracted significant attention and scrutiny. Each of the groups involved has devoted a paper to a critical review of the events and the analysis leading to their energy assignment [6, 7]. As will be shown, a detector with sufficient collecting power will be able to determine the sources of such energetic particles. This is because of their limited range and their high magnetic rigidity in the weak intergalactic magnetic field.

3.1.1 Acceleration

Acceleration in astrophysical plasmas occurs when large-scale macroscopic motion is transferred to individual particles. The macroscopic motion could, for example, be associated with turbulence and/or shock waves. The magnetic field, B, embedded in the plasma plays a crucial role. Generally, the maximum possible energy for a particle of charge $Z\,e$ is of the form

$$E_{max} \sim \beta \times Z\,e \times B \times L, \tag{3.1}$$

where L is the size of the acceleration region and β is a dimensionless constant ≤ 1 related to the macroscopic velocity and/or the geometry. In the most conventional approach to shock acceleration, β is of order 0.01, v/c, the shock velocity [8], but depending on the configuration of the shock and the magnetic field it could be of order 1-3 [9]. Within a factor, this equation simply states that the gyro-radius of the particle being accelerated has to be contained within the acceleration region, as in a terrestrial accelerator.

In many cases the maximum energy can be less than suggested by Equation 3.1. This occurs when conditions are such that some energy loss rate exceeds the acceleration rate. One example is synchrotron loss, which can become important even for protons at very high energy in regions of extreme magnetic fields. Losses due to photoproduction (e.g. $\gamma p \rightarrow \pi^+ n$) can be important in compact regions with intense thermal radiation or when the acceleration occurs over very long time scales in large regions of space. In the latter case it is the background radiation itself that provides the target photon field; indeed this is the mechanism of the GZK cut-off.

An alternative to stochastic acceleration and to diffuse shock acceleration is acceleration by a one-shot mechanism in electrostatic fields aligned with magnetic fields. This configuration of electrostatic fields parallel to flux surfaces arises during reconnection of magnetic fields in laboratory and space plasmas. Pulsars may be another site of such a configuration, with the advantage of avoiding the space and flux limitations of stochastic acceleration by shocks. It has been proposed that a single traversal by a singly-charged particle of a reconnection surface associated with the twisted flux surfaces extending from a quasar accretion disk to the radio lobes can lead to particle energies well above the presently observed limit [11].

Figure 3.2 shows where some potential astrophysical accelerators lie in the B–L plane. Only a few of the objects in this example seem able to accelerate particles to 10^{20} eV. Objects below the diagonal lines cannot accelerate particles to 10^{20} eV. The dashed line is for iron nuclei, $\beta = 1$, the solid line for protons with $\beta = 1$ and the top of the shaded region for protons with $\beta = 1/300$.

Figure 3.2 illustrates the remarkable fact that the most likely accelerators seem to have a maximum energy just in the range where the GZK cut-off comes into play. In addition, for a given configuration of magnetic fields and plasma motion, the maximum total energy for nuclei is approximately Z times higher than that for protons. Thus we expect the observed mass spectrum to have interesting and revealing structure in the energy range above 10^{19} eV. The experiments will need to have both good energy resolution and at least some sensitivity to the charge or mass of the nuclei responsible for the showers in this energy region in order, for example, to distinguish between a GZK cut-off for a proton source and the maximum energy of an accelerator for which $E_{max} \propto Z \times e$.

Possible sources in Figure 3.2 include, in addition to large objects such as radio galaxies, compact objects with very large magnetic fields, such as neutron stars and Active Galactic Nuclei (AGNs). In such systems, acceleration could be by a one-shot mechanism or in an accretion shock. In such models the upper limit on the energy is given by a dimensional formula similar to Equation 3.1 [12]. It is generally true, however, that for compact systems

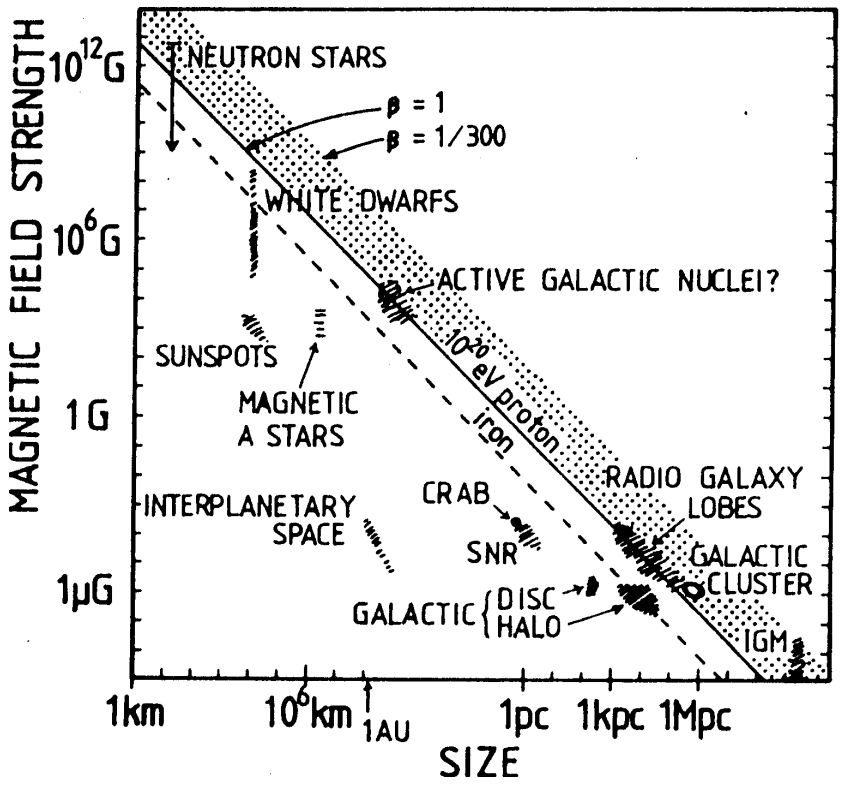

Figure 3.2: Size and magnetic field strength of possible sites of particle acceleration [10]. Objects below the diagonal lines cannot accelerate particles to 10^{20} eV. The dashed line is for iron nuclei, $\beta = 1$, the solid line for protons with $\beta = 1$ and the top of the shaded region for protons with $\beta = 1/300$. The parameter β from Eq. 3.1 is related to shock velocity relative to velocity of light in the most conventional approach to diffusive shock acceleration. Hence the example $\beta = 1/300$, a typical value. The figure does not include effects of synchrotron losses and interactions with the microwave background.

the energetic particles which may be produced suffer significant degradation of their energy in the intense local radiation fields (for example by photodisintegration of nuclei or photopion production by protons).

Inspection of Figure 3.2 suggests that none of the proposed astrophysical accelerators can easily account for energies as high as 10^{20} eV. Indeed, the possibility exists that the very highest energy particles come not from these "conventional" objects but are produced directly by some exotic mechanism (e.g. the so-called "topological defects"). Such sources could produce jets of hadrons and photons with energies well above 10^{20} eV that would cascade down to lower energy. This particular exotic scenario has its own potential difficulties, which will be mentioned below. Nevertheless it is clear that cosmic rays in this energy range have the potential to teach us about particle physics far beyond the reach of even dreamt-of accelerators.

3.1.2 Propagation

For a cosmic ray nucleus of charge Z in a magnetic field $B_{\mu G}$ in μGauss, the Larmor radius in kiloparsecs (kpc) is

$$R_{kpc} \approx E_{18}/(Z\, B_{\mu G}), \tag{3.2}$$

where E_{18} is the total energy of the particle in units of 10^{18} eV. Since the disk of the Galaxy is significantly thinner than 1 kpc, if all cosmic rays are from sources in the disk they must exhibit a tendency to come from the galactic plane at higher energies. At present there is no statistically significant evidence for large-scale anisotropy. Since magnetic fields in the Galaxy are on the order of a few μGauss, it is reasonable to assume (even for iron, $Z = 26$) that particles with $E > 10^{19}$ eV are extragalactic in origin. (An intriguing suggestion has been made that it may be possible to use the large-scale magnetic field in the disk of the Galaxy as a magnetic analyzer for nuclei entering the Galaxy from known source directions.)

There are several processes that can degrade the energy of energetic particles as they propagate through the cosmos. We have already mentioned one mechanism whereby protons produce pions via interaction with the microwave background. They may also lose energy through the production of electron-positron pairs in the background radiation. After each interaction the proton is likely to emerge (sometimes as a neutron) with a reduced but still very large energy. Further interactions occur until its energy is below the GZK cut off. Nuclei undergo photo-disintegration in the background microwave and infra-red radiations [13]. Although the latter process occurs at a lower energy per nucleon than photopion production by protons, the thresholds for the two processes are nearly the same when expressed in terms of the total energy of the nucleus. All particles, regardless of their nature, lose energy due to the general expansion of the universe (red-shift). The attenuation lengths for these processes are shown in Figure 3.3. Also shown are the interaction length of high energy photons which interact with the background to produce electron-positron pairs. In this case we show separately the attenuation of photons in diffuse infra-red radiation and in the radio background as well as in the 2.7 K microwave background. The radio and infra-red backgrounds are, however, not as well determined as the microwave background.

As a consequence of the various background radiation fields, there are limits to how far away the sources of extremely energetic particles can be, no matter how high their initial energy. This is illustrated for protons in Figure 3.4. Stated more generally, because the attenuation length of protons and nuclei in the microwave background depends strongly on energy, especially in the region of the threshold for photopion production, the expected spectrum depends strongly on assumptions about the distribution in time and space of the sources as well as the energy spectrum at the sources, as illustrated in Figure 3.5 and 3.6.

It is not easy to fit the observed spectrum with combinations of the assumptions of Figure 3.5. For example, a sufficiently nearby source to account for the events above 2×10^{20} eV tends to yield more particles than observed just below this energy. However, existing detectors have insufficient exposure for the apparent gap in the spectrum around 10^{20} (Figure 4.3) to be considered to be statistically significant.

Because particles with $E > 2 \times 10^{20}$ eV must come from relatively nearby (Figure 3.4) and because extragalactic fields are expected to be weak (generally $\sim 10^{-9}$ Gauss [16]) we can expect to do particle astronomy with these particles, *if enough of them are found.* This is a major goal of the Auger Project.

The observation of extragalactic sources of ultra high energy cosmic rays by the Auger Project can provide important information on the presently unknown structure and strength of extragalactic magnetic fields. The study of the spectrum, composition, and directional distribution of cosmic rays with energies above $\sim 10^{19}$ eV will probe extragalactic magnetic fields below the present observational upper limit of $B_{EG} \sim 10^{-9}$ Gauss [16]. The angular distribution of the arrival directions of charged cosmic rays with respect to their source(s) conveys information about extragalactic fields. In addition, ultra high energy photons should exhibit a feature in their spectrum around $\sim 10^{19}$ eV for extragalactic magnetic fields in the range $10^{-9} - 10^{-11}$ Gauss [17]. Probing extragalactic fields will help answer the question of how they originated and whether the galactic magnetic field is purely a primordial relic or was dynamically enhanced from a much smaller cosmological seed field. Either case will have important consequences which extend from understanding galaxy formation to the study of processes in the early universe (e.g. phase transitions) which generate magnetic fields.

3.2 Recent theoretical work

There are several broad classes of theoretical explanations for the highest energy events:

- Gradual acceleration in large objects, such as radio galaxies;
- One-shot acceleration mechanisms, such as unipolar induction mechanisms in the strong potentials of accretion disks and compact rotating objects;
- Acceleration in catastrophic events, e.g. in association with gamma-ray bursts;
- Exotic sources, e.g. topological defects.

3.2.1 Acceleration in diffuse sources

There are several possible mechanisms for accelerating particles in large scale structures. That the highest energy particles require extragalactic sources has long been recognized [18]. The following are examples which have been investigated in some detail:

- Large scale structure formation in the universe could lead to very large scale shocks and associated particle acceleration [20];
- Galaxy cluster accretion shocks, possibly already observed in an absorption feature in the Perseus cluster, can accelerate particles to high energy, given suitably strong magnetic fields [21];
- Collisions of galaxies are expected to lead to large scale shock waves [22];
- Shock waves induced by the motion of galaxies in clusters may accelerate particles;
- Shocks in the outer regions of high speed jets of powerful radio galaxies may be sites of particle acceleration, with some sufficiently nearby to supply the events above 10^{20} eV.

As an illustration of the issues involved, we discuss the latter possibility in more detail. One of its attractions is that high power radio galaxies show clear evidence (via synchrotron emission, sometimes extending to optical frequencies) for acceleration of electrons in hot spots associated with high speed jets extending over huge distances into the intergalactic medium [23]. It is reasonable to suppose that protons are also accelerated. Many objects with strong radio jets have been observed to be emitters of GeV gamma-rays by the Compton Gamma Ray Observatory [24]. There is also strong evidence that the gamma ray spectrum from two AGNs (Markarian 421 and 501) continues into the TeV energy range [25]. These high energy gamma rays are produced by electrons or protons of still higher energy. In either case, they indicate the tremendous luminosity of the jets.

Hot spots within the lobes of high power radio galaxies are usually interpreted as large scale shock waves, possibly weakly relativistic [23, 26]. In these shock waves particles may be accelerated to very high energies, possibly even approaching 10^{21} eV [27, 28]. The maximum particle energy depends on the magnetic field in the flow from the central engine, and is expected to scale with the power of the source. Under the hypothesis that high power radio galaxies are in fact the source for most cosmic ray particles beyond $\approx 3 \times 10^{18}$ eV, several implications have recently been suggested and tested against a data set derived principally from Haverah Park [29]:

- The arrival directions of the high energy events should be related to the distribution of strong radio galaxies in the flattened local supercluster. Although not statistically conclusive, there is evidence for a supergalactic equatorial enhancement in the data set for energies greater than 4×10^{19} eV.

- The arrival directions of primaries above 10^{20} eV should correlate with specific radio galaxy directions. The radio galaxy 3C134 is 12° from arrival direction of the 3×10^{20} eV Fly's Eye event; similarly, NGC315 is 10° from the Akeno event at 2×10^{20} eV. Each of these is a powerful radio galaxy. For a Hubble constant of 75 km·s^{-1}·Mpc^{-1}, NGC315 is at a distance of 50 Mpc. The distance to 3C134 is not known since it is behind a dense molecular cloud in our own Galaxy; it is a viable candidate only in if its redshift is sufficiently small. Measuring its redshift would therefore be a test of this acceleration model.

- It might be expected that radio galaxy sources of the events above 10^{20} eV would also produce an excess of particles of somewhat lower energy from those same general directions. There is suggestive evidence that excesses in arrival directions of particles above 2×10^{19} eV are found near the arrival direction of the particles above 10^{20} eV.

An important test of this model will be to see if the observations from Akeno and Fly's Eye exhibit similar characteristics.

The scenario just described is an example of a more general situation discussed by Berezinsky et al.[12] in which there is an excess of sources in the local supercluster. The prediction of clustering in the supergalactic plane is more general than the radio galaxy model discussed above. It would hold for any mechanism associated with mass concentrations in our part of the Universe.

The form of the spectrum near the expected cut-off may tell us about the relative density enhancement of nearby sources. This is particularly true if all sources are of a similar nature. However, if different source types are involved the situation is considerably more complicated. Even if the sources are of a similar type, such as the lobes of radio galaxies, each system would be expected to have somewhat different parameters and correspondingly different values of E_{max}, some above and some below the GZK cut-off.

3.2.2 Association with gamma-ray bursts?

The origin of gamma-ray bursts (GRBs) is still unknown, and they are currently one of the great mysteries of astrophysics. Based on the little we know about GRBs, it has recently been suggested by Waxman [30], by Vietri [31], and by Milgrom and Usov [32] that the same physical mechanism (as yet unknown) that produces GRBs might also be producing cosmic ray particles with energies above 10^{20} eV.

Recent observations suggest increasingly that GRBs originate from cosmological sources [33]. If they are indeed cosmological, then two remarkable coincidences arise, which suggest that GRBs and the highest energy cosmic rays have a common origin [30, 31]. First, the average rate (over volume and time) at which energy is injected into the universe as γ-rays by GRBs is comparable to the rate at which energy should be injected as protons above 10^{20} eV in order to produce the observed cosmic ray flux. The second coincidence is related to the energy of the most energetic cosmic rays. Although the source of GRBs is unknown,

their observational characteristics (variability on a millisecond time scale, hard spectrum extending to about 100 MeV, and luminosity of order 10^{51} erg s $^{-1}$ for a cosmological distance) pose strong constraints on the physical conditions in the γ-ray emitting region [34]. If these conditions have been correctly inferred, then protons may be accelerated in the γ-ray emitting region to 10^{20} eV [30, 31]. This energy estimate depends only on the luminosity and bulk Lorentz factor of the source, which are directly estimated from observations (assuming a cosmological origin for GRBs).

Even if the energy output of GRBs is similar in gamma rays and high energy protons, such bursts could still not account for the $> 10^{20}$ eV flux without significant dispersion in arrival times. High energy cosmic ray experiments observe a cone of opening angle $\sim 45^o$ around the zenith. The rate of cosmological GRB events in a cone extending to 50 Mpc, the maximum distance likely to be traveled by a cosmic ray of 2×10^{20} eV, is ~ 1 per 400 yr. Thus, the probability of these experiments to observe a high energy cosmic ray "outburst" associated with a GRB event during 10 years operation is very small, unless the outburst is broadened in time, due to propagation through the inter-galactic medium (IGM), over a time scale ≥ 100 years. Such a temporal broadening would actually be expected due to the combined effects of deflection by random magnetic fields and energy dispersion of the particles, provided that the IGM magnetic field exceeds 10^{-12} G. (See discussion of arrival direction patterns below for estimates of time broadening.)

It is important to understand that time broadening implies that no correlation would be expected between the arrival directions of cosmic rays and observed gamma-ray bursts. It was pointed out [32] that the error boxes of the arrival directions of the two recent events with energies above 2×10^{20} eV overlap with those of strong GRBs. However, the probability that two cosmological GRBs would occur close enough to produce these two cosmic ray events is very small ($\sim 10^{-4}$). Nevertheless, if the suggested correlation is confirmed by subsequent observations, this would imply that the rate per unit volume of GRB events is much higher than that expected of a cosmological distribution. This would strongly suggest that GRBs are not in fact cosmological but rather of Galactic origin.

Confirming the suggested associations of the highest energy cosmic rays with GRBs (either Galactic or cosmological) would have a profound impact on our understanding of both phenomena, and (in the cosmological case) would also provide information on the unknown IGM magnetic fields. Of course the flight times of any charged cosmic rays will always be much greater (eg. centuries) than for gamma rays, so no time coincidences will occur. The associations may be confirmed (or ruled out) by accurately measuring the cosmic ray flux above 10^{19} eV. If the highest energy cosmic rays are associated with Galactic GRBs, one expects new $> 10^{20}$ eV events to be similarly associated. On the other hand, if they are associated with cosmological GRBs, one expects an isotropic cosmic ray flux exhibiting a GZK cut-off. Confirming the existence of such features requires observation of the cosmic ray flux to and beyond 10^{20} eV with much better statistics than currently available.

3.2.3 Exotic sources

In contrast to the two classes of mechanism discussed so far which basically consist of "bottom-up" acceleration of charged particles from lower energies there might also be a "top-down" mechanism at work where primary charged or neutral particles are actually produced at ultrahigh energies. An example would be supermassive elementary "X" particles related to Grand Unified Theories (GUTs) which typically decay into quarks and thereby into mesons and nucleons, charged leptons (e, μ, τ), gamma rays and neutrinos. Sources of such particles today could be topological defects left over from phase transitions in the early universe. The spontaneous breaking of symmetries underlying these GUTs may cause such phase transitions. It is conceivable that these mechanisms could dominate the cosmic ray flux above 10^{20}eV but they cannot explain the flux at considerably lower energies since the corresponding injection spectra are typically harder than for "bottom-up" acceleration [35].

The initial energy scales associated with such scenarios are of the order of the GUT scale ($\sim 10^{15}$ GeV or 10^{24} eV). As a consequence, the associated fluxes of photons (and neutrinos) can be quite high. When the models are normalized to account for the observed events at 2–3 $\times$ 10^{20} eV, definite predictions will follow for the accompanying fluxes of photons, both at higher and lower energy. The associated fluxes will be depend on whether the highest energy events are protons or photons. On the one hand, the predicted associated fluxes must be consistent with observed levels of diffuse gamma ray fluxes and with the observed all-particle cosmic ray spectrum in order for a given model to be viable at all. On the other, the predicted accompanying fluxes are likely to offer characteristic signatures by which such a scenario could be recognized and identified. The configuration of secondary fluxes associated with top-down scenarios, including cascading in extragalactic photon fields, is currently under intensive investigation [36, 38].

If a considerable rate of superhigh energy events above 2×10^{20} eV is found by the giant arrays proposed here, and if the apparent gap between these events and the lower energy data should persist, then the need for some kind of "exotic" processes would become pressing [39]. The basic reason is that conventional acceleration sources that are near enough to reproduce the superhigh energy events beyond the GZK cut-off would at the same time predict events in the "gap" which are not yet seen. Confirmation of the existence of an "exotic" component would potentially provide insight into the conditions in the early universe, as well as into particle physics beyond the "Standard Model."

3.3 Observational capabilities needed for the Auger Detector

The origin of the highest energy cosmic rays is a long-standing mystery. Recent detection of particles well above the expected GZK cut-off have added intrigue to this mystery. The situation now is that no conventional ideas of acceleration and propagation can satisfactorily account for all the observations. This is an assurance that either new fundamental physics

or unanticipated astrophysics will result from solving this mystery. With only incremental increases in detector aperture, however, the discoveries will be a long time coming. The promise of new physics is ample motivation to increase the collecting power now by a large factor. The largest current detector (AGASA) has an area of 100 km^2. The Auger Project will achieve a 60-fold increase in collecting power with an area of 6000 km^2. Uniform celestial exposure is essential for a sensitive anisotropy study. The detector must also measure cosmic ray directions and energies accurately and be able to resolve different primary mass groups.

3.3.1 Mass and energy resolution

The mass composition of cosmic rays is a powerful constraint on theories. Highly charged nuclei are easier to accelerate to high energies than protons, but they are susceptible to photodisintegration at the source and during propagation. The mass composition should be determined at all energies. It is especially important to identify the particle type(s) arriving with energies above the expected GZK cut-off. The goal is to achieve sufficient energy and mass resolution to understand a situation above 10^{19} eV that could involve all of the following:

- A GZK cut-off;
- Contribution from nearby sources beyond the GZK cut-off, which might have a characteristic dip-bump structure if there is a new, possibly exotic, source for the highest energy component;
- Energy-dependent composition associated with the upper limiting energies of different contributing sources.
- Energy-dependent composition associated with different attenuation in the intergalactic medium.

To accomplish this goal it will be necessary to be able to distinguish among the three major groups of potential primaries: primordial nuclei (protons and helium), products of stellar nucleosynthesis (carbon and heavier), and photons (expected in some models of exotic sources).

Figure 3.7 shows a comparison of the highest energy Fly's Eye event [6] with longitudinal profiles for different types of primaries. The figure shows that the profiles expected from heavy nuclei are clearly different from profiles expected for protons. Due to statistical and systematic errors in the reconstruction of that monocular Fly's Eye event, the observed profile has an atmospheric depth uncertainty not shown in the figure. The entire shower profile (plotted data points with error bars) can be moved together (left or right) by ± 60 g/cm^2. This hinders the particle identification and underscores the importance of better resolution. It should be noted that current uncertainty in hadronic interactions at such high

energy causes uncertainties also in the expected depths of maximum for iron and proton showers, although their difference is not strongly model dependent. The shaded bands in the figure indicate the 1 σ range of fluctuations for each type of primary. Note that the photon band includes the cascading in the geomagnetic field as well as the Landau-Pomeranchuk-Migdal (LPM) effect [37]. The thin line shows the profile that would be expected for a single photon neglecting both cascading in the geomagnetic field and the LPM density effect. The calculated profiles for protons (and to a lesser extent heavy nuclei) also have inherent systematic uncertainties at a level comparable to the data, as a consequence of the need to extrapolate hadronic interactions many orders of magnitude beyond accelerator energies.

An accurate measurement of the spectrum requires both adequate statistics and also good energy resolution. Energy measurement errors distort a steeply falling spectrum because each energy bin gains many more erroneous showers from lower energies than it loses due to mismeasurements. By designing the detector to have good mass resolution, it will necessarily have adequate energy resolution. The Auger Observatory fluorescence detector should measure the atmospheric depth of shower maximum (X_{max}) to an accuracy of 20 g/cm^2. (The mean X_{max} for iron differs from that for protons of equal energy by approximately 100 g/cm^2.) As will be seen in Chapter 6 (Table 6.2) a 20 g/cm^2 X_{max} resolution implies that the integral of the longitudinal profile (i.e. the total energy) can be fitted with less than 10% uncertainty. (Systematic uncertainties from modeling the atmosphere may also be present.) Similarly, the ground array should have sensitivity to composition by measuring separately the muon and electromagnetic ($e + \gamma$) particle fluxes. By achieving adequate accuracy in the muon/electromagnetic ratio, particle density measurements will necessarily provide good energy resolution.

3.3.2 Arrival direction patterns

Detector requirements for anisotropy studies depend on the particular energy range of interest. For energies above 100 EeV, magnetic deflection of protons by galactic or extragalactic magnetic fields is expected to be so small that detector angular resolution is an issue. For charged particles of lower energy, point source resolution is limited by magnetic scattering, and detector angular resolution is important only if there is a flux of neutral particles. A very large exposure is needed in that case in order to identify sources by statistically significant clusters of charged particle arrival directions. At the detector's energy threshold, magnetic scrambling of arrival directions may be so severe that the pattern of arrival directions differs from isotropy in only a subtle way. Besides massive statistics, uniform exposure will be vital for sensitive detection of such patterns.

For a source at distance L_{kpc}, the trajectory of a charged particle in a uniform magnetic field is bent through an angle (in radians)

$$\theta \approx \frac{L_{kpc} Z B_{\mu G}}{E_{18}} = \frac{L_{Mpc} Z B_{nG}}{E_{18}}. \tag{3.3}$$

This is an immediate result of approximate Equation 3.2 using $L = R\theta$. The particle energy E_{18} is in EeV, the field strength B transverse to the particle motion is in μG when L is in kpc

(relevant for bending in the Galaxy) or nG when L is in Mpc (appropriate for extragalactic paths), and Z is the number of electric charges on the particle. Figure 3.8 displays this angle of bending (in degrees) as a function of energy for protons. It is calculated for a path length of 0.5 kpc in the Galaxy's magnetic disk with a 2 μG transverse B-field. The figure also pertains to a path length of 1 Mpc through a transverse extragalactic field of 1 nG.

Intergalactic field strengths and coherence lengths are not well established, but fields are not expected to have coherent directions on scales larger than about 1 Mpc. A trajectory might be deflected by multiple scatterings, each roughly the magnitude given by Figure 3.8, with the number of scatterings given by the number of Mpc in the path length. The average total angular deviation of the arrival direction from the line of sight to the source would then be $\sqrt{L_{Mpc}}/2$ times the angle plotted in Figure 3.8. This also provides an estimate of the dispersion in arrival directions for a flux of particles of variable rigidity from a single source. These assumptions about extragalactic field strength and coherence length are not verifiable, but they provide a specific model for examining the energy dependence of magnetic deflections.

Magnetic bending of particle trajectories causes them to arrive later than photons emitted simultaneously from the same source. For a circular arc path, the expected delay is given by

$$\triangle t \;\approx\; 120\ yrs \;\times L^3_{kpc} Z^2 B^2_{\mu G}/E^2_{18} \;=\; 120{,}000\ yrs \;\times L^3_{Mpc} Z^2 B^2_{nG}/E^2_{18}.$$

For multiple scattering with step size l_{Mpc}, the delay is

$$\triangle t \;\approx\; 60{,}000\ yrs \;\times L^2_{Mpc} l_{Mpc} Z^2 B^2_{nG}/E^2_{18}.$$

Figure 3.8 shows the expected proton time delay as a function of energy for galactic and extragalactic path lengths. The galactic path is taken to be a circular arc of length 0.5 kpc ($B_{\mu G} = 2$). The extragalactic path length is taken to be 30 Mpc ($B_{nG} = 1$) and the step size is $l_{Mpc} = 1$.

The case E > 100 EeV

Figure 3.8 gives an angular deflection of 0.6° for protons of 100 EeV. This is the estimated amount of deflection due to the Galaxy's magnetic field. If extragalactic deflections are negligible, then charged particle astronomy is certainly possible and a detector angular resolution which is small compared to 0.6° would be desirable in order to locate the sources as precisely as possible. Extragalactic deflections are likely to exceed the galactic deflection, however, even though pion photoproduction limits the path lengths to about 50 Mpc. According to the model of multiple scattering outlined above, the arrival directions from a single source would be dispersed by $(\sqrt{50}/2) \times 0.6° \;=\; 2.1°$. It is important that the detector angular resolution be better than this in order to take full advantage of the high magnetic rigidity. Based on the present uncertain intensity determinations, the Auger Observatory may detect about 180 such particles in three years. It may then be obvious if the number of contributing sources is much less than 180, based on the presence of tight clusters. Sensitivity to "repeaters" depends on angular resolution. If the angular resolution is limited only by this 2.1°

magnetic deflection, the expected number of error circles overlapping by chance if randomly distributed on the sky would be 23. If degraded further by a 3° detector angular resolution, for example, the number of chance overlaps would be 66. Detector resolution better than 2° is desirable in case extragalactic magnetic deflections are less than estimated here and in case there is a flux of neutrons or γ-rays.

The case E > 40 EeV

The recent analysis of Haverah Park data [29] suggests that there is an excess of arrival directions associated with the supergalactic plane at these energies. If confirmed, this is an exciting result because it would verify a variety of expectations. The first expectation is that particles of such energy should be magnetically rigid enough to preserve their general direction through many megaparsecs of path length. Another expectation is that such particles have not traveled cosmological distances because of the GZK effect. They should point roughly toward sources not more than $\sim$ 200 Mpc away. Within that volume of space, the mass density of the universe is biased toward the supergalactic plane. Any theory of energetic particle production would predict the source locations to be correlated with the mass distribution. The importance for this discussion is the observational evidence that the cosmic ray population above 40 EeV is not isotropic, implying that the shower directions do indeed carry information about source locations.

In three years of running, the Auger Observatory will collect more than 1100 showers above 40 EeV with approximately uniform sky exposure. Figure 3.8 gives the expected angular deflection for protons as 1.4° at 40 EeV. If 200 Mpc path lengths are typical, the assumptions here suggest that the multiply scattered arrival directions should be distributed about the source directions by $(\sqrt{200}/2) \times 1.4^\circ = 10^\circ$. Unless there are very many sources, clusters from individual sources should be evident. Figure 3.9 shows a simulation of the Auger sky at energies above 40 EeV after 3 years if all the cosmic rays come from 15 sources of approximately equal flux. Each source is smeared by sampling its arrival directions from a 10° Gaussian. A realistic map would have a variety of source fluxes and magnetic dispersions. Higher flux and smaller dispersion makes a discrete source easier to detect.

The case E > 10 EeV

The anisotropy analysis is expected to be more complicated using all the Auger Observatory showers above 10 EeV. The problem is not lack of statistics, as 18,000 showers should be collected in three years. The difficulty is partly because there is no GZK distance limit imposed, so the detected particles will have suffered magnetic scrambling over cosmological times, perhaps having originated from a source distribution which reflects the large scale homogeneity of the universe. There may also be a non-negligible contribution from the Galaxy at 10 EeV. If the cosmic rays of galactic origin are all heavy nuclei at this energy (due to preferential acceleration and confinement), an analysis excluding small mass primaries could reveal a pattern produced by sources in the galactic disk compounded by propagation through the Galaxy's magnetic field.

A sensitive anisotropy analysis is greatly facilitated by uniform sky exposure. This is a primary reason for building identical detectors in both the northern and southern hemispheres. Previous experiments have been compromised by highly non-uniform exposure, including large areas with no exposure whatsoever. A search for arrival excesses or deficits under those conditions is extremely difficult, and analysis by spherical harmonics is not feasible. Even the simplest search for a dipole harmonic cannot be conclusive. This point was emphasized in the 1980's when an apparent negative gradient was reported in galactic latitude [40, 41, 42]. The initial interpretation was that the intensity of cosmic rays is greater from southern latitudes than from the galactic northern hemisphere. Wolfendale and Wdowczyk [43] pointed out, however, that for a detector with a north-dominated exposure, such a gradient could also be construed as evidence for an excess from galactic *equatorial* regions, without any actual north-south asymmetry in the cosmic ray intensity. With poor exposure to south galactic latitudes, two radically different interpretations were viable.

Identical installations in both the northern and southern hemispheres will automatically endow the Auger Observatory with approximately uniform exposure to the entire sky. A small exposure dependence on declination will remain, but it is well known and can easily be corrected for. The Auger Observatory will be the first opportunity to study cosmic ray arrival directions over the full celestial sphere with good efficiency.

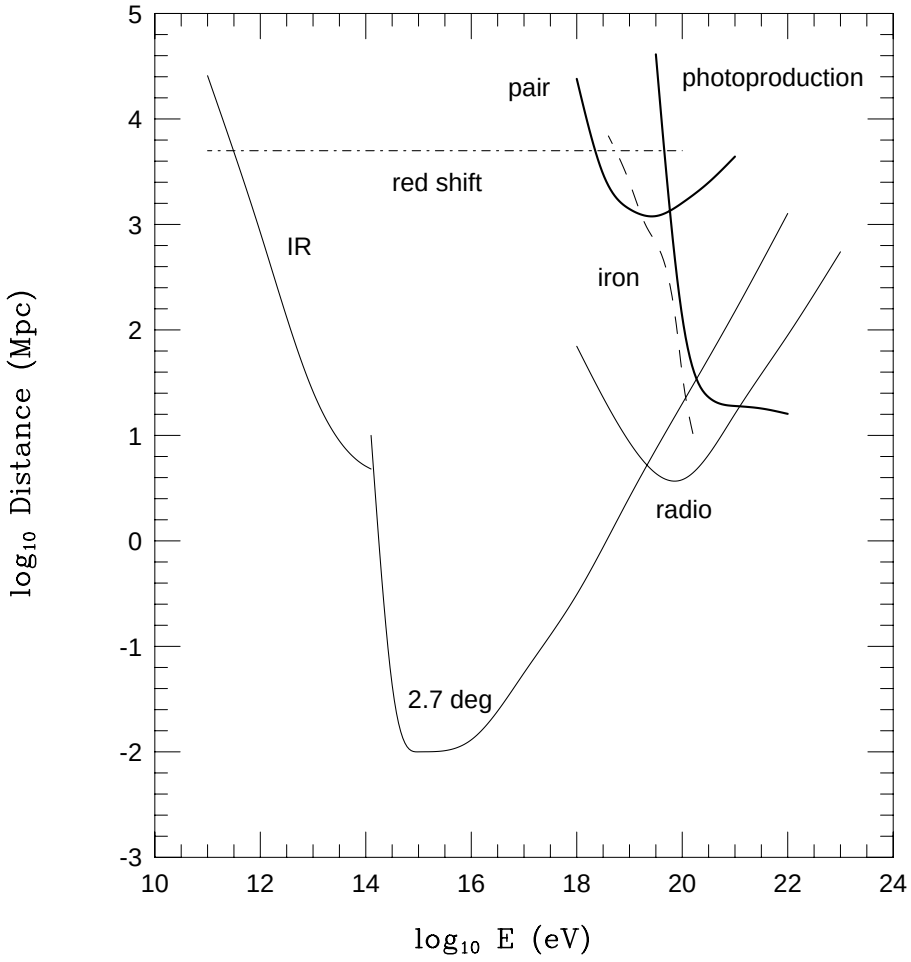

Figure 3.3: Attenuation length of photons, protons and iron in various background radiations as a function of energy. The three lowest and left-most curves refer to photons, showing the attenuation by infra-red, microwave background and radio. The upper, right-most solid curves refer to propagation of protons in the microwave background, showing separately the effect of pair production and photo-pion production. The dashed curve illustrates the attenuation of iron nuclei [13].

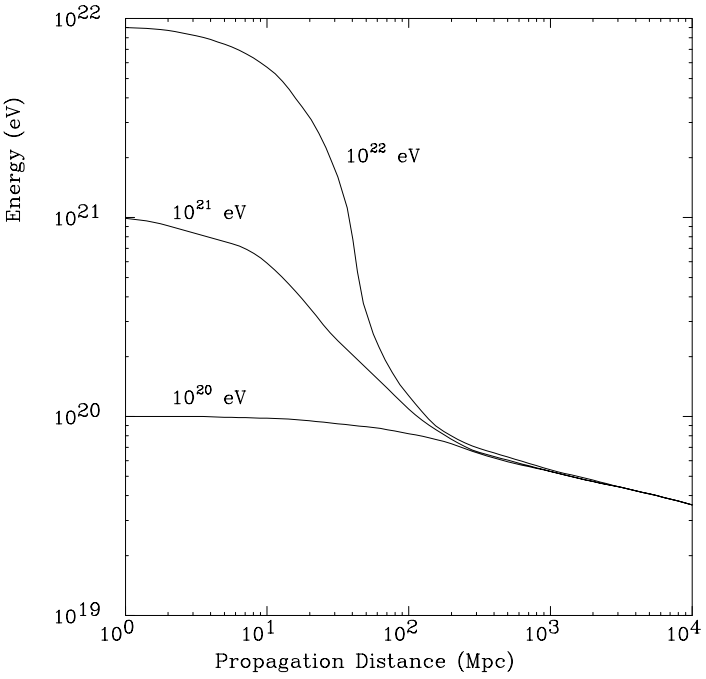

Figure 3.4: Energy of a proton as a function of propagation distance through the 2.7 K background radiation for various initial energies [19].

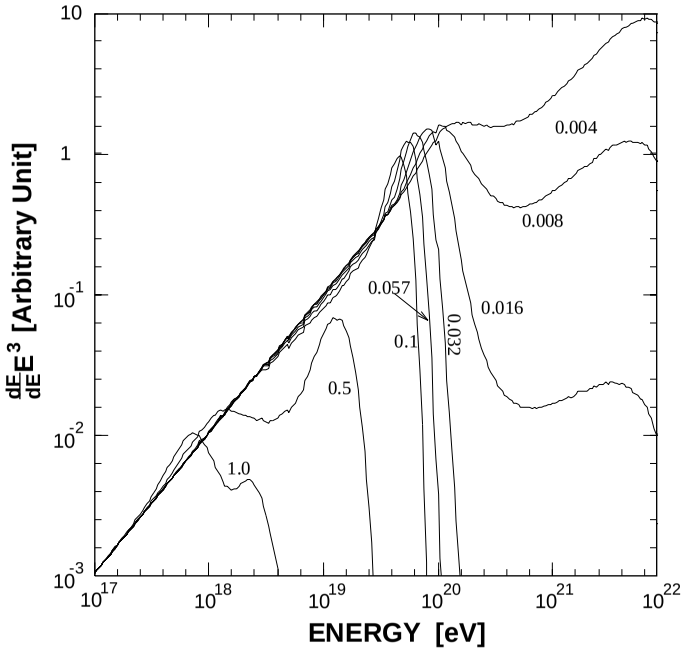

Figure 3.5: The observed energy spectra for a single source with E^{-2} injection spectra at fixed distances corresponding to redshifts 0.004 to 1 (as indicated) [15].

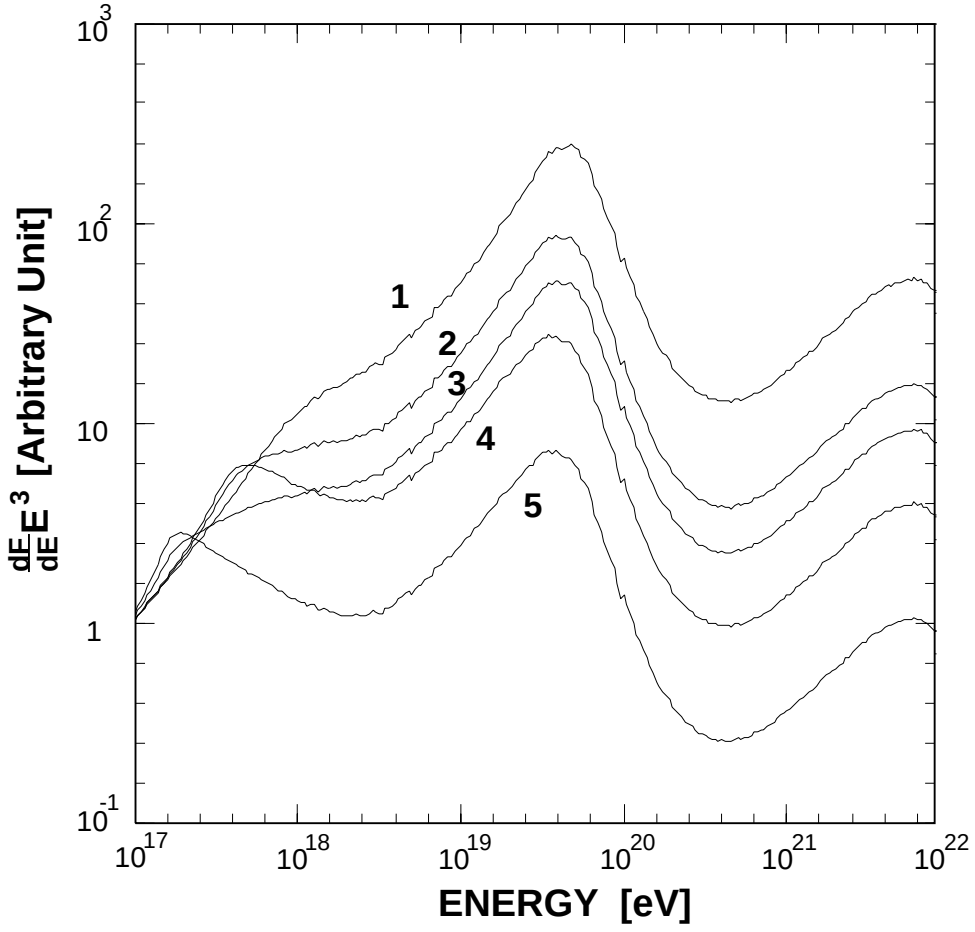

Figure 3.6: A complementary picture to Figure 3.5 showing the spectra from several cosmological distributions of sources [15], leading to a strong cut-off below 10^{20} eV. The five curves correspond to models in which the cosmic ray production is increasingly important in the past and for which the cut-off effect is therefore more severe. For example, the curve labeled 1 corresponds to a uniform distribution of sources up to a red-shift of $z = 2$ but with no cosmological evolution. The curve 5 is a model in which the sources extend back to red-shift $z = 4$ and the sources are assumed to be significantly more active in the past than at present.

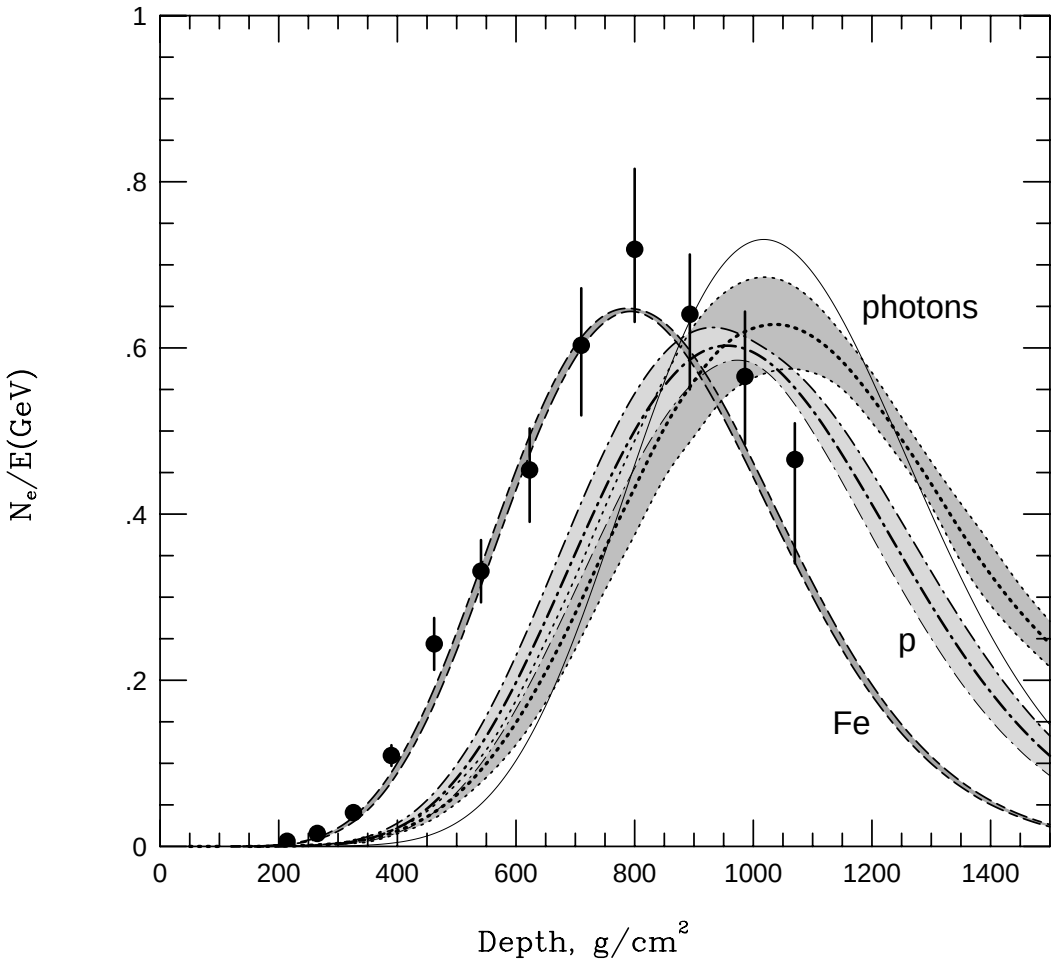

Figure 3.7: Longitudinal development of the highest energy Fly's Eye event compared to model calculations for primary protons, iron and photons. There may be systematic detector biases which have not been applied to these model calculations.

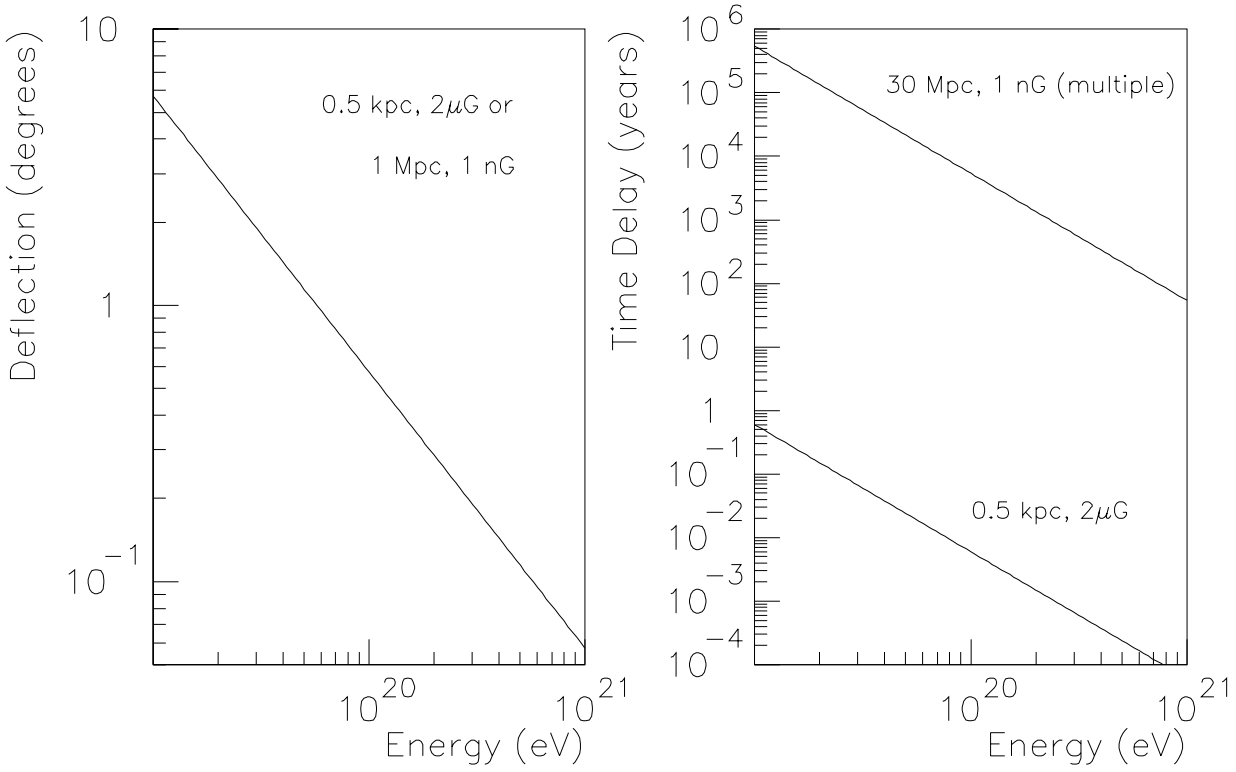

Figure 3.8: Magnetic bending of protons. On the left, the angle of bending expected after penetrating the Galaxy's magnetic disk or a 1-Mpc extragalactic cell. On the right, the time delay relative to a straight line trajectory. Two cases are shown: the bend due to the Galaxy's field and multiple scattering by extragalactic fields over a 30 Mpc path.

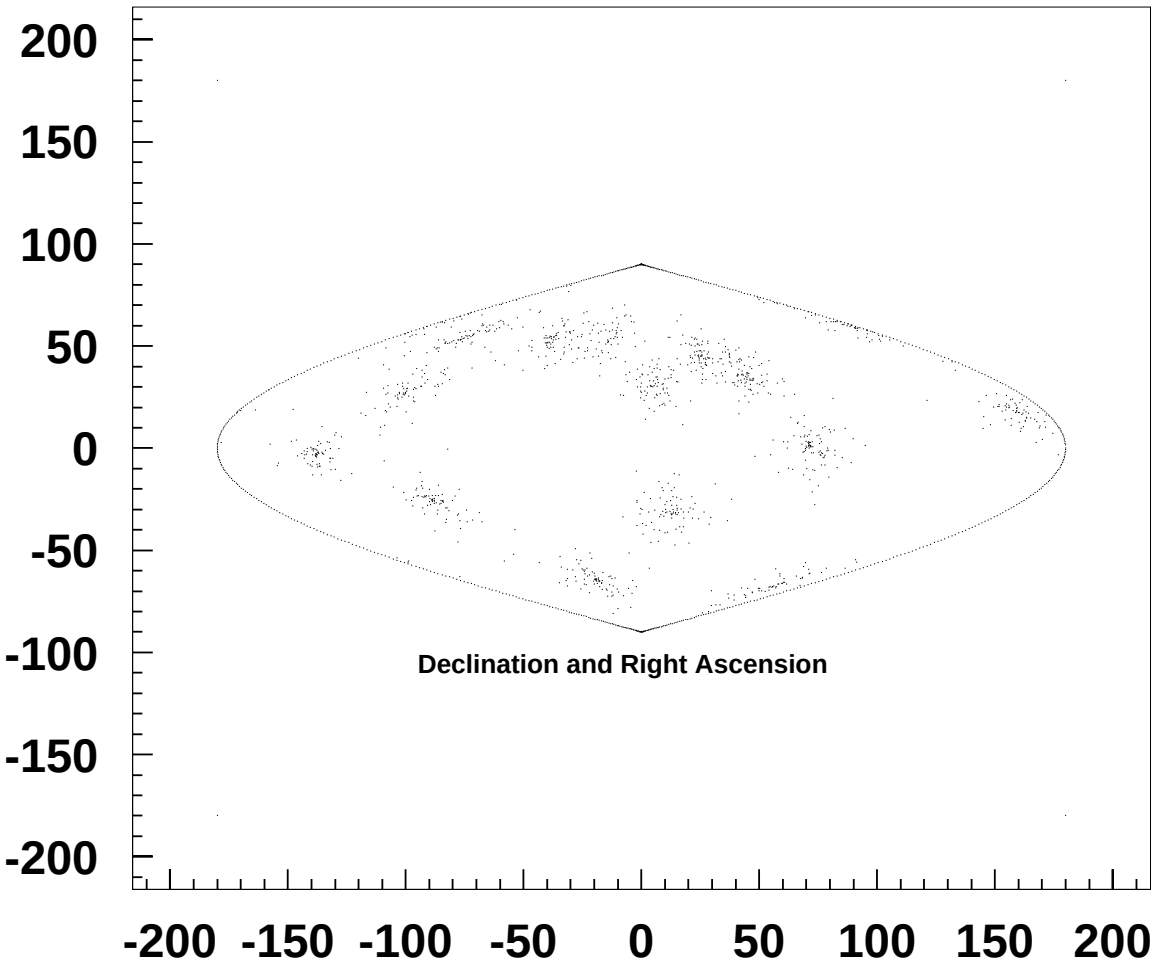

Figure 3.9: Simulation of the Auger sky for showers with energy greater than 40 EeV after 3 years (1165 showers expected). Positions for 15 point sources of approximately equal flux were chosen randomly. Each simulated source is smeared by sampling a Gaussian of 10° width.

Chapter 4

Observations of the Highest Energy Cosmic Rays

4.1 Background

The aim of this chapter is to introduce the observations of the highest energy cosmic rays and to describe the conclusions drawn about the energy of the events detected above 10^{18} eV. In the 1920s and 1930s studies of the trajectories of cosmic ray particles in the Earth's magnetic field demonstrated that some had energies in excess of 20 GeV, more than 2,000 times that of the most energetic particles from radioactive sources. In the 1930s Auger and his group discovered the phenomenon now known as "extensive air showers", EAS, and soon showed that the energy spectrum of cosmic rays extends beyond 10^{15} eV - a jump of five orders of magnitude from the previous highest energy particles. The estimates of energy made by Auger were based on the understanding of electromagnetic cascades at that time: with hindsight the estimates were probably quite conservative. It is now possible to use massive emulsion chambers, flown to high altitude by balloons, to detect individual cosmic rays of nearly 10^{15} eV and to identify, from their ionization trails, the charges of the individual particles. Relatively conventional calorimetric techniques, using emulsions interleaved with lead, permit estimates of the primary energy: an outstanding example of this work is the JACEE project funded by American, Japanese and Polish agencies.

The flux of cosmic rays at 10^{15} eV is $10^{-2}\mathrm{m}^{-2}\mathrm{hr}^{-1}\mathrm{sr}^{-1}$. Above this point the flux decreases even more rapidly, as the energy increases, than at lower energies. Thus individual events can no longer be detected efficiently by balloon-borne calorimeters at a useful rate and one relies instead on developments of the technique pioneered by Auger. The post-war availability of large area scintillation counters led to a series of important experimental advances, particularly by the MIT group under Rossi. A detailed understanding of the shower phenomenon was acquired, and the ability to measure both the size of the shower and its arrival direction with considerable accuracy was developed. The regular registration of events having energies greater than 1 Joule (6.24×10^{18}eV) resulted from the construction

of the first of the giant shower arrays by Linsley (MIT) [44] at Volcano Ranch, New Mexico, during the late 1950s. This work was innovative and the experiment was the first to claim the detection of an event with an energy of 10^{20} eV.

The Volcano Ranch work, and all other work carried out in this field until 1966, was motivated largely by the recognition that a proton of 10^{18} eV in a magnetic field of 2μG (typical of our Galaxy) has a Larmor radius of about 0.5 kpc, somewhat greater than the thickness of the disc of the galaxy. It was thus a reasonable expectation that study of the arrival directions of cosmic rays above 10^{18} eV would reveal, at least, large scale anisotropies, the amplitudes of which were expected to increase with energy. Point sources, perhaps associated with neutrons which have a mean free path before decay of about 10 kpc at 10^{18} eV, were also anticipated and there was considerable interest in what the ultimate energy of detectable cosmic rays might be. Following the recognition by Greisen[3] and by Zatsepin and Kuzmin[4] in 1966 that cosmic rays above 4×10^{19} eV would be exceedingly rare if the cosmic ray sources were at cosmological distances (> 300 Mpc or so) attention focussed more and more strongly on searching for an end to the cosmic ray spectrum. At the same time it became recognized (see Hillas [10] for a detailed review) that 10^{20} eV was rather close to the limit of acceleration by known mechanisms.

It is now known that the rate of cosmic rays above 10^{18} eV is about 60 $\mathrm{km^{-2}sr^{-1}yr^{-1}}$. How that energy scale is established will be explained in Chapter 5 but it is clear from this rate that one requires a collecting area of at least 1 $\mathrm{km^2}$ to collect a large sample of events. With one exception the approach adopted has been to cover the monitoring area, more or less uniformly, with a relatively small number (a few tens) of detectors, each having areas greater than about one square metre. The original configuration of the Volcano Ranch array is shown in Figure 4.1: here the spacing between the 3.3 $\mathrm{m^2}$ scintillators was 884 meters. At each detector of such an array the particle density - more strictly the energy loss - is measured together with the arrival time of the signal at the detector relative to the other detectors. The location of the densest part or "core" of the shower is determined under the assumption of circular symmetry (which has been tested experimentally). The number of particles in the shower is estimated by integrating an empirically determined relationship between density and distance. The event shown in Figure 4.1 was initially ascribed an energy of 10^{20} eV: this was subsequently revised upwards to 1.3 x 10^{20} eV[121].

No Monte Carlo calculations were used to make these estimates but rather a detailed understanding of the physics of electromagnetic cascades was invoked. The event illustrated shows some important features. Although the core of the shower impacts outside the geometrical boundary of the array it is well located by symmetry. Note also that significant signals, on 3.3 $\mathrm{m^2}$ of detector, are seen as far as 2.5 km from the shower axis.

The shower particles travel in a disc which moves, essentially at the velocity of light, perpendicular to the direction of the incoming particle. The relative arrival time data allow reconstruction of the primary direction to about 2^0, this accuracy being a strong function of the number of detectors hit and of the area of each detector. The area is important because the earliest particles are muons which comprise only a small fraction, of order 20% at 1 km, of the total number of charged particles in the shower. This fraction decreases to only $\sim 1\%$ if you include photons. The time dispersion increases as the distance from the shower axis

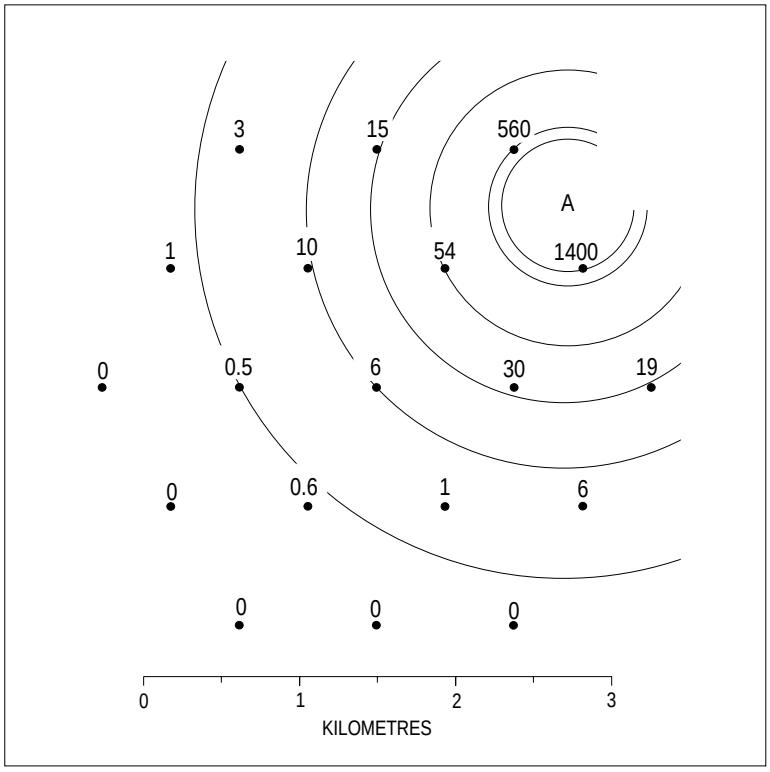

Figure 4.1: EAS observed at Volcano Ranch with energy above 10^{20}eV. The numbers indicate the observed particle densities (cm^{-2}.

increases largely for geometrical reasons. The RMS spread of the scintillator signal at 1 km from the axis is about 500 ns. At the same distance the mean muon arrival time is about 100 ns earlier than the mean arrival time of the electrons.

Other arrays at Yakutsk (Russia), Akeno (Japan), and Narrabri (Australia) were also constructed using scintillation detectors. At Haverah Park (UK) the detectors were water Čerenkov detectors (1.2 m deep and of various areas from 1 m^2 to 34 m^2) spread over 12 km^2: the array ran more or less continuously for twenty years. Much of the design information from the Monte Carlo calculations used by the Auger collaboration have been checked against results from this experiment (see Chapter 5). A particular advantage of the deep water Čerenkov detectors lies in their ability to respond to the large number of photons of relatively low energy (less than about 10 MeV) present in the shower. Empirical studies using unshielded and lead-covered scintillators and the water Čerenkov detectors, now confirmed by the Monte Carlo calculations, demonstrated that photons outnumbered electrons by about a factor 10 at the large distances of interest. The depth of the tank, 3.4 radiation lengths, allowed conversion of the bulk of the photons so that electrons, photons and muons were recorded with high efficiency. The large area (13.5 m^2) of the detectors at the periphery of the array permitted densities to be measured as far as 3 km from the core in the largest events. The rise-times (10-50%) of the water Čerenkov signals were measured at four 34m^2 detectors which were on a 500 m grid at the center of the array.

A completely different method of recording the extensive air showers relies upon the scintillation light (fluorescence) produced through interactions of the charged particles with nitrogen. The light is produced dominantly in the 300-400 nm band and although the fluorescent yield is small (typically 4.5 photons per meter of electron track) a detector has been built to observe the emission. The light can be seen above the sky background on clear moonless nights. This feat was achieved by the University of Utah group who have built a device containing two separated "Fly's Eyes" made up of 880 and 460 photomultiplier tubes respectively, 3.3 km apart. With these units it has been possible to map out the longitudinal development of individual shower events for the first time.

4.2 Energy Spectrum Measurements

The unique feature of the fluorescence detector is that it allows direct measurements of the depth of maximum of the shower and of the shape of the cascade curve. The energy of the particle which initiates each cascade is obtained from the track length integral of the shower-development curve, i.e.,

$$E_{em} = \frac{\epsilon_0}{X_0} \int N_e(x) dx$$

where E_{em} is the total energy dissipated in the electromagnetic channel, ϵ_0/X_0 is the ratio of the critical energy of electrons to the radiation length and $N_e(x)$ is the observed size of the shower as a function of atmospheric depth, x. A correction of about 10% must be made

for the energy which goes into muon, neutrino and hadronic channels. The measurement of N_e depends on accurate knowledge of the factors responsible for light production and transmission through the air, calibration of the optical detection system and determination of the shower trajectory. Allowances for these factors have been discussed in detail by the Fly's Eye group [45].

In both the Fly's Eye detector and the ground array analogies can be seen with the calorimeters used in accelerator based high energy physics experiments. In the former case the atmosphere acts as a homogenous calorimeter just as would a block of scintillator, but on a vastly different scale, and the shower is observed by a large number of photomultipliers to give spatial information. The ground array is a sampling calorimeter, by far the most common type in high energy experiments, but with a single detector layer. Even that is only sparsely implemented. In this case the atmosphere is analogous to the absorber of the calorimeter, usually lead or iron plates. Even though, in a sampling calorimeter, only a small fraction of the energy is actually detected, the principle of calorimetry is that the detected energy can be proportional to the incident particle energy. In the ground array with a single layer non-linear effects arise which can be estimated by Monte Carlo simulations, many features of which (such as the transverse shower shape) can be checked against real showers. Unfortunately we cannot calibrate this calorimeter in a well defined beam! Accordingly the primary energy estimates deduced from the events recorded by the particle detector arrays are dependent to varying degrees on Monte Carlo model calculations. Ingenious methods have been devised to reduce this dependence but, until the calorimetric measurements of the Fly's Eye device were finalized, considerable doubt existed about the validity and systematic errors associated with these approaches. This was despite efforts at cross-calibration made, for example, by operating scintillators within the Haverah Park water Čerenkov array. The proof of the efficacy of these efforts lies in the excellent agreement between the spectral shapes and absolute intensities deduced by Akeno and AGASA, Fly's Eye, Haverah Park and Yakutsk. All groups [121] [46] are agreed that:

1. The shape of the spectrum from 10^{17} to $\sim$ 2 x 10^{18} eV follows a power law $E^{-\gamma}$ with $\gamma = 3.0$ (± 0.05).

2. Above about 2 x 10^{18} eV the energy spectrum steepens ($\gamma \sim -3.2 \pm 0.1$) before recovering to a slope of γ = - 2.7 $\pm$ 0.2, flatter than the slope from 10^{17}eV to 2 x 10^{18}eV. The differential intensities at 10^{19} eV are in excellent agreement (see Table 4.1) demonstrating that the processes of energy derivation and the systematic errors are well understood.

The spectra from the Haverah Park, Fly's Eye and AGASA work are shown in Figures 4.2a, 4.2b and 4.3 where the slope changes just described are clearly seen. This is particularly evident in the data from the latter two experiments which have a much greater exposure below 10^{19} eV than the Haverah Park array. It is clear from the diagrams that the agreement in flux estimates above 5 x 10^{19} eV, where the exposures are similar (see Table 4.2) is less good, at least in part because of the limited exposures. At 10^{20} eV the flux is $\sim$ 0.5 km^{-2} century^{-1} sr^{-1} and with the present exposures it is not surprising that

Array	$m^{-2}\ s^{-1}\ sr^{-1}\ eV^{-1}$
AGASA	2.91×10^{-33}
Fly's Eye	2.38×10^{-33}
Haverah Park	2.22×10^{-33}
Yakutsk	3.39×10^{-33}

Table 4.1: Comparison of differential intensities at 10^{19} eV for different experiments

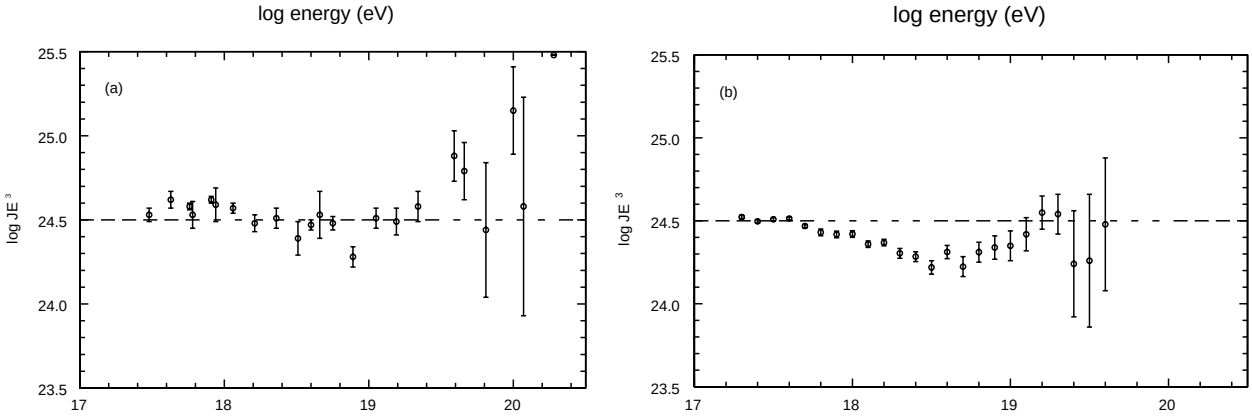

Figure 4.2: Differential energy spectrum ($\times E^3$) as observed by, (a) the Haverah Park array, (b) the Fly's Eye experiment.

there are uncertainties. Only a few events are expected from extrapolations of the spectrum measured at lower energies. It is precisely the question of the spectrum above 10^{20} eV that we seek to answer with the Auger detector. The exposures so far achieved at 5 x 10^{19} eV are shown in Table 4.2. For the particle detector arrays, these exposures correspond to showers detected within 45^0 of the zenith. Even at 10^{20} eV the maximum of the shower is above the level of the detectors, and its amplitude is attenuated at a rate which depends on the shower components detected. For scintillators the attenuation length is $\sim$ 320 g $\cdot$ cm^{-2}, but for water Čerenkov detectors the corresponding figure is 750 g $\cdot$ cm^{-2}, so that showers can be detected at a useful rate at even larger angles. This is most clearly seen by comparing the declination distributions registered by Volcano Ranch (all zenith angles) and Haverah Park (zenith angle $< 60^0$) shown in Figure 4.4. The current total exposure of 1000 km^2 y sr will thus be exceeded by <u>one</u> of the two 3000 km^2 detectors of the Auger project in about 100 days.

The limited data available above 5×10^{19} eV have, until recently, made it difficult to answer unequivocally the question of whether or not events exist above the GZK cut-off. However the early claims by Volcano Ranch[122] and Haverah Park[123] that events with energies close to 10^{20} eV do exist have recently been supported by results from the other groups. In 1990 the Yakutsk group described[124] an event with an energy of $(1.1 \pm 0.4) \times 10^{20}$ eV. While this is undoubtedly an event which has been produced by a very energetic primary,

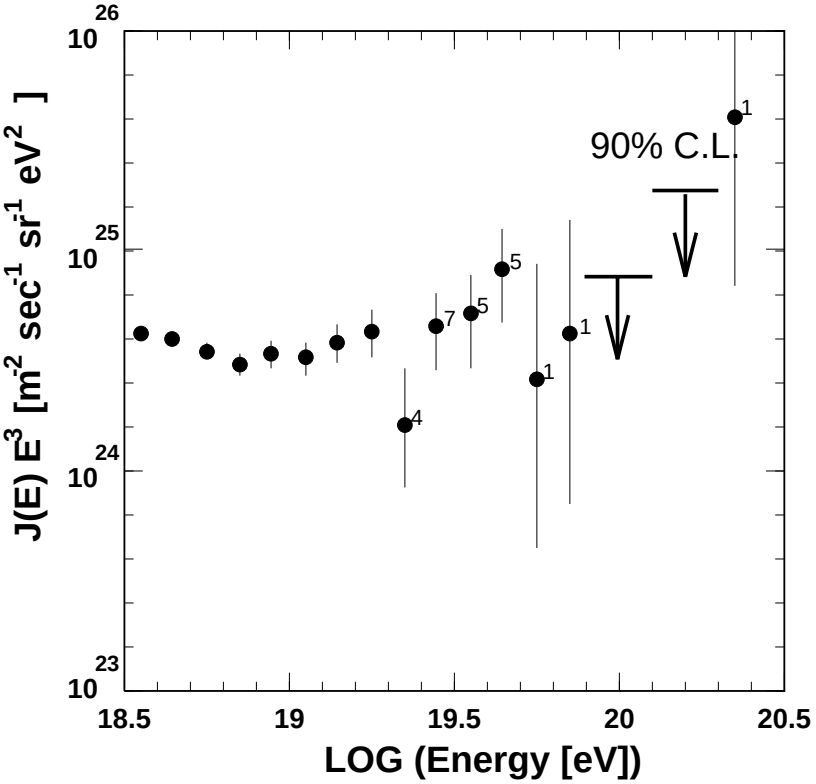

Figure 4.3: Differential energy spectrum ($\times E^3$) as observed by the AGASA experiment.

Array	km^2.y.sr
AGASA (100 km^2)	171
Fly's Eye (stereo)	151
Fly's Eye (monocular)	930
Haverah Park (12 km^2)	270
Yakutsk (25 km^2)	490
Total	1082

Table 4.2: Comparison of integrated exposure at $\sim 5 \times 10^{19}$ eV for different experiments. Note that the AGASA experiment is still operating, and that the total excludes Fly's Eye monocular exposure.

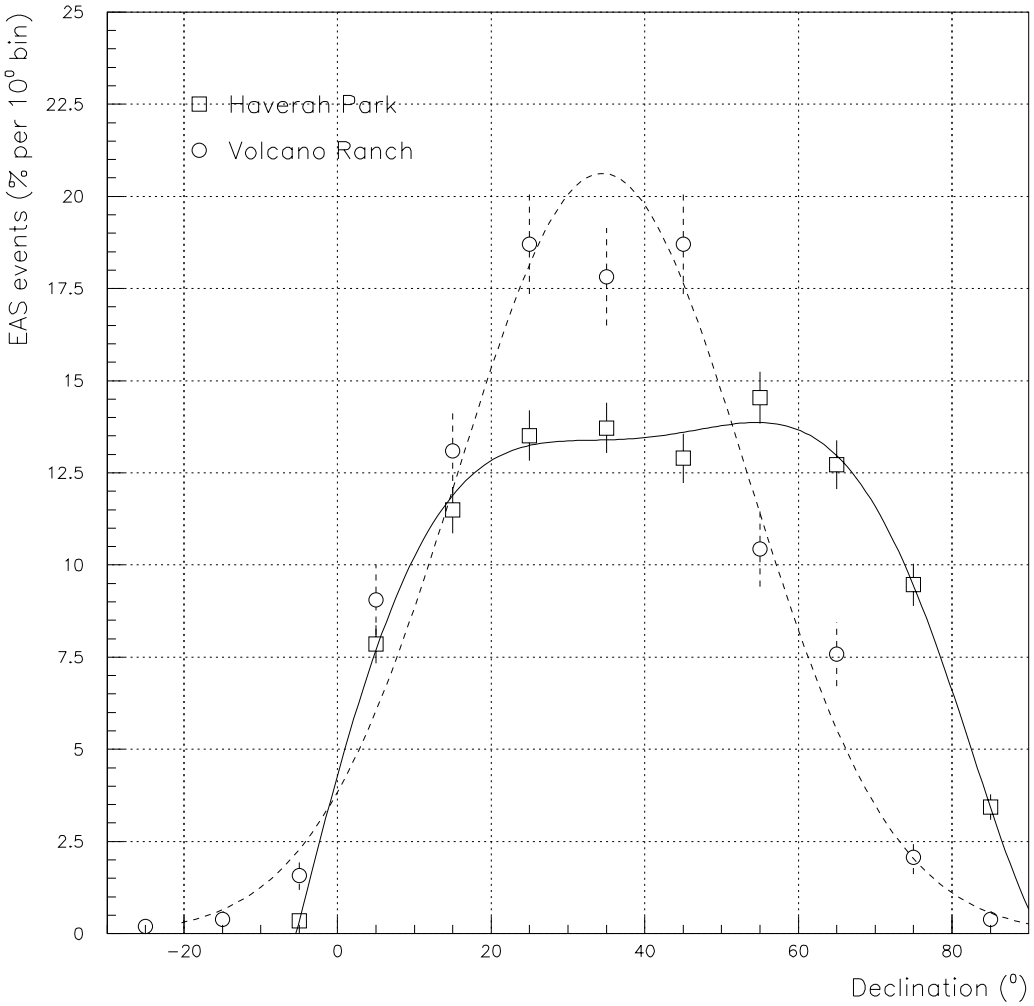

Figure 4.4: A comparison of the declination distributions of showers recorded by large water Čerenkov and scintillator EAS arrays. The water Čerenkov data is taken from the Haverah Park array at an atmospheric depth of 1020 g cm^{-2} and latitude of 54^0 N, and the scintillator data from the Volcano Ranch array at an atmospheric depth of 834 g cm^{-2} and latitude of 35^0 N. Shower size is $1 \times 10^{18} < E < 4 \times 10^{18}$ eV. Haverah Park data are restricted to zenith angles $< 60^0$, whilst the Volcano Ranch data are for all zenith angles. The FWHM of the Haverah Park distribution is $\approx 60^0$ as opposed to $\approx 45^0$ for Volcano Ranch. The water Čerenkov array has approximately twice the solid angle sky coverage.

the almost completely muonic nature of the particles detected and its relatively large zenith angle (58.7^0) make it hard to be definite about the energy assignment.

In 1993 the Fly's Eye group reported[6] a monocular event for which the assigned energy is $3.2_{\pm}0.9 \times 10^{20}$ eV. This is the highest energy event ever recorded and its reconstructed cascade curve is shown in Figure 4.5. Although the shower size at maximum is extraordinary, there is nothing unusual about the shape of the longitudinal profile. The amplitude rises and falls with the characteristic smooth functional form of air showers. Because this event was not measured stereoscopically, there is some uncertainty in the geometric reconstruction. If the shower were closer to the detector, the inferred size would be smaller, so the geometric uncertainty implies an energy uncertainty also. The shower depths would also be different, however, if the shower were closer. Changing the geometry to bring the energy down below 10^{20} eV would require the primary particle to have penetrated more than 800 g/cm^2 before interacting. That would mean an incredible penetration of more than 20 mean free paths as well as an implausibly large error in the geometry. Another source of energy uncertainty is atmospheric attenuation of the fluorescence light. If the light suffered less attenuation than calculated, then the true light production and shower size would have been smaller than estimated. However, even using a perfectly clear atmosphere (Rayleigh scattering only), the energy is still calculated to be 2.2×10^{20} eV. It should also be noted that the fluorescence energy measurement is a calorimetric measure of the electromagnetic cascade. The electromagnetic cascade energy measurement for this event was 2.9×10^{20} eV, and it was assumed that 10% additional energy is in muons and neutrinos. Although some systematic error in energy calculations can be attributed to uncertainty in the atmospheric fluorescence efficiency, this uncertainty is not greater than 20%. The lower bound on this particle's energy is well above 10^{20} eV.

Using their 100 km^2 array of 111 2.2 m^2 scintillators, the AGASA group have observed a particularly clean event, at a zenith angle of 23^0, for which the primary energy is measured [7] to be in the range of 1.7 to 2.6 x 10^{20} eV. This event fell in such a position that the core of the shower is in a part of the array which is relatively densely populated with detectors. The largest scintillator density is $\sim$ 25,000 m^{-2} and is only about 250 m from the core. The primary energy is derived by first obtaining the area density of particles at 600 m, $S(600)$, from the density data, normalizing this to what would have been observed had the event come from the zenith rather than from 23^0 and then converting this number to primary energy using a Monte Carlo calculation. There are thus three sources of uncertainty in the energy estimate. These will be discussed briefly in turn. For this event $S(600)$ is measured as 892 m^{-2}.

The use of $S(600)$ as an energy estimator is a technique which is well established. It is a development of an earlier idea of Hillas's first applied extensively to the Haverah Park water Čerenkov array. Extensive series of model calculations by him and others have shown that variations in shower models and mass composition affect the primary energy estimates only weakly. $S(600)$ can be found rather accurately from the data: Monte Carlo studies of the analysis techniques give the uncertainty as +21% and -6.6%. The normalization from 23^0 to the vertical depends upon empirical information about the attenuation length (see above). The vertical value of $S(600)$ is between 892 and 1065 m^{-2}, where the smaller

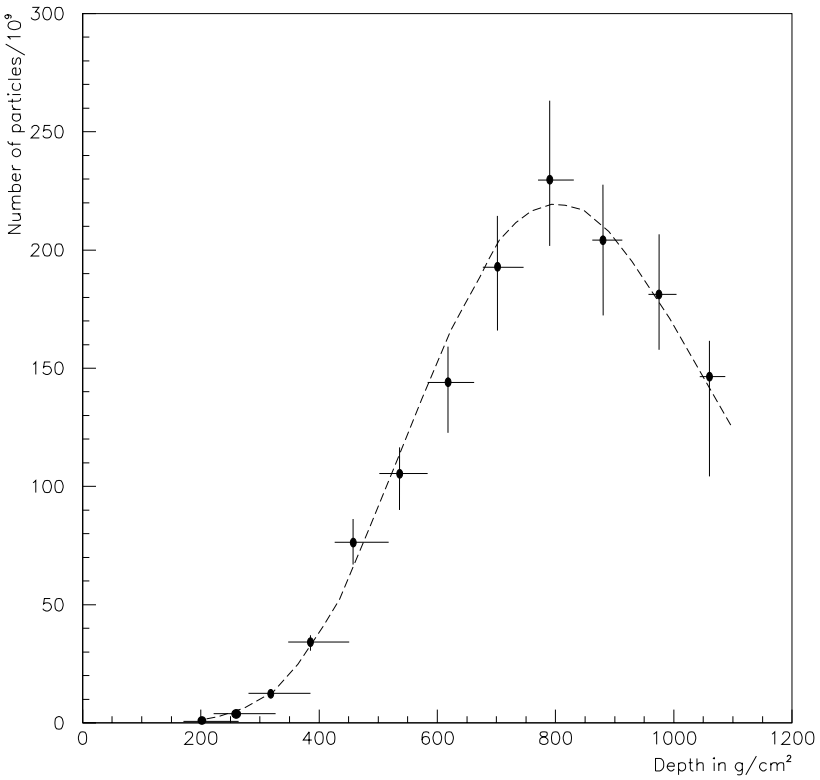

Figure 4.5: Longitudinal cascade development profile for the Fly's Eye 3×10^{20} eV event, the largest cosmic ray air shower ever recorded.

value would apply if there was no attenuation correction to be made. Taking the smaller figure and subtracting 6.6%, gives a lower bound (68% confidence) limit of 833 m^{-2}. The conversion of the vertical $S(600)$ value to primary energy is model dependent; that used by the AGASA group is a QCD model which gives $E = 2.0 \times 10^{17} S(600)$ eV. The systematic error which may be present can be estimated by comparison of the 10^{19} eV differential intensities measured by AGASA and Fly's Eye (Table 4.1). This would suggest that the two quite different approaches to energy estimation agree within 10%, with the AGASA energies being systematically greater than the Fly's Eye estimates at 10^{19} eV.

The extrapolation by a further order of magnitude is, of course, uncertain. However, the fall off with distance of the unshielded scintillator signals is not anomalous by comparison with expectation from lower energies. Furthermore muons are detected in seven detectors at a normal density level. The temporal distribution of the signal in the 30 m^2 scintillation counter at 1920 m from the shower axis is also consistent with expectation. There is thus high confidence that the AGASA event is above 10^{20} eV and well above the GZK cut-off.

While the energy estimates must be subject to still uncertain systematic errors, the very good agreement between the intensity measurements from four rather different experiments (Table 4.1) argues strongly that there is a proper understanding of the uncertainties at the 20% level near 10^{19} eV. Furthermore, the characteristics of the showers recorded by Fly's Eye and by AGASA are totally consistent with what is expected for such events by straightforward extrapolation from well-known and understood behavior near 10^{19} eV. The agreement of the different methods makes it quite convincing that the discovery of these two events finally settles the question of the existence of cosmic rays above the GZK cut-off. What is not yet decided is the spectral shape and, of course, the fundamental question of the limit to the energy reached by cosmic rays. These are further problems which the Auger observatories are designed to answer.

4.3 The Immediate Future

The only high energy cosmic ray observatory currently taking data is the 100 km^2 scintillator arrays at AGASA. It is planned to continue operating this device until the year 2000, by which time the exposure will have reached about 1000 $km^2 \cdot sr$ year. A further 10 events might be expected above 10^{20} eV, though with only limited information about mass composition. The Yakutsk array has been contracted in size to study some specific features of shower properties near 10^{19} eV. Two projects are under development. The Utah Fly's Eye group has entered into collaboration with the University of Adelaide, Columbia University and the University of Illinois to construct a next-generation air-fluorescence detector, Hi-Res. The first stage of construction of this detector has been funded and is underway. Two sites, twelve kilometers apart, have been chosen at which a total of 56 two metre diameter mirrors will be installed. The mirrors are arranged in rings, each ring subtending 14^0 of elevation. Two complete rings at one site and one partial ring at the second site will be built. Each mirror will have a 256 phototube array at its focal plane. Each phototube will view a one degree by one degree section of the sky. The signals from the phototubes will be digitized

using FADC electronics so that both the amplitude and the detailed pulse shape will be available for later analysis.

All events will be recorded by both sites in stereo for good control of experimental uncertainties and redundancy of measurement. The aperture for this Stage I detector is optimized for greater than 10 EeV energy (1 EeV = 10^{18} eV) and approaches 7500 km^{2}sr at 100 EeV. With a 10% duty factor, this detector should record 10 events per year above 100 EeV and 200 events per year above 10 EeV if the stereo spectrum observed by the Fly's Eye, quite consistent with that of other groups, continues. This is an order of magnitude increase in statistics over the monocular Fly's Eye. The resolution in energy and X_{max} is also much improved over the Fly's Eye detector, approaching 10% statistical uncertainty in energy and 15 gm/cm^2 mean uncertainty in X_{max}. This detector can also search for a possible gamma ray and neutrino flux.

A second fluorescence detector is at the prototype stage. Known as the Telescope Array, it is proposed by a consortium of Japanese universities and the University of Utah, led by the University of Tokyo. The goal is to build an air fluorescence detector with a pixel size of $1/4^0$ by $1/4^0$ using multi-anode photomultiplier tubes. With this small pixel size, sky noise is essentially negligible. The array is designed to be sensitive also to low energy gamma rays above 100 GeV by detecting Čerenkov light from these showers. It includes 120 fixed and 120 steerable altazimuth 3 m diameter mirror dishes positioned at two stations 40 km apart. The aperture of such an array at 100 EeV, excluding the duty cycle, is estimated to be approximately 40,000 km^{2}sr. The energy resolution is 10% and the resolution in X_{max} is 10 gm/cm^2. Prototype mirror and PMT clusters are being tested at Dugway and AGASA. The Japanese groups have indicated their willingness to provide a fully developed version of this detector for one of the sites of the Auger project.

4.4 The Physics and Astrophysics Potential of the Auger Project

The unambiguous discovery of cosmic rays above 10^{20} eV is of exceptional astrophysical interest as judged by the recent flood of theoretical papers. The sources of the most energetic events are required, by the GZK cut-off, to be rather close (less than $\sim$ 50 Mpc) and energy arguments (eg Greisen 1965[125], Cavallo 1978[126], Hillas 1984[10], Cesarsky 1992[127]) imply that they must be rather remarkable. The Auger observatories are planned to provide a high statistics measurement of the energy spectrum (with a typical error of 20%) and arrival direction (with a typical error of 2^0) distribution of the highest energy events. At the same time inferences about the mass composition will be drawn from a careful study of the variations of detailed shower properties with energy as well as from anticipated differences in the arrival direction patterns of sub-sets of "heavy" and "light" nuclei. There is no doubt that there are events to observe beyond 10^{20} eV. In ten years of operation of the two detectors, each of 3000 km^2, between 600-1000 events above 10^{20} eV are expected from the whole sky. If the power law spectrum measured at 10^{19} eV continues to 10^{21} about 5 events will be observed above that energy.

It is important to recognise that detectors in both the Northern and Southern Hemispheres are essential, as the radio galaxies (one of the putative conventional sources of the highest energy cosmic rays) close enough to be the sources of such particles are anistropically distributed around the supergalactic plane, and thus across the two hemispheres. A detector at a single site cannot properly address the arrival direction problem. Further development of either of the fluorescence detectors under study to provide the aperture needed is not the most cost-effective way to make the necessary measurements. Furthermore, the use of a hybrid device, with a fluorescent detector and a particle detector combined, offers unique opportunities to study many parameters in the same event. In particular, one will be able to obtain the depth of maximum, the muon-electromagnetic ratio and the spread of the particle arrival times, all of which are crucial parameters in attempting to measure the primary mass composition.

High statistics observations of cosmic rays beyond 10^{20} eV will increasingly constrain theories of cosmic ray origin whatever the outcome of the observations. Most clear cut would be the identification of specific sources by the observation of clusters of the most energetic events from a few regions of the sky. A spin-off from such an outcome would be much needed information on the magnetic field structure in the region out to 50 Mpc from our galaxy. At the other end of the scale, isotropy at ever increasing energy might favour the exotic models which associate the most energetic events with topological defects or gamma ray bursts. The higher the energy of the most energetic event recorded, the more intriguing the theoretical problems become. The wealth of data to be obtained promises new insights into particle physics and astrophysics as discussed in Chapter 3.

Chapter 5

Air Shower Measurement Techniques

5.1 Extracting the information

An air shower is a particle cascade in the atmosphere initiated by the interaction of an energetic cosmic ray. If the primary particle is a nucleon or a nucleus, the cascade starts with a hadronic interaction. The number of hadrons in the shower increases through subsequent generations of particle interactions. In each generation, however, a significant fraction (about 20%) of the energy is transferred to an electromagnetic cascade by the rapid decays of π^0 mesons. The hadronic cascade eventually gives up all its energy. The electromagnetic cascade dissipates roughly 90% of the primary particle's energy through ionization. The rest of the energy is taken by muons and neutrinos from charged pion decays.

Each air shower is a swarm of particles moving at the speed of light through the atmosphere. They ionize atoms in the air, and the ionized nitrogen radiates near-UV photons. From a distance, therefore, the fluorescence detector sees the shower as a spot of light whose motion is along the *shower axis*. The particle swarm is not however confined to the shower axis. Largely due to multiple Coulomb scattering, the particles spread out in a pancake-shaped *shower front* which can be detected over a large area on the ground.

5.1.1 The shower axis

"Geometrical reconstruction" is the important procedure of determining the shower axis. The direction of the shower axis is the cosmic ray's arrival direction. If three ground stations record the shower, the shower direction can be computed by triangulation, finding the unique downward going speed-of-light shower front which accounts for the three positions and arrival times.

If more than three stations trigger, a least squares method is used to find the plane front which fits best. The shower *core*, where the axis meets the ground, must be determined in order to know how far from the axis the various particle density measurements were made. The core can be determined by exploiting circular symmetry and fitting the measured

densities to an expected *lateral distribution function.* "This functional dependence of particle density on core distance is known empirically at slightly lower energies (see discussion in section 6.2.3), and it should be determined by HiRes and the Telescope Array using FADC measurements of how a pixel responds as it accumulates light starting with the near edge of the shower and ending with the far edge [57]. Those observatories should be able to determine how the shape of the lateral distribution correlates with X_{max}. The Auger Observatory's fluorescence detector will also make an empirical determination of the lateral distribution for nearby showers this way, and those shapes will then be further correlated with muon densities.

A better determination of the axis is achieved if the shower is also measured by the fluorescence detector. The entire axis, including the core, is then constrained to lie in the plane containing the fluorescence detector and the pointing directions of those pixels illuminated by the shower axis. Locating the shower axis within that shower-detector plane is achieved using timing, both of the ground station detectors and of the fluorescence spot as it passes the various pixels.

With or without the fluorescence detector, determination of the shower axis improves with the size of the shower. This is because greater numbers of particles (photons for the fluorescence detector pixels) give a better measure of the passing shower front, and because more ground stations can be used in the fit. For measurements by the ground array alone, the typical angular resolution for vertical showers at 10 EeV is 3°, improving to 1.3° at 100 EeV. The core position error decreases from 82 m to 47 m. For hybrid measurements (fluorescence detector with ground array), the angular resolution improves from 0.25° to 0.20° over the same energy decade, and the core position uncertainty decreases from 35m to 20m. (See the following chapter for details of these methods and results.)

5.1.2 Energy

The cascade of ionizing particles can be monitored in the atmosphere via nitrogen fluorescence. The amount of light produced at each atmospheric depth is proportional to the shower *size*, i.e. the number of charged particles. By measuring the light produced at many depths, the fluorescence detector determines the shower's *longitudinal profile* $s(X)$. The atmospheric depth X is measured in units of g/cm^2 along the shower axis. As the shower size increases, the original energy gets divided among more and more particles. The average energy eventually becomes low enough that ionizing particles are removed from the cascade, by ionization energy losses, at a rate exceeding their production rate by bremsstrahlung and pair production. The shower size therefore reaches its maximum size s_{max} at some atmospheric depth X_{max} (its *depth of maximum*), and the size decreases beyond that depth.

The integral of the longitudinal profile is a calorimetric measure of the total electromagnetic shower energy,

$$E_{em} = 2.2\ MeV/g/cm^2\ \times \int s(X)\ dX,$$

since an average charged particle in the cascade deposits 2.2 MeV into the atmosphere in

each depth interval of 1 g/cm^2 [58]. The portion of the electromagnetic cascade reaching the ground is included by fitting a functional form to the observed longitudinal profile and integrating that function past the surface depth.

This electromagnetic cascade energy is a lower bound for the energy of the primary cosmic ray. The amount of unmeasured energy which goes into the ground as muons and neutrinos depends on the shower development and is subject to fluctuations. For protons, the unmeasured energy is about 5% on average. For iron primaries, the mean is about 15%. The Fly's Eye analysis assumed a uniform 10% unmeasured energy. That gives no more than a 5% expected error for any nucleus and a 10% error for γ-rays. The energy not measured by the fluorescence detector can be estimated using the measured muon densities. (The measured X_{max} provides correlated information. Larger X_{max} at fixed electromagnetic energy implies less energy in muons and neutrinos, as will be discussed below with composition issues.) The fraction of primary energy not dissipated by the electromagnetic cascade can be estimated shower by shower by exploiting the ground array's muon information and the X_{max} measurement.

Ground arrays have traditionally determined the shower energy by reducing the measurements to a single quantity which is known from shower simulations to correlate well with total energy for all primary particle types. The Haverah Park energies are based on energy correlation with $\rho(600)$, which is the energy deposition per square meter in water tanks at a distance of 600m from the shower core. The AGASA detector uses $S(600)$, the energy deposition density in plastic scintillators at 600m from the core. Because of the larger spacing between particle counters in the Auger ground array, it is more reliable to determine densities at 1 km from the core rather than at 600m. An important advantage of the Auger detector will be the separate measurements of muon density (mu) and the electromagnetic particle density (em), both at 1 km. The pair (mu,em) should be a more powerful indicator of energy than either density by itself or a combination of them such as $\rho(600)$.

The hybrid data set will provide a distribution function on the 3-dimensional parameter space (mu,em,E). Here E is the fluorescence detector's energy measurement (optimally corrected for unmeasured energy based on its measured X_{max} and the mu/em ratio measured by the ground array). For any pair (mu,em) there should be at most one value of E around which the distribution function is non-zero. In this way, the hybrid data set provides a map from the ground array measurement (mu,em) to the shower energy. The ground array is thereby able to measure shower energy without reference to any hadronic interaction model or cascade simulation.

In the determination of shower energy, there are numerous advantages in the Auger detector's hybrid configuration. A shower measured in hybrid mode has an internal consistency check on the energy, since the ground array and the fluorescence detector independently measure the shower size at ground level. The fluorescence detector "trains" the ground array as explained in the previous paragraph, so the ground array can determine a shower's energy without the fluorescence detector and without reliance on any air shower development simulation. The ground array will also assist the fluorescence measurements. Many showers will be detected at large distances where atmospheric attenuation uncertainty can cause uncertainty in the longitudinal profile normalization. The array's measurement of shower size at

ground level will provide the crucial normalization for those longitudinal profiles.

5.1.3 Primary mass

An air shower's depth of maximum X_{max} is a clue to the mass of the primary nucleus. At the same total energy, an air shower from a heavy nucleus is expected to develop faster than a shower initiated by a proton. This is partly because a heavy nucleus has a larger cross section, so it tends to interact sooner than a proton. More importantly, however, the heavy nucleus behaves much like a superposition of its constituent nucleons. An iron nucleus produces an air shower which can be approximated as the superposition of 56 nucleon showers, each with 1/56th of the iron nucleus' energy. The depth of maximum for nucleon showers increases by at least 55 g/cm^2 for each decade of energy, so reducing the energy by 1/56 decreases the expected X_{max} by approximately 100 g/cm^2. An iron shower therefore has an expected X_{max} about 100 g/cm^2 less than the expected X_{max} for a proton shower of the same energy.

The muon content of air showers may be an even more powerful indicator of primary mass. The same superposition model of a heavy nucleus can be invoked to explain why an iron shower produces more muons than a proton shower. The energy is divided among the constituent nucleons, so it takes fewer generations to distribute the hadronic energy into low energy pions which can decay. That means less energy is lost to the electromagnetic cascade, which results in more low energy pions than in a proton shower of the same energy. This is a general argument which pertains to all hadronic interaction models.

To evaluate quantitatively the relative muon production in heavy nucleus showers *vs.* proton showers, one can start with the fact that muon production in proton showers increases with energy as $E^{0.85}$. Muon production does not increase linearly with energy because more generations are required at higher energy to reduce the average pion energy down to where decay becomes likely. The extra generations mean a larger fraction of the energy is lost to the electromagnetic cascade, so a smaller fraction of the original energy gets delivered to those low energy pions which decay. Considering a nucleus-initiated shower as a superposition of A showers, each with energy E/A, we find that the total number of muons is

$$N_\mu^A \propto A(E/A)^{0.85},$$

or, comparing to proton showers,

$$N_\mu^A = A^{0.15} N_\mu^p.$$

Thus we expect that an iron shower ($A = 56$) will produce about 80% more muons than a proton shower of the same total energy.

The foregoing explanations for why X_{max} and muon number both correlate with primary mass may suggest that X_{max} and muon production are both controlled by the same shower development feature, so measuring both is redundant. To some extent that is the case. If a proton's primary collision were somehow to yield 56 equal-energy hadrons which all go on to interact, then its longitudinal profile should resemble the expected iron profile for the same total energy, and its muon content should be consistent with what is expected in an iron shower. In shower simulations, X_{max} and muon number are indeed correlated. But

the correlation is far from perfect because of additional fluctuations which do not produce strongly correlated effects. For example, fluctuations in the number of charged *vs.* neutral pions in the first generation affect the number of low energy pions – hence muons – more than the shape of the electromagnetic longitudinal profile (e.g. X_{max}). While not independent, X_{max} and muon density are separate handles on composition. Moreover, they are measured with totally independent instruments.

Similar remarks pertain to a third measurable quantity which correlates with the primary mass: the rise-time ($\tau_{1/2}$) of the particle pulse far from the shower core. Like X_{max} and muon density, its correlation with mass can be understood in terms of the shower development. Earlier shower development means more nearly equal paths for detected particles, so they arrive more tightly bunched in time. The effect is accentuated by the larger fraction of muons in the pulse since they undergo less scattering and arrive earlier, on average, than electromagnetic particles.

These three quantities – depth of maximum, muon density, and rise-time – should be used in concert to determine the cosmic ray nuclear composition and to find the most likely mass for each primary particle. The hybrid data set will provide a distribution function on the 3-dimensional space (mu:em,$\tau_{1/2}$,$\hat{X}_{max}$). Here mu:em is the muon to electromagnetic density ratio at 1 km from the core,$\tau_{1/2}$ is the rise-time for pulses at that distance, and

$$\hat{X}_{max} \equiv X_{max} - \frac{d < X_{max} >}{d\ Log\ E}(Log\ E - Log\ E_0)$$

is the measured X_{max} corrected to a convenient reference energy E_0 using the observed *elongation rate* $\frac{d<X_{max}>}{d\ Log\ E}$. Because the three measured parameters are correlated, the distribution function might be concentrated around a 1-dimensional curve in this space, where the curve could be parameterized by shower development speed.

The observed distribution function on (mu:em,$\tau_{1/2}$,$\hat{X}_{max}$)-space should be compared with the expected distribution function for alternative composition hypotheses. A potential difficulty is that the expected distribution function may also depend on untestable properties of hadronic interactions at the highest energies. It is conceivable that the composition determination could be hindered by inadequate knowledge of the first generations of hadronic interactions.

It is likely, however, that the relevant interaction model parameters (e.g. energy dependence of cross section, inelasticity, and multiplicity) will be well enough constrained that ambiguities due to the model freedom will be small compared to differences expected from different composition hypotheses. Significant constraints on the hadronic model have been imposed by the Fly's Eye data. HiRes, AGASA, and the Telescope Array data will provide stricter constraints. By combining muon and electromagnetic particle measurements with X_{max} measurements, shower by shower, the Auger Project will provide valuable additional constraints. The Fly's Eye analyses have demonstrated that such data can be used both to constrain the interaction model and also to make composition inferences. In the Fly's Eye case, the model constraints derived from the need to explain the full range of the X_{max} distribution with nuclei of $1 \leq A \leq 56$. The energy dependence of the mean X_{max} was then used to infer a composition changing from heavy nuclei to light nuclei in the energy decade

from 1 to 10 EeV.

Above 10 EeV, γ-rays produce a characteristic signature due to the LPM effect [37]. This effect reduces the high energy electromagnetic cross sections, so the longitudinal profile becomes longer than that obtained using Bethe-Heitler cross sections. At Auger Observatory shower energies, a γ-ray shower is expected to have a significantly broader profile than any hadron-induced shower of equal energy, and the γ-ray showers should exhibit large fluctuations in X_{max}. The LPM effect grows with the γ-ray primary energy. The fluorescence detector's longitudinal profile measurements will enable a sensitive search for any γ-ray population.

After an approximate composition determination has been achieved, it will be possible to evaluate a maximum likelihood mass A for each shower, based on its measured (mu:em,$\tau_{1/2}$,$\hat{X}_{max}$) values. It may be very useful for anisotropy studies to exclude low rigidity heavy nuclei in order to search for sources with protons whose trajectories have suffered less magnetic bending. Moreover, mass likelihoods should make it possible to measure the energy spectrum separately for different mass groups, if the composition is mixed. This mass separation can be done for the full Auger data set, not just the showers measured in hybrid mode. Since $\hat{X}_{max}$ is significantly correlated with mu:em and $\tau_{1/2}$, the likelihood analysis can be done also for events without an $\hat{X}_{max}$ value.

At the time of writing, work on the multiparameter composition sensitivity is still in progress. The composition resolution based on mu/em alone is exhibited in Figure 5.1. The resolution based on $\hat{X}_{max}$ alone is shown in Figure 5.2. Note that, in both cases, the air shower and detector response have been simulated with all relevant fluctuations. Changing the hadronic interaction model at the highest energies could change the locations of the peaks in those plots, but their separations should have little dependence on model variations.

5.1.4 New particle physics

Almost all the physics of air showers is well established. Electromagnetic subshowers can be modeled with great confidence. The hadronic interactions can also be confidently modeled, except for the first few generations of interactions where center-of-mass energies greatly exceed those of collisions studied in accelerator experiments. Collider experiments have explored hadronic interactions up to $\sqrt{s} = 2\ TeV$. The Auger Project focuses on cosmic rays with energies above 10^{19} eV, for which the (nucleon-nucleon) center-of-mass energy is $\sqrt{s} = 140$ TeV.

Cosmic ray studies have a tradition of augmenting basic knowledge of particle physics. The Auger Observatory can expect to provide valuable information about particle interactions at a new frontier of energy. As happened with the Fly's Eye X_{max} distribution, combined measurements of mu:em, $\tau_{1/2}$, and $\hat{X}_{max}$ can be expected to constrain the interaction model even without independent knowledge of the composition. Measuring air showers provides not only information about the cosmic ray population (arrival direction patterns, energy spectrum, and composition), but there is also new particle physics to be extracted.

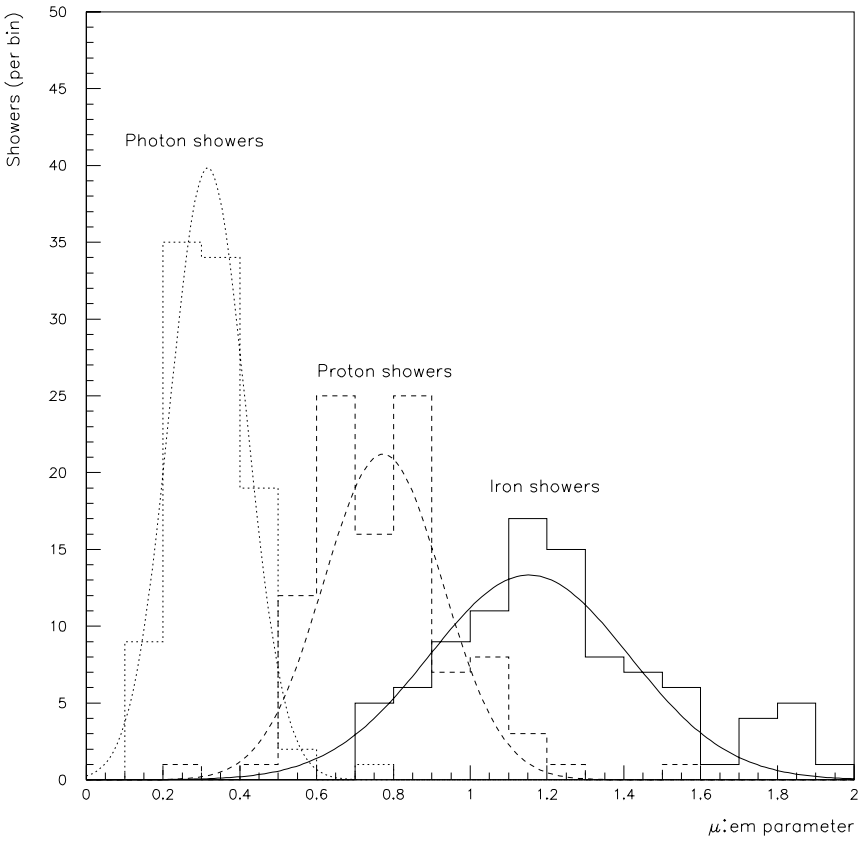

Figure 5.1: Predicted primary particle separation for the proposed Auger water Čerenkov surface array. Each distribution is from 100 showers at 5×10^{19} eV incident at 30°. The mu:em parameter is extracted from the simulated PMT time/amplitude profiles of all triggered detectors more than 1.4 km from the shower core.

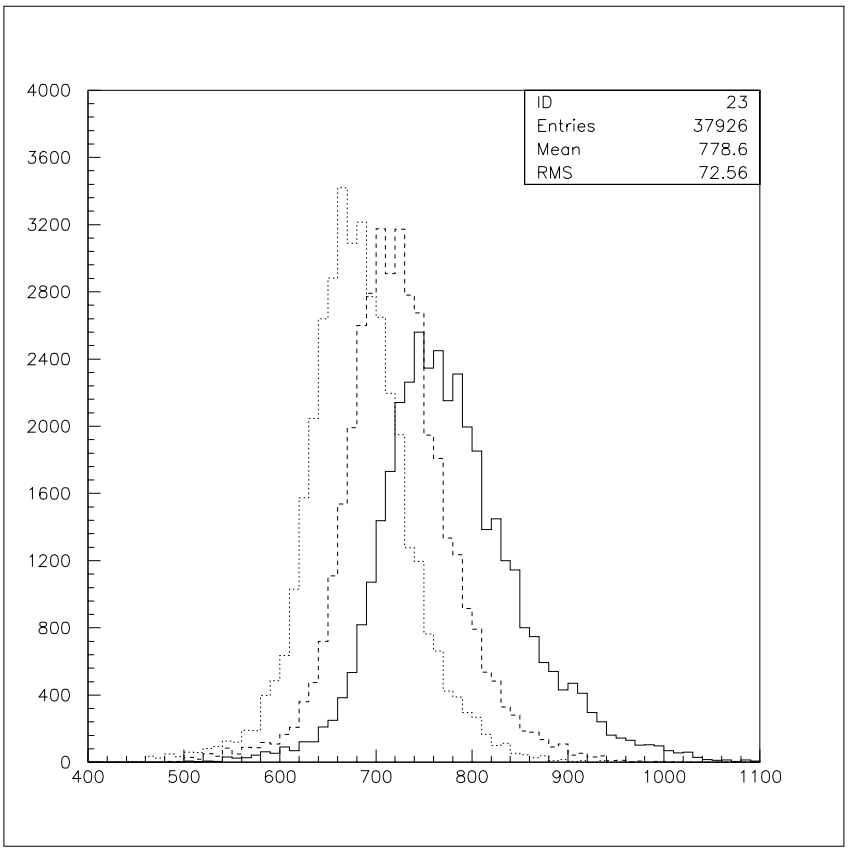

Figure 5.2: The reconstructed depth of maximum distributions for three mass components (iron, carbon and protons). Showers up to 30 EeV are included, and all X_{max} values have been corrected by the elongation rate to a reference energy of 1 EeV. There are equal numbers of events in each histogram.

Lack of complete *a priori* knowledge of hadronic interactions at the highest energies has only a limited impact on the Auger cosmic ray studies. The arrival directions can be measured completely independently of any model ambiguity. The electromagnetic shower energy is also measured without any reference to the hadronic model. It provides a solid lower bound for the cosmic ray's energy. The unmeasured energy is expected to correlate with shower development in a manner which is easily modeled. (However, systematic energy errors are conceivable if, for example, there were an unmodeled enhanced production of prompt muons which steal a non-negligible fraction of the total energy in the first interaction.) Composition studies cannot be totally divorced from models of the hadronic cascades' first few generations, but the relevant model parameters should be determined well enough to allow analysis of the mass distribution.

Learning how to model the highest energy interactions is vital for a comprehensive composition determination with the Auger data set. Developing and testing the interaction model will be a high priority of the Project. A meeting in conjunction with the Design Group Workshop was held at Fermilab in early April to discuss the issues and set a course for future work.

5.2 Numerical simulations

Numerical simulation of air showers is an essential tool for designing the detector and evaluating its performance. The simulation program needs to be efficient. All Auger Observatory showers produce at least tens of billions of particles. It is computationally prohibitive to simulate so many particles or to record simulated data for so many particles. A viable computer program must have an unbiased method for computing all relevant shower properties using a sampled subset of the full shower. The simulation program must also be accurate in modeling the relevant aspects of particle interactions. It must produce results which are consistent with those properties of giant air showers which have been measured.

As discussed above, almost all of the relevant physics is well established. Ambiguity in modeling the highest energy hadronic interactions has little impact on evaluating detector performance. The detector resolution concerns differences in measurable quantities (e.g. particle density from a 15 EeV shower *vs.* density from a 10 EeV shower, or X_{max} for an iron nucleus *vs.* X_{max} for a proton at the same energy). Such differences in measurable quantities have less model dependence than the quantities themselves.

We have elected to use principally the MOCCA program for the design of the Auger Project detectors. This program is described below. We then discuss some aspects of hadronic interactions which are addressed by a different program (SIBYLL) which can be used within the MOCCA code. Following some comments on the ways in which the nucleus-nucleus interactions are treated, we conclude by highlighting important verifications of MOCCA using air shower data.

5.2.1 The MOCCA Simulation Program

This program was created by A.M. Hillas for use with the Haverah Park experiment [52]. Variations have since been successfully used by many cosmic ray experiments studying events from 10^{12} eV to 10^{20} eV. The code performs both of the main functions required of an EAS simulation: the generation of the electromagnetic cascade through the atmosphere and the details of individual hadronic interactions and decays.

At the time MOCCA was created, the speed of computers was very slow by today's standards. This program employs novel and efficient methods for generating and following the many particles in large air showers.

Particle production in hadronic collisions is simulated using a splitting technique [54]. The center-of-mass energy in the collision is apportioned between a leading particle and the production of new particles. The energy assigned to new particles is subdivided into four parts. Each part is further split in two, one of which is assigned to a single pion. The process is iterated on the unassigned energy packets until all the energy of the initial interaction is exhausted. The leading nucleon and newly produced pions are tracked until they interact again or decay, as appropriate.

This algorithm produces a spectrum of produced particles in accord with data from fixed-target accelerator experiments. This results both from the nature of the algorithm as well as *a priori* assumptions (e.g. cross sections). Specific features include a flat Feynman-x distribution of the leading nucleon, Feynman scaling of resulting momentum distributions, KNO-like charged particle multiplicity distributions whose mean values increase with energy as ln(s), constant mean transverse momentum, and momentum and energy conservation.

All newly produced particles are assumed to be pions. In reality, roughly 10% of these particles would be kaons. This does not seriously alter the resulting muons, electrons, and photons of the air shower, since the interactions and decays of pions and kaons are similar.

Variations can be made in the algorithm to alter the probability distributions in the assignment of pion energies. Such changes can affect the inelasticity of the interaction and consequently the kinematics of the produced particles. The effect on air shower particles at the ground is not enormous, but it can be measurable. The effects of different variants of MOCCA are described below (cf. Figure 5.4).

It is not computationally possible to follow all the particles in an air shower. MOCCA uses a technique called "thinned sampling" to track semi-randomly selected particles. Those arriving at the ground have associated weights to indicate how many others were neglected in the procedure. For the 10^{19} eV showers used in this work, the weights may be as large as 10^5or 10^6. The method allows accurate computation of the total energy arriving at the ground and shower size (i.e. the total number of particles at the ground), but the study of fluctuations requires special care.

5.2.2 The SIBYLL Interaction Generator

As mentioned above, the MOCCA program uses an algorithm to generate the details of hadronic interactions which yields results that match fixed-target accelerator experiments. Certain new aspects of particle production became apparent with the advent of higher energy accelerators such as the CERN proton-antiproton Collider. SIBYLL is a hadron interaction simulator which was developed to address these developments.

SIBYLL is described fully elsewhere [53]. Pertinent to the design of EAS detectors are the following features. Hadron interactions are modeled with parton strings, similar to the algorithms in the Lund Monte Carlo extensively used in analysis of accelerator experiments. The multiplicity increases more quickly (as $ln^2(s)$) than at lower energy and exhibits violations of the KNO distribution. The proton-proton cross section increases more quickly with energy, there are correlations of transverse momentum with multiplicity, and there is the onset of a "hard part" of the cross section ("minijets").

These new features of particle production and kinematics match data from the CERN Collider. The onset of these features is made smoothly as the collision energy increases. Thus, SIBYLL produces hadronic interactions which are quite similar to those of MOCCA even when the particle energy approaches 100 TeV. The algorithms differ more as the energy increases. The number of pions produced in an air shower is not substantially different from what would be obtained from MOCCA in its basic form. The main effect of SIBYLL arises from the scaling violations which soften the energy distribution of pions and so ultimately alter the number of muons in the cascade.

SIBYLL can be used within MOCCA instead of the usual algorithm. The difference between the two approaches will occur mainly in the earliest interactions in the showers, after which the energies are reduced to levels where the algorithms give similar results. Figure 5.3 exhibits the distribution of the energies of hadron collisions in proton air showers. Only a small fraction of these occur in regimes where SIBYLL and basic-MOCCA differ significantly.

We thus can expect that features of air showers which do not depend on the first few interactions in the cascade will be relatively insensitive to whether the basic MOCCA algorithms or the more sophisticated SIBYLL approach are used. The depth of maximum of the shower is an example of a quantity which does depend on the location and features of the first interaction. X_{max} has been shown to be rather different when SIBYLL is employed. On the other hand, the total number of charged particles at the ground is not greatly changed. The number of muons at ground level shows somewhat more sensitivity to the choice of hadron interaction algorithm. (Ground particle differences are discussed further in Section 6.2 below.)

Finally, it must be considered that there is uncertainty in extrapolating the dynamics of particle interactions to the highest energies. The predictions of the MOCCA program, with or without SIBYLL, will be affected by the choice of extrapolation. Some interesting propositions can probably be tested by analysis of the structure of air showers. But it must also be stressed that only a limited set of basic shower characteristics are necessary to properly design a detector to achieve the stated goals of the Auger Project. These characteristics, such

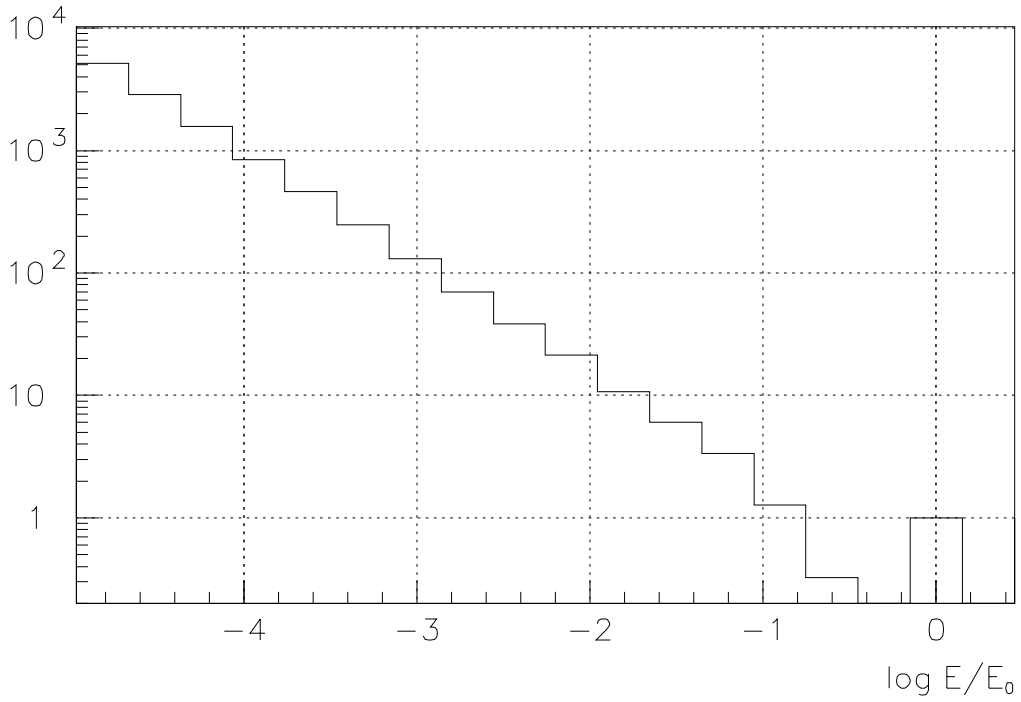

Figure 5.3: The distribution of interaction energies of hadron collisions in proton air showers, expressed as a fraction of the primary cosmic ray energy. This plot shows the highest energies of the distribution, obtained from an average of 100 showers at 10^{17} eV.

as the lateral distribution of particles and the timing structure of the shower front, derive mainly from the lower energy interactions in the shower. They are not greatly affected by reasonable physics assumptions. This, and the demonstrated good agreement with existing data (discussed below), leads us to conclude that the features of air showers most critical to the design of the detector can be confidently predicted using MOCCA.

5.2.3 Nucleus-Nucleus Interactions

It is more difficult to construct algorithms which simulate the details of nucleus-nucleus collisions. A simple approximation which is often used is the *superposition model*. In this approach, the interaction of a primary nucleus with A constituent nucleons and total energy E is modeled as A independent single nucleon collisions, each with energy E/A.

It has been rigorously shown [51] that this approximation will correctly produce the average values of "additive" quantities in air showers such as the total muon or electron numbers at the ground. The fluctuations in these same quantities will however be underestimated. Note that the depth of shower maximum is not an "additive" quantity in an atmospheric cascade.

It is to be emphasized that the SIBYLL interaction code simulates hadron interactions

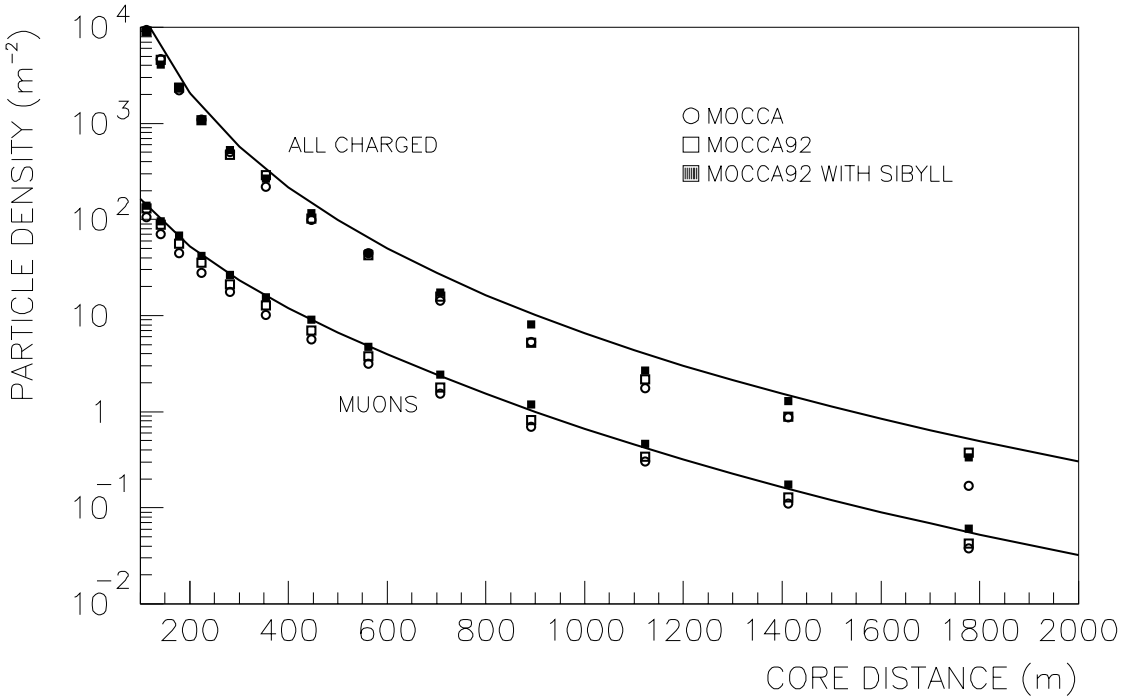

Figure 5.4: Lateral distributions of electrons and of muons from MOCCA simulations of 10^{19}eV oxygen showers. Three different interaction models are indicated: original MOCCA, the modified MOCCA92, and MOCCA92 with the SIBYLL interaction generator. Points are simulations, solid lines are published fits of the Akeno data. The upper curve and points are all charged particles, the lower for muons only.

only. SIBYLL is usually augmented with auxiliary code which generates features of nucleus-nucleus interactions in a somewhat more sophisticated manner than the simple superposition model. The fragmentation of nuclei during collisions and the cross sections of nuclei-on-nuclei are modeled after accelerator data. The interaction is thus reduced to a set of individual nucleon-air collisions which are simulated by SIBYLL.

5.2.4 Comparing Simulations to Existing Data

The MOCCA simulation reproduces many characteristics of air showers measured by ground arrays. One very important feature of EAS is the lateral distribution of particles. Figure 5.4 shows the results of the simulation compared to data from the Akeno experiment. While the reference design of the Auger Detector differs significantly from the hardware of the Akeno array, comparisons between the simulation and this experiment are more direct. Detailed simulations of MOCCA air showers in the reference design detector are presented in later chapters.

Figure 5.4 shows several separate simulations done with MOCCA under a variety of

assumptions. Results for three variants of the code are shown. One is the original MOCCA algorithm. Another is a more recent version of the code called "MOCCA92" which incorporates some slight changes in: pion transverse momentum distributions (harder), proton-air collisions elasticity (more elastic), and multiplicity of some interactions (higher). Finally, a variant using MOCCA92 and the SIBYLL interaction generator is shown, which also employs some small updates in various secondary hadron cross sections. All three simulations were done using 10^{19} eV oxygen nuclei as the primary cosmic rays in order to account for the fact that the cosmic rays seen by Akeno are probably neither purely protons nor purely iron. We note generally good agreement between data and simulation, especially for the muons.

The MOCCA92-SIBYLL version best matches the muon lateral distribution data. The different physics assumptions inherent to the three variants of the code result in systematic differences of as much as 60% in the muon densities. Given that the density itself varies over more than 5 orders of magnitude over the lateral range examined, such differences do not seriously alter our thinking about the design of the array. These differing results should be interpreted as indicating the degree to which "reasonable" physics assumptions affect the predictions of the simulation programs.

The arrival time of particles at the ground is another aspect of air showers of great importance in the design of a detector. The shower front has a roughly conical shape. The MOCCA prediction for the delay times of particles as a function of core distance is given in Figure 5.5. Also shown is a parametrization of this quantity obtained from fits to the Akeno data [55]. There is excellent agreement between the simulation and the data from 30 m to 3 km from the core (The Akeno fit is not intended to be valid at closer core distances). Similar good agreement is found when comparing the r.m.s. spread in arrival times between MOCCA and the Akeno data.

Having confidence in the ability of MOCCA to properly represent the timing structure of the shower front, we use the results of the simulation to guide our thinking on the design of the detector electronics. Figure 5.6 gives information from MOCCA on the thickness of the shower front. It can be seen that particles will be arriving over a span of several μs, with the muons arriving earliest. As a more extreme example, MOCCA predicts that a 20 μs wide window contains virtually all the particles in the shower front of a 10^{21} eV event at 3.5 km from its core. The majority of the data will be at lesser energy and the particles would easily occupy smaller time intervals (see Chapter 6, Section 6.2).

5.2.5 Ongoing studies

Many of the most important features of air showers relevant to the design of the Auger detector are insensitive to details of the interaction models used in the simulations. For example, while the multiplicity of charged particles produced in hadron interactions is uncertain at the highest energies, the shower size at the ground has been found to be unchanged by "reasonable" extrapolations of lower energy data. Characteristics of the muons at ground level do show possibly measurable effects, as discussed previously, but in most cases not of a sufficient magnitude to seriously alter the conclusions arising from the simulation studies

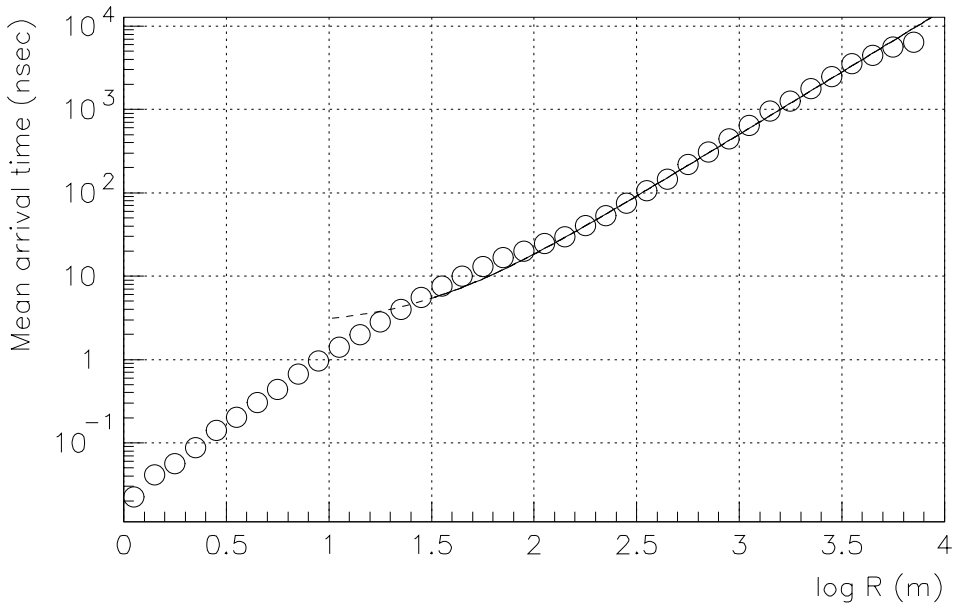

Figure 5.5: Mean arrival time of charged particles with respect to those at the core, from MOCCA simulations of 10^{19} eV proton showers, sampled at 900 m from the core. The solid line is a published fit of Akeno data.

described here.

An ongoing program has been organized to compare different simulation codes, to produce more efficient drivers, and to develop the most realistic interaction models.

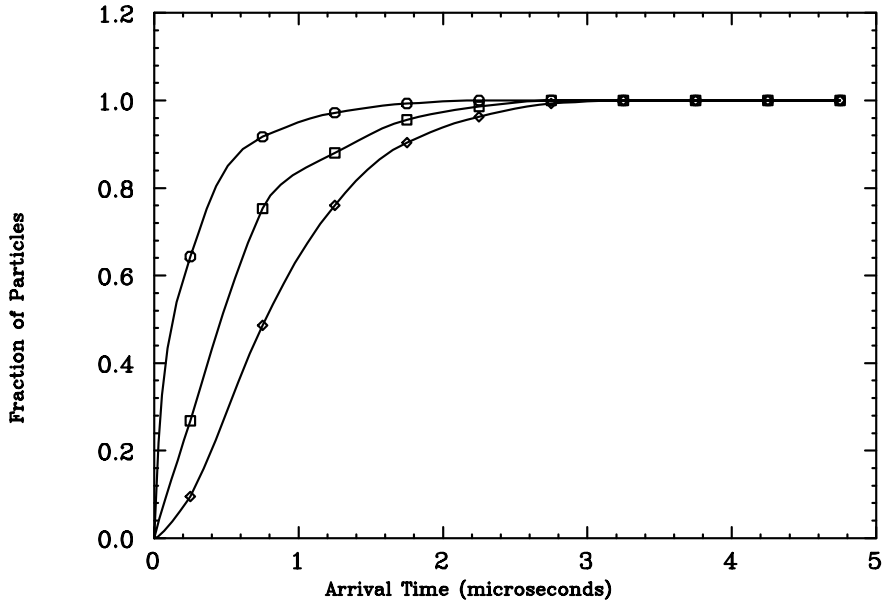

Figure 5.6: Integrated arrival times of charged particles with respect to those at the core, from MOCCA simulations of 10^{19} eV proton showers, sampled at 900 m from the core. The three curves indicate respectively the muons, photons, and electrons. The muons arrive the earliest. Solid lines are to guide the eye.

Chapter 6

Performance of Reference Design

The performance of Auger Detector reference design is evaluated here. The detailed technical description of the elements of the design will appear in later chapters. In this chapter, knowledge of the properties of air showers is applied to determine how data from the experiment will actually look and how it can be analyzed in order to achieve the stated goals of the Auger Project.

The MOCCA simulation program was described in the previous chapter. This code is the basis for most of the predictions concerning the details of extensive air showers. Where possible, data obtained from previous observations of the highest energy cosmic rays by groups such as the Haverah Park, Akeno, and Fly's Eye Collaborations have been employed to verify the simulations.

A description of the assumed parameters of the reference design is given first below, including both the surface and the air-fluorescence detectors. Next follows a description of a total simulation program employing MOCCA, a detector simulation, and analysis algorithms, constructed to predict the performance of the surface array. The chapter concludes with a similar discussion of a simulation and analysis procedure for the Hybrid Detector, the integrated surface array and fluorescence detector system.

6.1 Detector description

Water Čerenkov detectors have been selected as the technology for the Auger reference design surface array. This device consist of a volume of clear water acting as a Čerenkov radiator viewed by one or more photomultipliers. We have assumed a cylindrical detector 1.2 m deep with a top surface area of 10 m^2 (a radius of 1.8 m). The depth is a nominal value which allows a direct comparison with the existing experimental data from Haverah Park. We comment later (Section 6.2.4) on how a deeper tank may be useful for muon identification.

The volume of water is viewed from above by three large (200 mm diameter) photomultiplier tubes. The PMTs are placed at 120° intervals on a circle of radius 1.2 m (2/3 of the

detector radius), looking downward from the top surface of the tank. The inner walls of the tank have a diffusively reflective white surface. The detectors are assumed to be arranged on a triangular grid with 1.5 km spacing between each station and its nearest neighbors.

Calculations of the performance of a Hybrid detector (a surface array and fluorescence detectors as an integrated device) have been done independently of the simulations of the reference design surface array by itself. In the Hybrid study, generic fluorescence and ground array detectors are used. For example, the fluorescence detector uses mirrors and phototubes in the classic Fly's Eye approach, and the ground detector consists of an array of scintillators with the characteristics of the AGASA detectors, though with each detector having a larger area. Variants on these designs (for example replacing the scintillator detectors with water Čerenkov detectors of the same area and on the same grid spacing) will have only a small (probably negligible) effect on the geometrical reconstruction accuracy, and hence a negligible effect on our conclusions regarding the fluorescence detector's determination of energy and depth of maximum.

The Hybrid detector is assumed to be located at an atmospheric depth of 860 g/cm^2 for ease of comparison to Fly's Eye or Hi-Res data. The surface array component consists of 10 m^2 scintillator detectors on a triangular grid with spacing 1.5 km. The total ground area covered is 3000 km^2. The fluorescence detector used is a close approximation to the Cyclops 3000 reference design. Mirrors are 4.14 m in diameter, each with 256 pixels covering a solid angle of 216 deg^2. The reference design calls for 4.42 m diameter mirrors, with 225 pixels covering the same solid angle. In terms of signal to noise, which is proportional to the mirror diameter and inversely proportional to the pixel diameter, the eye used here has equal sensitivity to Cyclops 3000. It consists of 43 mirror units, 22 in the lowest ring and 21 in the second ring. The eye views a total azimuth of 350° and has a maximum viewable elevation of 31°.

6.2 Surface Detector Simulation

This section describes how the ground array is expected to function and fulfill the triggering and performance requirements set forth in earlier chapters. First, a summary is given of air shower characteristics which are important for our design. Next, a detailed simulation of the water Čerenkov tank system is given with attention paid to how the simulations are checked against earlier data. Finally, simulations are used to gauge the ability of the analysis algorithms to reconstruct the energy, direction, and composition of cosmic rays.

6.2.1 Air Shower Structure

The performance of the detectors is sensitive to the detailed charactersitics of the air shower particles. Before considering the details of a detector simulation, the air showers themselves are examined. The MOCCA simulation program which was described in the last chapter is used for this purpose. In that chapter (recall Figure 5.4) good agreement was shown

between the simulation and data from the Akeno experiment, demonstrating that MOCCA gives reliable predictions of air shower particles prior to their entering the detectors.

Features of the energy and arrival times of particles in the shower front are presented first, followed by discussion of the observable differences between showers initiated by protons and those from iron nuclei.

Particles in the shower front

A water Čerenkov tank differs significantly from other types of detectors (e.g. plastic scintillator or RPCs) in the way it responds to air shower particles. This kind of device will be disproportionately sensitive to muons. To understand why, it is necessary to consider detailed features of the particles.

At ground level, far from the core of an EAS, the shower front consists of gammas, electrons and muons. There is also a flux of (evaporation) neutrons which are generally sub-relativistic and so are delayed with respect to the main shower front, and large numbers of atmospheric Čerenkov photons. The relativistic hadron flux is negligible beyond 50 m from the core.

The muons and electromagnetic particles have very different energies. The distributions shown in Figure 6.1 were obtained from MOCCA simulations of vertical 10^{19} eV proton showers, sampled 900 m from the shower core. A typical muon has an energy of about 1 GeV, while the majority of electrons and gammas are below 10 MeV. Note that electromagnetic particles greatly outnumber muons within a few kilometers of the core.

As a consequence of their higher energies (and masses), air shower muons travel much further than electrons in water. Thus, they produce a great deal more Čerenkov light in the tank. Despite their relatively small contribution to the total number of particles at the ground, muons can dominate the signals obtained from water Čerenkov detectors.

Figure 6.2 shows the correlation between the energy, density, and arrival times of different particle types from a set of simulated showers with the same properties as in the previous figure. In addition to having higher energies, muons also arrive earlier and over a much shorter period of time than the electromagnetic particles. These features help distinguish muons from electrons, which will be useful in the study of cosmic ray composition. This is described next.

Shower features related to primary type

As was discussed in the last chapter, muons in air showers are expected to show particular sensitivity to the nature of the primary particle. Iron showers have significantly more muons, when compared with proton showers of the same energy. It is therefore useful to carefully consider the properties of air shower muons which will be relevant to their detection. Note that in this discussion, while there is no detailed detector simulation, certain features of the reference design detector will be anticipated. A description of specific detector-related

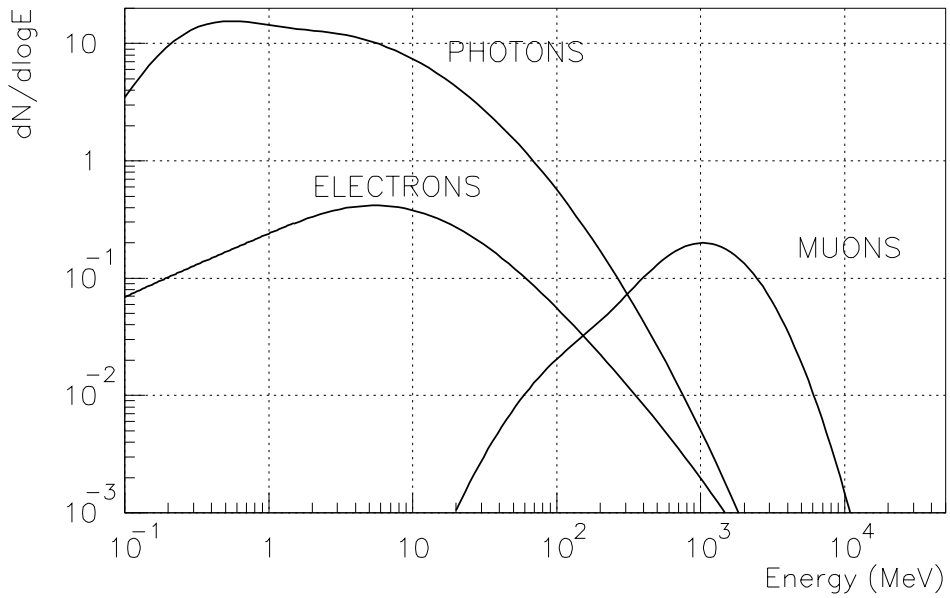

Figure 6.1: Distribution of particle kinetic energies at the ground for 10^{19} eV proton air showers, from MOCCA simulations. Ground level is taken to be 1000 g/cm^2 and particles are sampled at a core distance of 900 m.

measurements is deferred until the next section.

The predicted numerical density of shower particles at sea level in 1×10^{19} eV proton and iron nuclei initiated showers is shown in Figures 6.3 (a) and 6.3 (b).

At ground level the differences (other than the total number of muons) between iron and proton showers are relatively small; Figure 6.3c shows the predicted numerical density ratio of the shower component particles for iron and proton showers. The electromagnetic densities are similar, but that there are $\geq 75\%$ more muons in the iron showers at the core distances of interest (≥ 1 km). Although the absolute number of muons for a shower of given energy and primary type is somewhat dependent on the details of the hadronic interaction model, the *ratio* of the densities of proton and iron showers is much less model dependent.

The amount of Čerenkov light generated per muon is very different than the amount generated per electron. In 1.2 m depth of water a large fraction of the muons will "punch through" the detector volume. However, the majority ($\geq 90\%$) of the electromagnetic energy will be absorbed (the mean free path of gammas in water is $\leq$ 0.5 m). Additionally, Čerenkov light yield is only proportional to energy loss for particles which are fully relativistic, which is not true for much of the total electromagnetic track length. For these reasons interpretation of the light yield recorded by a water Čerenkov array must rely on comparison with shower and detector simulations to ultimately determine the shower energy. (In fact all EAS detectors are dependent on shower and detector modeling for event energy reconstruction). Roughly speaking, the water Čerenkov signal density is proportional to the sum of

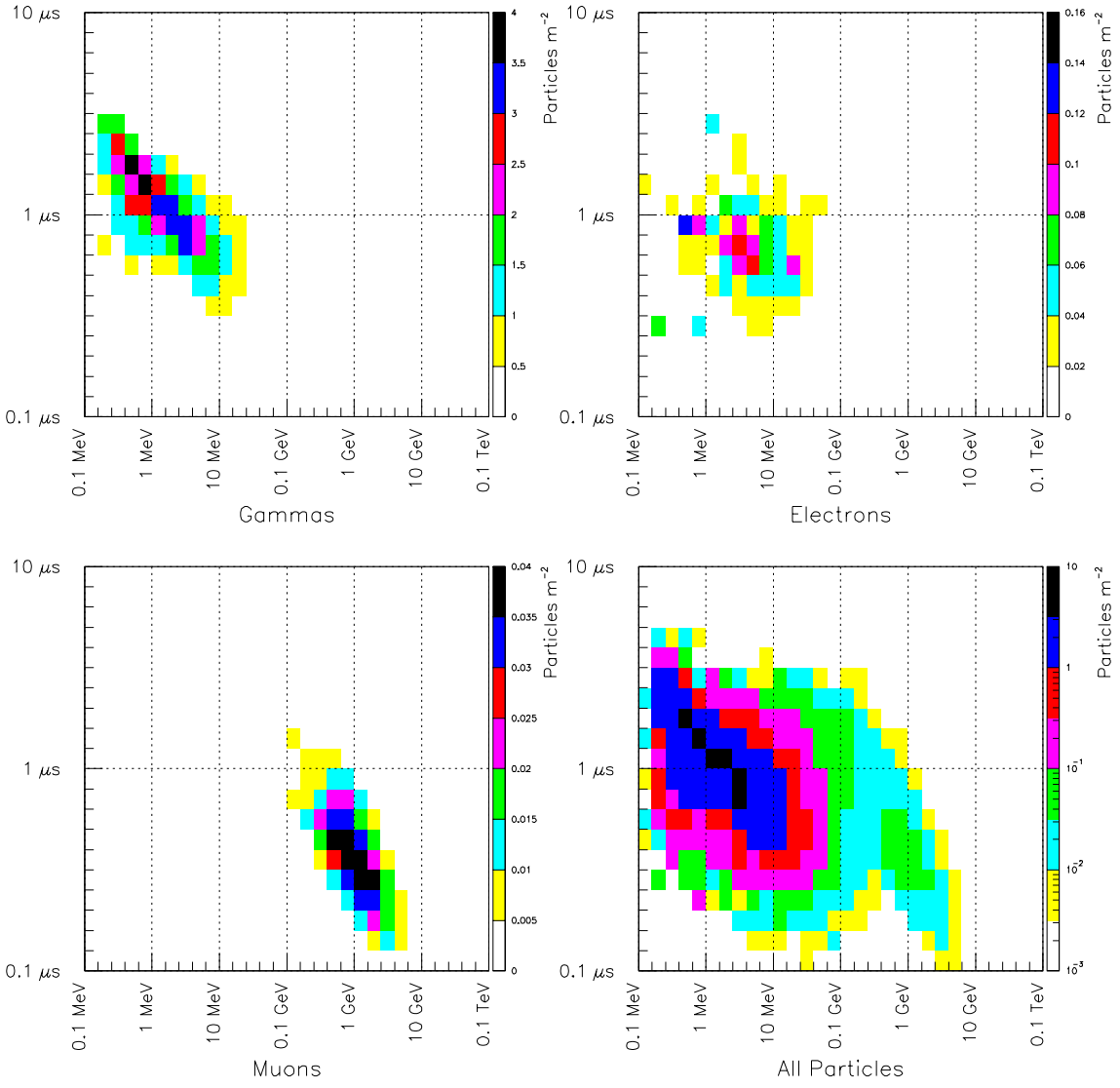

Figure 6.2: Correlations between energy, arrival time, and density for shower particles at 0.9 km from the core of a vertical 1×10^{19} eV proton initiated EAS, from a set of MOCCA simulated showers. Observation level was taken to be 1000 g/cm^2 atmospheric depth (near sea level). Note that the density scale for the all particles plot is logarithmic to allow the muons to be seen on the same scale as the electromagnetic particles.

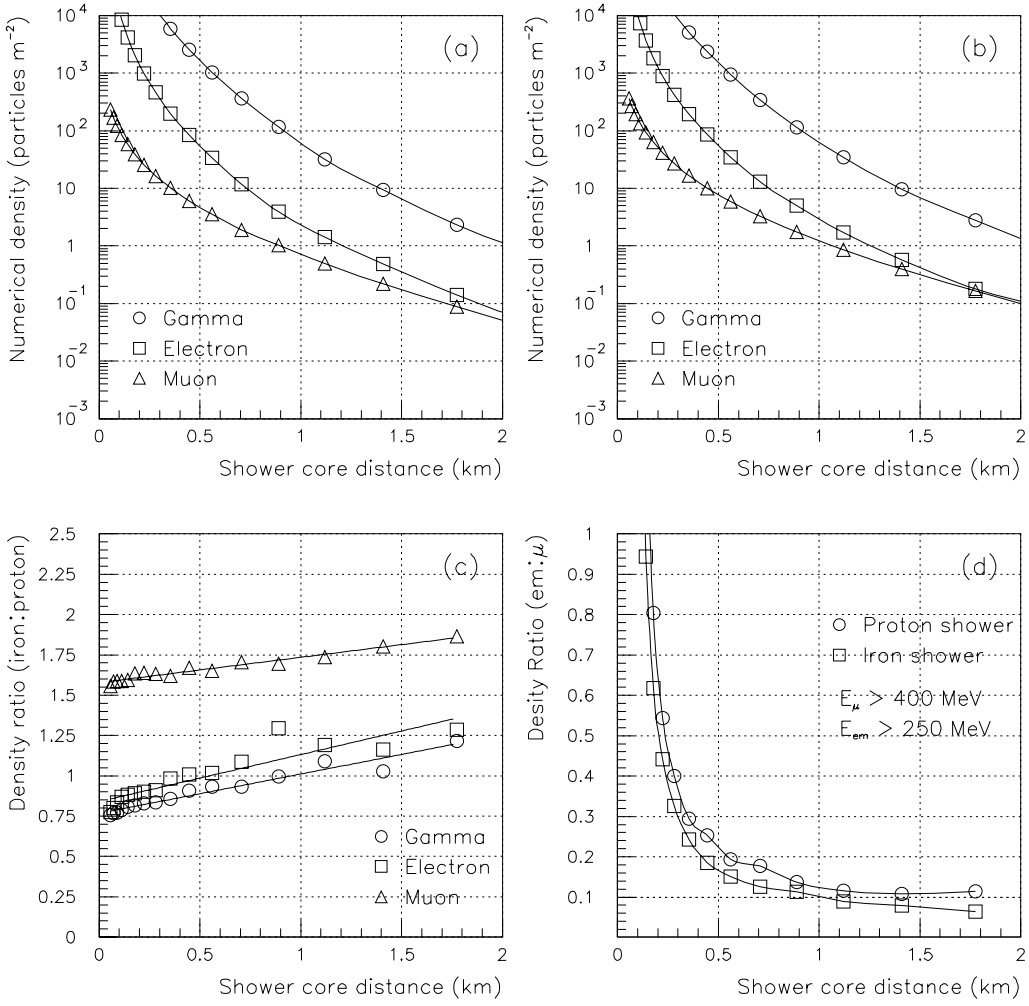

Figure 6.3: Predictions of shower front characteristics from the MOCCA EAS simulation program, without detector simulation. (a) shows the lateral distribution of an average vertical 1×10^{19} eV proton shower; (b) is identical but shows an average iron shower. Atmospheric depth is 1000 g/cm^2, (near sea level); (c) shows the ratio of (b) to (a) as a way of comparing properties of proton and iron showers at this energy; (d) is the number of electromagnetic particles which will produce a burst of Čerenkov light in a 1.2 m deep detector equal to that from a penetrating muon, shown as a fraction of the number of penetrating muons.

muon *number* density (multiplied by the average muon energy loss) and the electromagnetic *energy* density.

Later, in Section 6.2.4, the different signal characteristics of muons when compared to electromagnetic particles will be used to study the primary composition. Determining the fraction of the signal due to muons on the basis of pulse height will only be practical at large core distances where the density of electromagnetic particles is not so high as to overwhelm the muon signals. In a 5×10^{19} eV shower there will be ~ 5 detectors in the core distance range where the particle density is appropriate. Figure 6.3d shows the predicted proportion of electromagnetic "fake muons"; at core distances ≥ 1 km this is $\leq 10\%$. The possibility of muonic fraction measurement also demands that the proportionality of the detector be good; ie. that the signal observed be closely proportional to the Čerenkov light released.

6.2.2 Detector Simulation

A simple but very fast Monte Carlo simulation of the response of a cylindrical or rectangular water Čerenkov detector to incident gamma, electron and muon particles has been written. Air shower particles from the MOCCA program are passed to this simulation to assess the response of the surface array. This section gives the assumptions used to model physical processes in the detector, the methodology of the procedure, and finally the results and analysis of the simulated air shower events.

Čerenkov Radiation

Čerenkov light is produced by a charged particle moving through a transparent medium with velocity $\beta \geq 1/n$, where n is the refractive index ($n = 1.33$ for water). Hence a particle must have a kinetic energy greater than half its rest mass energy to radiate Čerenkov light (0.25 MeV for electrons and 73 MeV for muons). The angle of emission is $\theta = \cos^{-1}(1/\beta n)$ with respect to the particle trajectory: 41° for a fully relativistic particle in water.

The yield of Čerenkov photons with wavelengths between λ_1 and λ_2 for a small element of particle track dx is given by:

$$\frac{dN}{dx} = 2\pi\alpha \left(\frac{1}{\lambda_1} - \frac{1}{\lambda_2}\right)\left(1 - \frac{1}{\beta^2 n^2}\right),$$

where α is the fine structure constant. Figure 6.4 shows the Čerenkov emission spectrum for water calculated on the basis of the above equation.

Material Characteristics

The choices of the various elements of the reference design surface detector are described in detail in the next chapter. Reviewed here are some elements which are especially pertinent to the simulation.

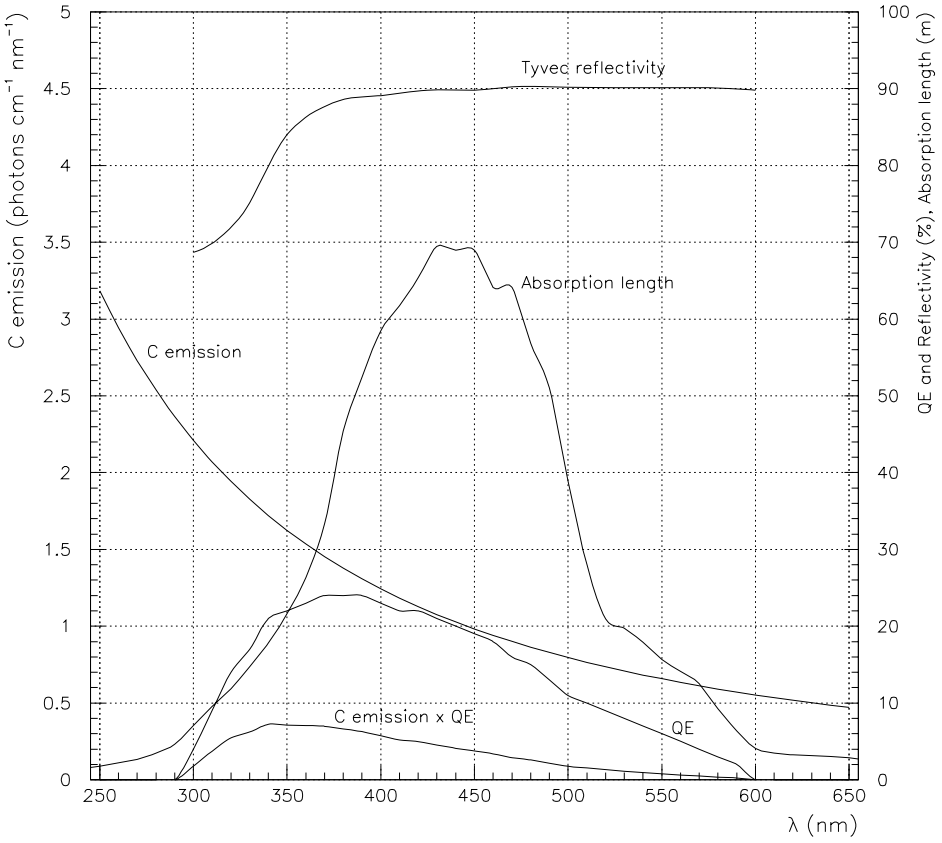

Figure 6.4: Some important spectral characteristics for a water Čerenkov detector. The quantum efficiency shown is for a bi-alkali photocathode. Absorption length is for ultra-pure water. Tyvec is a plastic material which may be used as a lining for the tank; see Chapter 7 for further details.

In Figure 6.4 photomultipler quantum efficiency[1] is shown as a function of photon wavelength. The convolution of quantum efficiency and the Čerenkov emission is also shown. Clearly the wavelength region between 300 and 500 nm is crucially important. The spectral diffuse reflectivity of a material called Tyvec[2], a possible interior lining material of the detector tank, is shown. Finally the absorption length of ultra pure laboratory water is shown[3], and is seen to exceed 10 m across the wavelength range of interest.

The spectral characteristics of the scattering (Mie scattering) and absorption of light in water containing particulate impurities are functions of the numerical density, size spectrum and composition of the impurity particles. Values much below the ultra pure curve shown in Figure 6.4 are expected for water whose quality is practical for this application. Behavior varies greatly depending on the source and purification processing of a particular water sample. See Chapter 7 for further discussion, and some preliminary measurements.

The complexity of the spectral dependence of the net absorption length of water requires that it be measured specifically for any samples of water used in a detector. So details such as assigning each Čerenkov photon a wavelength sampled from the emission spectrum have not so far been explicitly included in the simulations. Instead (and also to speed up the simulation process) the number of Čerenkov photons emitted for each particle track increment is set equal to the integral of the convolution of the emission and detection characteristics. Fixed water absorption length and lining material reflectivity are assumed. The validity of this approximation depends upon the extent to which these values vary over the spectral range of interest (300 to 500 nm) in combination with the size and geometry of the detector. Further work on this point is required.

Other approximations regarding the physical parameters of materials have been made for the purposes of simulation. The numbers used represent average or effective values over the range 300 to 500 nm, and are believed to be realistically achievable. Here, a summary of the numerical values used in the simulation:

- 15% photocathode quantum efficiency;
- 85% reflectivity of the tank lining material;
- 7 m water absorption length;
- 10% : 90% split between perfectly specular and perfectly diffuse reflection behaviour for photons reflected from the lining material. (It turns out that the split ratio assumed has little effect on the results).

It is to be emphasized that to a very good approximation the assumed parameter values affect only the absolute photoelectron yield for a given incident particle. They do not affect

[1]Taken from the Hamamatsu R1408 data sheet. This is a hemispherical PMT 200 mm in diameter in a borosilicate glass envelope which was used in the IMB experiment.

[2]The curve shown is for light incident at 30° to the normal, but there is little angular dependence. Measurements made by Surface Optics Corp. for UCI School of Physical Sciences.

[3]Taken from a 1981 review of the available data[104]

the validity of the comparisons with experimental data discussed in Section 6.2.3 below, where simulated detector calibration has been carried out.

Detector Simulation Algorithm

The full simulation of the response of the Auger surface detector has three distinct elements: production of air shower particles using MOCCA, calculation of the detailed response of the water Čerenkov detectors and electronics, and the construction of realistic event triggering.

The MOCCA program was described in the last chapter. Recall that an important aspect of this code is the *thinning* of the shower in order to keep the computation time manageable. Only a very small fraction of the total number of air shower particles, each with a large weighting factor, are provided by the simulation. The number of particles provided is very small at core distances (> 1 km) typical of events in the array.

To remove such artificial fluctuations due to small numbers, individual MOCCA showers are not used to create individual events. Rather, sets of showers are run under fixed conditions, the weights summed , and then averages are taken. This has the unfortunate effect of also averaging out the physical fluctuations due to variations in the atmospheric depth of the first interaction point and shower development. (Note that a different simulation procedure will be employed in simulations of the so-called Hybrid system, a combined surface array - optical detector described later).

Batches of 100 showers have been generated for proton and iron nuclei primaries at $0°$, $30°$, $45°$ and $60°$ zenith angles. All the simulations are for primary energy of 1×10^{19} eV and an atmospheric depth at ground level of 1000 g/cm^2. The energy threshold at which particle thinning commenced was 10^{-6} of the primary energy (10 TeV).

The generation of simulated experimental data is then done in the following steps:

- Output from the averaged MOCCA showers is in the form of a ground particle list giving particle type, impact coordinates, trajectory, thinning weight, and energy. Each particle is projected onto the plane perpendicular to the shower axis passing through the core impact point and then binned into a 5-dimensional array to give differential energy/time/density breakdowns for each particle type at given core distance. (Figure 6.2 was an example of the information in the annular bin centered at 0.9 km from shower core). The statistics available from 100 runs do not allow further dimensions of binning according to impact position relative to the shower axis, and particle trajectory angle.

- To generate individual showers for a particular primary type and zenith angle a random azimuthal angle and core impact position are selected and a shower projected onto the simulated array grid. For each detector the core distance in the shower plane is calculated and the pre-determined density array re-sampled to generate a list of shower particles striking that detector, each particle being assigned impact coordinates, an energy, and an arrival time. By sampling over an area in the plane of the detector top surface (but larger), all "corner clipping" effects are automatically included.

- The detector simulation program is invoked using the lists of particles striking the detectors. Each particle is tracked through the detector volume, interacting and radiating Čerenkov light. The resulting photons are ray-traced until absorbed in the water, upon reflection, or at a PMT. A list of photoelectron release times is updated for each detector.

- The photoelectron lists are used to construct simulated amplitude vs. time profiles for the summed signal from all tubes. Care is taken to represent the effects of the electronics. This profile is then scanned and an *alert* condition is imposed to simulate the lowest level (hardware) trigger of an individual detector station. A GPS event time stamp is generated which reflects the fluctuations of the trigger time relative to the shower plane arrival.

The simulation of the Čerenkov photons in the detector is illustrated in Figure 6.5. Here, the propagation of the individual photons from a single penetrating muon is shown. All the particles in the air shower which strike detectors are simulated in this manner.

Figure 6.6 shows the final output of the simulation process for a single shower. The data thus generated is then available for event reconstruction and comparison with experimental data. Note that because the shower input data from MOCCA has already been averaged, to a large extent intrinsic shower-to-shower fluctuations will not be reproduced. However, all detector imposed limitations due to limited size, non-proportionality, etc., are modeled in this procedure.

Note also in the lower part of Figure 6.6 how muons are seen to give larger, narrower pulses than the more numerous electrons and converted gammas. The ability to distinguish muons by their signal characteristics will be necessary when attempting to evaluate the nature of the primary particle causing the air shower, discussed later.

6.2.3 Comparison of Simulation and Data

To check the validity of the shower and detector simulations, their predictions have been compared to experimental results from the Haverah Park array. Since the reconstruction of the the lateral distribution of particles is central to all analyses from the surface array, substantial attention is devoted to this topic here. It will be shown that the simulation reproduces many details of the data.

Sets of showers have been run for various primary types and zenith angles using the procedures described above. Each of the Monte Carlo data sets presented in this section is the product of such a run. Event reconstruction errors have not been included at this point, the exact core distance being used to analyze the simulated measurement of particle lateral distributions. Note that one should not expect perfect agreement between the simulated events and the Haverah Park data since the simulated detector unit is not the same size and shape as the Haverah Park units. However, for the present case these effects will contribute second order discrepancies only.

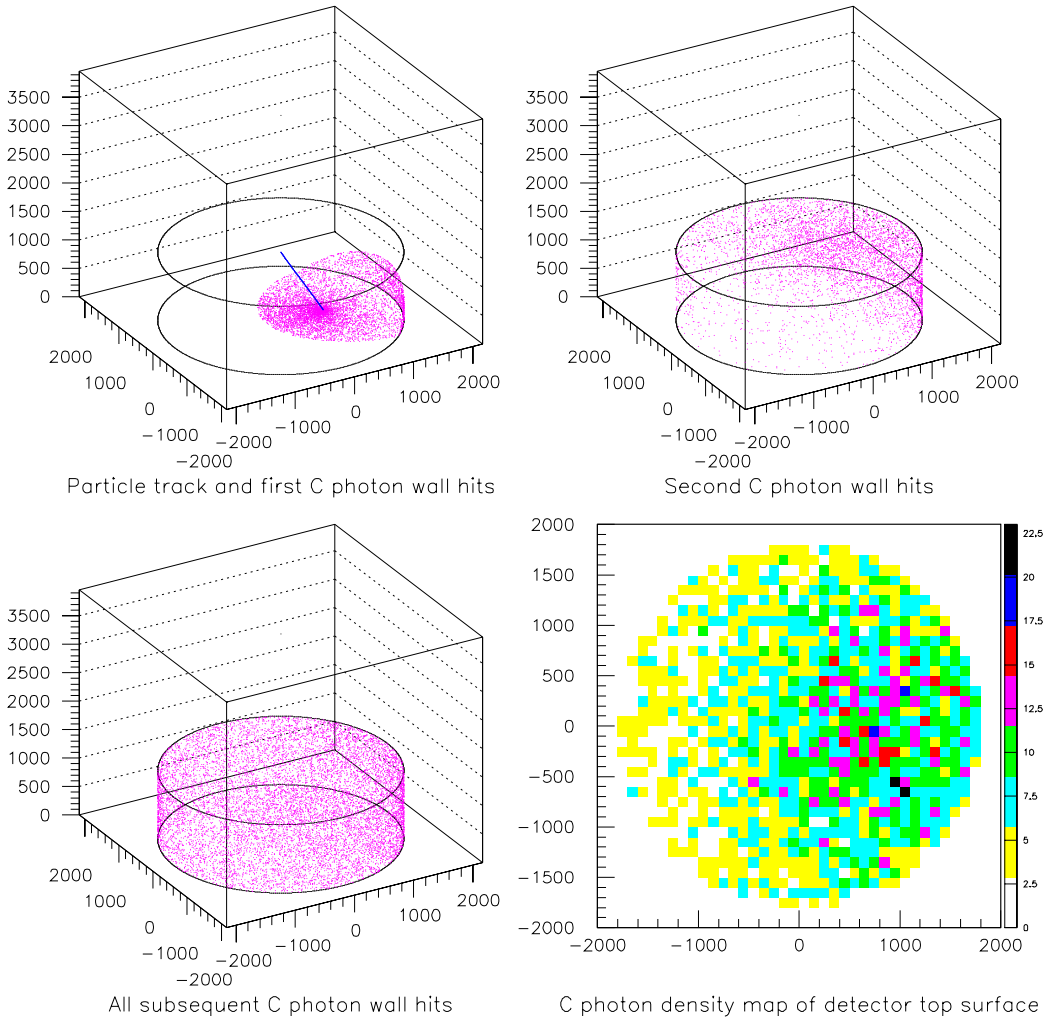

Figure 6.5: Simulation display for the reference design water Čerenkov detector unit. A single 1 GeV muon was injected at the center of the top surface travelling at 30° to the vertical. The upper left plot shows the incident particle track and the positions where the Čerenkov photons released first reflect from the tank walls. The upper right plot shows the positions of the second photon reflections. Reflections continue until the photons have been absorbed in the water or by the tank lining material; all reflection positions after the second are shown in the lower left plot. The distribution of reflection positions over the detector top surface integrated over all reflections is quite uniform. At lower right a density map of the detector top surface is shown.

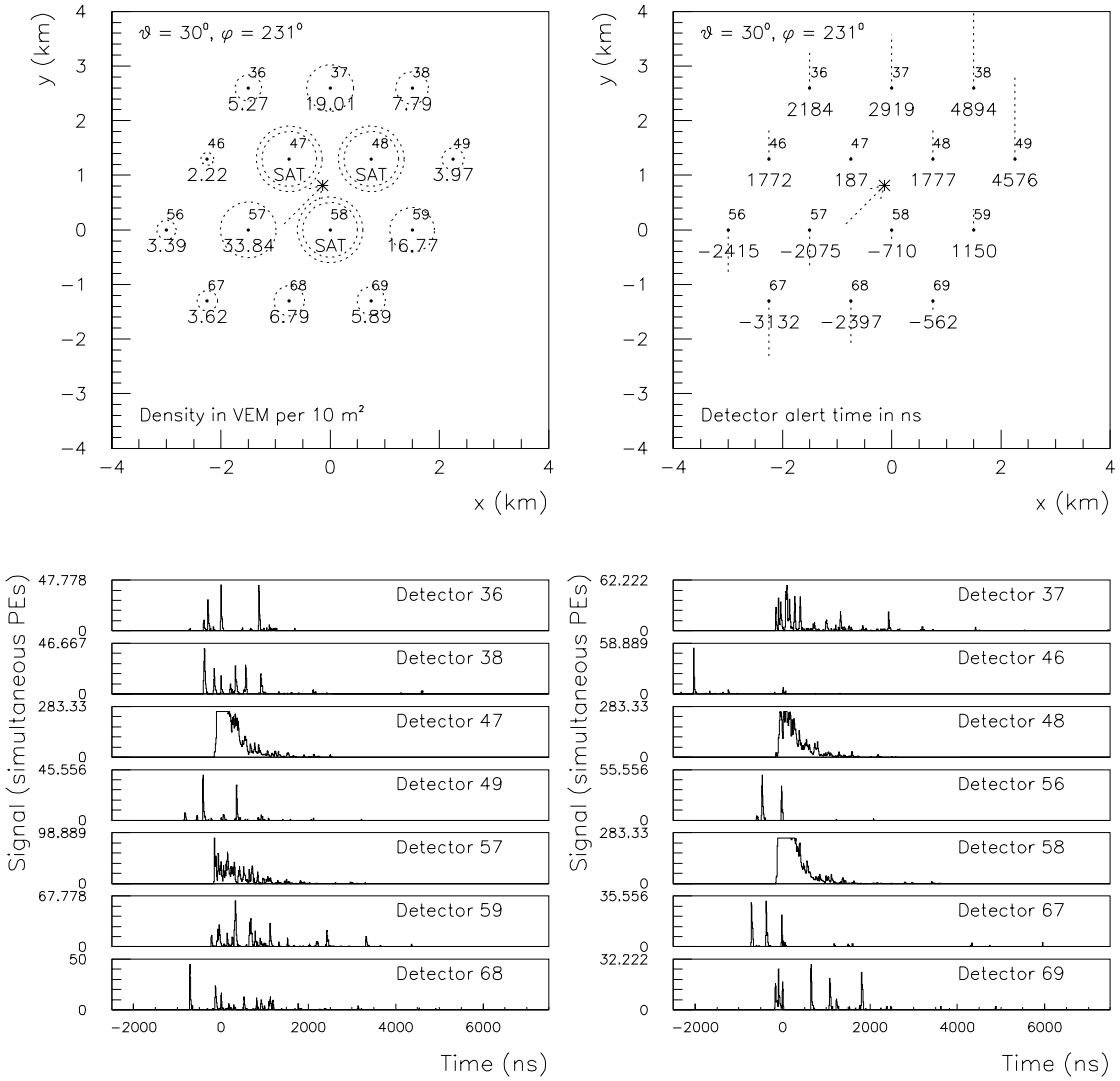

Figure 6.6: Illustration of a simulated EAS event falling on the reference design Auger water Čerenkov surface array. The shower was initiated by a 5×10^{19} eV iron nucleus incident at a zenith angle of 30°, the array being at sea level. The top left plot shows a ground plane density map, the radius of the circles being proportional to the logarithm of the density. At top right is a map showing detector trigger times, the length of the vertical lines indicating the time relative to shower core impact. The lower part of the plot gives the simulated time/amplitude signal profiles for each triggered detector.

Lateral distribution shape

To allow shower reconstruction using information from widely spaced detectors it is essential to know the relation between signal density $\rho(r)$ and shower core distance r, referred to as the lateral distribution function. For the Haverah Park Water Čerenkov detectors a good fit to the data was empirically found to be a modified power law function:

$$\rho(r) = kr^{-\left(\eta+\frac{r}{4000}\right)}, \tag{6.1}$$

where shower core distance r is in meters, k is a normalisation parameter, and η is given by,

$$\eta = 3.78 - 1.22\sec\theta + 0.15\log(\rho_\lambda(600)). \tag{6.2}$$

where θ is the shower zenith angle, and the quantity $\rho_\lambda(600)$ is a parameter which expresses shower energy (λ referring to the decay length of the shower in the atmosphere; see next section).

The parameters η and k control the shape and normalization respectively. Representative values are $\eta \approx 2.5$ and $k \approx 3.5 \times 10^8$ for vertical 10^{19} eV showers. The signal density $\rho(r)$ is expressed here in units of vertical equivalent muons per square meter (VEM m^{-2}), obtained by dividing the total observed signal by the average value from a vertical through-going muon. Use of this density unit allows simple calibration of water Čerenkov detectors using background muons.

As shown by Equation 6.2 the slope parameter η is a function of zenith angle θ and, to a minor extent, shower energy. Both of these effects reflecting the "aging" of a shower as it penetrates through the atmosphere. For four years 30 smaller water Čerenkov detector units also 1.2 m deep were operated in the central part of the Haverah Park array allowing detailed study of these effects and leading to Equation 6.2.

The lateral distribution shape given by Equations 6.1 and 6.2 is known to be valid for $50 < r < 800$ m, $\theta < 45^\circ$ and $1 \times 10^{17} < E < 5 \times 10^{18}$. It was noticed that in the biggest showers, where measurements were recorded well beyond 800 m, there was a significant departure from the predicted behaviour, the measured values of $\rho(r)$ being consistently higher. A special study of showers with $E \geq 1 \times 10^{19}$ eV indicated that these data were well represented by flattening the lateral distribution for $r > 800$ m. Thus, for the highest energy showers, Equation 6.1 is replaced at $r > 800$ m by the modified expression

$$\rho(r) = kr^{-\left(\eta+\frac{r}{4000}\right)}\left(\frac{r}{800}\right)^{1.03}. \tag{6.3}$$

Figure 6.7 shows four examples of actual Haverah Park data in this energy regime. Equations 6.1–6.3 are seen to do an excellent job of describing these data over the the entire measurement range. These events were experimentally very well measured. They fell close

to an infilled part of the array so their cores are reliably located by circular symmetry alone. This allows the lateral distribution at large distances to be observed with minimal reconstruction bias effects.

The flattening of the lateral distribution at large core distances seen in Figure 6.7 and expressed in Equation 6.3 can be understood in terms of a shift from an electromagnetic to a muon-dominated signal. It is a consequence of the broader muon lateral distribution which is predicted from simulation. The effect is enhanced in Water Čerenkov detectors, where the higher energy muons release much more Čerenkov light per particle (recall Figure 6.3).

Figure 6.8 compares sets of Monte Carlo events with the Haverah Park experimental parameterization. Two cases are shown here, one for proton and the other for iron primaries. Each set was incident vertically and had primary energy of 10^{19} eV. The lateral distribution shape given by Equations 6.1 and 6.2 has been used in fitting the normalization constant k in the region $400 < r < 800$ m. For $r > 800$ m the flattened extension given by Equation 6.3 is shown, but this data was not used in the fit. The qualitative agreement in shape is good, particularly for the iron primary simulations. This is shown on the right side of the figure where the ratio of the simulation points to the Haverah Park function is given. (Note that there is a slight overall normalization offset in the ratio plots; see the discussion of the parameter r_k in the next part of this section.)

Figure 6.9 shows comparisons as in the previous figure for iron and proton primaries, except here the results are given at various zenith angles. The shower-plus-detector Monte Carlo reproduces the change in slope parameter η with increasing zenith angle θ. When showers are observed at increasing angles from the vertical, and hence at greater atmospheric depth, the lateral distribution "ages" or flattens, i.e. the slope parameter η decreases. Note that at large zenith angles protons and iron showers of given energy produce very similar lateral distribution shapes. This is expected since the electromagnetic cascade has been almost entirely absorbed. The shape of the muon distributions in the two kinds of shower increasingly resemble one another as showers age beyond their maxima. The ability of the simulations to reproduce so well the change of η with zenith angle is a very encouraging result.

It is also seen in Figure 6.9 that the Haverah Park lateral distribution function appears to show slightly better agreement with the simulated iron showers than with the proton ones. This may be interpreted as a feature of the shower Monte Carlo rather than a real physical result. As discussed in the last Chapter (section 5.2), the number of muons at the ground is affected by the choice of hadronic model. This effect is not enormous but variations in the modeling may be sufficient to produce a better fit for proton primaries; further investigation is required. It is to be stressed that the effects of model assumptions do not seriously alter our calculations concerning the design of the array, but should be examined when performing detailed analyses of cosmic ray composition.

If the Auger experiment has a grid spacing of 1.5 km it will not be useful to fit events using a free slope parameter η, since only one detector will be < 750 m from the shower core and there will be few measurement points. Hence it will be necessary to assume a known slope η, either from the Haverah Park results or from Monte Carlo predictions which are capable

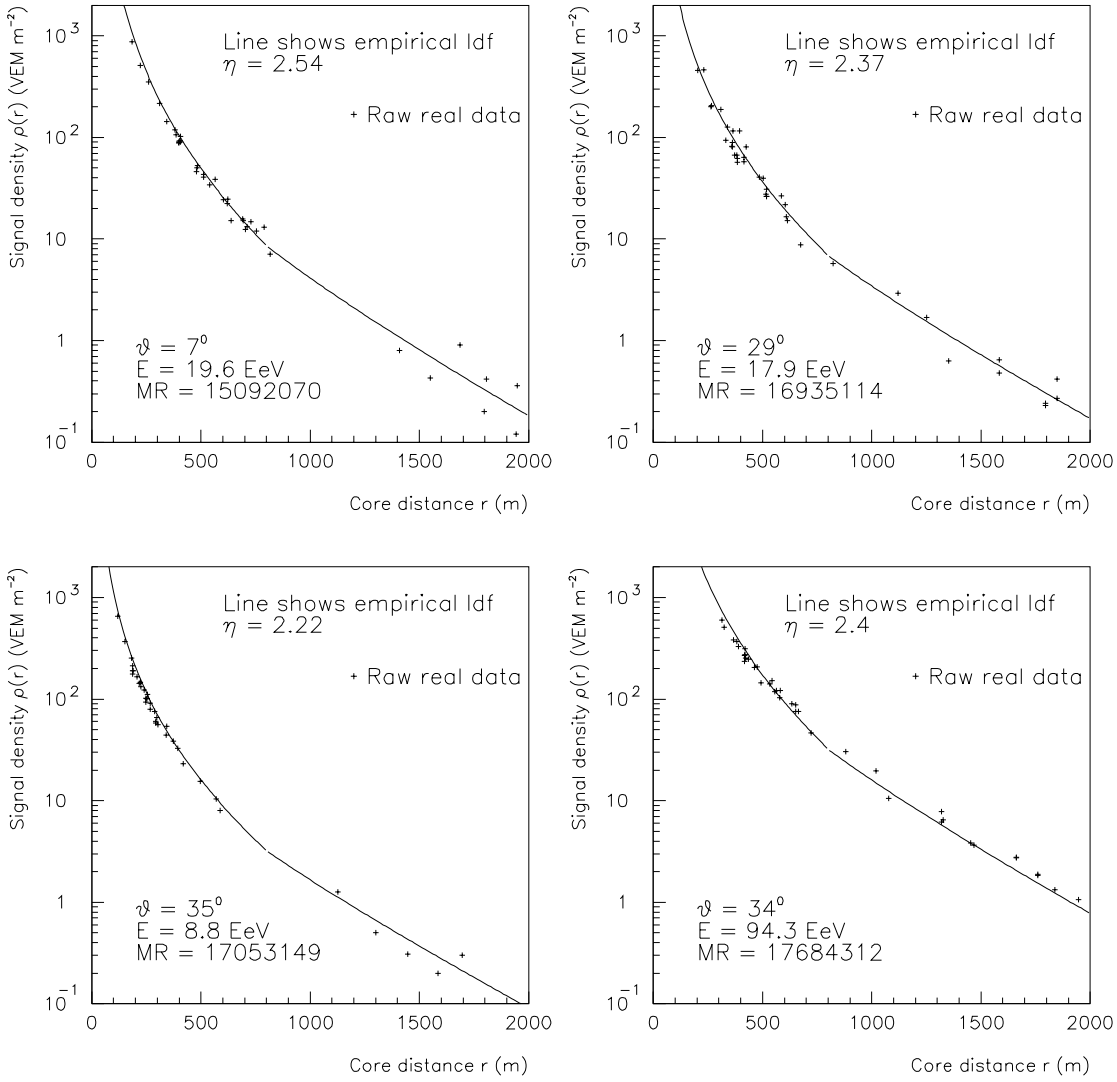

Figure 6.7: Actual Haverah Park data showing four exceptionally well measured events at very high energy. The solid line is the lateral distribution function from Equations 6.1–6.3. The value of the slope parameter η is shown for each event (see text), along with the fitted values for energy and zenith angle; MR is an event identification code.

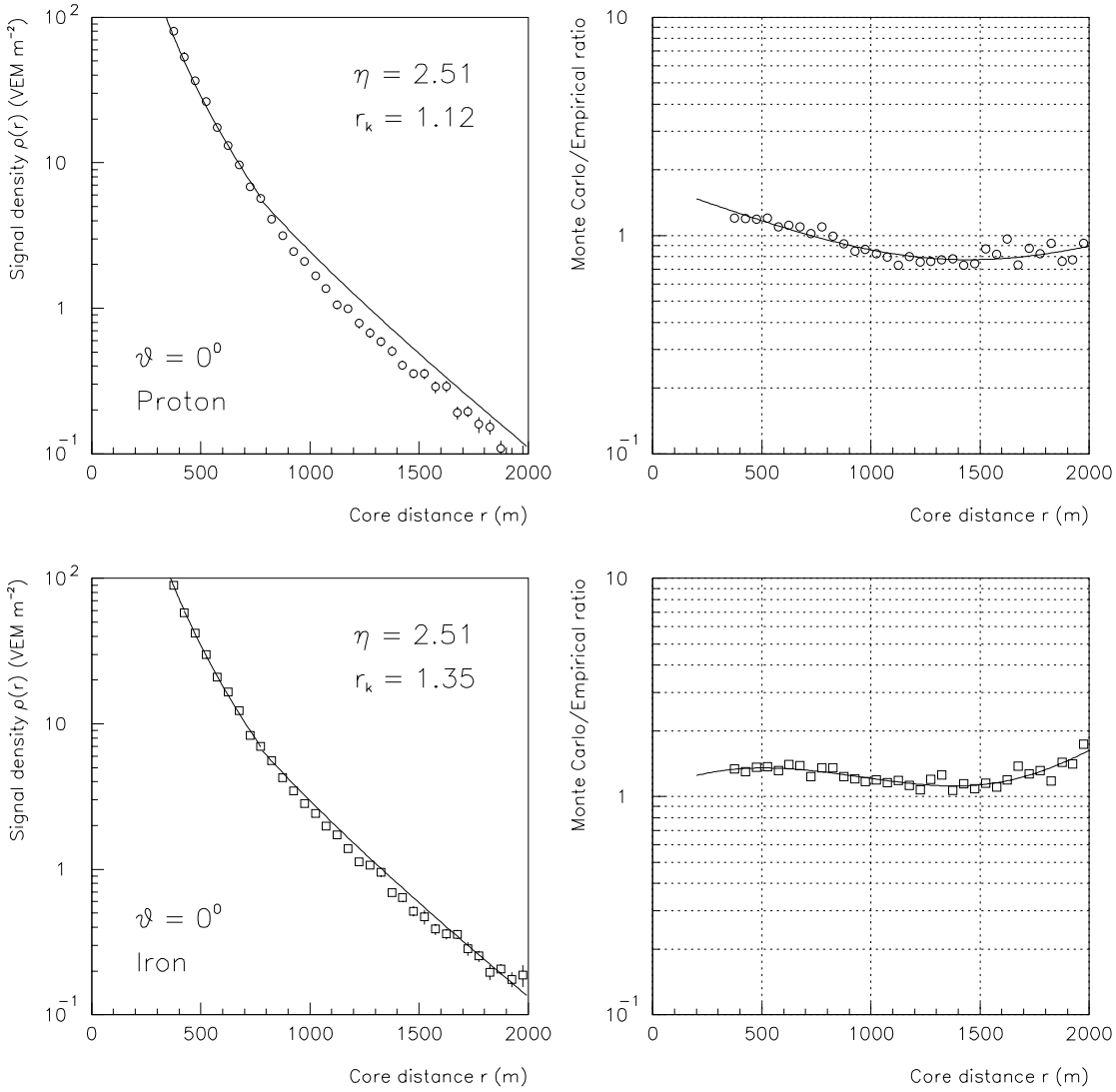

Figure 6.8: Left, comparison of simulated lateral distribution against measurements from the Haverah Park array. The points are Monte Carlo predictions for 10^{19} eV EAS, the lines experimental parameterizations given by Eqns. 6.3-6.2 in the text. The lateral distribution functions were computed using the indicated values for the slope parameter η and normalization correction r_k (see text and Table 6.1). On the right side, the ratio of the simulated points to the function.

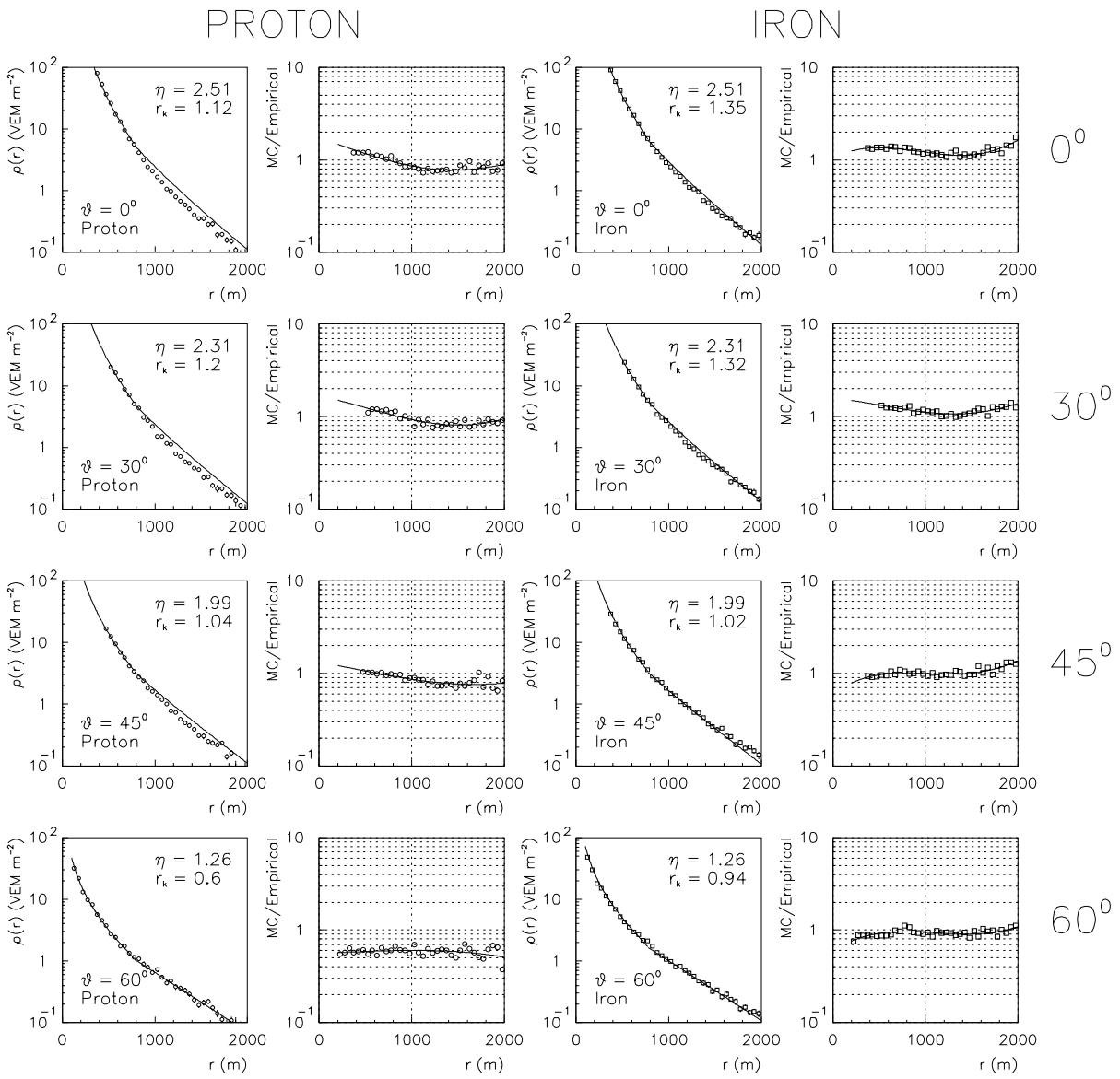

Figure 6.9: Comparison of simulation lateral distributions against measurements from the Haverah Park array, as in the previous figure. Here, simulated iron and proton showers at various zenith angles are shown.

of reproducing them. Note that independent measurement of the lateral distribution will be provided by the fluorescent detector (discussed in the last chapter, section 5.1.1). Ultimately it might be also be considered worthwhile to "infill" some portion of the array.

Lateral distribution normalization

The normalization constant k in Equations 6.1 and 6.3 is a function of shower energy and zenith angle. To account for the attenuation of a shower through the atmosphere, define a new density parameter $\rho_\lambda(r)$ by the relation $\rho(600) = \rho_\lambda(600)e^{-(\sec\theta-1)1018/\lambda}$, appropriate for the 1018 g/cm^2 atmospheric depth of the Haverah Park location. The measured value of the attenuation length λ at r =600 m was 760 ± 40 g/cm^2.

In the Haverah Park experiment shower energy was expressed in terms of $\rho_\lambda(600)$. When fitting experimental shower data with a free slope parameter, such as η, and using relatively few measurement points, errors in core location and slope parameter are interdependent. However, it turns out that the associated error in function normalization is on average minimal at a distance from shower core close to the array spacing distance (which for the Haverah Park system was typically 600 m). Simulations also suggest that shower-to-shower fluctuations produce smaller variations in density with increasing core distance, and that density dependence on primary particle mass is minimal near 600 m.

The relationship between primary energy, and lateral distribution normalization can only be determined from detailed calculations of shower development. Early Monte Carlo simulations by A. M. Hillas lead to the adoption of the relation $E = 7.04\times10^{17}\rho_\lambda(600)^{1.018}$ eV for the Haverah Park array.

The above two relationships allow calculation of the expected value of the normalization constant k in Equation 6.1 for given shower energy and zenith angle. The quantity r_k (shown above in Figures 6.8 and 6.9) is the ratio of the k value determined by fitting the expected lateral distribution shape to the Monte Carlo data in the region $400 < r < 800$ m relative to the predicted value of k. For vertical showers the absolute normalization is the same to $\leq 35\%$. This is no more than saying that the new Monte Carlo reproduces the result of the old. However, the atmospheric attenuation with increasing zenith angle is also relatively well reproduced; Table 6.1 shows the values of r_k for proton and iron initiated showers at four different zenith angles. Note that the attenuation coefficient used is only known to be correct for $\theta < 45°$, and also that the difference in shape between the Haverah Park detectors and the cylindrical design simulated here can be expected to produce a fall off of r_k at large zenith angles.

Shower front rise time

The timing structure of a shower front is greatly affected by muons. In a water Čerenkov detector at large distances from shower core a significant fraction of the total signal is due to muons. (The simulations predict $\approx 20\%$ at 0.5 km rising approximately linearly to 50% at 1.5 km, increasing somewhat with primary particle mass and zenith angle.) Muons scatter

Zenith angle (deg)	r_k (p)	r_k (Fe)
0	1.12	1.35
30	1.20	1.32
45	1.04	1.02
60	0.60	0.94

Table 6.1: Ratio of the fitted k parameter in normalization of the lateral distribution to the predicted value. Separate fits of the Monte Carlo data in the region $400 < r < 800$ m were done for protons and iron primaries at various zenith angles.

less than the electromagnetic particles and so tend to arrive earlier. So muons will also tend to dominate the signal if one considers only the earliest arriving particles. From simple geometry alone, if a shower is approximated as a line source of muons, then in a shower developing high in the atmosphere the path length differences between muons from the top and bottom of the hadronic cascade will be smaller than for showers lower in the atmosphere, leading to a smaller dispersion in their arrival times. Note also that showers initiated by primaries of higher mass are expected not only to be on average higher in the atmosphere, but also to have a larger ratio of muons to electromagnetic particles, and hence a greater muon signal fraction (recall Figures 6.2 and 6.3). All of the above effects produce a correlation between signal rise time and primary particle mass at given core distance.

At Haverah Park the water Čerenkov detector output pulses were integrated, displayed on oscilloscope screens, and recorded photographically. It was straightforward to measure not only the total time integrated amplitude, but also the arrival time dispersion of the air shower signal. The parameter chosen was called $t_{1/2}$, defined as the time taken for the trace to rise from the 10% to the 50% levels relative to the eventual total.

Figure 6.10 shows a comparison of the Monte Carlo predictions of $t_{1/2}$ against actual data from the Haverah Park archives using the cuts indicated. The qualitative agreement is good, particularly for the simulated iron showers. However, the same caution which applies to interpretation of the lateral distribution shape agreement also applies here. The disagreement at $r < 600$ m for the showers at $\theta = 60°$ is partly due to bandwidth limitation effects in the Haverah Park electronics.

As a final comment, the differences in rise time between iron and proton showers is greatly reduced if one instead considers the majority (say, 90%) of the particles instead of only the first 50%. This effect is described in Chapter 9 in relation to constructing an event trigger which is unbiased with respect to composition.

6.2.4 Reconstruction of simulated events

Analysis of the simulated events is done to estimate the ability of the Auger reference detector to achieve the physics goals. Given below are results of work on estimating the trigger

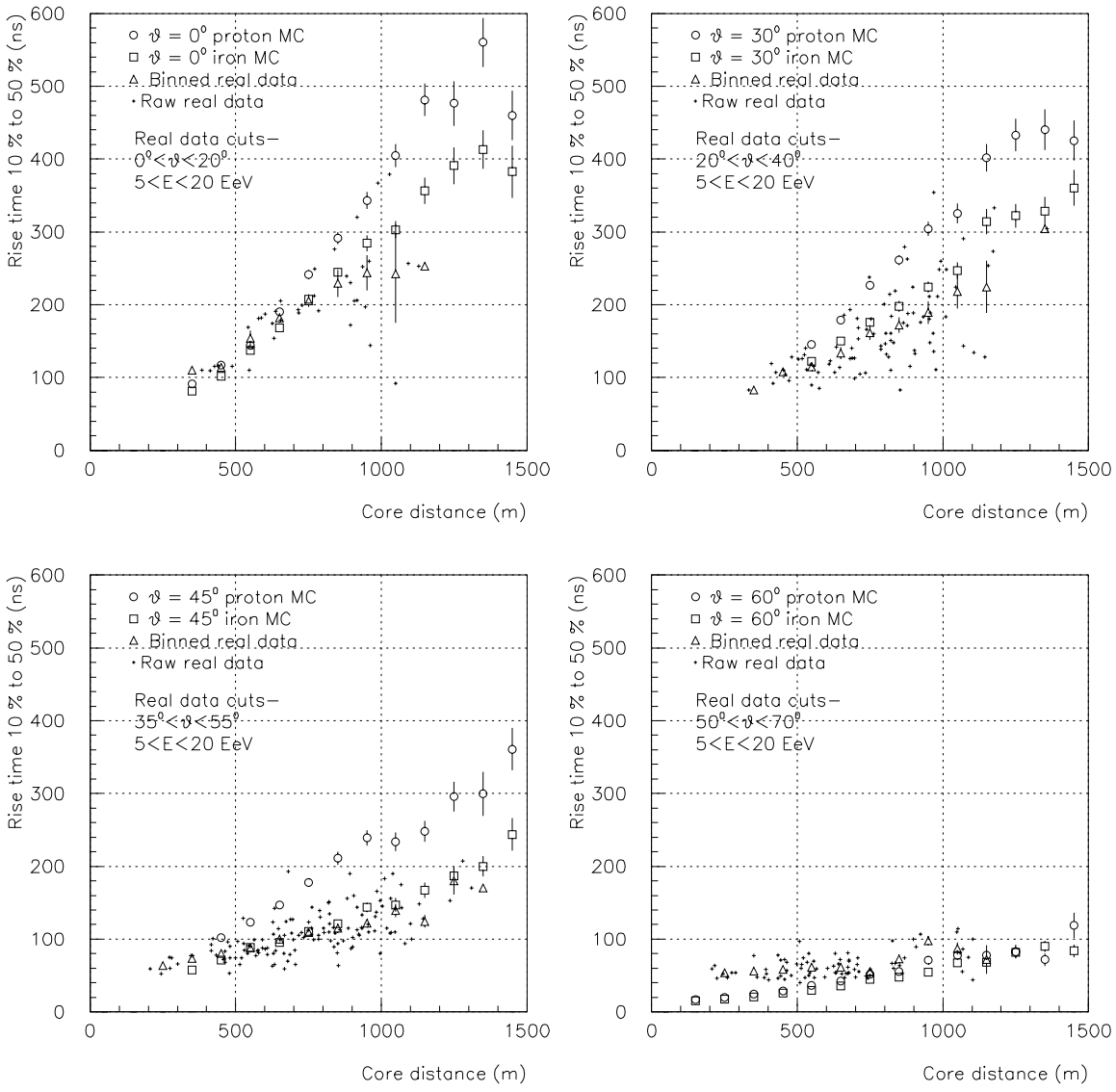

Figure 6.10: Comparison of simulated rise time against real data from the Haverah Park experiment. Comparisons are shown at zenith angles of 0, 30, 45 and 60 degrees. The "raw, real" observations have been extracted from the Haverah Park archives applying the data cuts indicated.

efficiency, the accuracy of energy and direction reconstruction, and the separation of proton and iron induced showers.

Triggering

Schemes for triggering an array of water Čerenkov detectors have been implemented in the simulation. As mentioned before, the signals of photomultipliers are carefully simulated, including the digitizing electronics. One specific feature incorporated in the triggering simulation is that the muon signals are "clipped", i.e., the magnitude of the largest pulses are not permitted to exceed modest levels in the formation of triggers. This will allow the detectors to register the time dispersed signals expected from large showers far from their cores without contamination from the high rate of fast, large pulses from random single cosmic ray muons. Hardware for this purpose is envisaged in the electronics and is described in Chapter 9.

The event trigger itself has been simulated here in a manner suggested by previous experiments such as CASA-MIA. While not exactly the same as the schemes discussed later in Chapter 9, it is expected to provide quite similar results to the actual proposed implementation.

The first step in constructing a realistic array "event" is to impose an *alert* condition on individual ground stations. The motivation is to have only those ground stations with activity beyond noise levels contribute to the trigger formation. This scheme has been used successfully by many experiments (such as CASA-MIA). Any station which registers a total pulse height from all particles penetrating it which is equivalent to that produced by two or more average vertical muons is considered to be alerted. The alert condition is done in hardware within individual stations and does not involve communication with neighbors.

It is useful to impose a *minimum* time constraint on the formation of alerts in order to combat detector noise. The rate of random alerts in individual stations can be several kHz due in part to lower energy ($\geq 10^{14}$ eV) airshower particles. MOCCA simulation of lower energy showers indicates that the time width of the shower front near the core of these showers is very much less than the μsec widths of useful (10^{19} eV) showers at core distances of order a kilometer. If one requires that the particles in a station arrive over a time *longer* than 200-500 nsec, alerts arising from air showers with energy $< 10^{16}$ eV are effectively eliminated and so random noise is substantially reduced.

The event trigger is formed by requiring some minimum number of stations to report coincident alerts within a minimum time. Figure 6.11 shows the efficiency at which vertical proton showers of various energies will trigger the array. Requiring 5 or more alerted stations within 20 μsec gives good efficiency at 10^{19} eV. Also shown are the efficiency curves at lower multiplicity requirements. While such low levels tend of course to eventually become noise-dominated, it will be possible to retain events with the additional constraint of requiring a separate trigger from the fluorescence detector. The reduced energy threshold of the ground array at the lower multiplicity levels (between 10^{17} eV and 10^{18} eV) is well matched to optical detectors such as those described in subsequent chapters.

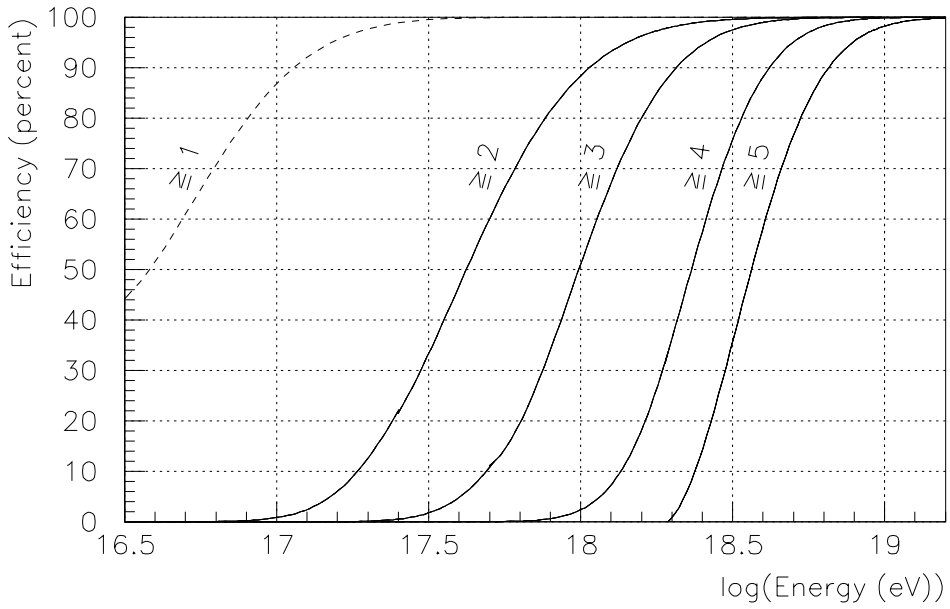

Figure 6.11: Trigger efficiency versus primary energy for vertical proton showers from MOCCA. Various alerted station multiplicity requirements are shown. Lower levels (and consequently lower energy) will be possible using addtional constraints, such as separate triggers from the optical detector.

Most showers recorded by the array will not be vertical. Figure 6.12a shows the 5-fold trigger efficiency and mean alert multiplicity for more typical events (30° from the zenith).

Direction Reconstruction

The determination of the arrival direction of a primary cosmic ray is done by reconstructing the resultant air shower geometry. Particles arrive at the ground in a shower front with a conical shape and a thickness of a few μsec (recall Figure 5.5 and Figure 5.6). If more than three ground stations report hits then the shower front geometry can be fit from the recorded arrival times.

The detector simulation described above is used to provide realistic timing information (including the intrinsic dispersion in the shower front) for alerted ground stations. The precision of the signal digitizing electronics and GPS systems is taken as 5 nsec. The times are those of the first particle to strike each detector. The fit itself is a least-squares minimization of the difference between the recorded times and those expected from the arrival of a plane whose orientation is varied. A conical geometry should properly be used to fit the times, but if the core of the shower is not near the array boundary a plane fit works nearly as well and is rather insensitive to the location of the core.

The accuracy of the fit is determined by comparing a vector normal to the best-fit plane

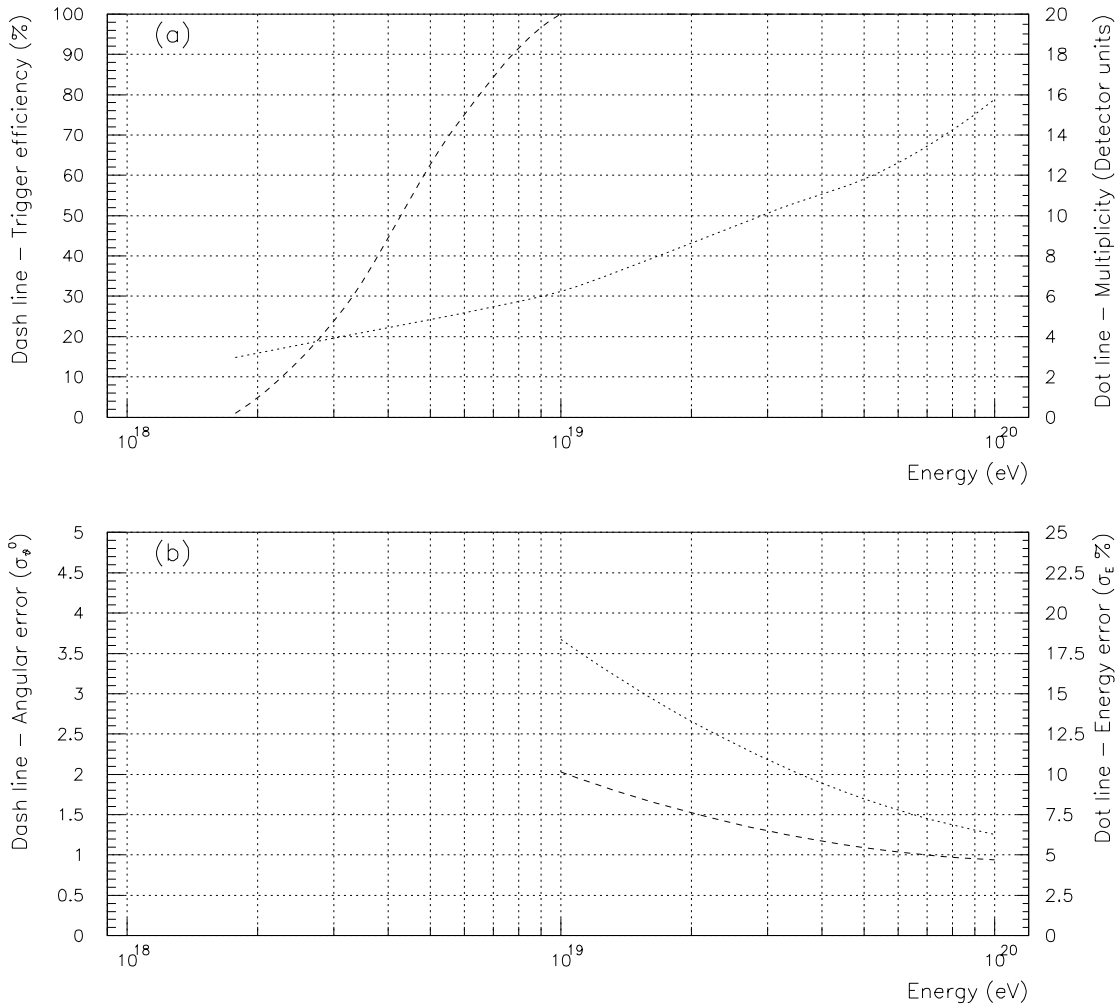

Figure 6.12: Summary of Auger water Čerenkov surface array experimental performance as determined by reconstruction of simulated events. The upper plot shows the detector unit multiplicity and array trigger efficiency if 5 fold events are demanded, and is for proton showers at 30° (compare to last figure which used vertical showers). The lower plot shows the expected reconstruction accuracy of direction and energy for vertical proton showers. Note that the energy error plotted here is only the random component. The assumption of primary particle type results in a systematic shift of some tens of percent, as will uncertainties in the high energy interaction models.

to the true direction of the shower. Under the assumption that the probability of observing some angle between these vectors is distributed as a symmetric two dimensional Gaussian function, Figure 6.12b shows the resulting σ obtained from our simulations. Alternatively, define the parameter σ_{63} to be the space angle with respect to the true direction within which 63% of events have been reconstructed. This parameter is commonly quoted as the "angular resolution" of an experiment since it is closer to the optimum signal-to-noise acceptance cone when searching for a point source in the presence of a uniform background. Note that σ_{63} can be easily computed without having to fit an assumed error distribution function. If the error distribution happens to be Gaussian, then $\sigma_{63} = \sqrt{2}\sigma$. We find that $\sigma_{63} = 3.0^\circ$ for vertical 10^{19} eV proton showers. The accuracy improves to about 1.3° at 10^{20} eV.

The geometry of water Cerenkov detectors is such that longer track lengths and consequently larger individual muon signals occur for showers away from the vertical. This causes the angular reconstruction accuracy to actually improve at large zenith angles. At 60°, for example, $\sigma_{63} = 1.3^\circ$ at 10^{19} eV and 0.5° for 5×10^{19} eV.

Reconstructions of iron showers at similar energies and zenith angles show slightly better angular resolution than proton showers. This presumably arises because the fitting procedure uses the times of the first arriving particles at each detector. Muons tend to be the earliest arriving particles in any air shower. Iron showers have more muons than proton showers of the same total energy, and so appear "bigger" when measured this way, with a corresponding improvement in reconstruction accuracy.

Energy Reconstruction

Algorithms for reconstructing the energy of the air shower have been developed using fits to the total numbers of particles at the ground. Event reconstruction is done using standard least square fit methods. The Haverah Park experimental parametrization of the water Čerenkov lateral distribution given by Equations 6.1–6.3 is used. The Haverah Park attenuation coefficient is also used to predict normalization shift at increasing zenith angle. Using a maximum likelihood technique, the energy of the shower is computed using a fitted size-energy relation obtained previously from an independent set of analyzed MOCCA showers.

Firstly, assume that the nature of the primary composition is known so that proton showers are fitted according to relations appropriate for protons. The error distribution of the reconstructed energy of the detectors is found to have a log-normal distribution, with a standard deviation shown in Figure 6.12b.

The reconstruction accuracy shown under these assumptions reflects only the random component from the sampling statistics of the detectors. This approach is relevant for showers with a single nuclear component or where the nature of the primary can be determined by other means, either from optical detector measurements or muon measurements. To avoid this requirement, the fits are also performed using an average of the lateral distribution functions of protons and iron. The accuracy of this method will depend on the true composition of the primary cosmic rays.

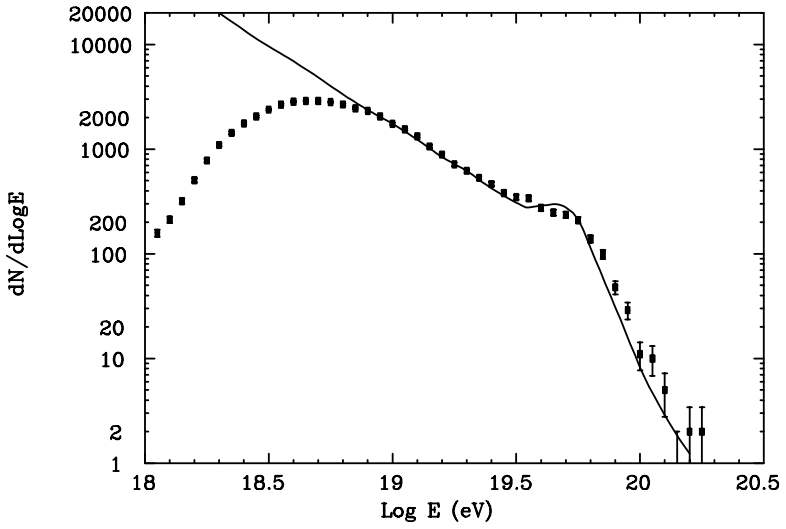

Figure 6.13: Reconstructed energy spectrum of cosmic rays, assuming an input spectrum shown with the solid line, an $E^{-2.5}$ power law and GZK cutoff. The points are from simulation corresponding to about 1.7 years operation of the Auger detector. The deviation of the points from the line at energies less than 10^{19} eV is an anomoly of the procedure used, due to a low energy cutoff in the generation of simulated events.

By means of a simple numerical Monte-Carlo study, estimates have been made as to whether the energy reconstruction will be sufficiently accurate to achieve the goal of identifying features in the cosmic ray energy spectrum. Shower energies are generated according to an input spectrum having an $E^{-2.5}$ power law character and a GZK cutoff [49]. Each energy is then altered according to a Gaussian distribution of $\log_{10}(E)$ to approximate the effects of reconstruction. The variance of this distribution includes both random errors as described above and another term corresponding to uncertainty in the primary composition which is assumed to be equal parts iron and protons. The two effects are added in quadrature. The net smearing of $\log_{10}(E)$ is about 25% at 10^{19} eV, improving to about 20% at 10^{20} eV. Note that this procedure is conservative and would overestimate the energy smearing of a sample of events which are dominated by one nuclear type.

The "reconstructed" energy spectrum is compared with the input. Figure 6.13 indicates how well an assumed cosmic ray energy spectrum can be measured in this way. In this plot, a total number of events corresponding to about 1.7 years of operating the full Auger array were generated. It is clear that this level of resolution will permit the observation of the GZK cutoff. Rough inspection of the reconstructed spectrum suggests that changes in the power law slope of as little as 0.2 or features (bumps) greater than about 30% of the baseline power law can be discerned in this sample.

Composition Sensitivity

The simulated signal timing-amplitude profiles have been analyzed to determine the muonic signal fraction, and hence to separate showers on the basis of primary particle type. Large narrow pulses in the simulated detector signals are identified using a pulse height threshold criterion in the analysis (recall Figure 6.6). The fraction of the pulse height contained therein is taken to represent the ratio of muons to electrons. Figure 5.1 illustrates an example of this technique. It is likely that this can be improved, either through optimizing the selection technique or perhaps by increasing the tank depth from 1.2 m to about 2 m.

Estimates of the nuclear composition using Figure 5.1 could be made by constructing the μ:em parameter for events and comparing them to the curves shown. Also, considering that the composition may not be dominated by a single nuclear type, the *width* of the μ:em distribution for a sample of data can also be calculated and compared to the prediction of the simulation. This technique gives information on whether the composition is in fact mixed or pure and whether it is heavy or light. Such an approach has been employed previously by the Fly's Eye group.

Note that the muon/electron ratio measurements for the purpose of studying composition are relatively insensitive to changes in the physics models of the simulation at extreme energy. As mentioned in the last chapter (section 5.2.2), most ground-level particles originate from the lower energy interactions in the shower where the modeling has been well calibrated by accelerator experiments.

Again, caution must be applied when evaluating these reconstruction results. Although statistical and detector-imposed fluctuations are included in the simulation procedure, the shower-to-shower fluctuations caused by variations in depth of first interaction, etc., have been averaged out by the process used to overcome the "thin sampling" limitations of MOCCA. Some results may also be optimistic due to the lack of simulated events at the "edges" of the array. Work is on-going on more realistic simulation.

6.3 Hybrid Detector Simulation

The simulation methods employed to evaluate the performance of a Hybrid detector are described here. The term "Hybrid" refers to the combination of a ground array and an atmospheric scintillation detector. Advantage has been taken of the experience of, and existing detector simulation code from, two groups - the ground array simulation code of the AGASA experiment, and the HiRes (fluorescence) detector Monte Carlo. Both simulations have been developed over long periods, and have been refined using results from observations. Elements from both have been combined to study the geometrical reconstruction accuracy of a Hybrid detector, using the ground array shower arrival time as a constraint in the single fluorescence detector determination of the shower direction and core. The various elements of the simulation are discussed below, from the shower generation to the detector modelling.

It will be shown that the combination of a single fluorescence site and the ground

array provides reconstruction accuracy equivalent to a stereo fluorescence system, where showers are viewed by two fluorescence detectors, without a ground array. (The latter technique, called "stereo" reconstruction, is the method employed by the HiRes detector and the Telescope Array project.) Based on the solid footing of good geometrical reconstruction, we then discuss the energy and depth of maximum resolution of the Hybrid detector.

6.3.1 Methods

In our simulations of Hybrid aperture, geometric reconstruction, and energy and X_{max} (depth of shower maximum) resolution, parametrizations of the longitudinal and lateral structure of the showers were used. Fluctuations were introduced where appropriate. Each parametrization is discussed in turn.

Longitudinal Profile

Each simulation run was performed at fixed energy. For each energy, the *mean* depth of the shower maximum was determined from simulations [63]. Results appropriate to a proton primary beam are used, with an X_{max} of 780 g/cm^2 at 10^{19}eV and an elongation rate of 55 g/cm^2 per decade. Such a composition is consistent with the Fly's Eye data above 10^{19}eV.

Variations in the depth of maximum were simulated simply by introducing fluctuations in the depth of first interaction X_0. A mean interaction length of 70 g/cm^2 was assumed at all energies. This is clearly not accurate, though it is sufficient for our investigation of detector aperture, geometrical reconstruction and energy and depth of maximum resolution.

The primary energy determines the shower size at its maximum, N_{max} [64]. Given N_{max}, X_{max} and X_0, the complete longitudinal profile was described by the Gaisser-Hillas function [65].

Charged Particle Lateral Distribution

The Akeno lateral distribution function is used to determine the particle counts in the detectors. The function is given in [66] and has a dependence on shower zenith angle. The shape of the function has no energy dependence, since none has been detected in the real data.

The shower size at ground level (the normalization of the lateral distribution) is determined from the longitudinal profile discussed above, and the shower zenith angle. Thus the development fluctuations introduced in the fluorescence simulation are passed on to the ground array simulation.

Shower Front Timing Structure

To handle the shower front curvature and thickness data tables are constructed of the delay of shower particles behind an imaginary plane shower front using an ensemble of MOCCA-generated vertical proton showers at 10^{19}eV. These include the response of standard Akeno type scintillators to low energy gammas and electrons. The tables are embedded into a subroutine which, given the core distance, assigns a particle an arrival time with respect to a plane shower front. In other words, both curvature and thickness are simulated in a reasonable way.

6.3.2 Simulation of Fluorescence Detector Response

A brief description of the HiRes simulation code used in this study is presented. Mirror area and phototube aperture are parameters that may be altered. Details of some of the methods used here can be found elsewhere [67, 68].

The simulation is performed for the Dugway altitude (860 g/cm^2).

1. For a chosen energy determine the depth of shower maximum. Randomly choose the shower arrival direction (zenith angle less than 60°) and core location. The core location must be within the physical area of the ground array.

2. Calculate the light emitted from the shower along its track. Both fluorescence and Čerenkov light is calculated. The pressure and temperature dependence of the fluorescence yields are taken into account.

3. Calculate the light yield arriving at the detector site. The isotropically emitted fluorescence light, as well as direct and scattered Čerenkov light, is propagated. Rayleigh and Mie scattering processes are simulated, with full account taken of the spectral characteristics of the light. Night sky background noise is added to the signal at this stage.

4. Mirror area and reflectivity are used to determine the light falling on each phototube cluster. A treatment of the spherical aberration of the mirror is included, giving a more realistic treatment of the light spot as it traverses the cluster. Optical filter transmission and phototube quantum efficiency factors are folded with the light spectrum to give the photoelectron yield in each tube, due to signal and noise. The pulse width (the traversal time of the spot across the tube) is calculated, taking into account mirror aberrations.

5. For each tube viewing the shower, the photoelectron yield, the pulse width, and an estimate of the time at the midpoint of the pulse is recorded. The latter quantity is calculated, then fluctuated, using experience with the Flash ADC system currently being constructed for HiRes. The uncertainty of the mid-pulse time is a function of the pulse width and the number of photoelectrons.

6. The triggering scheme employed here is that used in the HiRes sample and hold (i.e. pre FADC) electronics system. A tube is said to trigger if its instantaneous photoelectron current (taking into account the time constant of the circuitry) is greater than the 4σ night sky noise level. A mirror will trigger if it contains a sufficient number of firing tubes. For trial detectors that contain 256 tubes per mirror, the HiRes mirror triggering scheme, which performs pattern recognition on a series of subclusters within the tube cluster, is used. Otherwise, a string of firing tubes covering a track length of at least 10° is required. As discussed later, the reference design (Cyclops 3000) is approximated with an eye containing mirrors with 256 tubes per cluster. This eye is triggered using the former scheme.

7. A trigger in at least one mirror defines an accepted event.

6.3.3 Simulation of the Ground Array Response

The main steps of this procedure are taken from the AGASA detector Monte Carlo. The array consists of 10 m^2 detectors made of 5 cm plastic scintillator arranged on a triangular grid of spacing 1.5 km. The array is placed at Dugway altitude (860 g/cm^2). For the reference design simulations, the total area of the array was set at 3000 km^2. The procedure is as follows:

1. Energy, shower direction and core location come from the fluorescence section of the simulation.

2. Determine the shape of the lateral distribution, a function of zenith angle.

3. Determine the ground level shower size from the profile used in the fluorescence calculation. In this way, fluctuations in the depth of maximum are translated into shower size fluctuations at the array. The shower size provides the normalization for the lateral distribution, which is used to calculate the particle count n_i in each detector.

4. Determine the number of particles registered in each detector by sampling from the Poisson distribution with mean n_i.

5. Each particle is assigned an arrival time relative to a plane shower front, using the data tables discussed earlier. The time of arrival of the first particle is recorded, as well as the mean arrival time and time dispersion of all the particles.

6. Detector resolution is folded into the particle density. This is based on results from Akeno detectors in the 1 km^2 array.

7. For an event to trigger the array, require that at least three stations register a particle count greater than 3. No pulse width discrimination is applied. Once a trigger is established, record data from all stations with counts of at least one particle. This approximates a possible trigger scheme.

Further details of this method may be found elsewhere [66].

6.3.4 Hybrid Geometric Reconstruction Method

A reconstruction method using the fluorescence detector alone is presented below, followed by a method of adding the ground array information to constrain the fluorescence fit.

Fluorescence Detector Geometric Reconstruction

The standard mono HiRes fitting procedure for the shower core location and direction starts with the determination of the plane containing the shower axis and the eye. This shower-detector plane (SDP) fit uses photomultiplier tube pointing directions, together with signal integrals. Tube timing information is not used at this stage, except to discard tubes with noise.

The SDP fitting procedure [69] uses trial planes which are compared with the pointing directions of fired phototubes, with the fit weighted by the signal amplitudes. Pulse width information which would be available with Flash ADC electronics has not been exploited. The pulse width would help determine the crossing point of the shower across each tube and constrain the plane fit even further.

Once the SDP is determined, the firing times of the tubes are used to determine the orientation of the shower axis within that plane. The times used here are estimates of the time at which each tube integral reaches 50% of its full value. This is our estimate of the tube-center crossing time. Figure 6.14(a) shows the geometry within the SDP. For a given geometry, the arrival time of light at a tube viewing the axis at an angle θ_i is

$$t(\theta_i) = \frac{R_p}{c} tan(\frac{\theta_i}{2}) + t_0$$

where t_0 is the time at which the shower reaches point A on the diagram, and $\theta_i = \pi - \psi - \chi_i$. A fit for R_p and the ground angle ψ is done. Together with the SDP, these parameters fully define the event geometry.

There is a problem with these timing fits, especially for short (i.e. distant) shower tracks. This has long been recognized, and is one reason the stereo Fly's Eye technique was pursued as an alternative to mono observations. With short tracks the range of θ_i sampled is often not large enough to detect significant curvature in the tangent function in the above equation. In other words, the shower appears to pass through the field of view with *constant angular velocity*. Unfortunately, this leads to ambiguity in the fit, with a family of possible (R_p, ψ) values (Figure 6.14(b)).

Hybrid Geometric Reconstruction

This ambiguity can be resolved by using other information, for example a SDP from another fluorescence detector, or information from a ground array. The most promising ground array parameter is the arrival time of the shower core at the ground. It is obvious from

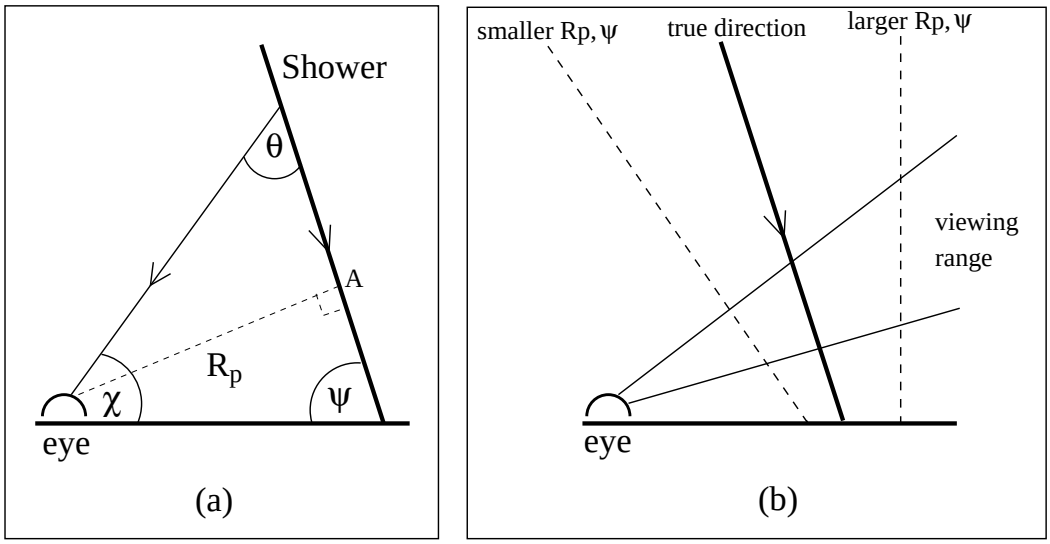

Figure 6.14: (a) Geometric reconstruction within the shower-detector plane. A phototube views the shower at an angle θ with respect to the axis. (b) Ambiguity in the position of the shower within the SDP for short tracks (highly exaggerated).

Figure 6.14(b) that if all eye and ground array times are measured with a common clock, then the ground array times will constrain the timing fit within the SDP.

The full Hybrid geometrical reconstruction proceeds in the following way:

1. The SDP is determined in the standard way, using fluorescence information only. Typically, the plane orientation is known to better than 0.1°, which corresponds to a distance of at most 50 m on the ground at a distance of 30 km. Thus ground array information is of limited use at this stage of the fit.

2. From this point on assume that the shower core is contained on the line forming the intersection of the SDP and the ground. Proceed with the timing fit, minimizing a χ^2 which includes the standard fluorescence timing term and an array timing term. The fluorescence timing term is

$$\chi_1^2 = \frac{ntbs}{\sum pe_i} \sum \frac{(t_i - t_{expected})^2}{\sigma_{ti}^2} pe_i$$

   where t_i is the estimate of the pulse mid-point time, and σ_{ti} is the mid-point time uncertainty for each tube. The elements of the sum are weighted by pe_i, the signal in each tube. Multiply by $ntbs$, the number of firing tubes, so that the appropriate weight is given to this term of the χ^2 when array component is added.

3. The array component of the χ^2 takes one of three forms. We will compare the results.

   Method 1: This first method uses a single array detector to define the shower arrival time. The detector with the largest particle count is chosen, and a model

of the curvature of the shower front is used to calculate the expected time in this detector for each trial geometry. The shower front curvature parametrization is the same one used in the generation of the data, but because this detector is close to the core, the dependence on details of the curvature is not strong. (In any case, it is expected that measurements of curvature will be one of the first tasks of the array). The χ^2 term is then

$$\chi_2^2 = \frac{(t_i^* - t_{expected})^2}{\sigma_{ti}^{*2}}$$

where

$$\sigma_{ti}^* = \frac{\sigma_{0i}^*}{\sqrt{n_i^*}}$$

and t_i^* is the mean arrival time of particles at the detector with the largest particle count, σ_{0i}^* is the dispersion in the arrival time, and n_i^* is the number of particles detected.

Method 2: While the method above is conceptually simple, it does not use all of the available array data. In the second method, the mean arrival time of all array detectors with particle counts greater than 10 is used. The expected times are again calculated using the shower curvature parametrization used in the data generation.
The term is

$$\chi_2^2 = \sum \frac{(t_i - t_{expected})^2}{\sigma_{ti}^2}$$

where

$$\sigma_{ti} = \frac{\sigma_{0i}}{\sqrt{n_i}}$$

where the sum is over all detectors with particle counts greater than 10 particles. t_i is the *mean* arrival time of the particles at each detector, σ_{0i} is the dispersion in the particle arrival time, and n_i is the number of particles detected.

Method 3: What if the form of the shower front curvature is not known? The following form of the array χ^2 was also found to work well. Here, times from all array detectors that fire with particle counts greater than 10 are used. The time of the *first* particle in each detector is used, and the expected time is calculated assuming a plane shower front. Surprisingly perhaps, this method works very well. It is true that the first particle will arrive closer to a plane front than the majority of the particles, which will be delayed. However, the success of this method probably relies on there being time measurements on all sides of the core. The method may produce a systematic error in direction for showers landing near the edge of the array.
The form of the χ^2 term is the same as in Method 2, but here t_i is the arrival time of the first particle at each detector. Again σ_{0i} is the dispersion in the arrival time of all the particles, and n_i is the number of particles detected. Only detectors with at least 10 particles are used in the sum.

4. The final χ^2 minimization was performed on the linear sum of the fluorescence and ground array components, with the ground array component taking one of the three forms discussed above. That is,

$$\chi^2 = \chi_1^2 + \chi_2^2$$

6.3.5 Resolution in Energy and Depth of Maximum

The ability to make accurate determinations of a shower's longitudinal profile with a fluorescence detector depends critically on the geometric reconstruction discussed above. Once the geometry is determined, the conversion of measured light intensities into a longitudinal profile relies on an understanding of the light propagation properties of the atmosphere. The analysis assumes the same atmospheric parameters used in the generation of the simulated data. The model used is in excellent agreement with the "1976 US standard" atmosphere with a desert aerosol profile. The atmosphere at the observatory site (particularly the aerosol structure) is assumed to be monitored and characterised using lasers, in a way similar to that being used at the HiRes site.

The method of profile reconstruction is that used in the Fly's Eye and HiRes experiments [67]. Essentially, it is the reverse of the process described in the simulation section above. Photoelectron counts in a particular tube are converted to a shower size at the shower axis by a process which takes into account the physical parameters of the detector, atmospheric transmission and shower light production (fluorescence light and Čerenkov light, both direct and scattered). Finally, the Gaisser-Hillas function is fitted to the measured profile to extract the shower size at maximum, N_{max}, the depth of maximum, X_{max} and the depth of first interaction X_0. The energy is then determined by integrating the profile, taking account of the small fraction of energy not carried by the electromagnetic portion of the shower.

6.3.6 Results

Figure 6.15 shows the reconstructed Hybrid aperture as a function of energy. Shower cores are limited to those landing within the array boundaries, and shower zenith angles are less than 60°. The array trigger used here requires at least three detectors to have a particle count greater than three. No cuts have been placed on reconstruction accuracy. The quality of the reconstruction will be seen in subsequent figures and in Table 6.2.

Beginning with geometry determined by the fluorescence detector alone, the error distribution is shown for the *normal* to the shower-detector plane (SDP) in Figure 6.16. All showers triggering the hybrid detector at 10^{19}eV were used. The differential and integral forms of the error distribution are shown in this figure. It can be seen that 50% of the plane normal errors are smaller than 0.11° and 90% are smaller than 0.9°.

Within the shower-detector plane, the fluorescence detector uses tube firing times to determine the impact parameter R_p and the ground angle ψ (see Figure 6.14). The resolution

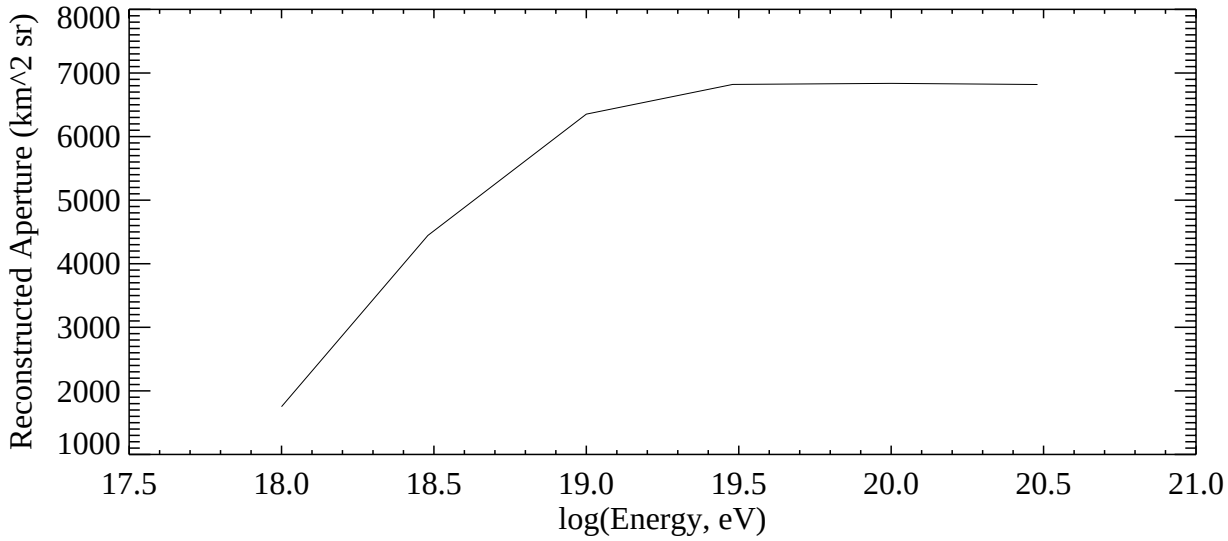

Figure 6.15: The reconstructed Hybrid aperture as a function of energy.

in these measurements is strongly dependent on the length of the shower track viewed by the eye. Results are given in Figure 6.17, again for 10^{19}eV showers triggering the hybrid array. Only fluorescence information is used in the reconstruction here.

Array information is applied to the fits using the three methods described earlier. Figure 6.18, for 10^{19}eV triggers, shows the impact parameter R_p error distributions for (a) Method 1, (b) Method 2 and (c) Method 3. Note how the dependence on track length has dramatically lessened. Similar results are found for the ground angle ψ (Table 6.2 below). Method 1 represents a significant improvement over the "fluorescence only" fits in the previous figure. The fits are further improved by using more ground array information in Methods 2 and 3. A median R_p error of 45 m is found using the latter methods.

The final core location and shower direction errors for showers at 10^{19}eV are displayed in Figure 6.19. Results are given for (a) Method 1 and (b) Method 2. (Method 3 gives similar results to Method 2 - see Table 6.2). Method 2 gives a median core location error of 35m and a median shower direction error of 0.25°.

Figure 6.20 and Figure 6.21 show results from the profile reconstruction for 10^{19}eV showers. As with all figures in this section, no quality cuts have been applied to the distributions. All showers triggering the Hybrid array have been included here. In (a), the X_{max} error ($Xmax_{reconstructed} - Xmax_{true}$) is shown for showers analysed using the fluorescence information alone. Also shown are results for the same showers analysed using (b) Hybrid Method 1 and (c) Hybrid Method 2. Again, the results for Method 3 are similar to those of Method 2. Even with good geometrical reconstruction, it is clear that a long track length improves the reconstruction of a longitudinal profile. The poorer fits to X_{max} and energy are generally associated with short tracks.

Figure 6.21 shows the energy resolution $(E_{reconstructed} - E_{true})/E_{true}$ for 10^{19}eV showers

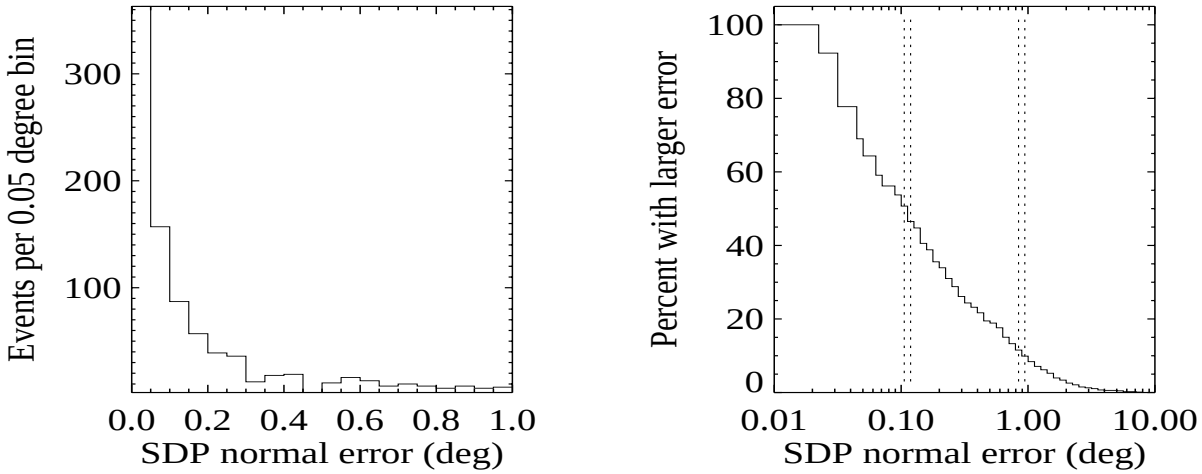

Figure 6.16: Error distribution for the normal to the shower-detector plane (SDP), for all showers triggering the hybrid detector at 10^{19}eV. The differential and integral forms of the error distribution are shown. It can be seen that 50% of the plane normal errors are smaller than 0.11° and 90% are smaller than 0.9°.

analysed with data from the fluorescence detector only (a), and with Hybrid data using (b) Method 1 and (c) Method 2. Again, no quality cuts have been applied. There is a slight (6%) systematic energy error, probably due to somewhat different treatments of mirror aberrations in the simulation and the analysis.

At an energy of 10^{18}eV, the array described is not fully efficient. However, showers of this energy may trigger two or three array detectors. Figure 6.22 shows results for 10^{18}eV analysed with Method 2. The array trigger requirement has been relaxed at this energy to allow events to trigger with only two detectors at the three particle level (instead of three detectors). Method 2 uses array times from detectors with a particle count of more than 10. In some events, this may mean that only one or two detector times are used in the fit. Despite this, good reconstruction appears possible for most events. Results for Methods 1 and 3 are given in Table 6.2.

A summary of reconstruction resolution is given in Table 6.2. In each case the value of the error parameter bracketing 50% and 90% of the distribution is given. Methods 1,2 and 3 have been previously described. (Given the similarity of geometrical reconstruction for Methods 2 and 3, the energy and X_{max} resolution is given for Method 2 only). Method 0 represents the reconstruction due to the fluorescence data alone.

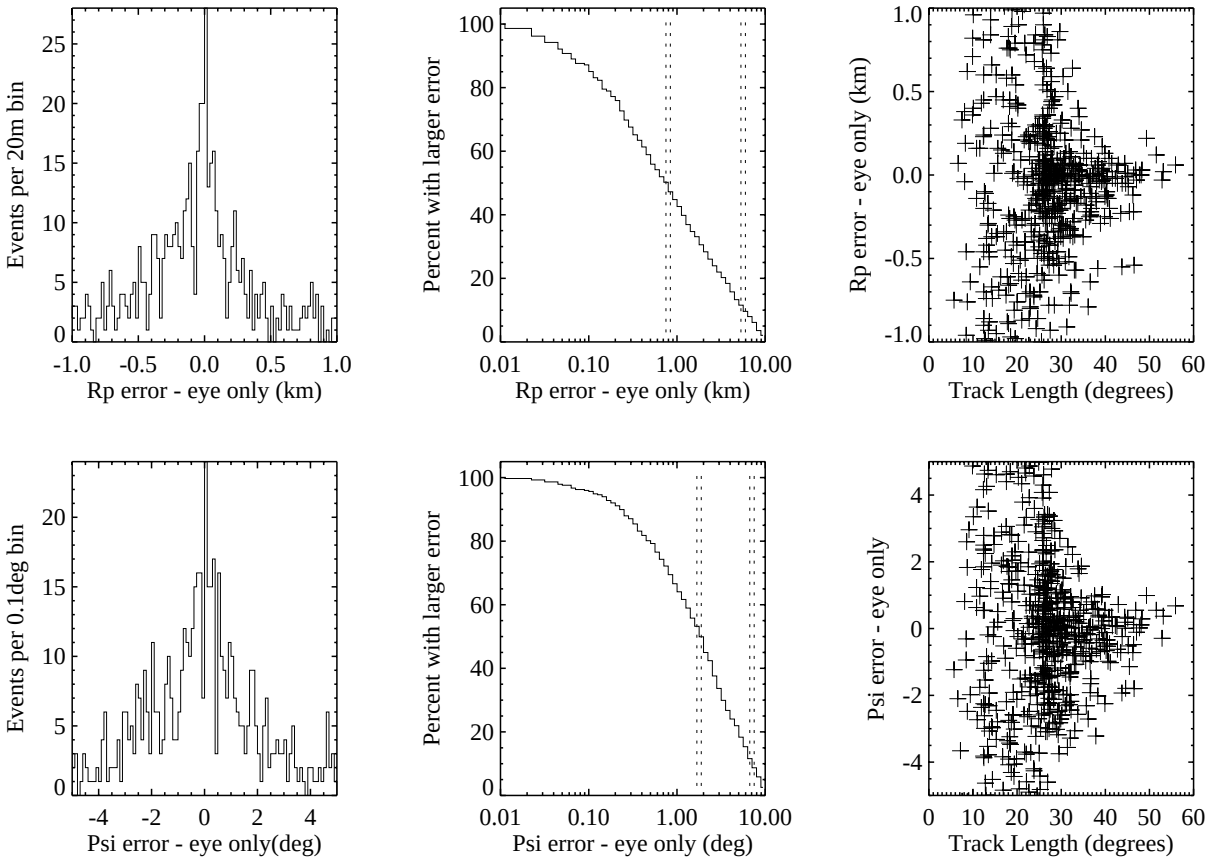

Figure 6.17: Reconstruction errors for impact parameter R_p and the ground angle ψ (see Figure 6.14). The resolution in is strongly dependent on the length of the shower track viewed by the eye. Results shown for 10^{19}eV showers triggering the hybrid array.

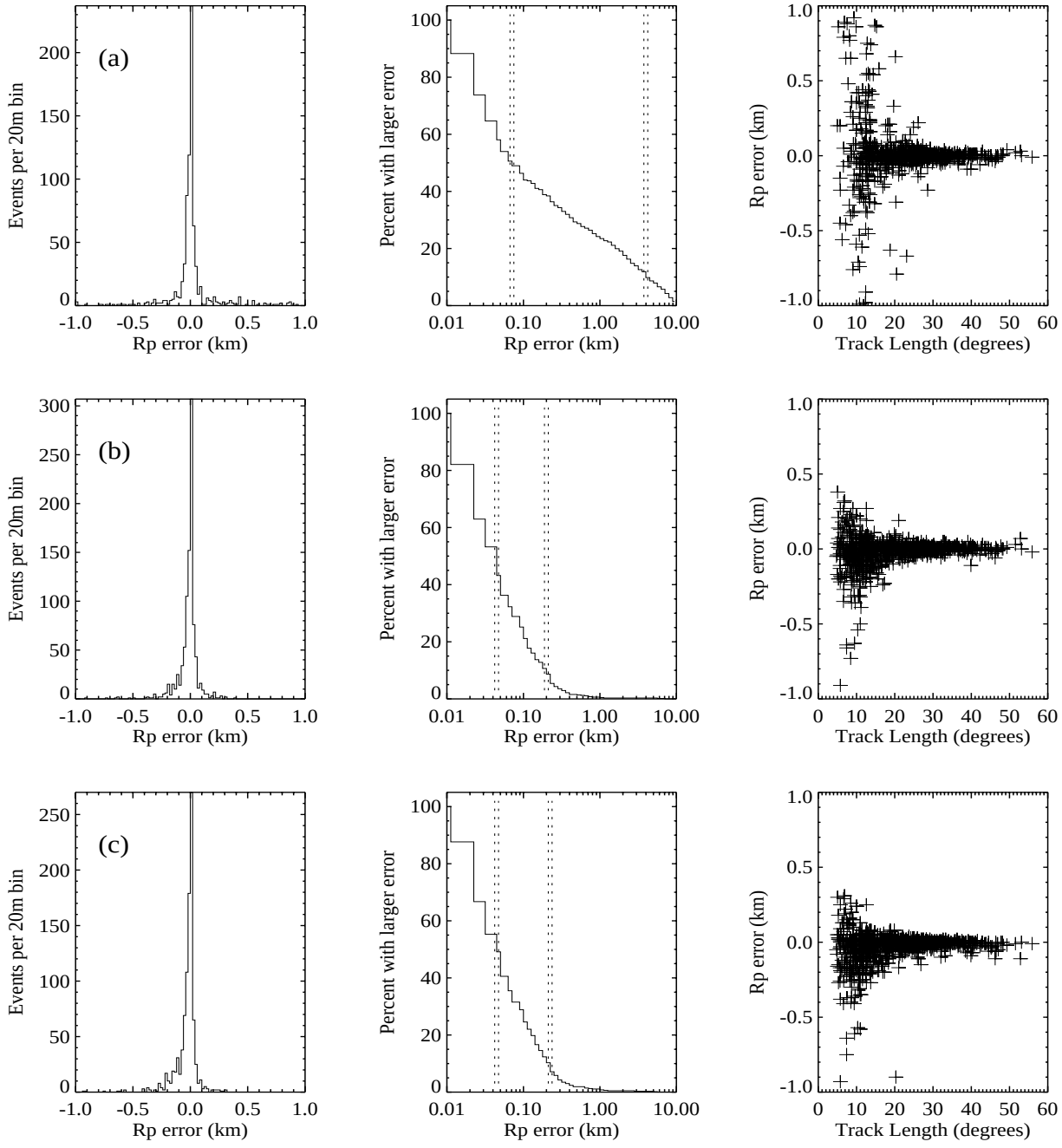

Figure 6.18: Impact parameter error distributions using (a) Method 1, (b) Method 2 and (c) Method 3 on 10^{19}eV triggered showers.

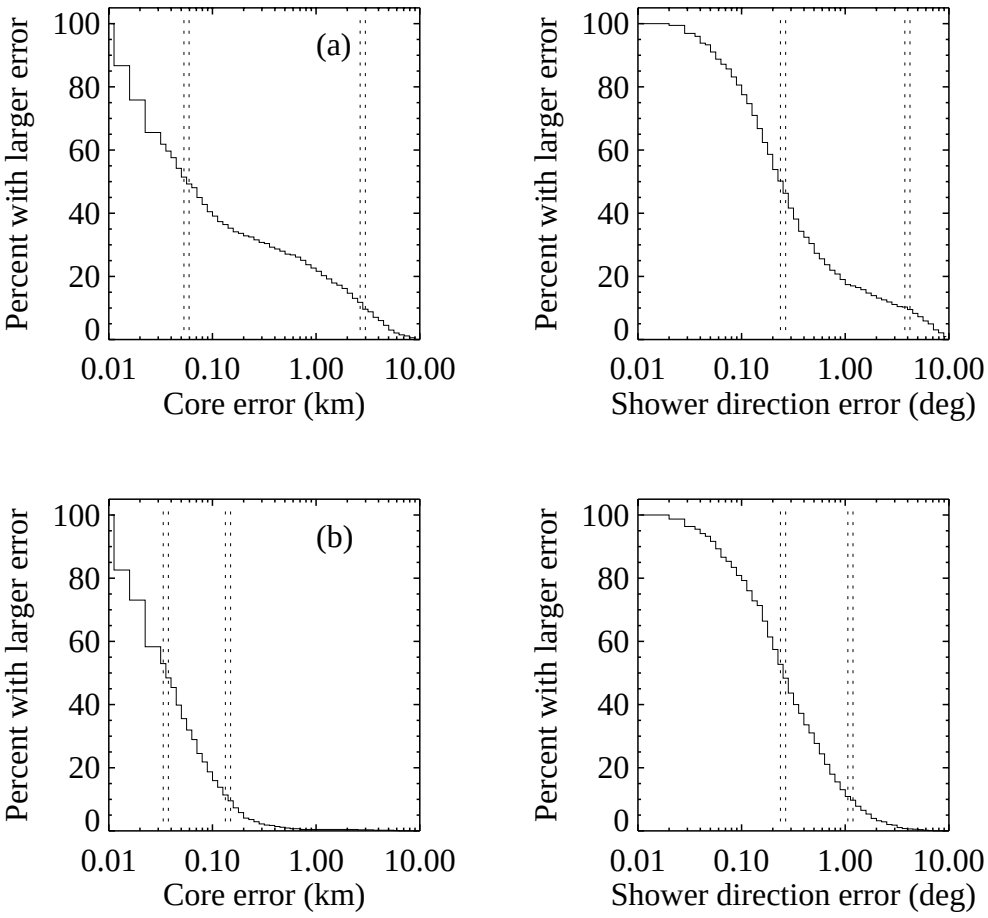

Figure 6.19: The final core location and shower direction errors for showers at 10^{19}eV. Results are given for (a) Method 1 and (b) Method 2. (Method 3 gives similar results to Method 2)

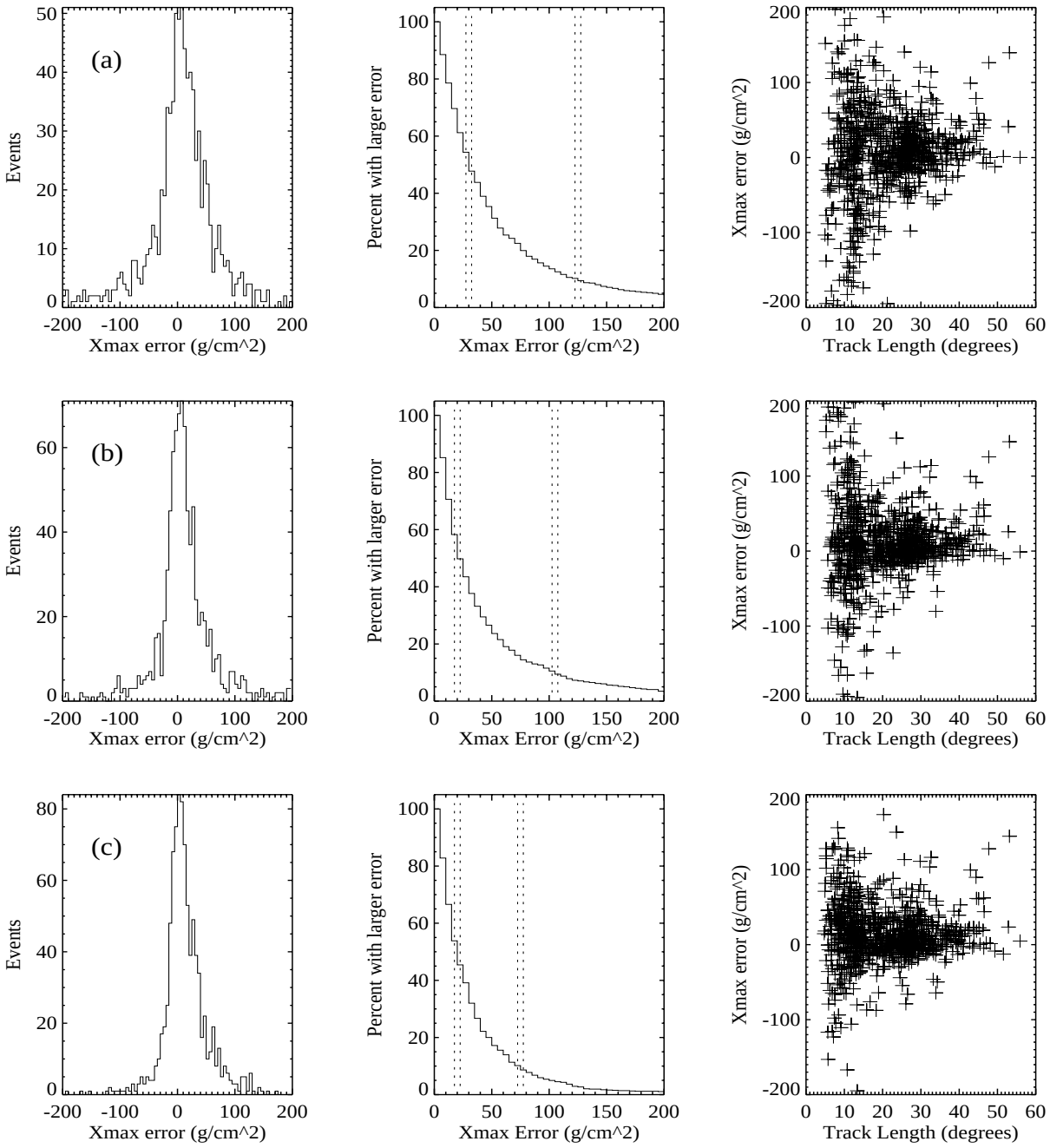

Figure 6.20: Profile reconstruction of 10^{19}eV showers. All showers triggering the Hybrid array have been included here. In (a) is shown the X_{max} error ($Xmax_{reconstructed} - Xmax_{true}$) for showers analysed using the fluorescence information alone. Also shown are results for the same showers analysed using (b) Hybrid Method 1 and (c) Hybrid Method 2.

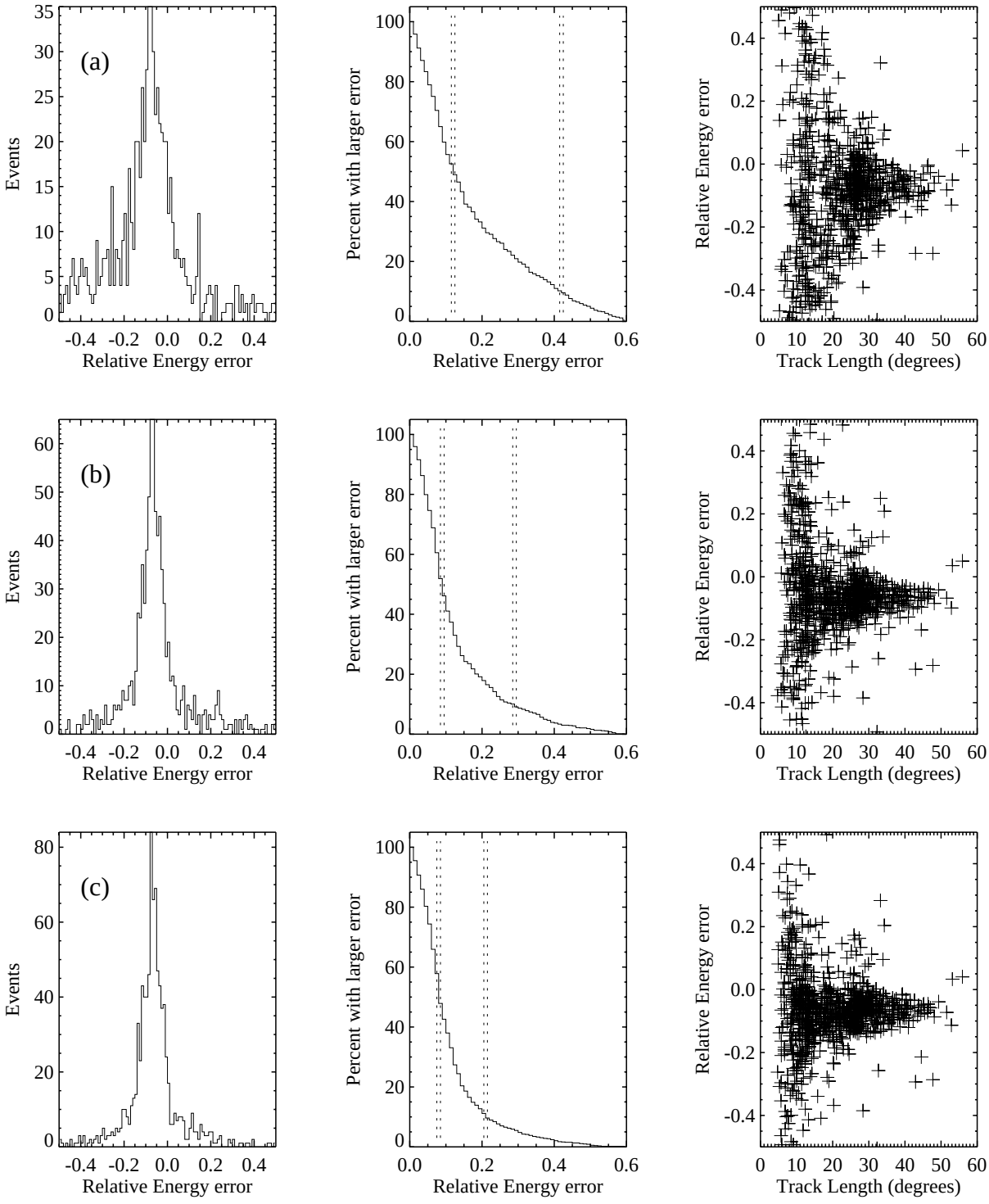

Figure 6.21: Energy resolution $(E_{reconstructed} - E_{true})/E_{true}$ for 10^{19}eV showers analysed with data from the fluorescence detector only (a), and with Hybrid data using (b) Method 1 and (c) Method 2.

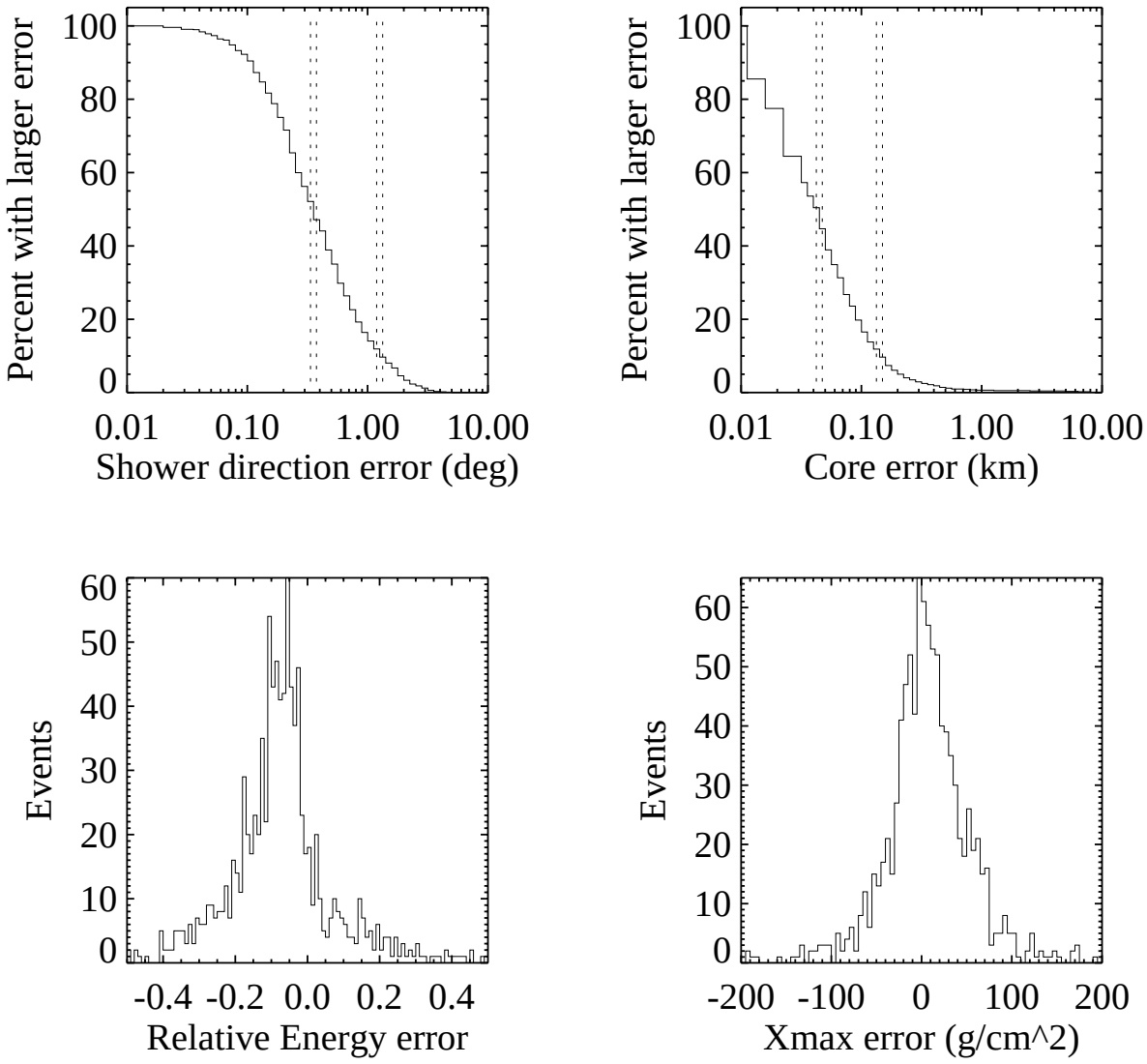

Figure 6.22: Reconstructions of lower energy (10^{18}eV) showers, analysed with Method 2.

Meth.	Δdirec.(°)		ΔCore(m)		ΔR_p (m)		$\Delta\psi$(°)		$\Delta E/E$		ΔX_m(gcm^2)	
	50%	90%	50%	90%	50%	90%	50%	90%	50%	90%	50%	90%
10^{18}eV (median plane normal error 0.18 deg)												
1	0.35	1.9	43	2200	43	1200	0.25	1.3	0.10	0.31	25	100
2	0.35	1.2	43	120	30	130	0.25	0.90	0.10	0.28	25	80
3	0.31	1.1	40	150	43	150	0.21	0.90				
3×10^{18}eV (median plane normal error 0.11 deg)												
1	0.30	2.2	50	3500	50	3300	0.21	1.9	0.10	0.31	25	95
2	0.31	1.1	43	180	43	190	0.21	0.90	0.10	0.25	20	80
3	0.30	1.1	43	180	43	200	0.20	0.80				
10^{19}eV (median plane normal error 0.11 deg)												
1	0.25	4.0	55	2900	70	4000	0.20	4.0	0.09	0.29	20	105
2	0.25	1.1	33	120	43	200	0.20	0.80	0.08	0.21	20	75
3	0.25	1.1	40	150	43	210	0.19	0.70				
3×10^{19}eV (median plane normal error 0.09 deg)												
1	0.25	5.5	58	3000	100	4300	0.22	5.5	0.08	0.27	20	95
2	0.22	0.70	22	90	30	160	0.18	0.62	0.07	0.17	20	65
3	0.20	0.70	30	105	43	200	0.18	0.62				
10^{20}eV (median plane normal error 0.06 deg)												
1	0.31	5.5	90	1900	120	4000	0.30	5.5	0.08	0.28	20	100
2	0.20	0.62	21	80	30	120	0.18	0.60	0.07	0.14	20	60
3	0.20	0.58	21	90	30	150	0.15	0.50				
3×10^{20}eV (median plane normal error 0.06 deg)												
1	0.60	6.2	110	2500	210	4000	0.60	6.3	0.05	0.30	25	95
2	0.20	0.63	21	70	30	110	0.19	0.60	0.04	0.20	20	70
3	0.15	0.50	21	70	30	130	0.12	0.45				
10^{19}eV (median plane normal error 0.11 deg)												
0	1.8	7.0	630	5500	620	5000	1.8	7.0	0.12	0.42	30	125

Table 6.2: Summary of reconstruction resolution for the Hybrid Detector.

Chapter 7

Surface Detector Array

Water Čerenkov detectors have been selected as the primary detector technology for the Auger ground array. It is believed that a suitably designed water tank array can adequately address the physics requirements discussed in the previous two chapters, whilst proving more cost effective than other competing techniques. The reference design presented here calls for an array of 10 m^2 cylindrical detector units arranged in a 1.5 km spaced hexagonal grid. In the sections which follow several aspects of the design and performance of the basic surface array units are discussed.

For twenty years a 12 km^2 EAS array employing more than 200 water Čerenkov units was operated at Haverah Park in the UK [100]. The experience gained during this experiment provides much useful information for the Auger project, demonstrating that an array based on this technique can operate for a long period with both high stability and low maintenance.

At moderate altitudes a surface array observes EAS well past the shower maximum. (Sea level is 1040 g-cm^{-2} while shower maximum for a 1×10^{19} eV shower is typically 750 g-cm^{-2}). In this regime the cascade curve decay can be approximated by an exponential. The overall shower is dominated numerically by electromagnetic particles, but at large core distances (> 500 m) most of the energy is carried by the muonic component. The electromagnetic component attenuates much faster than the muonic component. Hence different types of detector produce different effective shower attenuation lengths dependent on their relative sensitivities to these two shower components.

For the Haverah Park water Čerenkov array the attenuation coefficient for signal density at 600 m from shower core was found to be 760 ± 40 g-cm^{-2}, whilst for the Yakutsk scintillator array a value of 500 ± 40 g-cm^{-2} was derived[100] (both sites are close to sea level). This effect makes a water Čerenkov array less sensitive to the atmospheric depth of the site. Also, at a given atmospheric depth, the array energy threshold will rise more slowly with increasing zenith angle providing greater solid angle acceptance at given energy. This results in more collecting power per detector unit, but most importantly, a more uniform sky view in terms of declination angle. The experimental declination distributions from the Haverah Park and Volcano Ranch arrays which illustrate this point are shown in Figure 4.4.

A secondary advantage of the "deep" ($\geq$ 1 m) water Čerenkov detector is the large depth to lateral size ratio. This results in the detector projected area in the plane perpendicular to the shower axis falling much more slowly with increasing zenith angle. Hence statistical sampling fluctuations are smaller in the very low density shower front at large distances from the core. Thin detectors are inferior in this respect.

7.1 The proposed design

In its simplest form a water Čerenkov detector can be described as a volume of (clear) water acting as a Čerenkov radiator viewed by one or more sensitive light detectors. In this application the fact that the water also acts as a massive absorber and detector of the very numerous shower gamma rays is very important.

Conceptually, the reference design proposed for the Auger ground array detector unit is a cylindrical volume of water viewed from above by three large (200 mm diameter) PMTs. The walls of the tank are highly reflective diffusive white surfaces. A concept for the complete ground array detector station is shown in Figure 7.1

7.2 Detector geometry and array spacing

The required detector area is a function of the array grid spacing and shower threshold energy desired. Since each station entails many fixed costs independent of the detector area, (electronics, deployment, etc.), and for given array coverage the number of stations required is inversely proportional to the square of the array spacing, it is vitally important that this spacing should be as large as possible. It is an experimental requirement that the array should be fully efficient at a shower energy of 1×10^{19} eV. For a 1.5 km spacing a detector area of 10 m^2 will give adequate performance (see Chapter 6). With a spacing of 1.5 km the number of triggered stations will be large enough ($>$ 15 to 20 units) at the very highest energies ($\geq$ 10^{20} eV) to allow high quality and unambiguous event reconstruction.

In all the following work we have assumed a cylindrical detector 1.2 m deep with a radius of 1.8 m (top surface area 10 m^2). The depth is a nominal value selected to allow direct comparison with the existing experimental data from Haverah Park. As discussed in Chapter 6, 3.5 radiation lengths of water is sufficient to absorb $\geq$ 90% of the incident electromagnetic shower particles. However, a somewhat greater depth (e.g. 2.0 m) may be preferred to enhance the muonic content information which can be extracted from the differential time/amplitude signal profile.

For practical reasons it might be desirable to form each detector station from a number of smaller units, but this would degrade the muonic content information which can be extracted. The measurement of total time integrated light yield and arrival time dispersion is only affected at second order by the lateral size (and shape) of the detector units. However, it is important to keep "corner clipping" effects to a minimum, to maximize the pulse height

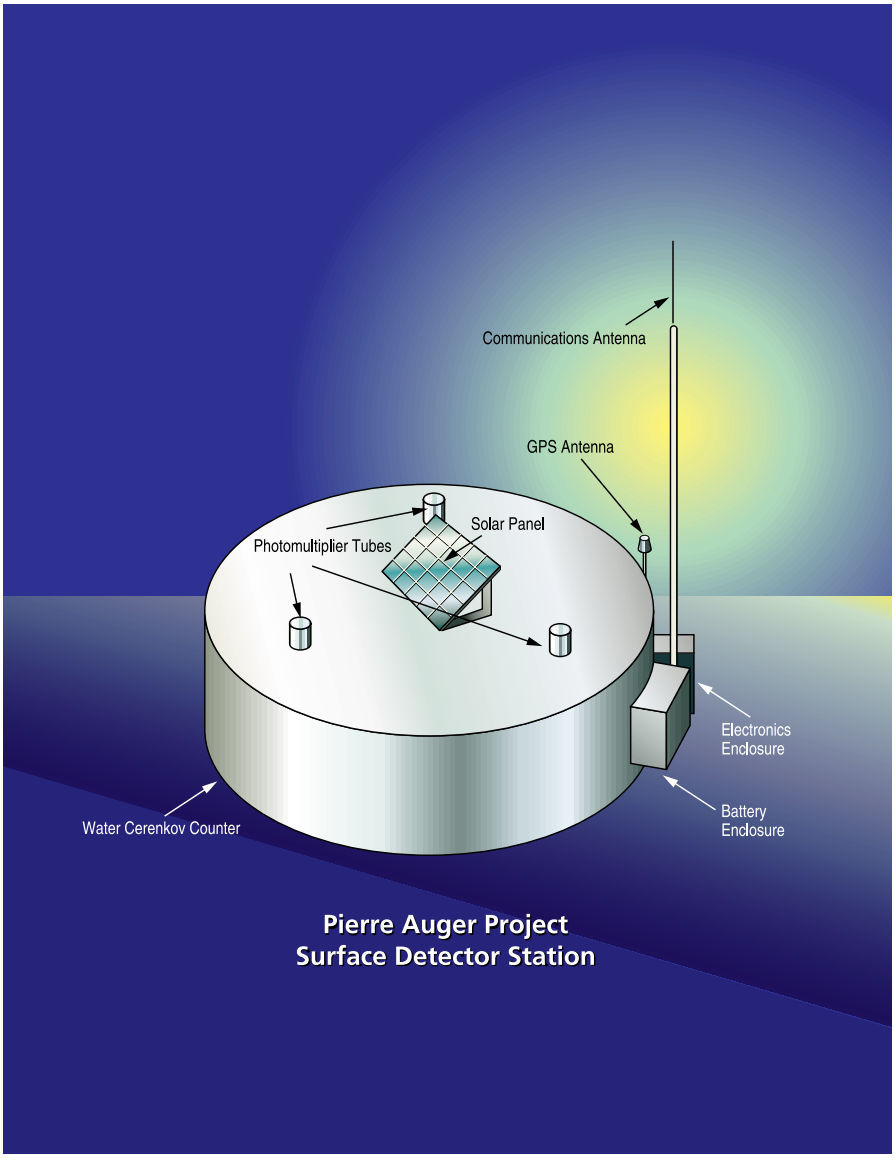

Figure 7.1: Concept for the Auger Project surface detector station.

difference between through-going muons and photons or electrons. This implies a detector with as large a lateral size to depth ratio as possible, and hence a single unsegmented unit. (Note that internal subdivision would still be allowable if the individual PMT signals were summed together).

A single unsegmented tank is also most efficient in terms of the photocathode area required for a given photoelectron yield; ie. the ratio of photocathode to tank wall area is maximal. The cylindrical shape is favored as it has inherently uniform response to showers of given zenith angle incident from different azimuthal angles.

7.3 PMT positioning and Detector Uniformity

With the assumed material parameters the simulation indicates that three large (200 mm diameter) PMTs will be sufficient for the 10 $m^2 \times 1.2$ m deep reference design unit. Arranged looking downward from the top surface of the tank a mean photoelectron yield of ≈ 50 is predicted in response to a vertical through-going muon, which results in acceptable Poisson fluctuations. Very good proportionality between Čerenkov light released and photoelectron yield is obtained when the PMTs are placed at 120° intervals on a circle of radius 1.2 m (2/3 of the detector radius).

To maintain proportionality it is vitally important to avoid direct Čerenkov radiation onto the photocathode. Figure 7.2 illustrates this point.

Even with the PMTs on the top surface, direct irradiation of the photocathode can still occur when a particle travels through the tank at $> 48°$ zenith angle (since the angle of Čerenkov emission in water is $\leq 42°$). Use of plane faced PMTs would completely suppress direct radiation up to the maximum 48° angle between particle trajectory and the zenith, and hence would be preferable to the more usual hemispherical designs. Near-isotropic decay of muons which stop in the detector volume is an unavoidable source of direct photocathode irradiation.

It should be noted that the shower particles arrive with a large spread of angles relative to the shower axis. However, the high energy particles which produce significant Čerenkov radiant track lengths have a much smaller spread of angles. (Shower simulations indicate that particles with energy > 10 MeV have median space angle deviation of $< 20°$ relative to the shower axis). Particles do not scatter significantly away from their incident trajectory while passing through the water until the last few centimeters of the track, where little or no Čerenkov radiation is produced.

Note that the effect of Čerenkov radiation in the glass of the PMT face has yet to be simulated. Minimization of this effect is a secondary reason for positioning the PMTs downward looking and in direct contact with the water.

Tests on a cylindrical 6.6 $m^2 \times 1.2$ m deep prototype tank constructed at Fermilab are qualitatively consistent with the simulation shown in Figure 7.2, although conditions were not identical. The prototype tank had 4 Hamamatsu R1408 200 mm diameter PMTs arranged

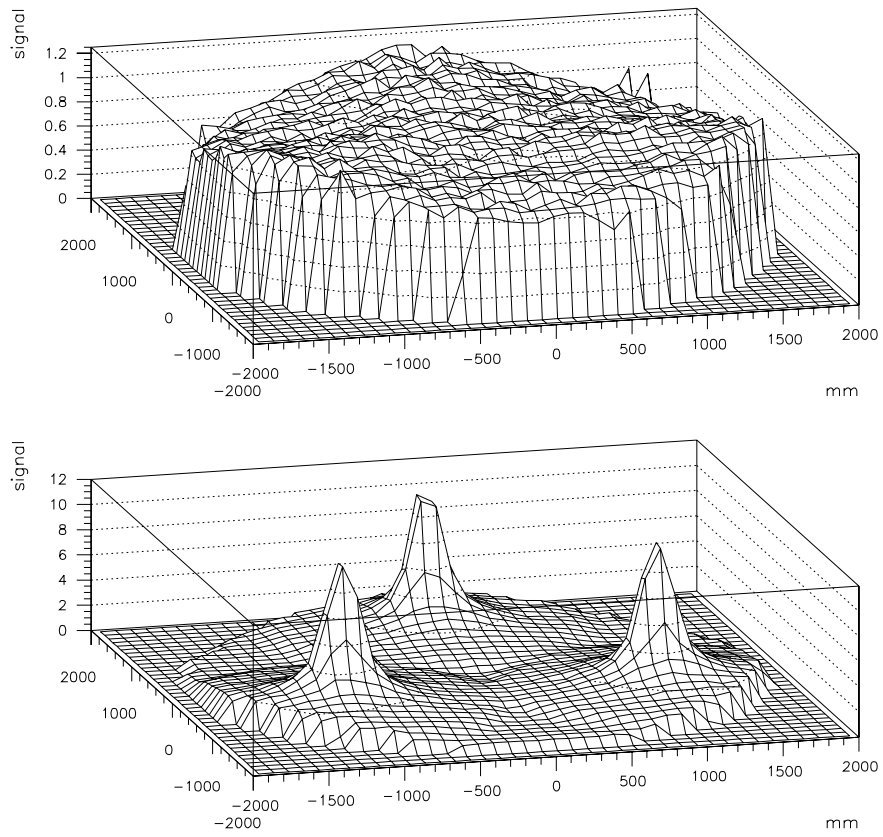

Figure 7.2: Simulated non-proportionality plot for the reference design water Čerenkov detector unit. The upper plot shows response with PMTs placed at the top looking down, and the lower plot is identical with the PMTs at the bottom looking up. Many 1 GeV muons were injected vertically at random positions over the detector top surface, and the resulting photoelectron yields averaged in 10 cm square bins. The vertical axis scales are relative to the overall mean signal in the down looking case.

in a circle with diameter 2/3 that of the detector. Using a 4 paddle scintillator telescope trigger, the analog sum of the signals from all 4 tubes was recorded for muons penetrating the tank vertically. The charge distributions derived from sets of several thousand events at 3 positions are shown in Figure 7.3. It is thought that the large high side tail of the "above tube" distribution is due to the sub-set of muons which pass through the tube itself.

7.4 Mechanical Realization

The Haverah Park detectors were made from galvanized iron tanks of rectangular cross section (1.85 m$\times$1.24 m$\times$1.29 m high) filled to a depth of 1.2 m. The walls (sides, top and bottom) were lined with a white diffusing PVC material supplied by ICI under the commercial name "Darvic". The side and top sheets were suspended from pins welded near the top of each vertical side. The tanks were air tight and were opened only to replace defective photomultiplier tubes (on average once every five years). A single 100 mm diameter plane-faced PMT was positioned in the center of the top surface with the face dipped into the water. Only two tanks were refilled during the entire 20 year run of the experiment, and the loss of performance over this time was $< 10\%$.

A total of 225 tank units were deployed in clusters of up to 34 m^2 total top surface area. Each cluster was housed in a heated concrete-floored wooden hut.

For the Auger project a detector unit is required which can withstand a harsh desert environment for a period of at least 20 years. A major goal of any design intended for mass production is, of course, low unit cost. Additionally, the experimental logistics demand near zero maintenance requirements from the surface array unit.

In terms of cost efficiency and durability steel is probably the best material available for fabrication of large tanks. By using stainless steel, inexpensive light weight tanks of suitable performance can be constructed. A prototype tank 6.6 m^2 $\times$ 1.2 m deep was fabricated at Fermilab using $\approx$ 2 mm thick 304L grade material. Problems of water corrosion in the region of the welds were encountered only a few days after filling, but techniques are known which produce welds not susceptible to corrosion. Further investigation is required.

The possibility of using a thicker carbon-steel tank, sand-blasted and coated inside and out with several layers of high grade epoxy paint is being investigated. A full scale 10 m^2 prototype is under construction. Experience in the water storage and processing industry proves that correctly applied epoxy paint of certain grades can withstand water immersion for at least 10 years. Durability of the paint is enhanced by immersion, and by non-exposure to sunlight.

A major factor motivating the use of epoxy paint is the possibility that it can both protect a steel tank from corrosion and also serve as the reflective internal lining material. Conventional white epoxies use titanium dioxide as the reflective pigment. This has poor reflectivity in the crucial 300 to 400 nm wavelength range, and is not suitable for this application. Investigation is under way to determine if a suitable pigmentation compound which is epoxy resin misible can be identified. An epoxy paint containing barium sulphate

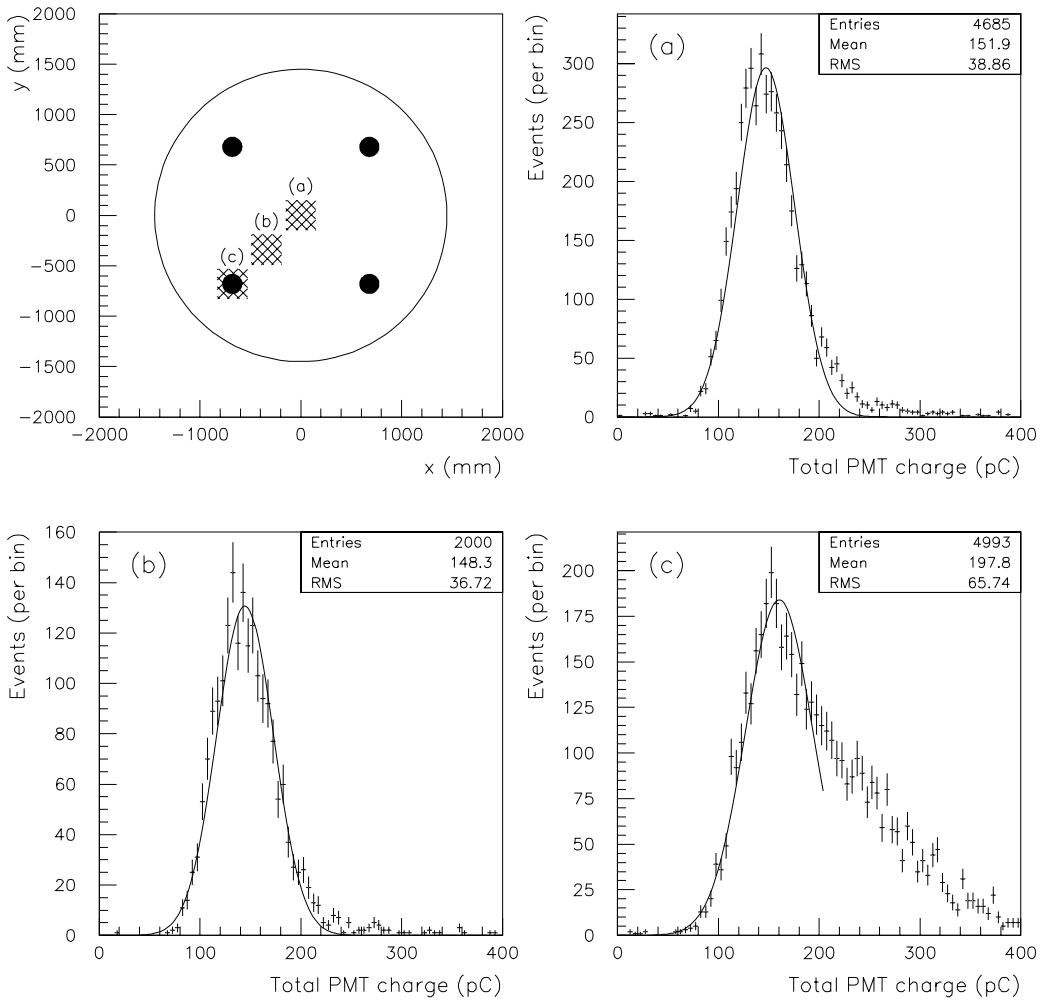

Figure 7.3: Test results from the cylindrical 6.6 $m^2 \times 1.2$ m prototype water Čerenkov tank. The top left plot is a diagram of the detector top surface showing the positions of the 4 PMTs. Also indicated are the positions of scintillator paddles placed abovew and below the tank to trigger on through-going muons for the three calibration runs labelled (a), (b), and (c). The charge distributions shown are the analog sum of the signals from all 4 tubes. It is thought that the high side tail of plot (c) is due to muons which pass through the tube itself.

is being formulated and tested.

If this turns out to be impossible, or if epoxy paint is rejected for some other reason, a galvanized steel tank lined with a reflective sheet material might be considered (much like the Haverah Park tanks). Tyvec, a white fibrous plastic material manufactured by Dupont for various industrial and commercial purposes, has proven diffuse reflectivity, measurements of which are shown in Figure 6.4. It also has the advantage of being relatively inexpensive. Consideration is required to find a suitable mechanism which can be used to secure the sheet material to the walls such that it will not be dislodged when 12 tons of water are pumped into the tank.

7.5 Water purification and reliability issues

During the construction of the Auger ground arrays about 15,000 tons of sufficiently purified water will need to be generated at each site, or brought in from the nearest available source of suitable natural water. The Haverah Park tanks were filled with untreated water from a nearby borehole in magnesium limestone which proved to be perfectly adequate. The transport of water across the array to each individual detector site represents a considerable challenge. It is likely that a large and durable vehicle will have to used. These questions will be easier to address when specific sites have been chosen.

Some preliminary tests of water purification via filtration were conducted at Fermilab. A 55 gallon oil drum was adapted for use as a small water Čerenkov tank. A Hamamatsu R1408 200 mm diameter hemispherical PMT was mounted in the center of the top surface. The interior was lined with Tyvec and completely filled with water.

The tank was successively filled with distilled water, unfiltered water from the site main supply, and mains water passed through a simple disposable cartridge filter. A 4 paddle scintillator telescope was used to trigger readout for vertically penetrating muons passing through the tank. Figure 7.4 shows the average time/amplitude profiles for sets of 100 events collected with each grade of water. Repeatability was checked both for a given fill of water, and also for refills of the same type. The filtered water results were found to be fully reproducible. However, it was discovered that some barrels of distilled water from the laboratory stores gave better results than others, presumably due to contamination in the barrels. Two examples are shown, one being little better than the 1 μm filtered water.

During these tests it was found that even very small amounts of iron oxide contamination have a very adverse effect on the ability of water to transmit light in the important 300 to 500 nm wavelength region. If a steel tank is to be used it is therefore vitally important that the corrosion is perfectly suppressed. Note that galvanization has proven successful in this application.

A technique used to suppress biological activity in water is displacement of the dissolved oxygen by bubbling through nitrogen, as the water is prepared for installation, combined with the use of a nitrogen overblanket to prevent reabsorption.

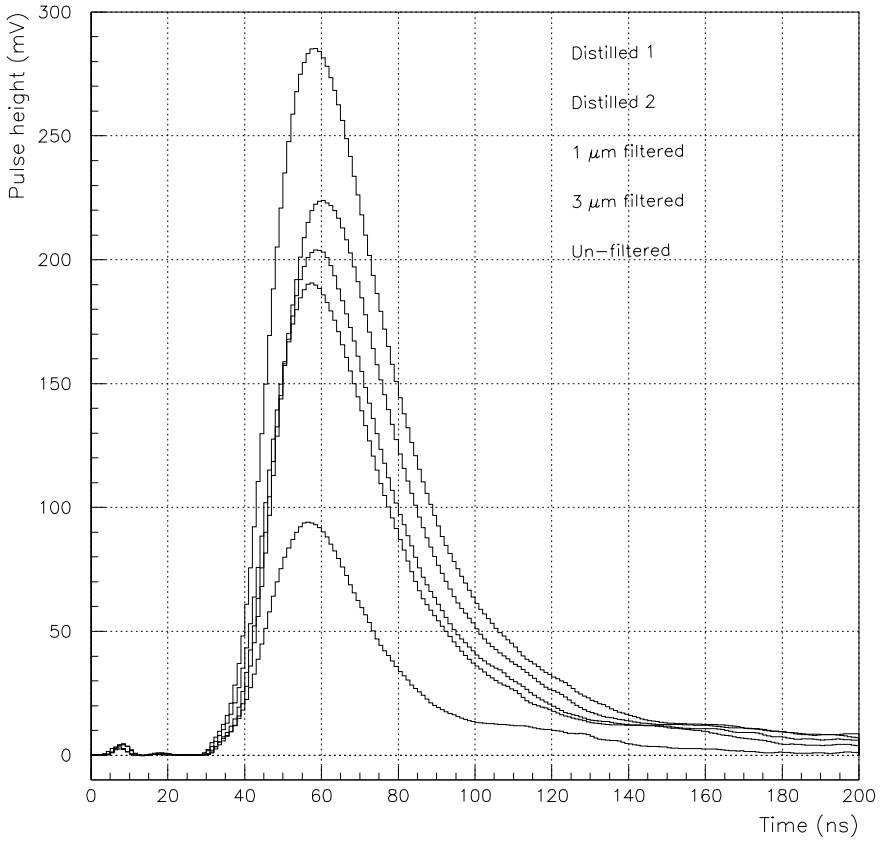

Figure 7.4: Water filtration test results. The time/amplitude profiles shown are each the average of 100 vertically penetrating muon events recorded on a 400 mega sample per second (MSPS) digital oscilloscope. (A cut has been made to remove multiple muon air shower events).

7.6 Possible use of waveshifting materials

It may be possible to enhance the performance of the proposed water Čerenkov detector by use of waveshifting materials, either dissolved in the water, incorporated into the tank lining, or coated directly onto the PMT faces. Referring to Figure 6.4 we can see that there are many Čerenkov photons in the 200 nm to 300 nm wavelength region beyond the reach of a glass encapsulated photomultiplier. If these could be absorbed and re-radiated in the tube response region (300 to 500 nm) a factor 2 to 3 gain in light yield would be achieved.

The substance 4-Methyl Umbelliferone is probably the best water-soluble wavelength shifter which is known[105] [106]. Concentrations of 10 mg-l^{-1} reportedly increase light yield by factor ≈ 2 in Čerenkov detector applications. This particular substance also exhibits good long term stability, and the light yield is relatively insensitive to the pH of the solution.

However, since the re-radiation from a dissolved waveshifting material is isotropic, problems may arise due to pseudo-direct tube face irradiation. A particle whose trajectory passes very close to a PMT will produce an anomalously large number of photoelectrons, leading to a degradation of the proportionality between total radiated Čerenkov light and detected signal.

For this reason it may be preferable to incorporate the waveshifting dye into the tank lining material. The absorption length of water in the wavelength range of interest is still several meters, so much of the UV light will reach the tank walls. However, the mean path length to reach a photomultiplier tube is much longer, and hence it is probably not efficient to coat the waveshifter onto the PMT face.

Chapter 8

Fluorescence Detector

8.1 Introduction

The Auger Observatory is to be a hybrid detector. A giant array of particle counters will measure the lateral distribution of air shower particles at ground level. An optical component will measure the air shower longitudinal development in the atmosphere, using the technique established by the Fly's Eye. Simulations of the combination are discussed in Chapter 6.

The atmospheric fluorescence (scintillation) measurements, although only available on clear moonless nights, will play an essential role by providing a subset of showers measured both laterally and longitudinally. This special subset will form the basis of the cosmic ray mass composition determination, as well as providing crucial cross-checks on the ground array's geometric reconstruction and energy determination. In particular, longitudinal measurements are necessary to search for the Landau-Pomeranchuk-Migdal (LPM) elongation signature of gamma ray showers at the highest energies [56].

The primary role of the fluorescence detector is to measure the longitudinal profile of each shower. The integral of that profile is a direct measure of the shower's energy deposited in the atmosphere. The measured profile also yields information like the atmospheric depth X_{max} at which the shower reaches its maximum size. For showers of fixed energy, X_{max} correlates with the mass of the primary particle. The reference design seeks to minimize the cost of the optical detector while guaranteeing an accurate measurement of the longitudinal profile for every shower above 10 EeV which is recorded anywhere in the ground array on clear moonless nights.

At this design stage of the project, it is possible that some basic parameters of the Observatory may change in response to new observations by other experiments, the choice of the project site, the funding schedule, etc. It is important to have an understandable method for adjusting the design of the fluorescence detector to accommodate changes in the Observatory's specifications. Emphasis will therefore be placed on the methods which lead to the reference design.

The methods outlined here are based on approximations. Monte Carlo simulations are essential for testing and fine-tuning the detector design. The simulation results presented in Chapter 6 support the reference design which will be derived here.

The considerations in this chapter apply to any type of fluorescence detector which collects light on photosensor pixels. The reference design calls for mirrors and phototubes, a technique which has been demonstrated to work in the Fly's Eye experiment. The same considerations would apply, however, if new techniques were to make the "lobster eye"[1] competitive, if Fresnel lenses or Winston cones were deemed more suitable as light collectors, or if another type of photosensor were found to be superior to PMTs.

What is needed is an algorithm which produces a specific design for any values of these input variables:

- Total detector area;
- Profile resolution criteria;
- Cost per pixel;
- Cost per unit area of light collector;
- Site preparation cost;
- Site operation and maintenance cost.

The output design must specify how many different sites (how many "eyes") the fluorescence detector will have. It must also determine the solid angle per pixel and the area of light collector accessible to each pixel. If mirrors and phototubes are to be used, the design must specify how many mirror units per site and how many PMTs per mirror camera. The methods described in this chapter focus on these basic aspects of the fluorescence detector design. There are other design issues which will not be specifically addressed here such as triggering and data acquisition (see Chapter 9). It is anticipated that much of the electronics can be modeled after HiRes or the Telescope Array.

The design procedure is first to convert the resolution criteria into a specific signal-to-noise requirement. For a specified total detector area, one calculates how much it would cost to build a one-eyed (Cyclops) detector. Together with the site preparation and operation costs and an assumed atmospheric extinction length, that allows an evaluation of the optimal number of eyes, minimizing the total cost. It is then known how far each eye must be able to "see." Balancing the cost of light collectors *vs* pixel costs, the signal-to-noise requirement then determines the pixel solid angle and the light collector area.

[1] A "lobster eye" configuration refers to a refractive outer hemisphere which focuses light onto a "retina" hemisphere of about half the radius. The refractive hemisphere is not segmented into separate solid angle units as is the case for a fly's eye.

After developing this algorithm, the latter part of this chapter applies it to the Observatory's specifications. The resulting reference design is called Cyclops 3000 (a one-eyed giant array of 3000 square kilometers).

The Cyclops 3000 fluorescence detector is designed to work symbiotically with the ground array, and to measure the longitudinal profiles of air showers above 10 EeV which trigger the ground array. Monte Carlo simulations (Chapter 5) support analytic arguments [57] that excellent geometric determination of each shower axis can be achieved with monocular observation of the shower, when combined with the arrival times of the shower front at ground stations. The reference design will therefore require only monocular shower measurements by the fluorescence detector.

The tasks for the hybrid detector's optical component differ significantly from those of fluorescence detector experiments like HiRes in Utah or the Japanese Telescope Array Project. Unlike those experiments, the Auger Observatory is focusing exclusively on the highest energy cosmic rays (above 10 EeV). More importantly, HiRes and the Telescope Array are stand-alone instruments, designed to measure air showers without the benefit of ground station counters. Their designs therefore call for stereoscopic shower measurements, effectively doubling the detector cost. There are notable advantages to stereo measurements, however, which would also be valuable to the Auger Observatory. Stereo measurements of air showers provide consistency checks and extra information for the longitudinal profile measurement. There is less susceptibility to errors from detector calibration, atmospheric attenuation compensation, Čerenkov light subtraction, etc. An ideal detector would be a giant ground array with a fluorescence detector whose *stereo* aperture spans the area of the ground array. An attractive scenario would be to build the Auger Observatory coextensive with HiRes or the Telescope Array. It could be, however, that there will be no site which is suitable for such a combination of projects. Moreover, an expectation of the Auger Project is to have equivalent observatories in the Northern and Southern Hemispheres. Combining the Auger Project with an existing fluorescence detector experiment would make it difficult to meet that expectation. It is therefore important to design a fluorescence detector specific to the requirements of the Auger Observatory.

8.2 Signal-to-Noise

Measuring longitudinal shower profiles (both the shape and the integral) is the primary role of the fluorescence detector. Its design depends on the accuracy with which such profiles must be measured. One way to quantify accuracy criteria is to specify requirements for the energy resolution and X_{max} resolution. The energy in the electromagnetic cascade is simply the shower profile's integral (times a known constant), and X_{max} is the atmospheric depth (in g-cm^{-2}) at which the shower attains its maximum size (maximum number of charged particles). If a detector can accurately determine the depth of each shower profile's peak and the profile's integral, then it can be said to be measuring the profiles adequately.

The experimentally determined shower profile is a size (we use the term to mean intensity or brightness) measurement at different depths X. Each size measurement is obtained

by collecting light emitted while the shower front is in a certain range of depths X. The width of these X-bins can be adjusted arbitrarily, since the FADC electronics will sample the light flux at finely separated times. Since the bin size should not be large compared to the desired X_{max} resolution, a bin size of approximately 15 g-cm^{-2} would be suitable. For this analysis, it will be more convenient to fix the bin by its time window rather than its depth range. At typical air densities near the ground, it takes 0.6 μs for the shower front to pass through 15 g-cm^{-2}. We will therefore consider how accurately the shower size can be determined by collecting its scintillation light for a time interval of 0.6 μs.

Numerous factors affect the accuracy of the size determination based on the measured amount of collected light. It will here be assumed that the detector itself is well calibrated so that it does not dominate the measurement uncertainties. Moreover, it will be assumed that the geometric reconstruction is correct and that there is no uncertainty in the atmospheric scintillation efficiency or atmospheric transmission. Under these assumptions, there is no uncertainty in converting measured light flux to shower size. The measurement uncertainties are then dominated by fluctuations in the background light from the night sky and Poisson fluctuations in the number of detected signal photoelectrons. Unless the pixel size is extremely small, shower detectability is background-limited rather than signal-limited. Near the threshold of detection, the number of signal photoelectrons is generally less than the number of background photoelectrons, but larger than the background fluctuation and hence detectable with AC coupling. The relevant noise is fluctuation of the night sky photoelectron count rather than Poisson fluctuation of the signal. Hence we will take the signal S to mean the number of photoelectrons from the shower collected in 0.6 μs and the noise N to mean the square root of the number of photoelectrons in the same time interval (and pixel) due to background sky light. The signal-to-noise ratio S/N determines the fractional size uncertainty by its inverse:

$$\Delta n_e/n_e = N/S.$$

The signal S from scintillation light depends on the size of the shower, the distance to the shower, and the detector's sensitivity. The relevant detector properties are the light collecting area A and the quantum efficiency ε. The collecting area A is the effective area after correcting for mirror reflectivity and obscuration by the phototube camera at its focus. The quantum efficiency ε is the fraction of photons which produce photoelectrons in the PMT cathode. If R is the distance to the observed shower segment and ξ is the atmospheric extinction length, the signal S is given by

$$S \;=\; 2.4\;\frac{A\varepsilon n_e cT}{4\pi R^2}\;e^{-R/\xi}.$$

Here c is the speed of light (300 m-μs^{-1}) and T is the width of the time bin (e.g. 0.6 μs). The scintillation efficiency of the atmosphere in the frequency range appropriate to HiRes phototubes (with filters) gives the coefficient 2.4 photons/m per charged particle (so the above formula requires cT to be in meters). The atmospheric extinction in this formula is a crude approximation which neglects wavelength dependence and altitude variation.

The noise is governed by the background light from the night sky, which is approximately 40 photons-m^{-2}-deg^{-2}-μs^{-1} in the frequency range accepted by the HiRes filter and PMT.

(This is a representative value. The actual background intensity varies with elevation angle and atmospheric conditions.) The noise is the square root of the number of background photoelectrons collected in T μs:

$$N \;=\; \sqrt{40\varepsilon A\Omega T}.$$

Here Ω is the pixel solid angle in square degrees.

The signal-to-noise ratio is therefore

$$S/N \;=\; \frac{2.4 n_e c}{4\pi R^2}\,\sqrt{\frac{\varepsilon A T}{40\Omega}}\;e^{-R/\xi}.$$

This formula is used extensively in this chapter.

8.3 Balancing the costs of mirror area and pixels

We present here a general argument which shows that equipment money should be divided evenly between mirror area and pixels. The mirror area cost must include all costs associated with scaling up the mirror size (e.g. support frame, housing, door, filter). The pixel cost must include the costs which are proportional to the number of channels (e.g. PMT, base, FADC, memory, cable). It is assumed that the mirror costs scale in proportion to the mirror area and that the pixel costs scale in proportion to the number of pixels. Neither assumption is strictly correct, but both are valid in some approximate sense.

The argument is based on consideration of the signal-to-noise ratio presented in the previous section. The signal is proportional to the mirror area A. The noise is proportional to $\sqrt{A\Omega}$, where Ω is the solid angle of each pixel. The S/N (signal-to-noise ratio) is therefore proportional to $\sqrt{AP}$, where P is the number of pixels in the fixed solid angle of a mirror (P proportional to $1/\Omega$). A minimum acceptable S/N is determined by resolution requirements for the detector, and so the product AP has some fixed minimum acceptable value. Therefore $P = k/A$ for some constant k.

Now we use the fact that costs scale both with the mirror area and the number of pixels. The total equipment cost therefore scales like

$$Cost \;=\; \alpha\, A \;+\; \beta k/A,$$

where α is the cost per unit mirror area and β is the cost per pixel. This $Cost$ is a function of the one variable A. Its minimization yields the condition $\alpha A = \beta k/A$, which simply says that the equipment costs for mirrors should equal the equipment costs for pixels.

The remarkable thing about this result is that it does not require knowing how many "eyes" the detector will have, how big an area it must monitor, what resolution will be required, what the mirror unit cost is, or what the pixel unit cost is. Of course the actual mirror area and number of pixels will depend on all these factors and more. But the final design, whatever it is, should be such that the equipment cost for mirrors is approximately equal to the equipment cost for pixels.

8.4 Profile Resolution vs. Signal-to-Noise

The purpose of this section is to explore how the fluorescence detector's resolution depends on the S/N ratio. Physics objectives should establish requirements on the accuracy of air shower longitudinal profile measurements. We need to understand how those accuracy criteria govern what S/N ratio must be achieved.

"Profile resolution" will here be quantified by "energy resolution" and "X_{max} resolution." Energy is identified with a profile's integral, and X_{max} is the atmospheric depth at which the profile has its peak value. These resolutions will be studied as functions of S/N. In this section, S/N will mean the signal-to-noise ratio in a 15 g-cm^{-2} depth interval when the shower is at half its maximum size. This means that the size at half-maximum has a relative uncertainty $\Delta n_e/n_e = N/S$ based on observing the shower while the shower front traverses a depth interval of 15 g-cm^{-2}. The uncertainty in shower size Δn_e is constant if N is constant and S is proportional to n_e. The fractional uncertainty $\Delta n_e/n_e$ at X_{max} is therefore $\frac{1}{2}N/S$.

A simple Monte Carlo program can exhibit how the resolution depends on S/N. The input shower is a Gaisser-Hillas function. It determines a shower size n_e at the center of each depth bin of 15 g-cm^{-2} width. Those sizes are fluctuated in accordance with the assumed S/N parameter to produce simulated data. Those data are then fitted to a Gaisser-Hillas functional form to obtain an "output profile." An ensemble of such trials gives the energy and X_{max} resolutions by comparing the output profile parameters with the true (input) parameters.

Figure 8.1 shows the shape of a Gaisser-Hillas profile which reaches maximum size 750 g-cm^{-2} after the depth of first interaction. This is a specific example of the 3-parameter Gaisser-Hillas [59] functional form

$$n_e = S_{max}\left(\frac{X - X_0}{X_{max} - X_0}\right)^{(X_{max}-X_0)/70} exp[(X_{max} - X)/70].$$

The three parameters are the maximum size S_{max}, the depth X_{max} where S_{max} occurs, and the depth of first interaction X_0. This shower shape is used for the current study.

For this numerical study, simulated data are generated as follows for any value of the parameter S/N. First, the X-bin boundaries are shifted by a random multiple of 15 g-cm^{-2} so that X_{max} will occur at random positions within its bin. For the center of each bin where the shower is above half its maximum, the shower size at that X-value is fluctuated by adding an amount sampled from a Gaussian distribution of width $S_{max}/2 \cdot S/N$. The Numerical Recipes [60] program Amoeba is used to fit the 3-parameter Gaisser-Hillas functional form to the simulated data by χ^2 minimization. An ensemble of output profiles is obtained for values of $S/N \in [1.0, 6.0]$.

Each ensemble yields a mean energy and an RMS deviation from the true (input profile) energy. Nothing in these procedures introduces a systematic energy error, so the mean agrees well with the true value. The RMS width of the distribution can be used as a measure of the energy resolution. Figure 8.2 shows the percentage error – $100 \times (RMS\ width)/(true\ energy)$

– as a function of the Signal-to-Noise variable.

In a similar way, the distribution of output X_{max} values has an RMS deviation which is a measure of the X_{max} resolution. Figure 8.3 displays this as a function of the Signal-to-Noise variable.

Without assuming any functional form, one could identify X_{max} as the center of the X-bin with the greatest shower size. This "raw X_{max}" ignores constraining information from the shower rise and fall. It therefore has a bigger dispersion. Figure 8.4 shows the RMS deviation of the raw X_{max} from the true X_{max} as a function of the Signal-to-Noise variable.

It may be noted that the X_{max} resolution may govern the detector design parameters. If X_{max} can be measured to an accuracy of 20 g-cm^{-2}, for example, then the energy measurement is good to 7%. These are statistical fitting errors only, however. A complete analysis of energy resolution must also consider uncertainties in normalization due to scintillation efficiency, atmospheric attenuation, etc. The X_{max} uncertainty would *not* be sensitive to a renormalization if it were to apply equally to all parts of the shower.

8.5 How many eyes?

The optimal number of sites depends on three important variables:

1. The total area of the ground array to be matched. The Auger Observatory will cover the largest possible area. Cost considerations presently limit the design to 3000 square kilometers. That area could increase or decrease. It is best to keep this as a variable which can be specified in the optimization process.

2. The atmospheric extinction length. This can be defined as the distance over which a (350 nm wavelength) light beam is attenuated by 1/e. To make this precise, one needs to specify the elevation angle of the beam, since attenuation is less at greater altitude. The "clear desert atmosphere" model gives a horizontal extinction length of 8.4 km at Dugway's altitude. Measurements at Dugway [61] suggest that this is a reasonable estimate for a time-averaged value, but it fluctuates by perhaps 20% with the seasons and can have even greater variation with local weather patterns, regional forest fires, etc. For detection of distant showers (seen at low elevation angles) the effective extinction length may depend on whether or not the detector is on a hill. Analyses of scattering from light beams by the HiRes prototype suggest that the height of the mixing layer varies, but there is usually a great advantage in being hundreds of meters above the surrounding terrain. In view of the uncertainty in this parameter, the atmospheric extinction length should be left as a variable parameter. If the extinction length is short (poor visibility), it is cost-effective to build numerous near-sighted eyes; if the air is clear, the optimal configuration may be a single eye at the central facility.

3. The third parameter is the relative cost of equipment for a single eye to monitor the entire detector area (Cyclops configuration) vs. all costs – excluding equipment – for

preparing, maintaining, and operating each additional site. The Cyclops equipment cost includes the costs of phototubes, electronics, mirrors, shelters, etc. No infrastructure costs are to be included, since road, power, communication, and living facilities are presumed to be present anyway for the ground array central facility. The site preparation cost for each additional eye should include such infrastructure costs (road construction, stringing power lines, and establishing communications) and also the additional cost of maintaining and operating an additional site. Maintenance of each additional eye is dominated by upkeep of roads, etc., and the time and transportation costs for maintenance specialists to access the additional site. If there is negligible cost in adding another site, it is sensible to build lots of cheap near-sighted eyes; but if the costs for preparing and operating an additional site is high, then it may be cost effective to build a single far-sighted eye at the central facility site.

It should be noted that the Cyclops equipment cost depends on the atmospheric extinction length, so the third parameter is not independent of the second. For some purposes it will be helpful to define the third parameter for a specific extinction length, say 10 km. Then the three parameters are independent.

The analysis starts from the assumption that some minimum detector resolution has been established as a criterion. That resolution depends only on the signal-to-noise ratio (S/N), which is here taken to mean the number of photoelectrons received from the airshower in 0.6 μs divided by the square root of the number of background photoelectrons accepted in the same pixel in the same time interval. (See Section 8.2.) For showers of fixed energy, this S/N depends on the mirror area A, pixel size Ω, distance to the shower R, and the atmospheric extinction length ξ according to

$$S/N \;\sim\; \sqrt{\frac{A}{\Omega}}\;\frac{1}{R^2}\;exp(-R/\xi).$$

It will be supposed that the ground array can be divided into n circles of radius $R_n = R_1/\sqrt{n}$. The case n=1 corresponds to the Cyclops configuration. For any configuration, the total ground array area is πR_1^2. For n eyes, each eye must achieve the required S/N out to the radius of its circle R_n, so

$$S/N \;\sim\; \sqrt{AP}\;\frac{1}{R_n^2}\;exp(-R_n/\xi).$$

(Here the number of pixels P per mirror has been substituted for $1/\Omega$, since, for fixed mirror solid angle, the number of pixels is inversely proportional to the solid angle per pixel.) For a fixed value of S/N, one finds the following dependency on the number of sites n:

$$AP \;\sim\; R_n^4\;exp(2R_n/\xi) \;\sim\; \frac{1}{n^2}\;exp(2R_1/\sqrt{n}\xi).$$

In evaluating the equipment cost $E(n)$ per site when the array is divided into n circles, one can exploit the result that an optimal design will call for equal expenditure on mirrors

and pixels. The equipment cost per mirror unit is $\alpha A + \beta P$, where α is the cost per unit of mirror area and β is the cost per pixel. Note that α should include all costs which scale with the mirror area, including the filter. And β should include all costs associated with each pixel, including electronics. (In reality there may not be a perfect separation of these costs, since larger mirror area will entail a larger camera if the f-stop is constant. Unless Winston cones are used to collect light in the focal plane, larger phototubes may be necessary with larger mirrors, and larger phototubes may be more expensive. That possible coupling is neglected here.) The optimization of equal cost for mirrors and pixels means that $\alpha A = \beta P$. The equipment cost per mirror unit can therefore be written as $2\sqrt{\alpha\beta}\sqrt{AP}$. Since α and β are fixed constants, we can use the formula for AP above to find the n-dependence of the cost per mirror unit as

$$Cost\ per\ mirror\ unit\ \sim\ \sqrt{AP}\ \sim\ \frac{1}{n}\ exp(R_1/\sqrt{n}\xi).$$

For a configuration with many eyes, each shower will be seen at close range, and a large elevation angle coverage is necessary to make sure that the observed shower profiles include the region near the maximum shower development. Treating the number of sites n as a continuous variable, we can write the elevation angle coverage as a continuous function of n. To be explicit, let us require that a shower at distance of at least $R_n/2$ should be in view at all slant depths greater than 400 g-cm^{-2} if its zenith angle θ is not greater than 45°. Using an exponential atmospheric model of 7.2 km scale height and a detector depth of 860 g-cm^{-2}, the required elevation angle ζ is then given by

$$tan(\zeta) = \frac{h}{R_n/2} = -7.2km \times ln(\frac{400cos45^\circ}{860})/(R_n/2) = 16km/R_n.$$

Note that, for $R_n > 25$ km, ζ is less than 32°, so two rings of mirrors, each with an elevation angle range of 16°, is adequate. Additional rings of mirrors may be needed only for R_n values smaller than 25 km. Nevertheless, the cost dependence on n will here be made proportional to ζ as though the elevation angle were a continuous function of n, which is also treated here as a continuous variable. The equipment cost per site then has the following dependence on n:

$$E(n)\ \sim\ \frac{1}{n}exp(R_1/\sqrt{n}\xi)tan^{-1}\frac{16km\sqrt{n}}{R_1}.$$

The actual equipment cost $E(n)$ can then be expressed in terms of the Cyclops equipment cost $E(1)$ and the Cyclops radius R_1 and the independent variable n:

$$E(n) = \frac{1}{n}E(1)\frac{exp(R_1/\sqrt{n}\xi)\ tan^{-1}(16km\sqrt{n}/R_1)}{exp(R_1/\xi)tan^{-1}(16km/R_1)}.$$

It can be seen from this expression that the equipment cost $E(n)$ falls faster than $1/n$ as the number of eyes increases. If the non-equipment costs associated with additional sites were negligible, this would argue for building many eyes.

The total cost of the fluorescence detector is the sum of equipment costs and the site costs for the n-1 eyes not located at the central facility:

$$Total\ cost\ =\ nE(n)\ +\ (n-1)\mathcal{S}$$

$$= E(1)\frac{exp(R_1/\sqrt{n}\xi)\ tan^{-1}(16km\sqrt{n}/R_1)}{exp(R_1/\xi)\ tan^{-1}(16km/R_1)} + (n-1)\mathcal{S}.$$

The remote site costs, including site preparation, maintenance, and operating costs, are together denoted by $\mathcal{S}$. Inflating $\mathcal{S}$ and $E(1)$ by a common factor does not affect the value of n where this function has its minimum. Only the ratio $E(1)/\mathcal{S}$ is a relevant parameter for the minimization. One could choose monetary units such that $\mathcal{S}$=1; the numerical value of $E(1)$ would then be this ratio $E(1)/\mathcal{S}$.

In numerically minimizing this total cost, one finds that, for a fixed value of ξ, the dependence of the optimal number of sites is a strongly rising function of $E(1)/\mathcal{S}$, and that curve is only weakly dependent on the total array area. See Figure 8.5 for the case $\xi = 10$ km. It shows that the optimal number of sites is greater than 1.5 if $E(1)/\mathcal{S}$ is greater than about 2.5.

These optimization methods do not acknowledge the advantage of redundant shower measurements by stereoscopic viewing. With a one-eyed (Cyclops) detector, no showers will be measured stereoscopically. If two or more eyes are used to monitor the ground array's area by monocular measurements at 10 EeV, then many of the highest energy showers will be measured stereoscopically, since higher energy showers can be detected from greater distances. Such stereo measurement provides valuable cross-checks on the atmospheric attenuation, detector response, etc. If the costs are approximately equal, there is a strong argument for building two or more eyes rather than one.

8.6 A Design Algorithm

A design algorithm is presented here which is based on the results of the preceding sections. This procedure will be applied in subsequent sections to derive the reference design for the Auger Observatory fluorescence detector.

Step 1. Establish input information:

- Total area,
- Profile resolution (energy and/or X_{max}),
- Atmospheric extinction length ξ,
- Mirror cost α per unit area,
- Cost per pixel β,
- Additional cost $\mathcal{S}$ associated with a remote site: (e.g. site prep, maintenance, operation).

Step 2. Determine S/N corresponding to the specified resolution (see Section 8.4.)

Step 3. Compute, as follows, the equipment cost for a Cyclops detector whose viewing radius is $R_1 = \sqrt{(Total\ Area)/\pi}$. Substituting $P = 216/\Omega$, the S/N formula (Section 4.2) can be written as

$$S/N \;=\; 0.0021 \frac{n_e c}{R_1^2} \sqrt{\varepsilon T}\; e^{-R_1/\xi}\; \sqrt{AP}.$$

Here Ω, the solid angle per pixel in deg^2, has been replaced by $216/P$, where 216 deg^2 is the solid angle per mirror unit and P is the number of pixels per mirror unit. Solve this equation for the quantity $k \equiv AP$. Then solve the pair of simultaneous equations

$$AP = k$$

$$\alpha A = \beta P$$

for A and P. (The second equation is the balancing of mirror and pixel costs. See Section 8.3.) The Cyclops equipment cost per mirror unit is now given by $\alpha A + \beta P$. Multiply this answer by 48 for two rings of 24 mirrors, each ring covering 360° azimuth. This is the total equipment cost for the Cyclops configuration.

Step 4. Determine the optimum number of eyes n. (See Section 4.5.) The inputs for this optimization are now known: Cyclops equipment cost, additional site-related cost $\mathcal{S}$ per remote eye, and the atmospheric extinction length ξ.

Step 5. Similar to step 3. Now use $R_n \equiv R_1/\sqrt{n}$ in place of R_1 and solve again for A and P. Having completed this step, the basic design parameters are known: the number of sites n, the mirror area A, and the number of pixels P per mirror.

Step 6. Solve $tan(\zeta) = 16km/R_n$ for the desired elevation angle range ζ. Since the elevation angle coverage is quantized in units of mirror aperture (about 16°), the number of mirror rings should be the nearest integer to $\zeta/16$. (If this leads to an elevation angle less than ζ, Monte Carlo simulations may show that it is adequate nevertheless. If not, perhaps the elevation angle range per mirror can be extended, or the lowest ring might be tipped upward slightly, or a gap could be left between rings. The more expensive alternative would be to add another ring of mirrors.)

8.6.1 Summary

These steps yield the number of sites, the number of mirror units per site, the mirror area and number of pixels per mirror unit. The total equipment cost is then computed using the cost parameters α and β. To this equipment cost must be added the cost associated with remote sites: $(n-1)\mathcal{S}$.

8.7 Input variables for the reference design

8.7.1 Total detector area

The ground array area for each hemisphere (northern and southern) has been chosen to be 3000 km^2. The fluorescence detector should be capable of measuring any shower of 10 EeV or greater energy which lands anywhere in that detector area with a zenith angle up to 45°.

The shape of the detector's area has not been specified. The availability of suitable sites may later dictate a specific shape which could impact the fluorescence detector's design. For example, if the only available site is a highly elongated region of 3000 km^2, then two or more "eyes" may be appropriate for monitoring the area. Without any pre-established shape, it will be assumed here that the shape can be adjusted. For a Cyclops configuration (one-eyed giant array), one would want a circular or hexagonal ground array. If two eyes are to be used to monitor a 3000 km^2 area, it would be sensible to build an elongated ground array, perhaps in a peanut (or "Mastercard") shape. With three eyes, the ideal shape would have three lobes, perhaps like the six-sided "Superman" shape (see Figure 8.6.)

8.7.2 Resolution

The criteria for how accurately shower profiles must be measured are crucial to the design. That accuracy is largely governed by composition studies. The mass composition of cosmic rays at fixed energy can be inferred from the distribution of X_{max} values. The mean of the X_{max} distribution for an iron population is about 100 g-cm^{-2} less than the mean X_{max} for protons of the same total energy. For sensitivity to composition, a reasonable objective is to measure longitudinal profiles well enough that the depth of maximum, X_{max}, can be determined to an accuracy of 20 g-cm^{-2}. As shown in Section 8.4, this implies that the energy uncertainty, due to fitting the profile measurement data, should be less than 10%.

8.7.3 Atmospheric extinction length

The design of a far-sighted eye depends strongly on the atmospheric clarity. Much greater light collecting power is needed if the scintillation light from distant showers is highly attenuated. The atmospheric extinction length ξ depends on variable weather conditions as well as the site's climate, its proximity to urban pollution, whether or not the fluorescence detector is elevated above its surroundings, and also on the elevation angles at which showers are viewed. The Fly's Eye experience suggests that a *horizontal* extinction length of 8.4 km may be an average value at Dugway, Utah. This is the horizontal extinction length tabulated for the "clear desert atmosphere" at Dugway's altitude. The extinction length is greater for non-zero elevation angles. An effective atmospheric extinction length of 10 km is adopted for the analysis here. Monte Carlo simulations should be used to explore in detail a detector's performance with various atmospheric models.

8.7.4 Unit cost for mirrors

The reference design will exploit the proven Fly's Eye technique of focusing light onto photomultiplier tubes using large mirrors of spherical curvature. The cost per square meter (α) for such mirrors is an essential design parameter. An evaluation of the cost must include all components whose costs scale with the mirror area. These include the following:

- Mirror fabrication costs;
- The mount used to support and align mirror segments;
- A concrete foundation for the mount;
- A shelter for the mirror unit;
- A door to expose the mirror during operating times;
- A UV-pass filter over the PMT camera. (With fixed f/1 optics, the camera's area scales with the mirror area.);
- The camera box. (Only half of its cost is here included with the mirror costs, since there are also camera box costs which are size-independent.);

These costs can be estimated from experience with the Fly's Eye and HiRes. Mirror costs are found to be approximately \$3500/m^2. This is the cost per m^2 of effective reflecting area, after compensating for 13.3% obscuration by the camera and assuming a reflectivity of 0.8. (The cost per m^2 for actual mirror area is less, but it is the effective area which counts.)

8.7.5 Pixel costs

Each pixel consists of a PMT with base, FADC, memory, and cabling. The cost per pixel (β), is taken to be \$250.

8.7.6 Non-equipment costs associated with a remote site

In determining how many eyes should be used to monitor the ground array's area, it is necessary to consider the cost ($\mathcal{S}$) of establishing and operating an additional site. Such costs do not apply to a one-eyed Cyclops detector, because it can take advantage of the ground array's central facility. If two eyes are to be used in a Mastercard configuration of a 3000 km^2 array, they would be separated by 20 miles (32 km). Road construction (unpaved) is estimated to cost \$22,000/mile. Power lines cost about \$15,000/mile. An optical fiber for communications adds another \$8,000/mile. These site preparation costs of \$45,000/mile come to \$900,000 for adding a site 20 miles from the central facility. One must also consider the additional costs of maintaining and operating a remote site. A realistic cost may be

$500,000/year. A minimal cost (even if the remote site requires no operator) would be $200,000/year just to maintain the road and do routine maintenance at that site. For a 10-year experiment, one should probably budget $5.8M for the non-equipment cost of a remote site. A lower limit for the budget would seem to be $2.8M.

8.8 Design calculations

The signal-to-noise ratio was defined in Section 8.2 to be the ratio of signal photoelectrons to fluctuations in background light photoelectrons during a 0.6 μs time interval while a pixel is viewing a shower at half its maximum size. The formula for S/N in Section 8.2 can be written

$$\sqrt{AP} \;=\; \frac{(S/N)\; R_1^2\; e^{R_1/\xi}}{.0021\; n_e\; c\; \sqrt{\varepsilon T}}.$$

Here P=215/Ω is the number of pixels per mirror; $\varepsilon = 0.25$ is the PMT quantum efficiency; T=0.6 μs is the time interval used in our definition of S/N; $n_e = 3 \times 10^9$ is the number of electrons in a shower of 10 EeV at half its maximum size; c=300m/μs is the speed of light; $\xi = 10^4$ m is the assumed atmospheric extinction length; and $R_1 = \sqrt{3000/\pi}$km=3.09×10^4 m is the maximum distance at which showers must be measured. Substituting these values reduces the above equation to

$$AP \;=\; 822\; (S/N)^2.$$

As discussed in Section 8.3, an optimized design calls for equal expenditure on mirror area A and pixel number P:

$$\$3500 \cdot A = \$250 \cdot P.$$

Solving these last two equations for A and P gives

$$A = 7.7 \times S/N, \qquad P = 107 \times S/N.$$

Figures 8.2 and 8.3 can be used to convert resolution criteria to a minimum acceptable S/N ratio. To achieve a resolution of 20 g-cm^{-2} in X_{max} and better than 10% energy (fitting) resolution, it is sufficient to achieve S/N=2. Using S/N=2 in the above expressions for A and P gives

$$A = 15.3\; m^2, \qquad P = 215\; \textit{pixels per mirror unit}.$$

With two rings of 24 mirrors per ring, each ring spanning 360° azimuth and 16° of elevation angle, the Cyclops total equipment cost $E(1)$ is

$$E(1) = 2 \times 24 \times (\$3500 \times 15.3 + \$250 \times 215) = \$5.2M$$

Using the remote site cost $\mathcal{S} > \$2.8M$ gives a ratio $E(1)/\mathcal{S} < 1.9$. From Figure 8.5, one sees that the optimal number of eyes n is certainly less than 1.5, when regarded as a continuous variable. The total cost of a Cyclops detector (one eye) is less than the total cost if the job

were divided among two or more eyes. The design will therefore call for a single fluorescence detector site at the center of the 3000 km^2 ground array.

It is necessary to check that two rings of mirrors give adequate elevation angle coverage. There will be some showers landing near the eye for which X_{max} will be seen at high elevation angles. However, three-fourths of the showers will be farther away than $R_1/2$. For showers up to 45° zenith angle, one can ask that they be seen at all slant depths of 400 g-cm^{-2} and deeper. That condition (Section 8.5) requires viewing at least up to elevation angle

$$\zeta = arctan(16km/R_1).$$

For R_1=30.9 km, this gives ζ=27°. Two rings of 16° elevation angle each will give coverage up to 32°, which is more than the required 27°.

8.9 The reference design: Cyclops 3000

The foregoing analysis suggests that the most cost effective fluorescence detector to match a 3000 km^2 ground array will reside at a single central site. The natural configuration is a circular (or hexagonal) ground array with the fluorescence detector Eye located at its center.

The fluorescence detector will consist of 48 mirror units, 24 mirrors at each of two elevation angles. Each mirror will be 4.42 meters in diameter (15.3 m^2). It can be composed from 19 hexagonal segments of .81 m^2 effective area, which can be cut from circular glass disks of 53" diameter. Each mirror will be housed separately from its camera (see Figure 8.7) A motorized door, under software control, will prevent the mirror from ever focusing sunlight.

The camera at the focus of each mirror will collect light from a total solid angle of 216 deg^2. It will contain an array of 225 (15×15) photomultiplier tubes. Each pixel will correspond to a solid angle slightly less than 1 deg ×1 deg. The camera will be hermetically sealed, with a shutter to protect the phototubes from light when the detector is not operating. FADC electronics will digitally measure the signal in each pixel every 100 ns. The trigger and data acquisition systems can be modeled after the HiRes FADC system which will be prototype tested this year [62]. An alternative FADC system is being developed for the Telescope Array. The Auger electronics may borrow ideas from both systems.

The basic equipment costs can be calculated, using \$3500/m^2 for mirrors and \$250/pixel:

$$Basic\ equipment\ cost\ =\ 2 \times 24 \times (\$3500 \times 15.3 + \$250 \times 225)\ =\ \$5.3M.$$

Not included in this formula are some invariant costs associated with each camera (high voltage, half of the camera box cost not included with the mirrors, the box support, shutters and shutter controls). These costs total \$0.59M. The cost for a trigger system, control, and optical fibers is \$0.19M.

In addition to these basic equipment costs, there will be costs for a calibration system. That will consist of a laser with diode monitors, which distributes known light pulses to the

various cameras via optical fibers. Based on a similar system at HiRes, it is expected to cost approximately \$0.12M.

A system for monitoring the atmosphere over the entire array is also essential. This system will include a steerable lidar system, 12 low-power vertical flashers at a radius of 15 km, and 24 powerful flashers at a radius of 30 km. The total cost for this monitoring system is estimated at \$0.19M.

The budget for a transformer with pad, breaker panel, conduits and wire, workstations, computer peripherals, and communication devices totals \$0.10M.

All together, these costs for the fluorescence detector total \$6.5M. These costs are broken down in the budget table, Fig 11.1, where appropriate contingency and EDIA costs are added.

The fluorescence detector design is subject to change in response to specific characteristics of the selected site or developments in technology. The methods illustrated here can be applied to revise the design if the size and/or shape of the hybrid detector are set to different values, if 10 km is found to be an inappropriate value for the atmospheric extinction length, if mirror costs or pixel costs change, etc. This Cyclops 3000 design provides a specific reference design based on present assignments of the relevant parameters.

Further research and development may yield techniques which will result in cost reductions through minor design changes. For example, with the freedom to adjust independently the positions and orientations of the 19 mirror segments in order to minimize spherical aberration, it may be that a substantially larger solid angle can be subtended by each camera. If each mirror unit could monitor 20° of azimuth instead of 15°, then the number of mirror units could be reduced from 48 to 36. The Cyclops 3000 reference design is a conservative design, based on proven capabilities. Ideas for making it more sensitive at less cost will be explored during the next two years.

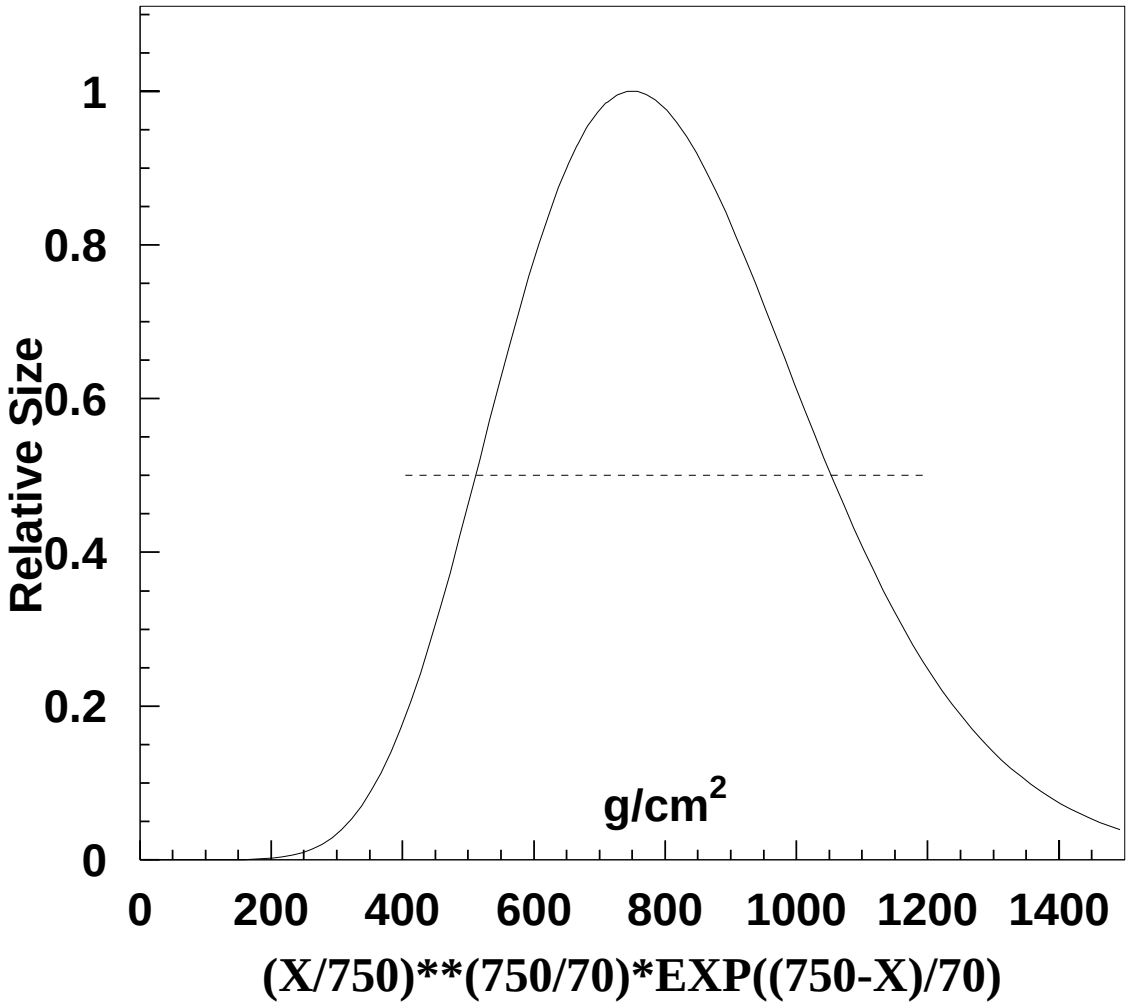

Figure 8.1: The shape of a Gaisser-Hillas function with first interaction at 0 g-cm^{-2} and X_{max} at 750 g-cm^{-2}.

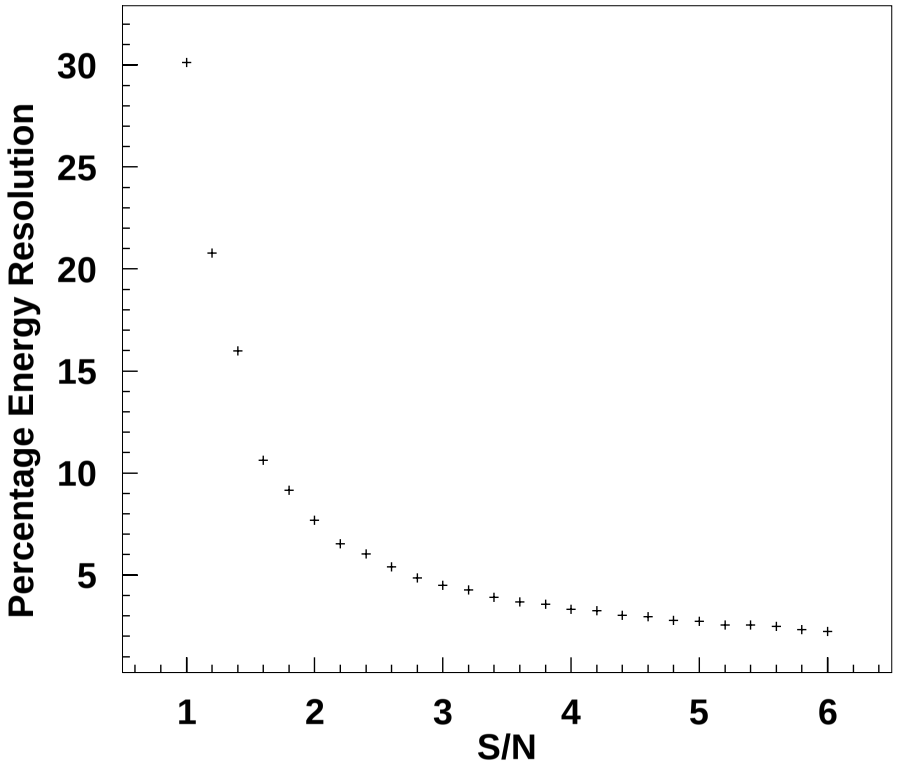

Figure 8.2: The percentage energy resolution as a function of the S/N ratio as defined in the text.

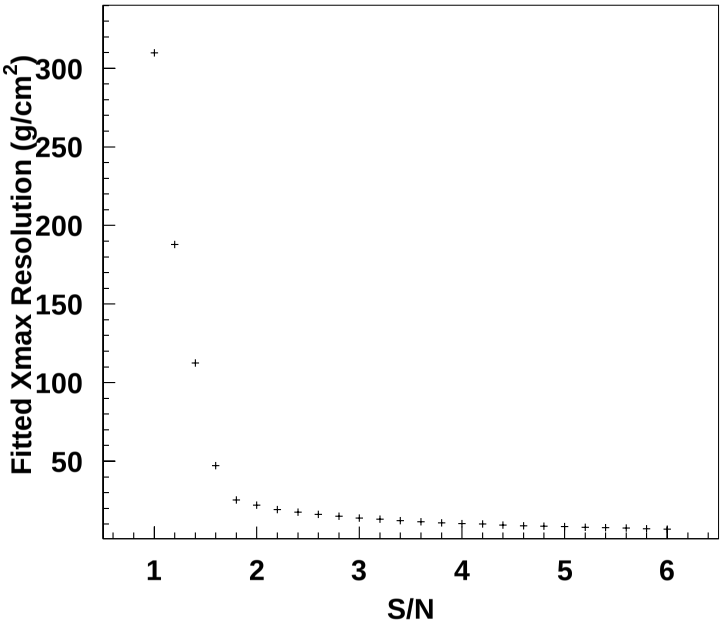

Figure 8.3: The X_{max} resolution (in g-cm^{-2}) as a function of the S/N ratio.

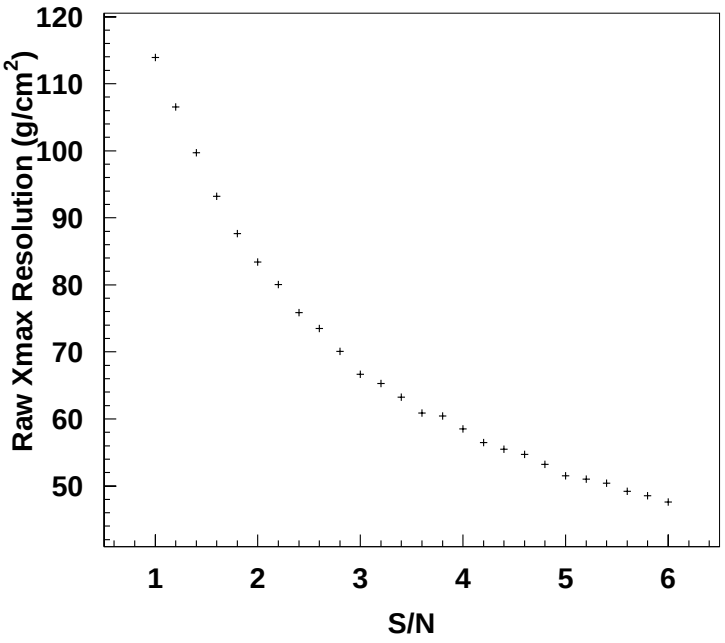

Figure 8.4: The raw X_{max} resolution (in g-cm^{-2}) as a function of the S/N ratio. (Raw X_{max} is the center of the X-bin in which the inferred shower size – including fluctuations due to night sky noise – has its maximum.)

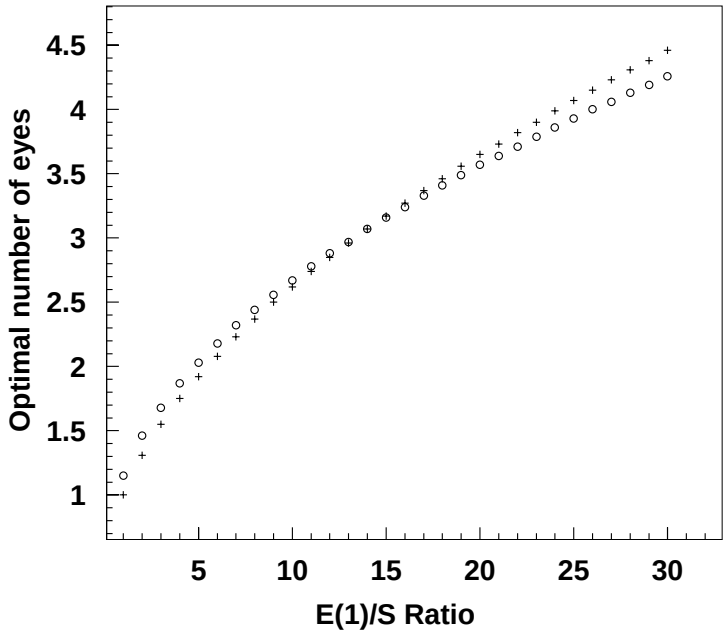

Figure 8.5: The optimal number of eyes n is plotted against the ratio $E(1)/S$ for atmospheric extinction $\xi = 10$ km. The plus symbols are for a 2500 km^2 detector, and the circles are for a 5000 km^2 detector.

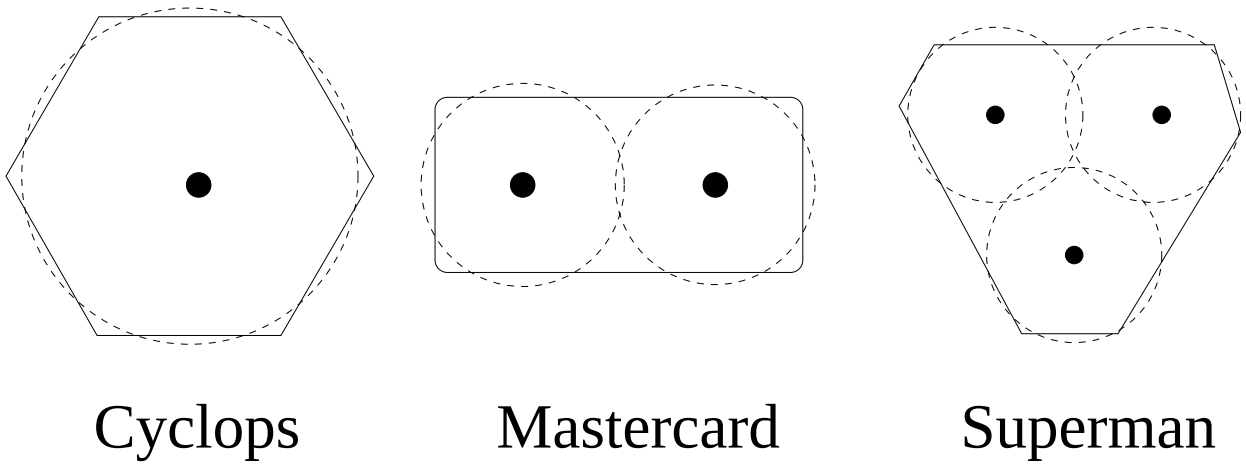

Figure 8.6: Possible array layouts for 1, 2 or 3 eyes. The solid dots indicate the eye positions and the dotted circles the limits of their apertures for 10 EeV showers.

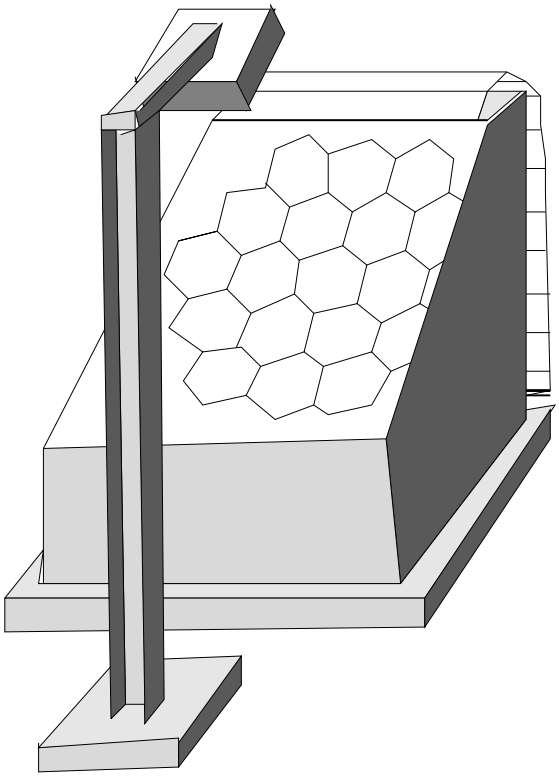

Figure 8.7: Each mirror, consisting of 19 hexagonal segments, will be housed separately from its camera. Neither the mirror nor the camera will be exposed when the sun is out.

Chapter 9

Electronics Systems and Software

This chapter of the report deals with the electronics systems and associated software for the experiment, focusing on the the ground array. These systems acquire data from the detectors, process the information, generate an event trigger, transport the data to a central site, archive it, and make it accessible to the collaboration. The optical fluorescence detector electronics and the lower levels of the fluorescence detector trigger will not be discussed in this chapter. They are briefly discussed in Chapter 8.

We begin with a discussion of the electronics located at each station, and follow the data flow back to the central site. Interspersed through the text we will introduce the various components of the multi-level triggering scheme and then tie that information together in a section dedicated to triggering. Figure 9.1 shows the block diagram of the station electronics. Each of the blocks will be discussed in more detail in following sections.

9.1 Station Electronics Packaging

A careful balance must be kept between modularity, to allow each component of the electronics to be optimized, and a requirement for exceptional reliability, which demands a minimum of interconnections and modules. For example, in order to keep the mean failure rate less than 1 station per day per site, a mean time between failures of 5 years for the station electronics system is required.

We envision using 6U VME packaging powered by solar power through DC-DC power converters. VME has proven to be one of the most reliable commercial packaging systems and variations meet military standards. The electronics will be split into three main modules: front end, station controller and communications. Spare slots will be included to allow the insertion of diagnostic modules and future expansion. For example, the electronics for an air Čerenkov detector could be plugged into one of the spare slots. As our data rates are modest, a 16 bit backplane is sufficient.

The electronics for each station will be housed in an standard commercial environmental

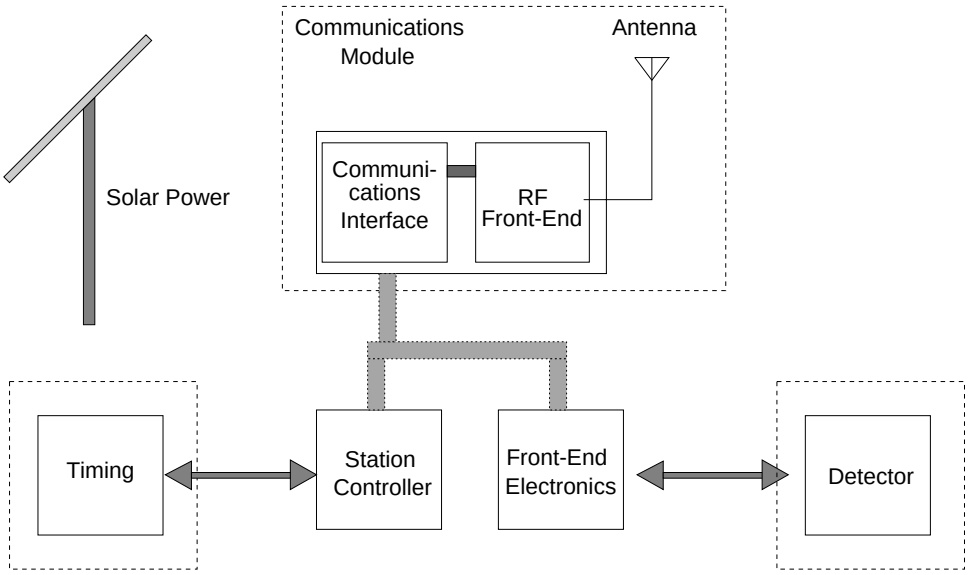

Figure 9.1: Block diagram of ground detector station electronics.

enclosure in thermal contact with the Čerenkov detector water tank to minimize thermal excursions. The PMT high voltage supplies will be integrated with the tube bases. The solar power system batteries will be housed in a separate enclosure, with a gas-tight electrical connection to the remainder of the electronics. Interconnections between the PMT housings, electronics enclosure, battery enclosure, etc. will be armored to prevent damage by animals and the elements.

9.2 Front End Electronics

The front end electronics at each station must both prepare the raw data for inclusion in a data event, and provide a level 1 trigger. Figure 9.2 shows the block diagram for the water Čerenkov detector front end board.

This board generates the level 1 trigger. This trigger provides a first level of discrimination against single muons and small showers. The cosmic ray particle flux impinging on a 10 m^2 detector is about 2.5 kHz. PMT noise will add another few kHz rate. We will refer to this as the level 0 trigger, which fires any time there is a PMT signal above threshold. The level 1 trigger reduces this several kHz level 0 rate to less than 100 Hz.

There are two primary functions of this trigger: clipping muon signals to reduce trigger sensitivity to the primary composition; and using integrated signal to bias against small showers close to the station which deposit signal over a very short time spread. The first function is motivated by the strong dependence of the muon content on the primary species, the muon content of the shower providing one of the best handles on the primary composition. Suppressing the peak of the signal pulse generated by a through-going muon before integrating the remaining signal produces a trigger which is less dependent upon the primary

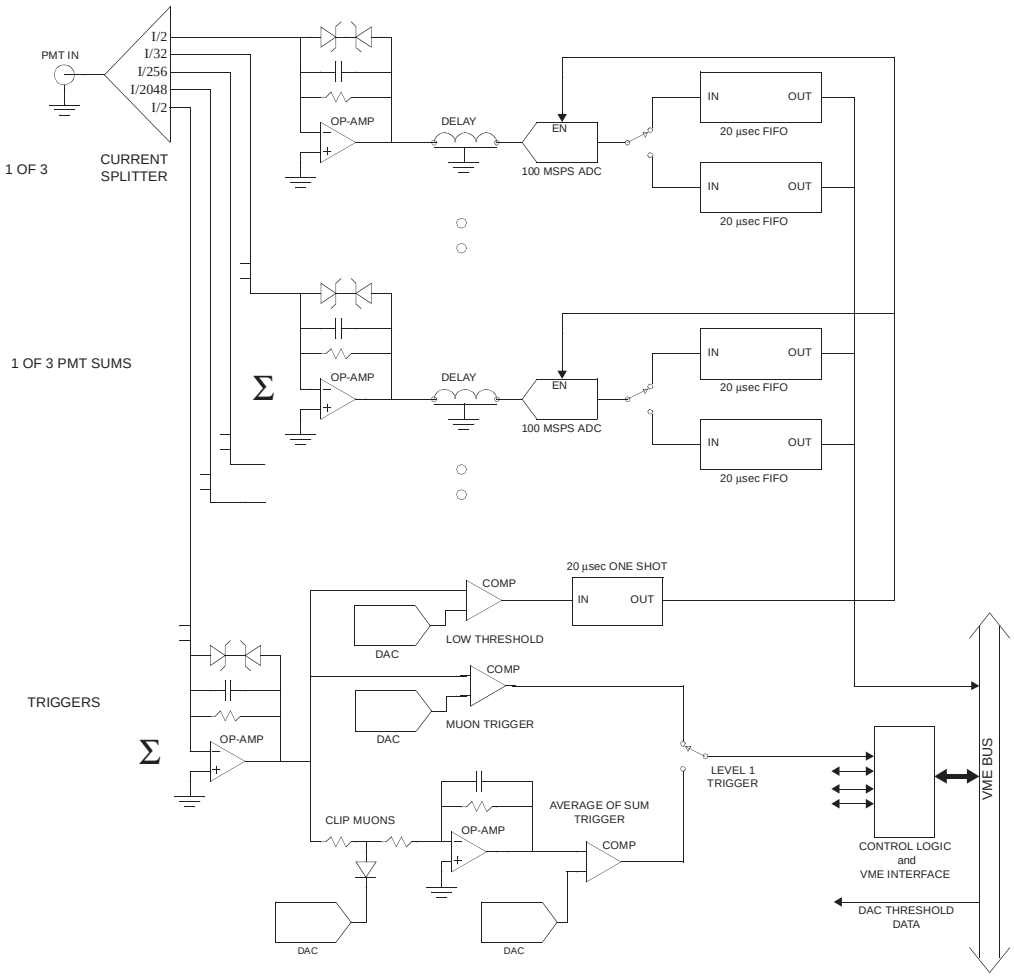

Figure 9.2: Block diagram of a possible front end board.

particle composition. The second function is motivated by the increase in the time duration of the signal (e.g. the width of the shower front) as one gets farther from the shower core, as indicated in Figure 9.3. Note that the 10-90% rise-time plotted in Figure 9.3 shows little distinction between proton and iron showers, a desirable characteristic for the trigger, whereas in Figure 6.10 the 10-50% rise-time shows a clear distinction. This is because the 10-90% rise-time is dominated by the electromagnetic component of the shower, which arrives late, and depends only weakly upon the primary composition. The 10-50% rise-time, on the other hand, is mainly influenced by the muon content of the shower, which arrives early, and depends strongly upon the primary composition. Requiring that the signal be distributed in time biases the trigger against the abundance of smaller showers which land near the stations. A total energy deposition "muon" trigger will be selectable to facilitate calibration of the PMTs on through-going muons and triggering on the very large signals near the core of large showers. The level 1 trigger is sent to the timing system and station controller via a VME interrupt request line, causing the time of each level 1 trigger to be latched and generating an interrupt to the station controller to read out the captured waveform.

The 100 Hz limit is imposed by dead-time considerations in the electronics. What does this mean in terms of the level 1 trigger condition? Using Poisson statistics, a 5 kHz level 0

trigger rate and a 20 μs trigger aperture (this will be justified later in this section), implies a 450 Hz random doubles rate, and a 23 Hz random triples rate of uncorrelated level 0 triggers. The additional rate of level 1 triggers due to correlated level 0 triggers from small showers can easily be reduced to a few Hz or less using the rise-time constraint. This has been measured at Havarah Park using an 8.9 m^2 water Čerenkov detector and a waveform digitizer. The detector outputs were measured (described in terms of rise-time from 10% to 50%) whenever the signal was above 3.7 particles (vertical equivalent muons). The spectrum was strongly peaked towards fast, bandwidth limited, rise-times. A rise-time cut of >100 ns reduces the rate by a factor of 1000. Our simulations exhibit a similar sharp reduction in the trigger rate when a rise-time cut is applied (see Chapter 6). The 100 Hz design rate limit for the level 0 trigger is comfortably above what is expected for triggers comparable to those used in the simulations.

A flash ADC is used on each PMT to maximize the information available for distinguishing muons from photons and electrons. A separate flash ADC for each PMT also simplifies gain matching of the PMTS, by allowing individual gains to be corrected offline. CMOS parts can be used for almost all of the components, including the flash ADCs. (Commercial 6-bit 100 MSPS CMOS FADCs are available for less than $9 in large quantities.) The front end board will have buffering for at least 2 events, minimizing the dead time incurred transferring the recorded waveforms to the station controller.

To increase the dynamic range of the electronics (to cope with the very large signals near to the shower core), additional ADCs with overlapping ranges (e.g. 1/16, 1/128, 1/1024 gain) are used to measure the summed pulse height from the 3 PMTs. This gives the front end electronics roughly a 16 bit dynamic range for measuring the total energy deposited in each 10 ns interval. The overlapping ranges allow the calibration of each FADC to be checked against its neighbor in gain, and give a $< 15\%$ accuracy (bin width) in the pulse height measurement over the entire dynamic range. The use of the same FADCs in the summed signal measurements and the individual tubes simplifies the design by allowing the same clocking, control, and power saving circuitry to be used. As a bonus the "rise-time" of the summed signals can be measured.

The front end board concept is similar to the "QIE" digital PMT ASIC chip developed by Yarema et al.[74][75] at Fermilab. Prototype chips have already been produced that have 16 bits of dynamic range and a fraction of a percent accuracy running at 53 MHz. Thousands of these chips will be used in the KTeV experiment at Fermilab, and they are being considered for at least 2 other large experiments. A crucial portion of this chip is the current splitter at the input, which has been demonstrated to preserve > 16 bits of dynamic range. This chip thus serves as a proof of concept, and is a possible starting point for our design.

The use of 6 bit FADCs requires a large number to achieve the desired dynamic range. Custom ASICs may be able to improve the design in this area. Double-correlated sampling might be a better way to process the PMT signals before feeding them into ADCs, as this may lower both the power consumption and noise in the front end signal shaping circuitry. It may also prove advantageous to run the ADCs somewhat slower than 100 MHz.

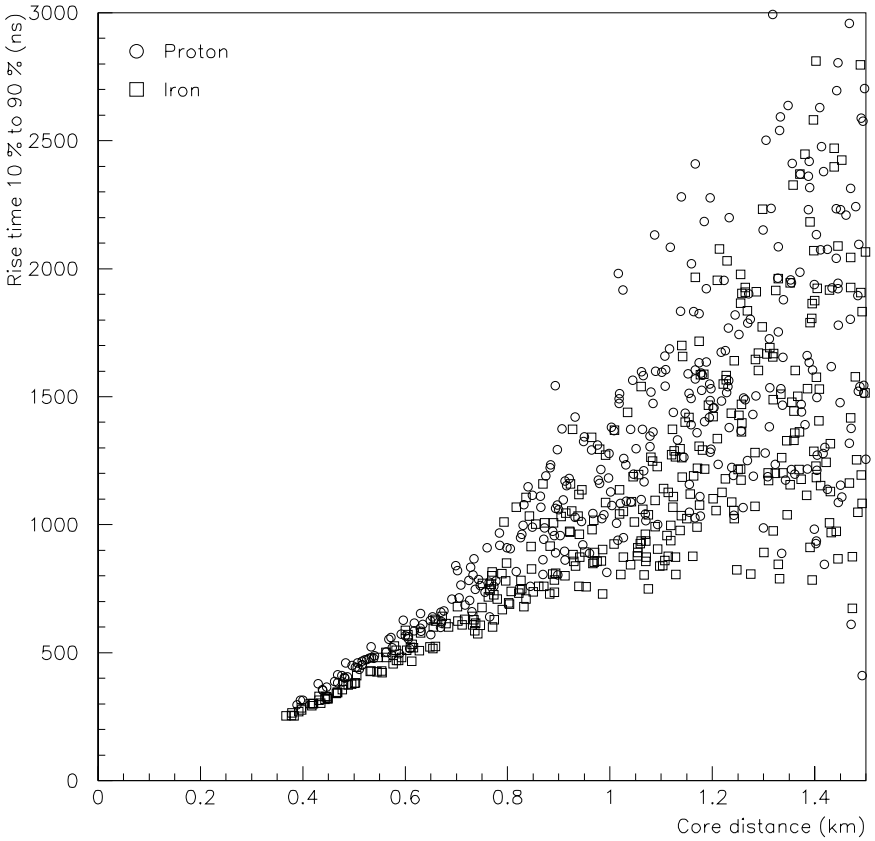

Figure 9.3: Distribution of 10-90% "rise-time" as a function of distance from the shower core for a sample of 100 simulated 10^{19}eV proton and iron showers. (*Cf.* Figure 6.10 where the 10-50% rise-time is displayed.)

With careful design, power requirements for the front-end electronics can be kept reasonably low. Two factors contribute to this: the timing resolution requirements are modest enough to be met with fast CMOS, and the duty cycle for cosmic ray events is low so that most logic can remain quiescent most of the time. Judicious use of ASIC circuits can also help to reduce power consumption and increase reliability. How long does the FADC record need to be? A conservative approach would be to have the record long enough to handle the full waveform of the very largest events one might expect to see. Showers with energies $\geq 10^{21}$ eV might be detected at a rate of 1 per several years. These showers will trigger stations out to about 5 km from the shower core. At this distance from the shower core a 20 μs window is required to catch $\approx 95\%$ of the particles. If we run the FADC system for 20 μs each time a $\sim 1/2$ photo-electron discriminator level is crossed ($\sim$5 kHz level 0 trigger), the system will be active only 10% of the time. Only the front-end amplifiers, comparators, and the clock crystal need to be operating in the intervening 90% of the time. This reduces the estimated power consumption of the board from 12 W to 2.6 W. The FADC window will

be extended for 15 μs after any level 1 trigger, so that the tail end of the waveforms is not lost even for events in which the FADC was started on a random signal.

9.3 Station Controller

The station controller provides the local intelligence at each detector station. It performs a large number of tasks: controlling the PMT HV supplies; monitoring HV, solar panel performance, battery state, etc., reading data from the front end electronics, reading the time tag for each event from the timing system and applying necessary corrections, performing one or more levels of trigger logic, transferring data to the central data acquisition system, and local detector monitoring. In order to perform these tasks, the station controller will use a real time operating system such as OS-9. The station controller board will integrate these functions onto a compact low power board utilizing a highly integrated low power microcontroller, such as the Motorola MPC505. Figure 9.4 shows the block diagram for the station controller code.

It will not, in general, be possible to reset a misbehaving station remotely. Therefore, the station controller code must be robust and must monitor itself for satisfactory operation, automatically restarting itself as necessary. Similarly, it will not be feasible to change EPROMs in over 1600 stations scattered over 3,000 km^2 in order to install updated station controller operating code. Operating code and run conditions must be down-loadable through the communications network.

Only a minimal, very thoroughly tested and debugged, core program will be stored in the PROM. The primary function of the core program will be to reset PMT high voltages to a safe state, and to interact with the communications network to download operating code. The operating code will contain modular links so that selected portions of the code can be updated via the communications network, minimizing the frequency that the entire program needs to be transmitted when program updates are installed. The entire program, including operating parameter storage, will reside in less than 0.25 Mb of memory.

The station controller implements the level 2 trigger in software. It analyzes the digitized waveforms from the three PMTs in order to tag muons, determine the deposited energy, and characterize the time distribution of the signal. Using this information it generates the level 2 trigger, reducing the trigger rate from $\leq$ 100 Hz to $\leq$ 20 Hz per station.

The FADC waveforms are highly compressible. For example, after compression by the widely available "gzip" file compression utility, the six 20 μs PMT waveforms described in the previous section are reduced to a mean aggregate size of 340 bytes in a sample of simulated 10^{19} eV proton showers. The overlapping summed FADC channels contribute $< 10\%$ of the compressed waveform size. Typical level 1 or 2 triggers will be near the trigger threshold and will compress even more. Associated with each event will also be a header of at most 32 bytes. Thus 0.75 Mb of buffer space can hold at least 20 seconds of level 1 triggered events. This is four times longer than the longest level 3 and/or 4 trigger formation time, and thus provides a comfortable safety margin.

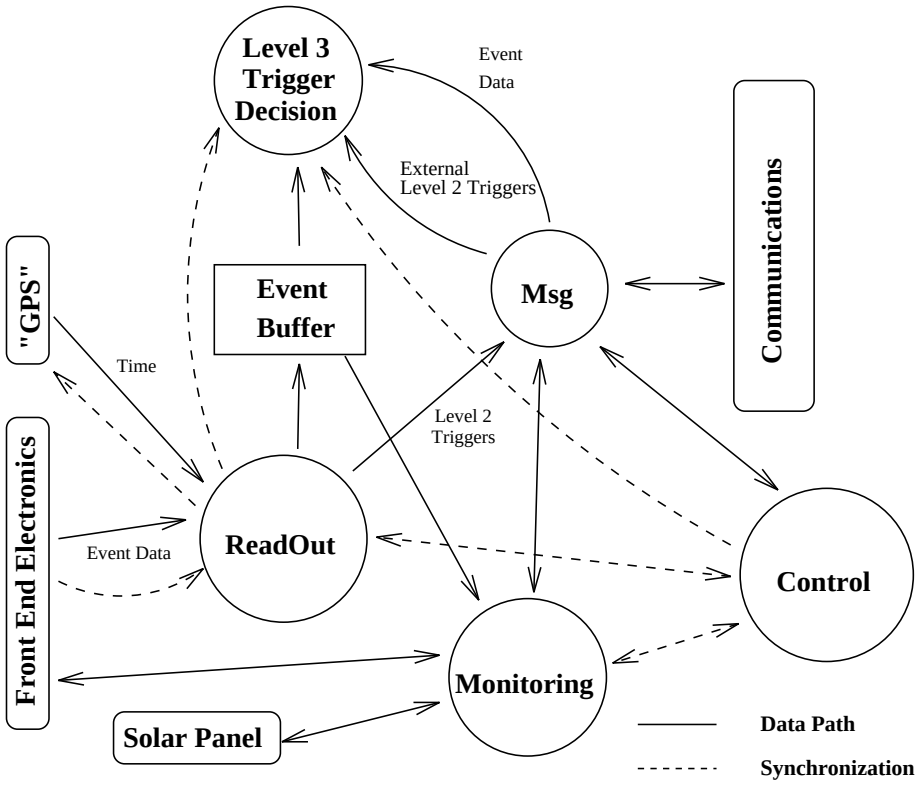

Figure 9.4: Block diagram of station controller code.

The station controller may also perform the level 3 trigger processing. The level 3 trigger requires a 20 μs coincidence of three level 2 triggers within any seven station cell and reduces the (ground array) trigger rate from 20 Hz per station to 0.2 Hz per site.

To minimize the number of boards, many of the miscellaneous interfaces will be incorporated on the station controller board. The station controller board will incorporate sampling ADCs for monitoring the status of the solar power system and PMT high voltages. It will contain DACs to control the PMT high voltage supplies and incorporate a GPS interface with a ≥ 2 event FIFO.

9.4 Timing

Each station needs an accurate time base to 1) match level 2 trigger data with its neighbors, 2) allow shower directions to be reconstructed, and 3) provide a time base for the communications system. In the reference design the timing system is based upon Global Positioning System (GPS) receivers. The Leeds group has demonstrated that nanosecond relative timing can be obtained using inexpensive off-the-shelf scientific GPS receivers. Power consumption is less than 1W.

To allow cross-matching of cosmic ray event times for on-line shower recognition and off-line direction reconstruction it is crucial that data acquisition at each detector station

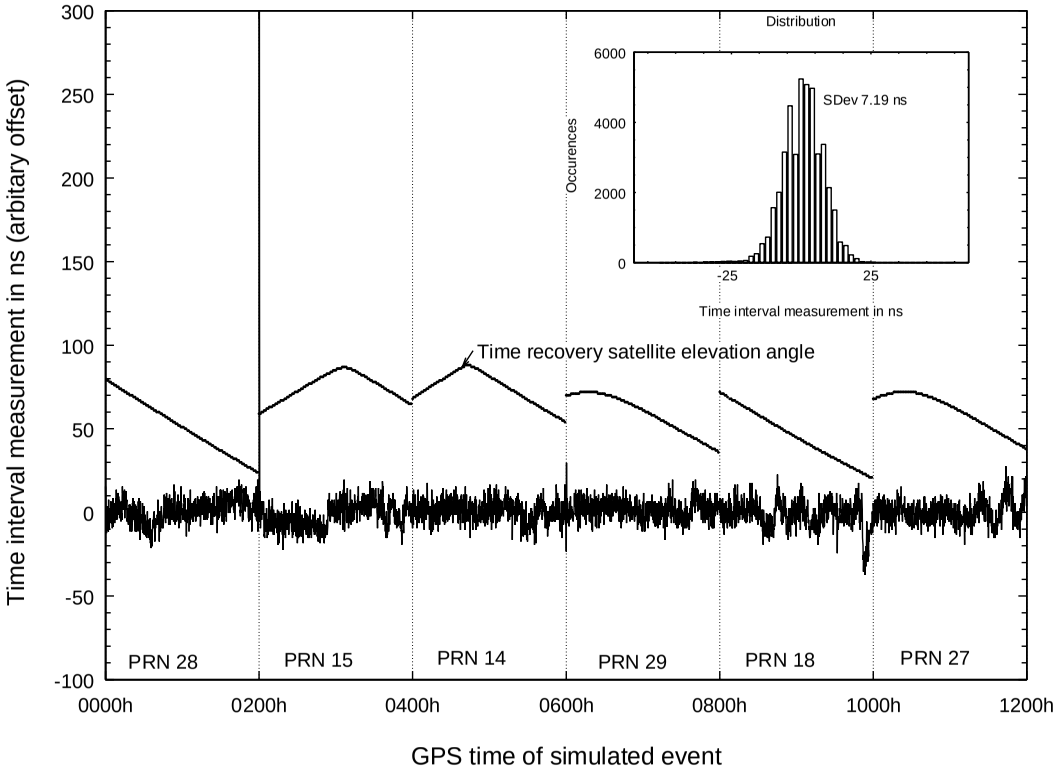

Figure 9.5: Apparent event time difference with the time-tagging systems separated by 11.2 km on the morning of 26/1/95. The upper line of the main graph shows the elevation angle of the satellite being used for time recovery, its PRN code being given at the bottom of the figure. The inset graph shows the distribution of the time interval errors shown in the main graph.

be synchronized. In order to measure a shower direction to better than 1°, the triggered stations must perform event time stamping with an accuracy of better than 25 ns. Higher accuracy timing measurements do not lead to significantly better shower angle measurement due to the sparse nature of the shower front at large core distances, and the limited area of practical surface detectors. In order that the contribution of the timing error to the total shower angle error be small, the timing system should have < 10 ns error.

The GPS is a US government satellite constellation which continuously disseminates position and time information worldwide by means of coded 1.5 GHz radio broadcast signals. The system is now fully operational and expected to remain so for several decades. Unrestricted civilian access to the deliberately degraded Standard Positioning Service (SPS) is allowed. By the use of a simple technique known as "scheduled common view" the effect of this degradation can be eliminated when only relative accuracy is required.

The prototype design is very simple and has demonstrated excellent results[76]. The basic technique is to exploit a commercial GPS receiver module, in conjunction with a custom designed 100 MHz twin channel counter latch assembly. These are both interfaced with a computer. In the final design the interface will be enchanced to include a multi-event FIFO

for the event trigger latch, and incorporated on the station controller board.

One of the latch triggers is fed from the GPS receiver 1 pps output, and the other from the event trigger source. By reading the latch values as they occur, in conjunction with information from the GPS receiver, the computer can calculate event time stamps by simple linear interpolation. In effect the GPS 1 pps is used to continuously calibrate the local counter time frame.

To remove the effect of the deliberate SPS accuracy degradation the scheduled common view technique referred to above is employed. The control computer instructs the GPS receiver to base the 1 pps output on information from a single satellite, which is periodically changed since the satellites remain visible for only a few hours at a time. Each system in the network uses the same satellite simultaneously by means of a pre-determined tracking list.

Initially two prototype systems were constructed which were tested, (a) at the same location and (b) separated by 500 m using a high bandwidth cable link. The time interval measurement error distribution had a standard deviation of 6 ns, with a systematic error of 5 ns. The maximum errors observed during 8 days of operation, with 800,000 test triggers, were +21ns and -35ns.

More recently the same two systems were tested over an 11 km baseline using a microwave link which form part of the MERLIN radio telescope interferometer at Jodrell Bank, UK. Figure 9.5 shows the results of this test, in which the time interval measurement had a standard deviation of 7 ns. It was not possible to measure directly the systematic error in this test. However, due to the variable geometry which occurs in the GPS system it is very hard to envisage a fixed source of error scaling with distance of separation. The largest EAS so far observed have footprint diameters of only 5-10 km. Even the largest showers will not have level 2 triggered stations more than about 5 km from the shower core.

Two more sophisticated systems based on the same technique have recently been deployed at the South Pole to allow cross-matching of the SPASE and AMANDA experimental data streams.

9.5 Communications

The communications system is used to correlate data from different detector stations to form an event trigger, transfer event data from detector stations to a central site, and transfer control and diagnostic information bi-directionally between the detector stations and the central site. The bandwidth required of the communications system depends not only upon the station trigger rate, but also on the topology chosen for the data links, and the level of local multi-station coincidence selected. The communications system design is based upon a maximum mean level 2 trigger rate of 20 Hz. We have chosen a wireless RF communication system for the reference design. Since the performance of the communications system is critical for the operation of the experiment, we will devote a number of pages to discussing the design considerations. This topic is discussed in greater detail in Ref [72].

Wired systems (copper or fiber optics) are easily rejected on the basis of cost considerations. For example, the length of copper or fiber (and trenches) needed to connect the stations is 7,200 km per site with 6 connections per station, or 3,600 km with only 3 connections per station (with minimal redundancy in case of link failure). The installed cost of copper or fiber is about \$10K/km. This is dominated by the installation cost and depends somewhat on site conditions. Even so, at an estimated cost exceeding \$72M, we need not consider the wired option further.

9.5.1 Licensing Issues

Any RF transmitter must comply with regulatory requirements in the site countries. This becomes a complex issue, as the regulations unfortunately vary from country to country. For example, in the US several of the ISM (Industrial, Scientific, Medical) bands are attractive to consider for the station transceivers, as these bands allow operation (of type-certified equipment) without purchasing a license for each station. In the US, the 902-928 MHz, 2400-2483.5 MHz, and 5725-5850 MHz bands are the most appropriate. FCC regulations part 15.247 [77] limit the maximum peak transmitter output power to 1 Watt, and the maximum equivalent isotropic radiated power (EIRP) to 4 Watts (36 dBm) in these bands. In addition, the transmitted signal must be spread in bandwidth. On the other hand, in Europe the maximum transmitter power in the ISM bands is 10 mW EIRP (10 dBm). Extensions to the class license in Australia have been proposed by the Spectrum Management Authority which will permit 1 W EIRP in the 915-928 MHz band and 4 W EIRP in the 2400-2483.5 MHz band. These ISM bands are available in most countries and generally do not require individual licenses. This makes it attractive to consider them for the reference design. A drawback of the ISM bands is that anyone can use them. This is not a problem for a controlled access site where we could restrict the use of other devices which might interfere with our communications system, but is a concern if the general public has access to the site. In some countries other bands may be available which might be dedicated to our experiment. This may provide an attractive alternative to the use of ISM bands if a low enough rate for the license fees can be negotiated. This will be investigated more fully after sites have been chosen.

9.5.2 Propagation

A critical parameter for the communication system is the strength of received signals relative to the noise. This will be function of the transmitter power, the transmitter and receiver antenna gains, propagation path loss, and atmospheric attenuation. Fortunately, atmospheric attenuation is less than 1 dB/km at frequencies below 3 GHz even in the heaviest rainfall, and thus is not a serious concern for propagation over 1.5 km distances.

Radio wave propagation in free space is given by the Friis equation[78]. For the case where the transmitting and receiving antennas are aligned and polarization matched, this equation reduces to

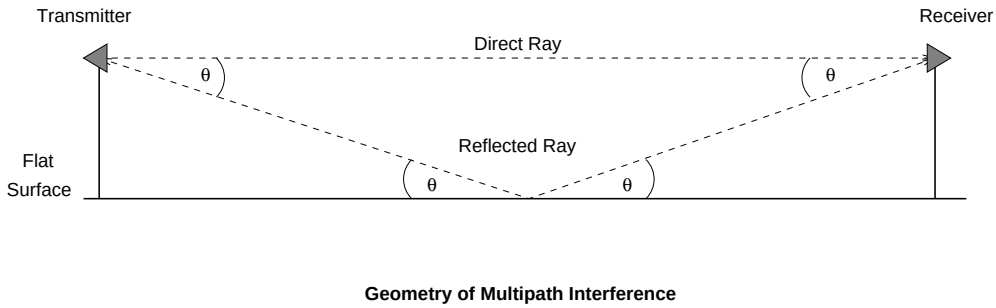

Figure 9.6: Multipath interference of radio waves.

$$\frac{P_r}{P_t} = \left(\frac{\lambda}{4\pi D}\right)^2 G_t G_r \tag{9.1}$$

where

P_t = power at output of transmitter,
P_r = received power at input to receiver,
D = distance between transmitting and receiving antennas (in meters),
λ = wavelength of the radio signal (in meters),
G_t = gain of transmitting antenna, and
G_r = gain of receiving antenna.

However, reflection of the radio waves from the ground and subsequent interference with the direct waves is an important factor which cannot be neglected. This is depicted in Figure 9.6.

A further complication is that the ground will not be precisely flat, but will have some undulations in it. Figure 9.7 displays the calculated propagation loss versus distance between two 8m high vertical full wave dipole antennas at 2450 MHz. The shaded area indicates the loss for a perfectly flat terrain. Each solid curve represents a different randomly generated terrain. The envelope does not vary strongly with terrain variations, as long as line of sight between the 2 antennas is maintained. The 8m antenna height is near optimum at 2450 MHz. At lower frequencies the received signal strength continues to increase for higher antennas.

The points where a bad fade occurs are problematic. One effective technique that is often used to combat bad fades is *antenna diversity*. That is, use multiple receiving antennas and pick the one that gives the strongest desired signal. We have simulated a two antenna receiver, where the second antenna is placed vertically below the first. The height of the second antenna is chosen such that the phase of the direct and reflected waves from a flat earth is changed by 90°. The calculated propagation losses are displayed in the right plot in Figure 9.7.

Another technique that is often used to combat fading is *frequency diversity*. That is, spread the signal over multiple frequencies (or a wide bandwidth) to mitigate the effects

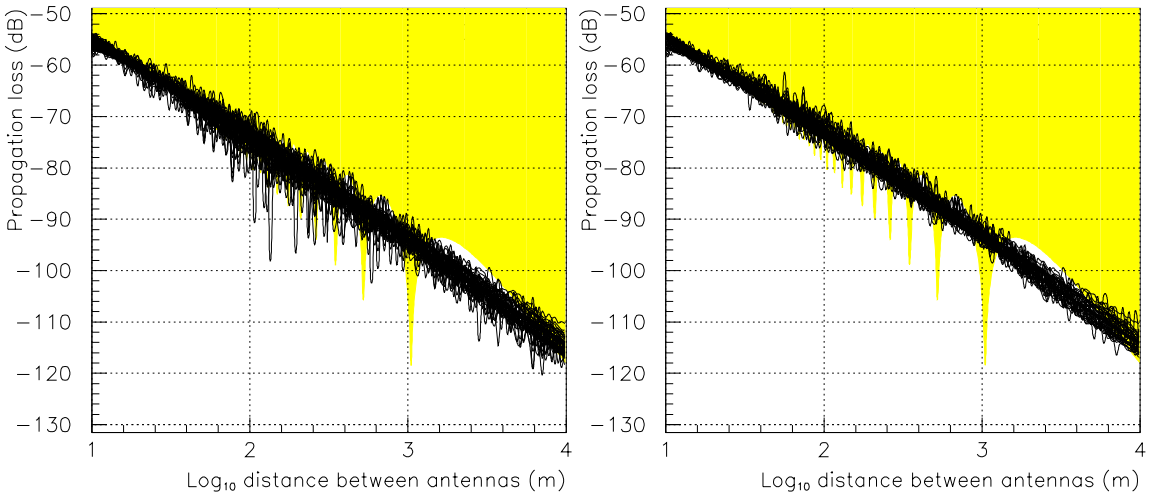

Figure 9.7: Calculated 2450 Mhz radio wave propagation loss for 8m high full wave dipole antennas. The shaded curve is for an ideal flat plane. The solid lines show simulation results for 100 different random terrains with up to $\pm$ 4 m hills). The left plot depicts the case where one receiving antenna is used. The right plot depicts the case where the strongest signal from one of two vertically separated antennas is used.

of a bad fade at one frequency. This will be effective if the path length for the interfering reflected signal is many wavelengths longer than the direct path. This can be the case for reflections from objects not in the plane of the two antennas. However, we are not able to adequately address this question with our current simulations, which only include reflections in the plane of the antenna systems. Radio surveys of the selected sites will be performed to obtain the necessary data.

The distribution of received signal strength in communications systems where there is a strong direct signal in the presence of a number of reflected signals (called multipath) can be shown to follow a Rician distribution. S_i, the received signal strength (Watts) from antenna i, has the (Rician) probability density function

$$f_1(s) = \frac{1}{2\sigma^2} \exp\{-\frac{s+\alpha_i^2}{2\sigma^2}\} I_0(\frac{\sqrt{s}\alpha_i}{\sigma^2}) \tag{9.2}$$

The distribution function is

$$F_1(s) = 1 - Q(\frac{\alpha_i}{\sigma}, \frac{\sqrt{s}}{\sigma})$$

where $Q(a,b)$ is called the Marcum Q function and is given by

$$Q(a,b) = \int_b^\infty \exp(-\frac{a^2+x^2}{2}) I_0(ax) dx$$

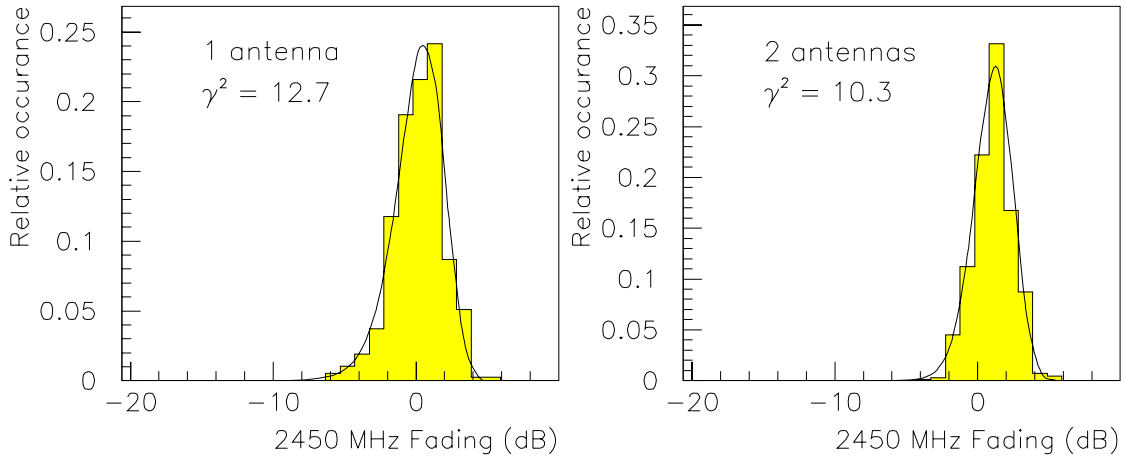

Figure 9.8: Calculated distribution of received signal strength relative to free space for 2450 Mhz radio wave propagation between 8m high full wave dipole antennas separated by 1.5 km. The histograms display the simulation results for 100 random terrains. The curve in the left figure is a least squares fit to Eqn. 9.2. The curve in the right figure is a fit to Eqn. 9.3.

The receiver measures S_1 and S_2 to determine which antenna has better signal-to-noise ratio (assuming the noise power and signal distributions are the same at both antennas). If we let $S = \max(S_1, S_2)$ then the density of S is

$$f(s) = 2f_1(s)F_1(s) \tag{9.3}$$

The ratio $\gamma^2 = \alpha^2/(2\sigma^2)$, which is the ratio of received power in the direct path to that in the faded path, is important when determining the performance. The total average received energy is , $= E(\alpha_i^2 + 2\sigma^2)$, where E is the received energy in the direct path. The error probability shown in later figures is plotted as a function of , $/N_0$, where N_0 is the noise power density.

The calculated distributions of propagation losses are displayed in Figure 9.8, along with least squares fits to $f_1(s)$ (left plot) and $f(s)$ (right plot). As expected by the assumption that the signals at the two receiving antennas have the same probability distribution, the fits produce the same value of γ^2 within errors, with a mean value of $\gamma^2 = 11.5$.

9.5.3 Performance Analysis of Frequency-Hopped Spread Spectrum.

In this section we will analyze the link level performance of a particular data communications system to demonstrate the feasibility of our communications links, using as an example the

Plessey DE6003 transceiver [73]. This is a frequency-hopped 2.4 GHz ISM band spread spectrum transceiver with two antenna inputs. A typical frequency-hopped spread spectrum system consists of a data source followed by an error control encoder. The error control encoder adds redundant bits to the data stream to protect against errors. The encoded data is then modulated using binary frequency-shift-keying (BFSK). The modulated signal is frequency-hopped over a set of frequencies. One goal in transmitting information at different frequencies is that the fading statistics will be different at different frequencies. Thus a given multipath situation will yield a particular fading statistic at one frequency but a different (and independent) fading statistic at another frequency. If a small percentage of the frequencies result in poor performance then an error correcting code will be able to correct the errors that occur when transmitting at those frequencies. The receiver consists of a dehopper/demodulator followed by the error control decoder.

There are several types of codes that could be used. These include convolutional codes and block codes. The convolutional codes are easier to decode with reliability information from the channel (eg. the received signal strength). The block codes have a larger variety of code rates (number of information symbols per channel symbol) available and are slightly easier to analyze. We will only consider the use of Reed-Solomon block codes (used in CD players) in this report.

In a block code (such as a Reed-Solomon code) a number of information symbols k is protected by transmitting not only the information symbols but in addition transmitting $n-k$ redundant symbols. These redundant symbols depend on the information symbols so that if an error occurs during transmission and several symbols are received erroneously the correct information can still be determined. Reed-Solomon codes operate on non-binary symbols typically of size 32 to 256 bits. These usually are called bytes. A non-binary symbol is formed by grouping together bits. For example, in a Reed-Solomon code with symbol size 32, each symbol consists of sequences of 5 bits. The encoder groups information symbols into blocks for the purpose of encoding. For the Reed-Solomon codes considered here $k \cdot m$ bits are grouped together. First m bits are grouped and called a code symbol. Based on k information symbols, $n-k$ redundant symbols are determined. The codeword then consists of the k information symbols followed by the $n-k$ redundant symbols. The decoder can correct any pattern of $e = \lfloor (n-k)/2 \rfloor$ errors.

The codeword generated by the RS encoder can be transmitted using BFSK. Usually there are a large number of bits transmitted during each frequency hop. However, a well designed system would transmit only one code symbol per hop. In order to transmit many bits per hop, and only one code symbol per hop, interleaving is required. Interleaving works as follows: instead of generating a single codeword at a time, L codewords are generated (from different data symbols) simultaneously. Then only one code symbol from each of the L codewords is transmitted during a particular hop. Thus there are $L \cdot m$ bits transmitted per hop.

It is very important to know what the correlation is between the amplitude of the fading at two different frequencies. If the fading amplitudes are independent then error control coding can significantly improve the performance by correcting the errors due to the occasional bad fade at a particular frequency. If, on the other hand, the fading amplitudes are

highly correlated between different frequencies, then error control coding will not be effective in reducing the error probability. As we do not yet have survey measurements or simulation results that can accurately estimate this correlation, we consider the two extreme cases: 1) different frequencies are independently faded and 2) different frequencies are identically faded (completely correlated).

The conditional error probability for making an error in determining the value of a received data bit, given a particular signal strength, is given by

$$P_e(S) = \frac{1}{2}\exp\{-\frac{ES}{2N_0}\}$$

The average error probability is given by

$$\bar{P}_e = \int_0^\infty f(s)P_e(s)ds$$

For coding purposes we are interested in the probability of error in a code symbol which consists of m consecutive bits transmitted at the same frequency and having the same fading value (not only the statistics are the same but the realization is the same). The conditional symbol error probability is given by

$$P_s(S) = 1 - (1 - P_e(S))^m$$

The average symbol error probability is given by

$$\bar{P}_s = \int_0^\infty f(s)P_s(s)ds$$

Given that the different code symbols are transmitted on different hops, the probability that a Reed-Solomon codeword is decoded incorrectly is the probability that there are more errors than can be corrected by the code. The error correcting capability is $e = \lfloor (n-k)/2 \rfloor$. The probability of error is then

$$\bar{P} = \sum_{l=e+1}^{n} \binom{n}{l} \bar{P}_s^l (1 - \bar{P}_s)^{n-l}.$$

It is usually the case that a Reed-Solomon decoder will fail to decode when there are more errors than can be corrected, rather than put out an incorrect codeword. This means that decoder errors will (with high probability) be detected.

Finally we consider the case where all code symbols experience the exact same fading amplitude. For this case the codeword error probability is given by

$$\bar{P} = \int_0^\infty f(s) \sum_{l=e+1}^{n} \binom{n}{l} P_s(s)^l (1 - P_s(s))^{n-l} ds.$$

Later we show the large difference between coding for independently faded channels and identically faded channels.

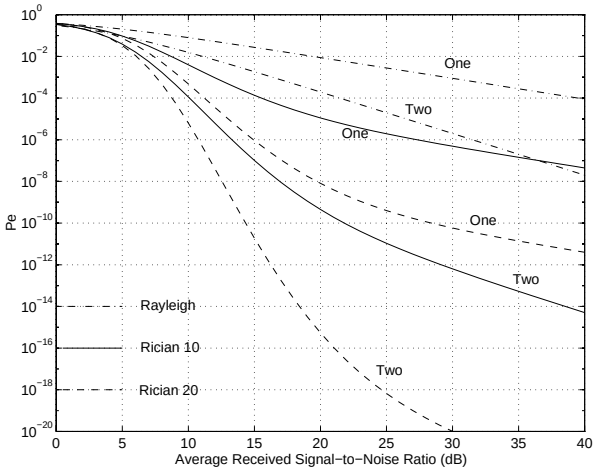

Figure 9.9: Bit error probability for fading without coding with one and two antennas.

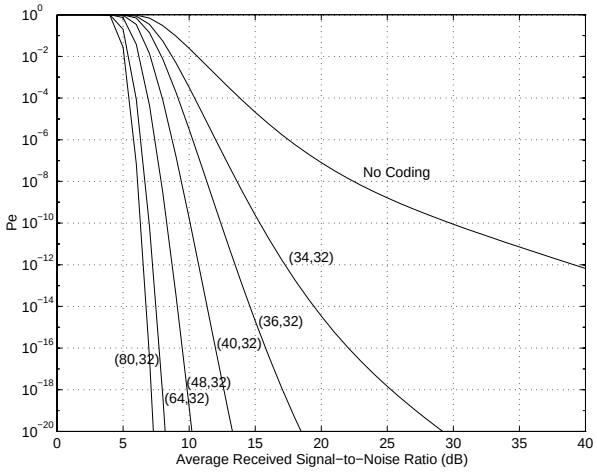

Figure 9.10: Block error probability for Rician fading with coding and symbols independently faded ($\gamma^2 = 10.0$).

9.5.4 Link Budget

In this section we consider the link budget for a system using a 20 dBm (100 mW) transmitter with stations separated by 1.5km. The transmitter and receiver have antennas which each provide 3 dB antenna gain. The loss due to free space at frequency 2.45 GHz is 103.7 dB. Thus the transmitted signal power is reduced by 97.7 dB. For a 100 mW transmitter the received power in the direct path is 16.8×10^{-12} W. The data rate considered (that used in the Plessey DE 6003) is 625kbps. From this the (direct path) energy per bit is given by $16.8 \times 10^{-12}/(625 \times 10^3) = 2.7 \times 10^{-17}$ joules/bit. In addition there is the energy from the multipath components. Based on simulations the ratio of the energy received from direct path and multipath components ($\gamma^2 = \alpha^2/(2\sigma^2)$ is 11.5. The total received energy is then , $= 2.7 \times 10^{-17}(1 + 1/11.5) = 2.9 \times 10^{-17}$ joules/bit. The noise level (from the DE6003 data sheet) is $N_0 B_{IF} = -103$dBm, where B_{IF} is the bandwidth of the IF filter (1.5 MHz for the DE6003). Thus the noise power density $N_0 = 3.3 \times 10^{-20}$ W/Hz. The average received signal-to-noise ratio is , $/N_0 = 29.5$dB. There are potential implementation losses which reduce the effective signal-to-noise ratio. Plessey estimates these to be of the order of 5dB for the DE6003. Thus the effective received signal-to-noise ratio of 24 dB may be appropriate (in the absence of other interfering signals). Although our simulations indicate $\gamma^2 \approx 11.5$, we will use a more conservative $\gamma^2 = 10$ below.

Interference from other transmitting stations must also be considered, as this may raise the noise. We are considering using a 7 slot time division multiple access (TDMA) scheme with about 237 stations transmitting simultaneously. In a frequency hopping system with 79 or more adjacent channels (like the DE6003) there would be three stations transmitting on each channel at the same time, and an additional six stations transmitting on neighboring channels. With fixed station positions we can arrange the frequency hopping sequence to

maximize the distance between interfering stations. In that case, interference from other transmitting stations will typically be 20 dB below the desired signal.

The bit error probability for an uncoded system with one or two antennas is plotted against the average received signal-to-noise ratio in Figure 9.9. In the case of two antennas the receiver is assumed to be able to select whichever antenna has the largest signal. It is clear from this figure that significant gains can be achieved by using two antennas. The three sets of curves correspond to the case of no direct path (Rayleigh, pessimistic), a direct path and faded path with $\gamma^2 = 10$ (Rician 10, realistic) and with $\gamma^2 = 20$ (Rician 20, optimistic).

The codes we considered all operate with the same number of information bits (256) grouped into 32 8-bit bytes. In the uncoded case we just transmit these 32 symbols without any extra redundant bits. The codes have different block lengths n but the same number of information symbols (32). The (48,32) code has $n - k = 16$ and can correct 8 errors in the block of 48. The (64,32) code has $n - k = 32$ and can correct 16 errors in a block of 64. In Figure 9.10 the block error probability is shown for the case where each symbol is independently faded, and the power in the direct path is ten times the power of the faded path (Rician 10). In this case the block error rate may be as low as 1 part in 10^{14}. However, if the fading is identical at different frequencies, the error coding is much less effective at reducing the error probability, reducing it by only a factor of two.

Radio surveys of the selected sites will permit us to refine these calculations, but at present it appears that commercial transceivers like the Plessey DE6003 will provide a satisfactory block error rate level when combined with error correcting codes.

9.5.5 Network Topology

Once we establish reliable radio links between neighboring stations we have, in principle, the means to transfer the information necessary to operate the project between detector stations. This is trigger information, data packets, software downloads, etc. The network topology and protocols are primarily implemented in software that operates on the communications hardware. It will be advantageous to conform to international standards, such as the ISO/OSI 7 layer model, as much as possible.

It is desirable for each station to have line-of-site communication with its six nearest neighbors. This provides alternative communication links in case of station failures, a prerequisite for a fault-tolerant network. Occasional obstacles (e.g. hills) can be tolerated.

Two competing designs are under consideration for the network topology: the "flat" or "fraternal" architecture where the level 3 trigger decision is performed by the station controllers; and the "hierarchical" or "federal" architecture where local stations send all level 2 trigger data to a central system via concentrators. The station transceivers that one would use for the "fraternal" network are also ideally suited for the "federal" network.

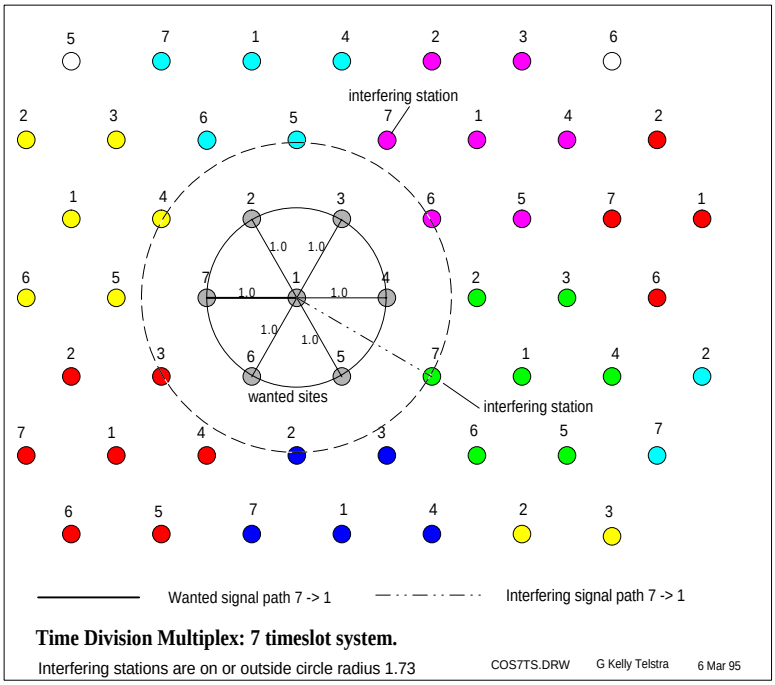

Figure 9.11: Flat communications network topology.

Flat Network

Figure 9.11 depicts the flat network topology, which is discussed extensively in Ref [72]. Each station communicates with its six nearest neighbors using time division multiple access (TDMA) spread spectrum techniques. The seven time slots used in each seven station cell are reused in adjacent cells. Spread spectrum techniques (either direct sequence code division or frequency-hopping such as the Plessey DE6003 uses) are used to discriminate against signals from unwanted stations. All stations in the array are equivalent in a peer-to-peer network.

Each station handles several basic types of information: level 2 trigger broadcast to neighbors; level 3 trigger broadcast; "external" level 2 triggers from the control center; event data to control center; monitoring information; command/control messages to/from control center; broadcast data from control center including software download, and array-wide commands.

Level 2 trigger broadcasts are transmitted only to immediate neighbors. The station controllers then use this information to form the level 3 trigger. Packets intended for other stations or the control center, or from the control center, are relayed station-to-station by routing algorithms based partly on geographic location within the array. Centrally generated level 2 triggers (from the optical fluorescence detector, for example) are also relayed station-to-station and incorporated in the level 3 trigger logic performed by the stations. This station-to-station relay can also be used to route level 2 trigger packets around obstructions (e.g. hills) or defective stations. The flat network is inherently fault tolerant. Multiple paths exist between all stations, and the forwarded packets themselves provide automatic

	Factor	bits/s	other/comments
1	Level 2 Trigger broadcast transmit	480	Broadcast, i.e. transmit to 6 neighbors
2	Level 2 Trigger broadcast reception	6·480	Receiving from 6 neighbors in respective time slots
3	Trigger broadcast receive	40	Latency of 1 sec hop to hop or less to limit buffer space.
4	Data forwarding to control center at 6 collector nodes	160	Low priority, not time response critical.
5	System monitoring traffic	220	Low priority, not time response critical.
6	Command/control	100	Latency is significant, prefer no more than 1/4 sec node to node. Packet rate is for short term only.
7	Parameter download	≈100	Mainly determined by latency which translates to station outage time, i.e. time to change the array operation
8	Software download	570	Includes final acknowledgement, objective 1 hour for 250K bytes. Does not have to co-exist with measurement activity.

Table 9.1: Basic data bit rate for various types of message in the flat network topology.

link acknowledgements for multi-link paths.

The raw bit rate required for various types of messages is shown in Table 9.1. The transmit rate for normal operation is the sum of 1,3,4,5,6 = 1000 bits/s average throughput, without overhead. In a 7 slot TDMA system the modulation rate required is then 7,000 bits/s, without overhead. Including overhead, error correcting coding, guard time, and ramp-up/ramp-down increases this to 20,000 bits/s. Including a factor of 4 safety margin, we aim for 80,000 bits/s.

In terms of frequency bandwidth allocation, our bit rate corresponds to a minimum of 8 mHz bandwidth allocation, which might reasonably be configured as about 80 adjacent 100 kHz channels. The 2.4 GHz ISM band contains 10 times this bandwidth.

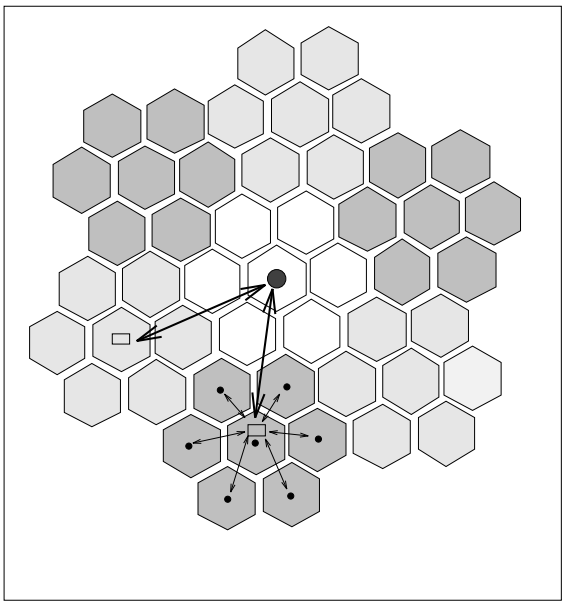

Figure 9.12: Cell configuration in the 2-level hierarchy. Each of the small hexagons represents one cell of stations depicted in Fig. 9.13. A base station at the center of each such cell communicates with a microwave repeater at the center of each cluster of 6 cells. These repeaters in turn communicate with microwave tranceivers at the center of the array.

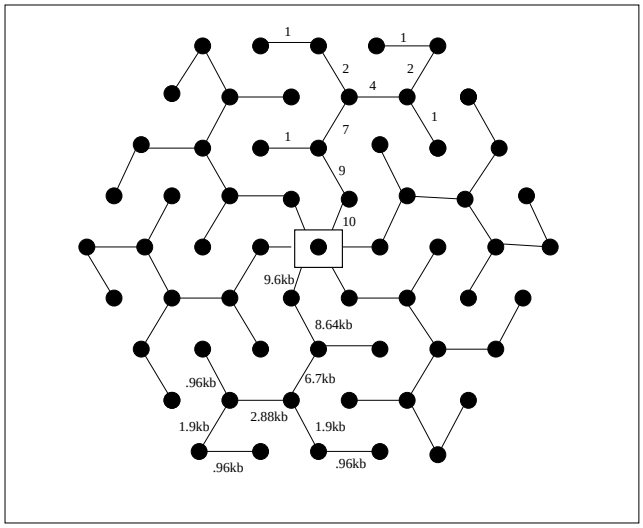

Figure 9.13: Communication links and data flow rates in a level-2 mini-cell. Each dot represents a detector station. The lines indicate the radio communication links between stations. At the center is a base station which communicates with a microwave repeater (see Fig. 9.12).

Federal Network Topology

A viable alternative to the flat network is a hierarchical network. In this scheme all level 2 triggers are sent to the central system for further trigger processing. This is depicted in Figure 9.12.

In each lowest level cell the concentration may be either by point-to-point links or TDMA global collecting down to the six "first ring" stations surrounding the local base station (see Figure 9.13). TDMA transceivers like those used in the flat network are also well suited for use in the federal network because they provide software accessible backup links which can be used in the event of a link failure, thus providing a high level of fault tolerance.

Higher bandwidth is required as the data is concentrated towards the center. This is satisfied with a hierarchy of directional microwave links.

Flat (fraternal)	Hierarchical (federal)
Trigger decisions made locally, reducing data rates and processing loads at the control center	Trigger decisions made centrally, allowing more general and complex trigger patterns
Normal trigger decisions made more quickly, reducing buffer memory requirement in local stations	Data propagated to control center more quickly, reducing central buffer requirements for event building
Additional local buffer memory required (same as for federal) to handle centrally generated triggers from external devices	No additional local buffer memory required for any centrally generated trigger
Less hardware required; lower hardware cost	Simpler network protocol (but more systems); less protocol development effort
Array boundary shape flexible; additional stations easily added (simplifying phased turn on)	Addition of new cells does not increase network load in existing cells
Requires line of site between each station and 6 neighbors	More tolerant of terrain variations; line of site to 3-4 neighbors adequate for fault tolerance
Network is inherently tolerant of station failures	Local station links can be made fault tolerant; susceptibility to failure of level-1 and level-2 links is a weakness

Table 9.2: Communications network model comparison.

Comparison of Flat and Federal Network Topologies

The critical features of the flat and federal networks are summarized in Table 9.2. It should be noted that both models will work satisfactorily. Each can handle the anticipated data rates and any reasonable trigger that has thus far been considered.

It is not critical that a decision be made before proceeding with the detector development. Identical local station communications hardware can be optimum for both models. The difference at station level is software. The cost for either system is modest. In the federal scheme one trades a more complex network protocol for additional hardware. The flat network hardware can also be later "upgraded" to the federal network by addition of level-1 and level-2 concentration equipment if strong physics justification arises.

The estimated equipment cost for the flat network is $870,000 per site. The federal network would cost an additional $600,000 per site for the microwave concentrators, towers, and additional solar power systems, but would have a lower protocol development cost.

Station Power Budget

System	Power Rqd (W)
High voltage	1.0
Front end	2.6
Station controller	2.5
GPS receiver	0.85
Communications transceiver	0.83
Transceiver interface	0.5
Total	8.3
Converter losses	$\times 1.2$
Total	9.9

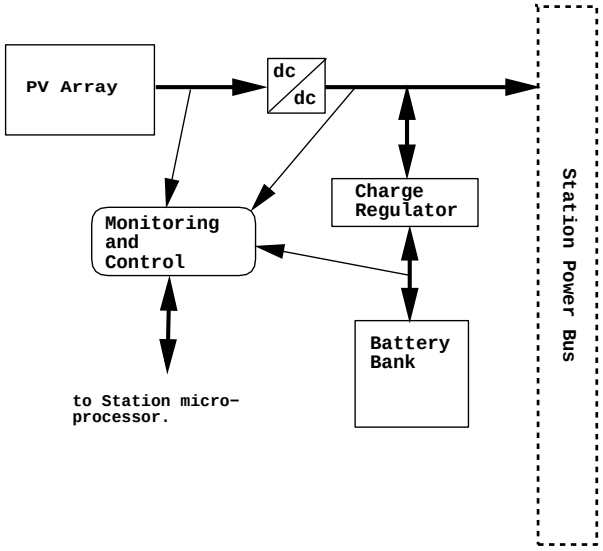

Figure 9.14: Block diagram of the solar power system for each station

9.6 Solar Power

The ground array stations will operate from solar power (photovoltaic,PV). The power budget for each station shown in Figure 9.14. The PV system must provide regulated power to the station electronics with minimal maintenance over the expected lifetime of the experiment. Each station will have its own PV array, battery bank, charging regulator, low battery voltage disconnect, and control/monitoring system as shown in Figure 9.14. The orientation of the PV array will be fixed at an angle which maximizes the solar exposure during the winter.

The number of required solar panels and size of the battery bank are estimated from a knowledge of the daily power requirements, the estimated availability of solar radiation at the site, and the percentage of down time due to insufficient power that can be tolerated. The statistical nature of the event data means that pushing for much less than 2% outage due to insufficient solar power is not warranted if it adds substantial cost to the system. However, as it turns out, this goal is easily achieved.

For planning purposes we have sized the system for a site with the solar radiation characteristics of Dugway, Utah. A simple but conservative analysis has led us to propose the use of two 53 peak Watt (Wp) silicon solar panel arrays for power collection and two 12 volt gel-cell lead-acid batteries for power storage. This provides sufficient Wp capacity such that with average insolation at Dugway (minimum of 3 hours Wp mid-winter) the batteries never discharge to 50%. The battery capacity is sufficient to power the system for more than 10 days without sun, discharging to 50%. The technology of both of these components is mature and their commercial use is common.

Although the outage probability has not yet been accurately estimated, this system is

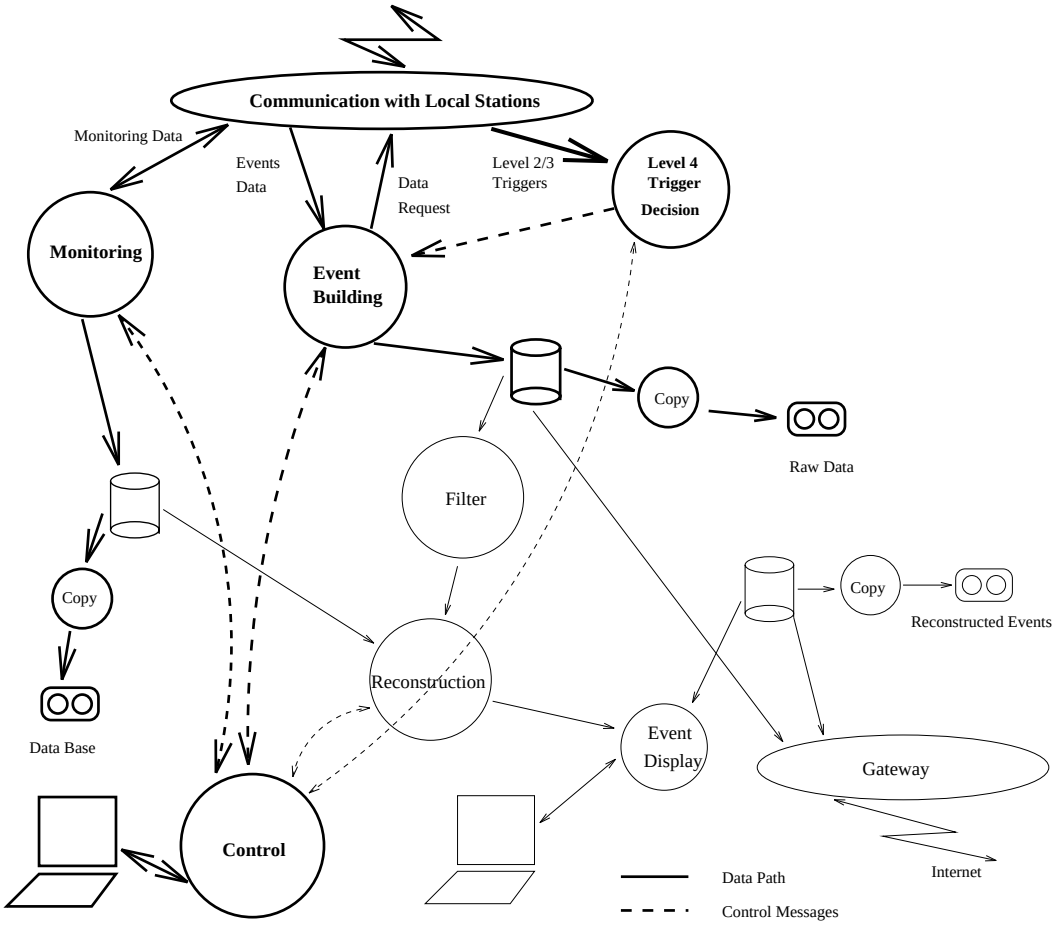

Figure 9.15: Block diagram of central station data flow.

expected to perform much better than the design goal of less than 2% outage probability per station. A more detailed analysis of the system sizing and outage probability will be performed using accumulated insolation data for the two sites, once they are selected.

9.7 Data Acquisition and Archives

The collection of data at the central site will be handled by Unix workstations. Figure 9.15 shows the block diagram for the control center data acquisition (DAQ) code.

The philosophy of the DAQ is the following. The ground array and the fluorescence detector have their separate acquisition hardware and computers. For each detector, there are two servers: one for the data acquisition (trigger, event-building) and archiving, the other for the monitoring, calibration and slow control tasks. The computing resources required are modest by present day standards and can easily be handled by low cost workstations. Each would have $\sim$128 Mb of central memory, a $\sim$2 Gb system disk, $\sim$8 Gb of temporary data storage space, and an output device (e.g. DAT tape or CD-ROM) where the data is permanently and locally stored. Software and licences were also considered (including

FORTRAN, PASCAL and C compilers).

A relatively high speed Internet access (>1 Mbit/s) to the site will be provided via fiber optic link or satellite link. This will allow collaborators to monitor the experiment from anywhere in the world and transfer moderate amounts of data.

The data acquisition hardware can only be outlined at present. We envisage one VME crate per detector. For the array, our estimate was based on the more expensive hierarchical communications architecture. In this case, the hardware includes seven telecom interfaces (six for the nearest antennas and one for the central level-1 station), a fast processor and a link to a LAN. Similar hardware would be required for the flat communications architecture with high speed links to the inner ring of six stations to reduce congestion. Absolute time reference will be obtained from GPS.

9.8 Trigger

We conclude this chapter with a discussion of the trigger, which must select interesting physics events from a large background of random coincidences of small air showers. In order to accomplish this we have adopted a multi-level trigger design which is distributed both between hardware and software, and geographically. Table 9.3 summarizes the trigger levels and associated rates at each level for the ground array. This rate is compared to the rate of $\geq 10^{19}$eV showers.

The level 1 trigger selects potentially interesting data from a background of several kHz of single muons, small showers, and PMT dark noise. This trigger is implemented in hardware on the front end board. The implementation of the level 1 trigger reduces the contribution of muons to the trigger sum by truncating the pulse height at a programmable level to minimize composition bias, and integrating the resultant signal below the clip level. The integration of the truncated signal biases the trigger against nearby small showers which deposit their energy over a short time interval. An additional level 1 trigger, which accepts large depositions of energy without regard to the time structure, will be implemented to trigger stations with interesting information that may fail the rise-time constraint, such as stations close to the core of large showers.

As it will take about 1 ms to transfer the FADC waveforms to the station controller memory, negligible (<1%) dead time will be incurred if trigger rate has been reduced to ≤ 100 Hz by the level 1 trigger and the FADC board is double buffered. The station controller then applies software algorithms to analyze the FADC waveforms to refine the level 1 trigger and produce the level 2 trigger. The level 2 trigger rate will be less than 20 Hz. This rate limit is imposed by the communications system, and is high enough that we will not be cutting out interesting physics events. Level 2 triggers are broadcast to neighboring stations (in a flat network topology) or to the control center (in a federal network topology).

The level 3 trigger correlates information from nearby stations (e.g. 3 in any 7 station cell within a 20 μs coincidence window) or nearby stations plus an external level 2 trigger (e.g. optical fluorescence plus two stations). The level 3 trigger contains the minimum

Trigger level	Where	How	Condition	Rate	Triggers /Shower	Randoms (%)
0	Station	Hardware	Single μ + small showers + PMT noise	$\approx$ 5 kHz per station	8×10^{10}	100
1	Station	Hardware	Limited/integrated energy	100 Hz per station	1.6×10^{9}	100
2	Station	Software	Level 1 + FADC info	20 Hz per station	3×10^{8}	100
3	Station Neigh-borhood	Software	3 fold level 2 in 20μsec window	0.2 Hz	1.5×10^{3}	100
4a	Central	Software	Level 3 + 1 ad-ditional level 2 in 1μsec window	15 / day	1.5	33
4	Central	Software	Level 3 + 2 ad-ditional level 2 in 1μsec window	10 / day	1	0.7

Table 9.3: Ground array trigger summary. In the last 2 columns the trigger rate is compared to the rate of $\geq 10^{19}$eV showers. Level 3-4 rates are for the whole array.

information required to reconstruct a shower. For example, a shower direction cannot be reconstructed from less than three ground stations. However, the background from random coincidences of single muons and small showers (estimated using binomial statistics and the 20 Hz level 2 rate constraint) is 1500 times larger than the rate of $\geq 10^{19}$eV showers. Thus, level 3 triggers are in general not useful for physics analysis without additional constraints. Nevertheless, due to their low rate (0.2 Hz per site), all level 3 triggers will be archived and made available for further offline analysis.

The level 4 trigger further reduces the background contamination. This will be used as the basis for the on-line analysis of data. For the ground array a level 3 trigger, plus 2 additional level 2 triggers (from the 19 station cell centered on the level 3 trigger) occurring within a 1 μs window around the shower front defined by the level 3 trigger will reduce the background to less than 1% of the triggers. In Table 9.3 we note (in line 4a) that one additional level 2 trigger is not sufficient in this scenario; 1/3 of the triggers would be random coincidences.

Item	Cost/Station	Total Cost	Comments
Front end board	$400	$1,325K	
Station controller board	$430	$1,425K	Includes OS-9 license
GPS receiver & antenna	$320	$1,060K	
Communications transceiver	$295	$978K	
Antennas, mast, & interface	$370	$1,226K	Flat network option
VME cage	$240	$795K	
DC/DC converters	$200	$663K	
Environmental enclosure & interconnects	$200	$663K	
Solar panels	$520	$1,723K	
Batteries	$590	$1,955K	
Enclosure, connections, & controller	$150	$497K	
Testing	$200	$663K	
Installation	$200	$663K	
Total	$3,565	$13,637K	

Table 9.4: Electronics Cost Drivers. Total cost is based upon two sites with 1657 stations each. Contingencies and EDIA are not included.

9.9 Cost Drivers

Table 9.4 summarizes the equipment costs for the electronics systems. The costs are well balanced. There is no single component that contributes significantly more than others to the total cost.

Chapter 10

Site Survey

10.1 Introduction

The responsibility of the Site Survey Group is to identify, explore, and characterize candidate sites, both in the Northern and Southern Hemispheres, suitable for construction of the Auger Cosmic Ray Observatories. The initial task of the Survey Group was therefore to establish the desirable characteristics of such a site. Contacts were then initiated with interested parties in Argentina, Australia, China, Europe, Russia, South Africa, and the United States. A summary of the site selection criteria was circulated to these groups, and they were asked to nominate candidate sites based on their knowledge of the respective areas.

Site visits to Argentina, South Africa, and Australia have been completed. Visits to Northern Hemisphere sites in Spain, Russia and Kazakstan, and the United States are planned for the second half of 1995. This is an interim report covering only the Southern Hemisphere.

The following sections outline the criteria to be used in site selection, describe site visits and the data being collected as part of the survey effort, summarize the results of site visits completed as of July 1995, and discuss future Site Survey plans.

10.2 Site Requirements

Discussions were held, especially with members of the Fluorescence, Surface Detector, and Communications Groups. These identified desirable site characteristics and led to a set of selection criteria — some motivated principally by physics considerations and others by more practical concerns. In the absence of a detailed detector design these "requirements" have the nature of guidelines; a site failing to strictly meet these criteria would not necessarily be excluded from further consideration.

The selection criteria arising primarily due to physics considerations include:

- a latitude between 30° and 45° North or South of the equator
- an area of about 3500 square kilometers;
- an altitude between 500 and 1500 meters above sea level;
- cloud cover less than $\sim$ 15% with little ground fog and moderate temperatures;
- good visibility, and no significant nearby sources of light pollution.

Among the constraints dictated by practical considerations are the following:

- the site should be relatively level with a mean slope less than 1% and not in excess of 2% to 3% over distances of a few hundred meters (i.e. both locally and globally flat);
- the vegetation, soil, and topography should not impede movement within the site;
- suitable infrastructure (e.g. power supply, freight access, telecommunications, and "goods and services") should exist; or means for its economical development should be at hand.

Of the practical considerations, two impose the most significant constraints:

The high frequency radio communications technology to be used for data acquisition and control necessitate line-of-sight contact between transmitter and receiver. The site must therefore be extraordinarily flat on scales of a few kilometers. This is largely true regardless of whether the so-called "flat" or "hierarchical" network is adopted. (Nevertheless, barring development of a non point-to-point trigger routing protocol for the flat network, the hierarchical approach does permit a greater degree of flexibility in the site's topography.)

Installation of the surface array, whether composed of water Čerenkov detectors or lead scintillator sandwiches, requires that very heavy loads (up to 2×10^4 kilograms) be moved throughout the site. Sites where large areas of unconsolidated soil (e.g. sand) or woody vegetation exist may seriously impede installation.

Prior to the site selection the following points need also to be addressed:

- the allocation and licensing of radio frequencies for data acquisition and array control;
- the means by which site access can be secured;
- clarification of the duty status of equipment, supplies, and materials which may be imported for the project.

In these issues in particular the support of the local scientific and civilian communities as well as of the government(s) concerned is of the utmost importance.

10.3 Site Visits and Relevant Data

Visits by the Site Survey Group have generally begun with a review of the materials collected by the host institution. These data include:

- "civil" maps indicating the position of roads, highways, railways, and airports; cities and towns; power and telecommunications links;
- topographic maps (preferably at scales of 1/100,000 or larger) with elevation contours suitable for verifying access within the array ($\leq$ 20 meter vertical separation);
- vegetation coverage and soil maps;
- long term (i.e. five years) weather records including cloud cover; precipitation, both rain and snow; high, low and mean temperatures; insolation; mean and maximum wind speeds;
- an indication of the level of infrastructure present at or near the site (e.g. technical support services; industrial properties for off-site assembly and storage; facilities for vehicle maintenance; access to housing, fuel and food, etc.);
- site-specific costs (e.g. freight shipment rates; the cost of leasing both industrial properties and off-site housing; the cost of construction materials; wage rates for skilled and unskilled labor).

On-site visits themselves have typically been for a period of two to five days depending on the weather encountered. During this period an effort was made to traverse the sites on existing roads wherever possible. No off-road travel was undertaken, and ease of access within any given site remains to be determined. Nearby towns which might provide the goods, services, and housing required by the project have also been visited.

Either by prior arrangement, or when the opportunity arose, meetings were scheduled with interested parties in the government, the scientific community, and in industry (e.g. Joe van Homelen — Woomera Area Administrator, Australia; Hector E. Otheguy — General Manager/CEO INVAP, Argentina). Topics discussed included access to the sites, the capacity of the existing infrastructure, and the possible impact of the detector on the local economy.

Photometric (UBV) observations of selected stars have been undertaken at each site (see Figure [**?**]).

These data, taken in drift-scan mode and throughout a range of zenith angles, yield both the background sky brightness and the apparent magnitude of the star under observation (the absolute magnitude diminished by wavelength-dependent atmospheric absorption and scattering). However, the limited time over which these observations were performed cannot provide a decisive indication of the optical quality of the sites. Nevertheless, these

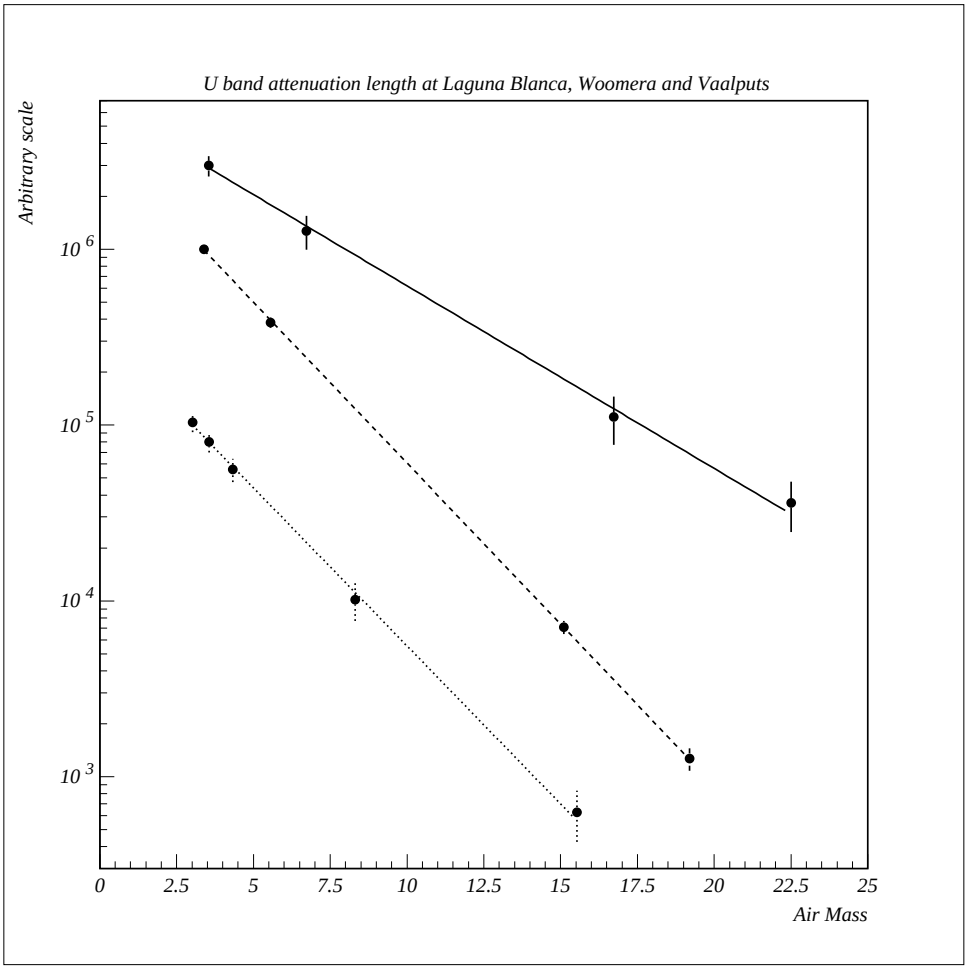

Figure 10.1: Rate vs Air Mass for U band ($\sim$ 365 nanometers) observations at Laguna Blanca (solid line), Vaalputs (dashed line), and Woomera (dotted line). For plotting purposes the data from Vaalputs has been multiplied by 10. The inverse attenuation length is found to be 0.24 $\pm$ 0.02 at Laguna Blanca, 0.42 $\pm$ 0.03 at Vaalputs, and 0.41 $\pm$ 0.03 at Woomera. Results are similar in the V and B bands.

observations do confirm that all of the sites visited to date are suitable from the perspective of having low background sky brightness levels. Analysis of these data is on-going.

Data made available by the "International Satellite Cloud Climatology Project" (ISCCP) provides fractional cloud cover estimates with 280 kilometer spatial resolution and three-hour-monthly averages (i.e. average each month at 00, 03, ... hours UTC, thus retaining sensitivity to diurnal variations). These data, derived from visible and thermal infrared radiances measured by US, European, Japanese, and Indian meteorological satellites, are being used to produce an unbiased estimate of the relative cloud cover at each of the candidate sites. Experience with these data suggests that they significantly over-estimate the cloud cover, at least in regard to clouds which are of concern to the proposed fluorescence detector.

10.4 Argentina

More than half a dozen sites had been identified as possible candidates in Argentina. Due to time constraints, however, only a few had been examined in significant detail prior to the Survey Group's arrival. Of these sites three were selected for further investigation: Laguna Blanca, La Humada, and Monte Coman.

(*Following the Site Survey Group's visit to Argentina it was recommended that "A thorough search be made for the best possible Argentine site — relevant topographic maps reviewed, and likely prospects inspected." Subsequently two additional candidate sites were identified — Nihuil and Somuncura. While a follow-on visit by the Site Survey Group is planned for October 1995, these sites have been carefully reviewed by members of the host institutions and are discussed below.*)

10.4.1 Laguna Blanca:

The village of Laguna Blanca (41.5° S, 65° W, 1000 m.a.s.l.) is north of Jacobacci and approximately 200 kilometers east of San Carlos de Bariloche. It was known *a priori* that the site was restricted in size. However, the area is believed to be representative of much of the Province of Rio Negro in terms of the night sky background and atmospheric clarity. Typically higher and more arid than other Provinces, Rio Negro has the potential for providing a very favorable site (see Somuncura below). On-site observations do indeed confirm that visibility is excellent and the sky extraordinarily dark.

10.4.2 La Humada:

The site near La Humada (36.2° S, 68° W, 750 m.a.s.l.) is 40 kilometers southwest of the small town of Santa Isabel. Santa Isabel, while a major crossroads in the Province of La Pampa, has itself somewhat limited infrastructure (i.e. it is not connected to the national

power grid — electrical power is locally generated).

The La Humada site is more than adequate in size, both level and flat, and at an altitude suitable for the use of any of the detector technologies now under consideration. However, the infrastructure in the area is very limited — no power, water, or telecommunications links exist in or near the site. Access is via a single good quality gravel road. The surface is composed of fine clay soils which are likely to be incompatible with fluorescence or other optical detector. The latter factor, together with the absence of infrastructure, has eliminated La Humada from further consideration.

10.4.3 Monte Coman:

The site (34° S, 67.5° W, 400 m.a.s.l.) is 40 kilometers northeast of the town of Monte Coman and occupies the southern portion of a uniformly flat area of nearly 20,000 square kilometers. Monte Coman is itself 60 kilometers east of San Rafael, one of the principal cities within the Province of Mendoza.

Physical Characteristics

The site is large, level, and with the exception of a few consolidated dunes, extraordinarily flat. The average elevation is 450 meters trending very slightly (0.1%) down towards the east. The surface is composed of compacted sedimentary material mixed with sand. Low vegetation ($\leq$ 2 meters in height) covers much of the area. The Diamante River forms the southern boundary of this extended region while to the east and west the land rises substantially.

Climate

While the area is classified as "arid" the annual precipitation approaches 400 millimeters. Mean monthly rainfall in January (summer) is nearly 70 mm, while in July it falls to 20 mm; the relative humidity is typically 60%. The average nocturnal cloud cover, based on the ISCCP data, is 35% (peaking in July). Temperatures are moderate, averaging 16°C with a mean maximum of 31° and a mean minimum of 1°. The wind speed is low, averaging 8 kilometers per hour.

Infrastructure

Substantial infrastructure is present in the area. The cities of San Rafael (pop 95,000) and San Luis (110,000), and to a lesser degree Monte Coman, provide most of the amenities required by the project. Regular domestic flights connect San Rafael and San Luis to Buenos Aires. Excellent rail and highway access as well as electrical power and water are available

at the site's periphery. A good tarred road crosses its southern edge and dirt tracks exist within the site itself.

10.4.4 Nihuil:

Nihuil (35.2° S, 69.2° W, 1400 m.a.s.l.) was "discovered" during the Site Survey Group's visit to Monte Coman. The site lies near the center of the Province of Mendoza, 80 kilometers west of San Rafael. Malargüe (pop 10,000), which supports the nearby resort of Las Leñas, is near the site's southwestern border. In the western portion of the proposed site some oil exploration and extraction is taking place.

Physical Characteristics

The site is largely circular in shape encompassing an area of 3100 square kilometers and having a mean slope of less than 0.5%. Incorporating regions for which the slope approaches 1.5% increases this area to more than 3400 square kilometers. The mean elevation is 1400 meters. In the western portion of the site a number of small drainages enter the area. Hence, the terrain can be quite irregular on small distance scales. Surface water, though very shallow, may also be present seasonally. The Atuel River crosses the site from west to east forming meanders; it can be traversed at almost any point. Vegetation throughout the area is sparse, nowhere exceeding 50% coverage.

Climate

Like Monte Coman, Nihuil is classified as "arid". However, the annual precipitation is considerably lower, at 280 millimeters, and nearly uniform through the year. The estimated nocturnal cloud cover is similar to Monte Coman (35%, peaking in July at nearly 50%). As expected for the higher elevation, temperatures are cooler. The mean annual temperature is only 12°, mean maximum 20°, and the mean minimum of -2° C; the mean winter temperature is approximately 4° with frost occurring 90 or more days per year.

Infrastructure

Nihuil is serviced by good tarred roads from San Rafael and Malargüe. Both cities can provide most of the necessary support facilities. Several low voltage power distribution lines cross the site and a high voltage transmission line lies along its western border. Water is readily available from the Atuel River and from underground aquifers.

10.4.5 Somuncura:

Somuncura (41.5° S, 67.4° W, 1200 m.a.s.l.) is near the southern border of the Province of Rio Negro and is the most southerly of the proposed Southern Hemisphere sites. Even by Argentine standards Somuncura is remote and sparsely inhabited; settlements which do exist lie on its periphery. Los Menucos, 70 kilometers to the north, lies on Route 23 and the rail line which connects San Carlos de Bariloche to the deep water port at San Antonio Oeste.

Physical Characteristics

The Somuncura Plateau is an extensive basaltic highland totaling nearly 12,000 square kilometers. Elevations extend from 650 to 1350 meters above sea level. The proposed site encompasses 4000 square kilometers at an elevation of 1200 meters and is reported to be extremely level with a few isolated hillocks which are volcanic in origin and typically 100 meters in height.

Climate

Local climatic conditions must be inferred from meteorological stations at some distance from the site. The estimated precipitation is 160 millimeters per year with a cloud cover similar to that observed at Monte Coman and Nihuil. The mean annual temperature is 9°, mean maximum 15°, and the mean minimum 3° C. Frost is observed typically 130 days per year.

Infrastructure

The area is virtually devoid of infrastructure with no electrical power, tarred roads, telecommunications, or other amenities. Serviceable gravel roads connect the site to Los Menuchos. Tracks provide limited access within the site. Underground rain-fed aquifers provide the only available water. In Los Menucos, wells drilled to a depth of 100 meters supply 90 cubic meters per hour while nearby sources produce perhaps one-third this amount.

10.4.6 Conclusion

No doubt exists that Argentina (alone or in concert with other Latin American States) is a strong candidate for the Southern Hemisphere component of the Auger Project. The scientific and industrial communities in Argentina have demonstrated a significant interest in the project and have provided very considerable assistance to the Site Survey Group in its efforts. Several institutions including CNEA (Comision Nacional de Energia Atomica) and INVAP (Investigacion Aplicada S.E.) are actively participating in the development of water

Čerenkov detectors. Finally, the Federal and Provincial governments have expressed strong support for the project.

Nevertheless, as with all the other sites under consideration, reservations remain. Based on the information presently available, all three sites appear to be "geophysically" acceptable (i.e. appropriate size, altitude, etc..). However, in regard to on-site access and atmospheric clarity, their suitability remains to be established. In addition, the infrastructure in some areas is extremely limited, often lacking electrical power, surfaced access roads, and many of the facilities required for construction and operation of the Project.

10.5 South Africa

Only a single site was selected for investigation in South Africa. It is, in several respects, the best of the sites visited to date.

10.5.1 Vaalputs:

The site is in the North Cape Province approximately 300 kilometers north of Cape Town and extends to the north-east from Vaalputs (29.8° S, 18.8° E, 950 m.a.s.l.). Vaalputs is operated by the Atomic Energy Corporation and is home to South Africa's low and intermediate level radioactive waste repository. The facility's primary mission is to receive waste from South Africa's civilian nuclear reactor program, verify the integrity of the casks in which it is transported, and to deposit these in clay-lined pits.

The main building at Vaalputs contains three crane-equipped high bay areas for off-loading waste shipments, a small machine shop, a service bay for heavy vehicle maintenance, and administrative offices. The "Camp", located 8 kilometers from the main building, provides comfortable hotel style accommodation for 35 and includes a large communal kitchen, a lounge, and conference facilities.

Physical Characteristics

The proposed site is roughly rectangular in shape extending 45 kilometers to the east and 85 kilometers to the north of Vaalputs. Deviations from the average elevation are everywhere less than 20 meters and slopes are less than 0.5%. The site is bounded in the east by the Koa Valley depression, a relic drainage which seasonally contains a few flooded pans. To the west the land rises slightly becoming quite uneven; this is the uplifted edge of the South African escarpment. Vegetation over the entire area is limited to grasses and widely scattered low shrubs; the soil is compacted sedimentary material, gravel, and some wind-blown sands.

Climate

Vaalputs maintains an automated meteorological station. Based on these and other records (from Springbok and Pofadder) the annual precipitation is estimated to be less than 40 millimeters per year. The mean annual temperature is 21°, mean maximum 37°, and the mean minimum 10°; temperatures can exceed 40° C in summer. No immediately relevant ground-based cloud cover data is available and the ISCCP data has not yet been examined. However, the atmospheric conditions at Sutherland, an astronomical observatory in the Karoo approximately 150 kilometers south of Vaalputs and sharing much the same weather, rival those of other well known astronomical observatories.

Infrastructure

The infrastructure in South Africa is, in the main, excellent. Even in the sparsely populated North Cape Province tarred roads connect most of the significant communities. To the east of the Koa Valley a heavy rail line connects iron mines in the north-east of the Province with the coast at Saldanha. The site, which is primarily utilized for grazing, is criss-crossed by a network of well-maintained gravel roads (the personnel at Vaalputs commute daily 120 kilometers to Springbok on these roads). Numerous dirt tracks afford access within the grazing lands themselves.

Two power lines, servicing Vaalputs in the sout-west and an air navigation beacon to the north-east, extend some 20 kilometers into the site. Both lines could be economically upgraded to 400 KVA. Other than in the seasonally flooded pans, no surface water exists in the area. However, as part of the preparatory work for the waste disposal facility, staff geologists at the Atomic Energy Corporation have thoroughly investigated the area's geo-hydrology. Substantial quantities of fossil water have been identified at depths of 60 meters at several points within the site. This water is highly mineralized and may require filtering and/or treatment by reverse osmosis.

Much of the economy of the North Cape Province is based on mineral extraction. Springbok provides most of the support required by the surrounding mining communities. Housing, industrial properties, and freight handling facilities are among the numerous services available at Springbok.

10.5.2 Conclusion

With few reservations it can be said that the site at Vaalputs is superior to the others visited to date. Without exception the site meets all of the physical criteria established for site selection. It can be added that South Africa has a technical capacity far more substantial than its size might suggest.

Significant uncertainties remain however. First, the issue of site access must be addressed. The land holders in the area, approximately 100 in number, are by nature an independent group. Some have expressed concerns regarding the impact of the detector's

installation and operation on the fragile grasslands on which they depend. Second, the scientific establishment in South Africa is small; estimated to be 400 in the whole of the country with perhaps a dozen directly involved in astroparticle physics. The impact of the Auger Project will be significant. The scientific community must not only strongly support the Project but also be prepared to assist in its implementation (e.g. liaising with the Federal and Provincial governments, the land holders, and the AEC). Third, it is difficult to envision direct monetary contributions by the South African government. South Africa has only recently emerged from the system of apartheid. Much of its attention in the coming years will be directed to redressing the many inequities which that era engendered. A high level effort seeking to establish alternative sources of funding or "in kind" support must be considered to be a high priority.

10.6 Australia

Australia has a long history of involvement in all aspects of ground based particle astrophysics. In particular, the University of Adelaide until recently operated an air shower array at Buckland Park and continues today to be involved in the design, construction, and operation of several atmospheric Čerenkov detectors at Woomera. Several individuals now at Adelaide have been members of the Fly's Eye collaboration in the past and bring with them a thorough understanding of all aspects of the Auger Project having to do with fluorescence detectors.

10.6.1 Woomera

The site is located in the south-east portion of the Woomera Prohibited Area (WPA; 31.1° S, 136.8° E, 150 m.a.s.l.), north and west of the town of Woomera which is itself 450 kilometers north of Adelaide. The WPA is operated by the Australian Department of Defense whose activities in the area are mainly directed to ammunitions testing. Most of the land, however, is leased for grazing and access is relatively unrestricted.

Physical Characteristics

The site is bounded in the south by seasonally flooded Lake Hart and in the east by uneven terrain and, eventually, Lake Torrens. Topographic maps indicate that a significant fraction of the northern portion of the site is covered by consolidated dunes with heights of 2 to 5 meters. Aerial photos confirm the presence of the dune field. Further, they suggest that the dunes run mostly east-west with level areas interleaved between adjacent dunes. Far to the west, though still within the proposed site, trees with heights up to 4 meters are present. Though not dense, over distances of a kilometer or more they do significantly obscure the line-of-sight.

Though for the most part flat, small pans and associated drainages are present within

the site. These can rapidly flood making access difficult if not impossible. Soils outside the dune fields or pans are principally "gibber". This surface is characterized by myriad small pebbles or stones on top of a fine soil. While wind-blown dust is not a concern, mobility over the surface following any significant rainfall is reported to be extremely difficult.

Climate

In a climatic sense Woomera is midway between the coastal zone and the continental interior. Temperatures are moderate with a mean annual temperature of 21°, and mean maximum and minimum temperatures of 32° and 8° C respectively. Rainfall annually averages 140 millimeters. The University of Adelaide has initiated a sophisticated program of atmospheric monitoring using a technique similar to that used by the Site Survey Group. Results are not yet available.

Infrastructure

At present Woomera has 1300 inhabitants. In the past the population has been as high as 5000 and the facilities are commensurate with that number. Electrical power, potable water, housing, and industrial space are all readily available. The Stuart Highway and a railway connect Woomera to Adelaide and ports on the Spencer Gulf. Pimba, just to the south of Woomera, has a rail spur and unloading facilities.

Woomera's infrastructure extends well into the site itself. Power, water, and communications are present at "Range E" 45 kilometers northwest of Woomera, at "Range G", site of Adelaide's Čerenkov telescopes, and at the so-called "Stack Frag" facility. A number of surfaced and gravel roads pass through the site.

10.6.2 Conclusion

Woomera's comprehensive infrastructure is one of its outstanding features; no other site provides such a wide array of facilities. (They are in most respects superior to those at Dugway, Utah.) Of equal importance is the presence at the University of Adelaide of an experienced group of researchers who are familiar not only with the field but also with the working environment at Woomera.

The principal difficulty at Woomera has to do with the array's line-of-sight requirement for data acquisition and control. Both the dunes in the north and the substantially vegetated area to the west *may* present a significant impediment to array communications. A radio propagation survey is planned for the area in the near future to investigate this issue.

The Stack Frag facility is also of some concern. Stack Frag is designed to investigate the safety of munitions storage bunkers. This work entails the detonation of up to 75 tons of high explosive at a point very near the center of the proposed site. The blast overpressure, estimated to be 1 kilopascal at 12 kilometers, would probably not be compatible with the

fluorescence component of the Auger Project. A more thorough study of this issue and its impact on the configuration of the detector must be undertaken.

10.7 Future Site Survey Efforts

Once the initial phase of the Site Survey effort is completed, and after a preliminary siting decision has been made, emphasis must turn toward a more intensive examination of the selected sites. These investigations include:

- long term comprehensive observations of the atmospheric conditions at each site;
- a detailed review of the existing infrastructure and costs needed to meet the project's requirements.
- analysis of site access issues, both in gaining tenure to the sites and in regard to physical access to and within the site.

These efforts will demand even greater cooperation from the host community and a more thorough understanding of the project's requirements.

Chapter 11

Central Station

In this short chapter we describe a model for the central station which we have used primarily to estimate costs. The estimated costs will be brought together with those of the detectors in the next chapter.

11.1 Central Station

We include in the Central Station a building containing office space and the central data acquisition system, a dormitory building and a shed to store material and assemble the detectors on the site. We assumed that the station should be able to house (office space and bedrooms) up to 10 people. Since the buildings are modular, the cost can easily be updated if other scenarios are envisaged. We include here the estimates of the civil-engineering and general equipment (details of the scientific equipment are given in the corresponding chapters).

11.1.1 The Office Building

We took as the basis of our proposal a barrack-type building of good quality available from a French firm. It has a total surface area of 153 m^2 obtained by using four identical modules each consisting of two office rooms, plus one specific module containing sanitary equipment and a kitchenette. The walls separating the individual office rooms can be suppressed to make larger rooms. Our proposal is to have 5 office rooms (including the kitchenette) and use the remaining space to install the data acquisition system and an electronics workshop. The office modules are 3 m wide, 10 m long (including a corridor separating the two face-to-face office rooms) and they can be added to or removed from the configuration we propose.

The building and equipment include all necessary comfort : thermal and acoustic insulation of roof and exterior walls, heating with thermostatically controlled electrical convection heaters, sanitary equipment, etc. The total cost given includes transport, labor and instal-

lation. The labor part of the cost would be around 25%. The furniture is included.

Four office rooms will be configured to contain the data acquisition system, terminal room and an electronics workshop. The latter would occupy the equivalent of one office room, and be equipped with standard laboratory instruments such as oscilloscopes, power supplies and pulse generators. A space equivalent to three offices would be devoted to the data acquisition system equipment and terminal rooms. The servers and electronic crates may be separated from the rest by an insulated partition wall to make a small air-conditioned room of about $10m^2$. The air-conditioning clearly depends very much on the local climatic conditions. We were given upper and lower limits for the cost on the basis of 15 m^2 office space. We foresee much more powerful air-conditioning for the small room housing the electronics crates and the servers.

The fire safety installation consists of a general alarm (that can be computer monitored) and two extinguishers for each of the three buildings. A 200 kVA uninterruptable power supply will provide clean power to the electronics.

11.1.2 The Dormitory

The dormitory building is also modular and consists of 6 modules of 3×11.2 m^2, out of which five are pairs of rooms (hence a total of ten bedrooms) and one provides space for two rooms : one is a kitchen and the other may be used as a laundry. The building is delivered with the following equipment included (apart from those mentioned for the office building) : 1500 W thermostatically controlled convection heaters, sanitary facilities (showers, WC in all bedrooms), water heater and equipped kitchenette. The total cost includes transportation and installation.

11.1.3 The Shed

The shed has a surface of 680 m^2 to house an assembly area for the detectors before they are transported to the assigned local station position. The (included) thermal insulation of the shed (if needed) represents 30% of the cost. There is a rather complete mechanical workshop inside the shed.

11.2 Civil Engineering

This is the strongly site and country dependent part. To have a realistic cost estimate, we asked (through the Civil Engineering Department of the French National Research Council, CNRS) a few firms to work on the following scenario. We need to bring electricity, telephone lines, water and a road to the central station. The distance over which all these items are required is 35 km, roughly that from the border of the array to the center. It is not excluded that the facilities are accessible much closer to the central station, so the cost estimates on

Equipment	Cost (k$)
Deployment and engines	424
Office building	375
Dormitory building	285
Shed/Assembly area	413
Roads	4359
Electrical and telephone lines	5213
Water	611
EDIA for access to site	1175
DAS (without Fly's Eye) and networks	276
Total	13131

Table 11.1: Central station and DAS overall cost estimates (per site).

those items should be considered as very indicative. The ground is supposed to be flat and easy to dig. No rocks or other hard-to-cross obstacles are to be removed. There are no construction works such as bridges, tunnels or viaducts. All raw materials are assumed to be close to the site, so that no transportation cost is included.

On the site itself, the civil engineering work comprises the concrete slabs for the three buildings (including parking places) and the sewers. The slab for the shed is thick enough to stand heavy loads (trucks). The others are thinner. The labor is estimated at approximately 50% of the total cost.

The road is 35 km long and 3.5 m wide with an asphalt surface. Every 2 km a 40m$\times$4m crossover area is installed. The work includes the clearing of the ground, earth moving (embankments, hard core) and digging two lateral ditches (one of them containing the pipework for water and cableways for electricity and telephone). The asphalt surface lies on foundations.

Both electricity and telephone are transported between two main stations 35 km apart. In each case, three substations relay the lines. The main cost ($100/m, i.e. 87% of the total) comes from the electrical cables. Installing underground cables (the situation envisaged here because of environmental impact issues) is much more expensive than aerial cables on poles. Depending of the site, the latter solution, if used, brings substantial economies on this item.

The cold water is transported over the 35 km through 3 pumping sub-stations.

We again wish to emphasize the uncertainty resulting from attempting to evaluate civil engineering costs without having selected the sites to be used. For example, the road may not need to be paved or the power lines put underground at some sites; the materials for road work may have to be brought in from a considerable distance for some sites, and water and sewer could be readily available at the central station or could be a difficult problem. The civil engineering costs will be re-evaluated when specific site information is available.

Chapter 12

Cost, Schedule and Organization

A cost estimate and a set of schedule milestones have been prepared for the Auger Project. As the R&D program proceeds and details of the design are refined, the cost estimate will become more precise. At the same time, the funding profile and availability of resources will determine the details of the schedule.

12.1 Cost Estimate

The cost estimate was constructed using a variation of Work Breakdown Structure (WBS) now in common use in the U.S. It is a "bottoms-up" estimate in which an attempt is made to identify in detail all components, materials, services, and labor for the construction and installation of the project. The basic units for the cost estimate are mirror units for the fluorescence detector and detector stations (tanks) for the surface array. The materials, labor, and EDIA (engineering, design, inspection, and administration) are detailed for each unit. Standard labor rates are used. Contingencies are applied to each line of the cost estimate according to a graded scale of the quality of the estimate. A set of simplified contingency assignments was used for this estimate.

Basis of estimate	Contingency
Vendor Quote	10%
Vendor Information	20%
Engineering Estimate	30%
Physicist Estimate	$\geq$50%

The cost estimate does not include the labor, support, or travel expenses for the physicists or post docs. These costs are assumed to be covered by the collaborating institutions.

12.1.1 Detector Specification

The detector specifications used for the cost estimate are as follows:

- Fluorescence Detector
  1. One fluorescence detector per site
  2. 48 mirror stations per site
  3. 225 pixels (PMTs) per mirror station
- Surface Detector
  1. 1657 detector stations per site
  2. 1.5 km station spacing
  3. Water Čerenkov detector tanks
  4. Tank dimensions: 1.2 m deep, 3.66 m in diameter
  5. Three 20.3 cm (8") photomultiplier tubes per tank
  6. Power supplied by solar panels
  7. Flat trigger and communication

Details of all these elements can be found in Chapters 6 through 9 and will not be repeated here.

12.1.2 Central station

Most of the costs given in the WBS tables are quite well defined. The part concerning the infrastructure of the central station and the operating and maintenance costs can only be estimated on the basis of assumptions about the two final sites to be chosen. Chapter 11 details the assumptions which result in the figures given in the tables. Some of these parameters (e.g. the DAS equipment) are described elsewhere and we shall not mention them in this section.

12.1.3 Summary of the Cost Estimate

A summary of the construction cost estimate (excluding operating costs), is shown in Figure 13.1. In order to keep the total project cost below $100M US, the area of each detector was set at 3000 square kilometers (1.5 km station spacing). The nature of the detector allows some flexibility. If the estimated cost per surface detector station changes, the total detector area can be increased or decreased as necessary. Fortunately, no exotic technologies are involved, so that once the site is chosen the cost estimate will converge quickly.

It should be noted that the cost estimate is sensitive to features of the site. The cost estimate includes over \$10 M for road and power access, but that will depend on the site. Access roads and power may already exist. The cost estimate also assumes that the site can be negotiated by commercial off-road vehicles carrying detector components and heavy loads of water.

The project management support, including project engineer, cost and schedule, quality assurance and administrative persons are assumed to constitute full-time professional staff during the period of construction and commissioning.

12.1.4 Operating Costs

To estimate the operating costs, we make the following assumptions :

- There will be two sites of about 3000 km^2 with 1548 stations per site ;
- The project will operate for 20 years ;
- The surface detector is based on water Čerenkov tanks of carbon steel construction similar to the prototypes tested at Fermilab, which require repainting every 10 years ;
- The electronics and communication system require 10 W of solar power at each station, and the batteries need to be replaced every 6-7 years ;
- A paved road to the central station, and a network of 150 km of unpaved roads will be maintained, although traffic will be minimal and road quality marginal ;
- A set of pathways providing access to each surface detector station will be required, but the effort to maintain them is completely site-dependent.

Site personnel costs

We assume that site maintenance and operations will need a number of permanent staff. These include a site manager, an administrative clerk, three electronics and three electro-mechanical technicians. The Auger detector is comparable to an observatory, hence the presence of three MS-level physicists as "observers". On average, two technicians and one physicist will be required by the fluorescence detector and the remainder will be required by the surface detector systems. A computer professional is foreseen for the maintenance of the sophisticated computer system for both the array and the fluorescence detector. A crew of two people will be required to maintain the roads, pathways, and grounds at the site. Finally a maid service is necessary for the housing facilities. Table 12.1 presents the cost estimates for the salaries of these personnel.

Personnel	Annual salaries (k$)
Site manager	150
Administrative clerk	60
Technicians	420
Physicist "observers"	300
Computer engineer	100
Road Maintenance Crew	130
Maid service	50
Total	1210

Table 12.1: Annual personnel costs for operations (per site)

Task	Cost (k$)
Battery replacement	91
Water tank repainting	75
Upgrade stations	15
Facilities maintenance	20
Road maintenance	50
Vehicles	46
Utilities	47
General materials and services	500
Total	844

Table 12.2: Annual task-specific operation costs (per site).

Task-specific operation costs

The following assumptions are used here. The solar batteries will all be replaced twice during the 20 year operating period. The water tanks will have to be repainted once during their lifetime. All stations will have to be upgraded once for a cost of $200 per station.

The figure given for the road maintenance is site-dependent and therefore highly uncertain. The site will be equipped with five vehicles. The maintenance cost assumes 200 miles per day per vehicle, one of which will be replaced on average every year. To the current utilities (electric power, water, sewers) we add $500K per year for general maintenance and services, of which $200K per year is allocated to the fluorescence detector and the remainder to the overall facility and the surface detectors. This is summarized in table 12.2.

Physics running costs

The project will be run by physicists from many institutions supported only partly by educational funds. For example, professors' salaries for the academic year are covered, but the salaries of research professors or associates, post-docs, graduate students as well as summer

Item	Cost (k$)
Personnel	1210
Task-specific/M&S	844
Total	2054

Table 12.3: Summary of the annual operating costs (per site).

salaries of professors from some countries are expected to come from research grants in some countries including the USA. One can expect even small institutions to have one post-doc, one student and two senior physicists' summer salaries and/or travel expenses and *per diem* to cover. To this one should add at least one technician and some software and hardware costs at the home institutions. The way such expenses are covered or included in the operating costs depends very much on the country. These costs have not been included in this report.

Table 12.3 is a summary of the overall operating costs per site and per year. If the site location is extremely remote, one would have to increase these expenses by amounts corresponding to the transportation of workers to the site and probably to some *per diem*.

12.2 Schedule and Milestones

A tentative schedule with major milestones is shown in Figure 13.2. It is assumed that funds can be raised in two years concurrent with the R&D program. The production of detector components would begin in mid 1997 with installation complete in 2001.

12.3 Project Organization

12.3.1 Overview

This project is a broadly-based international endeavor to design, build, operate, and analyze data from two giant cosmic ray detectors. The two detectors, in the Northern and Southern Hemispheres, are to be built and operated as one project. The diverse nature of the collaborators and the disparate location of the detectors require that a clear management structure be developed to build and operate these detectors. Close cooperation of groups from many parts of the world obtaining funding via different arrangements must be maintained for the project to meet its objectives.

12.3.2 Organization

The organization of the Auger Project is shown in Figure 13.3. The Collaboration Board is the primary governing body of the collaboration. The scientific and technical direction of the project is invested in the Spokesperson by the Collaboration Board. The Project Manager is responsible for building and operating the experiment. The Project Manager is supported by a staff consisting of engineering, budget, and administrative personnel and by the Technical Board. Each site has a local manager that directs construction and operations at the two sites. Five task leaders are responsible for the major components of the detectors, central station, electronics, and data acquisition.

Auger Project
Cost Estimate 10/2/95

W.B.S		Total	Total	Total	Total	Total	Total
	WBS Name	M&S	Labor	EDIA	Cont.	Site	Project
		K$	K$	K$	K$	K$	K$
	COMPLETE PROJECT	33,946.1	2,445.4	3,716.7	8,654.2	48,762.3	99,924.5
1.0	FLUORESCENCE DETECTOR	6,258.4	500.6	990.0	775.9	8,524.9	17,049.8
1.1	Detector System	5808.0	483.8	800.0	726.0	7817.8	
1.2	Calibration System	108.4	16.0	75.0	15.6	215.0	
1.3	Atmospheric Monitor	192.0	.8	100.0	19.3	312.1	
1.4	Power Distribution	100.0	.0	10.0	10.0	120.0	
1.5	Central Computer Facility	50.0	.0	5.0	5.0	60.0	
2.0	SURFACE DETECTORS	18,509.9	1,944.2	1,350.0	5,303.2	27,107.3	54,214.7
2.1	Detector System	6133.8	198.8	450.0	1264.5	8047.1	
2.2	Readout	5120.1	273.4	160.0	949.9	6503.4	
2.3	Electronics	3690.1	580.0	540.0	1510.3	6320.4	
2.4	Solar Power System	1826.0	207.1	100.0	316.2	2449.3	
2.5	Shipping (to site)	1657.0		100.0	878.5	2635.5	
2.6	Deployment	82.9	684.9	0.0	383.9	1,151.6	
3.0	CENTRAL STATION	9,177.7	0.5	1,376.7	2,575.1	13,130.0	26,260.0
3.1	Office Building	630.4	0.5	94.6	73.8	799.2	
3.2	Housing	219.7	0.0	32.9	31.8	284.5	
3.3	Assembly Area/Shop	294.1	0.0	44.1	74.3	412.5	
3.4	Access to Site	7,833.0	0.0	1,175.0	2,349.9	11,357.9	
3.5	Data Acquisition	128.5	0.0	19.3	36.4	184.1	
3.6	Telecommunications	8.8	0.0	1.3	2.6	12.8	
3.7	Acquisition Hardware	59.5	0.0	8.9	6.0	74.4	
3.8	Office Equipment	3.8	0.0	0.6	0.4	4.8	
4.0	PROJECT MANAGEMENT	500.0	1,900.0				2,400.0
4.1	Personnel		1,900.0				
4.2	M&S	500.0					

Figure 12.1: Summary of the Cost Estimate.

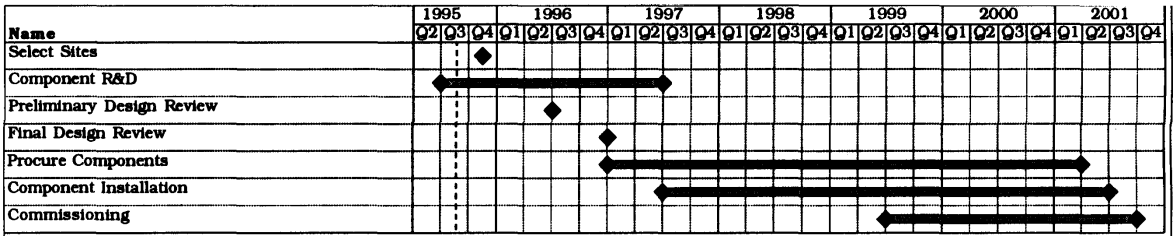

Figure 12.2: Pierre Auger Project Schedule.

A description of the duties and responsibilities of each part of the organization follows:

Spokesperson: The Auger Project Spokesperson is elected by the Collaboration and is representative of the Collaboration in scientific, technical, and management concerns, and speaks and negotiates on behalf of the Collaboration. The Spokesperson is responsible for establishing the scientific goals and the means for the Collaboration to pursue these goals successfully. He or she is also expected to pursue the identification of resources needed by the Auger Project and to seek the commitment of such resources toward the development and construction of the project. These resources come from the scientific groups and institutions who collaborate in the Auger Project, as well as their various sources of funding for that purpose. The Spokesperson serves a renewable three-year term.

Site Spokespersons: Each site will have a designated site spokesperson. The site spokesperson will be a member of the collaboration. He or she will act as liaison between the Project Spokesperson and the host country.

Project Manager: The Project Manager is responsible for the design and fabrication of the detectors. The Project Manager defines and carries out project tasks, and is responsible for meeting cost, performance, and schedule goals for the project. The Project Manager is responsible for managing the Auger Project technical efforts set forth in Memoranda of Understanding (MOUs) with Auger Project institutions.

Collaboration Board: The Collaboration Board, whose membership consists of one representative selected by each collaborating institution, deals with issues which concern the Collaboration as a whole. These include the governance of the Collaboration, the policy on admission of new members and institutions, and publication policy.

Technical Board: The Technical Board consists of scientists and engineers involved in leadership roles in the various technical areas of the Auger Project. The members of the Technical Board are task leaders and others appointed by the Spokesperson and the Project Manager. The Technical Board is chaired by the Project Manager. The Technical Board reviews and makes recommendations to the Spokesperson and the Project Manager on all major technical decisions relevant to the Auger Project.

Cost and Schedule: The cost and schedule officer is responsible for budget (WBS) and schedule development and tracking. He or she assists the Project Manager in developing contracts and Memoranda of Understanding for Auger Project tasks.

Systems Engineering and Integration: The Project Engineer is responsible for technical requirements and the engineering quality of the technical design. He or she maintains drawings, documents, and configuration control to assure effective technical interface among participating institutions, vendors, and task leaders.

Quality Assurance: The Quality Assurance Officer develops and maintains a Quality Assurance Program that will ensure the performance and reliability of the detector system. He or she will assist the Project Engineer in developing production quality control travelers and shop procedures for production of detector components.

Site Managers: The Site Manager is responsible for operations at the site both during

construction and later during data taking.

12.3.3 Management Documents

The following documents will be the basis for the construction and operation of the Auger Project.

1. Design Report
2. Performance Requirements and Technical Specifications
3. Controlled Set of Engineering Drawings
4. Project Management Plan
5. Quality Assurance Plan
6. Cost Estimate (Work Breakdown Structure)
7. Integrated Project Schedule
8. Operations Plan

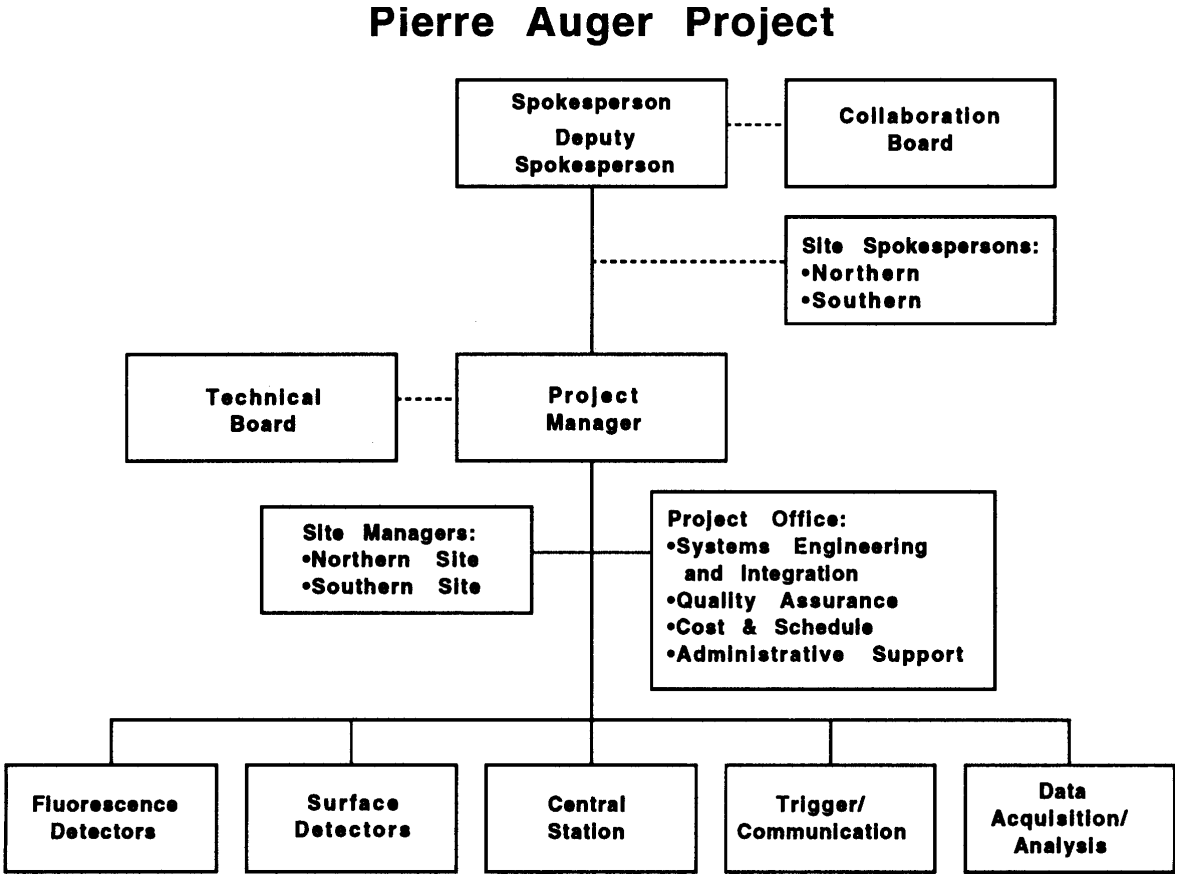

Figure 12.3: Pierre Auger Project Organization Chart.

Appendix A

Air Čerenkov Detection of Cosmic Rays with Solar Panels or PMTs

A.1 Air Čerenkov Detectors

The strongest signal generated by an Extensive Air Shower (EAS) in the atmosphere is the Čerenkov light emitted by charged particles. This signal is 3 to 7 orders of magnitude (in terms of particles per m^2) larger than the ground level particle flux or the nitrogen fluorescence signal. The large range in the above ratio results from the very different angular and spatial distributions of the different signals. Observations of EAS using atmospheric Čerenkov light have in the past used large mirrors to collect the light onto photomultipliers, as in the "Whipple Telescope". Such observations have only been possible on dark moonless lights or, recently, with a crescent moon out of the field of view. However for the much brighter showers of EeV cosmic rays the situation should change dramatically. The extremely bright Čerenkov light should be detectable by simple detectors, and we shall discuss both photomultipliers and solar cells, just looking at the sky. This was not a useful technique in the past because of S/N considerations, but for 10^{20} eV showers Silicon solar panels (of the type known as CZ-Si) can be expected to have a S/N of about 10. The dominant noise is electronic rather than fluctuations in the background light. Noise levels have been measured in the lab, and the Čerenkov signal can be reliably calculated.

One unusual property is the sheer magnitude of the Čerenkov light yield. A 100 EeV shower is brighter than fluctuations in the direct daytime sun over the Čerenkov light emission time scale, even when observed several kilometers from the shower axis! This extraordinary intensity allows one to observe 100 EeV cosmic rays optically during observation conditions with new moon, full moon, dusk, dawn, and possibly during the daytime. This capability overcomes the typical 10%-15% duty cycle limitation of other optical (nitrogen fluorescence) detection techniques.

An interesting consequence of the high Čerenkov photon flux is the possibility of using low cost silicon detectors to observe the signal. A 10^{20} eV cosmic ray shower creates a

Čerenkov signal strong enough to generate a milliamp current pulse in a large (1 m^2) solar panel, even when the solar panel is hundreds of meters away from the core of the EAS. Such large current pulses can be detected with existing low cost commercial electronics. An added benefit of using solar panels to detect the Čerenkov light is the possibility of using them for power generation during full daylight, and for Čerenkov light detection at other times. This 'dual-use' of the panels may allow the construction of a solar panel Čerenkov array detector at a cost of less than \$5k/station (stand-alone), or about \$2k/station (as an add-on to the Auger particle detector array).

The use of silicon solar panels gives the Air Čerenkov detector the ability to detect Čerenkov light at long wavelengths (600-1000 nm), where Rayleigh scattering and atmospheric attenuation are small. This allows detection of cosmic rays at substantially larger zenith angles than the particle array, possibly up to 80-85°. One may be able to use this steep angle detection capability to look for astrophysical sources of high energy neutrinos. The longer wavelength detection bandwidth, compared with the fluorescence detection, also gives less sensitivity to atmospheric conditions.

The narrow 'beamed' nature of the Čerenkov light provides a novel method for reconstructing the direction of the primary cosmic ray. Multiple solar panels are used at a single site to observe different hemispheres of the sky. The beamed light will illuminate the panels with different amounts of light, depending upon their orientation with respect to the incoming light beam. The panel amplitudes can therefore be used to reconstruct the original Čerenkov light and cosmic ray direction with an accuracy we estimate to be of order 1°, similar to or better than the surface particle detector array.

Perhaps the most important attribute of Čerenkov light is its usefulness in energy determination. Čerenkov light provides a direct calorimetric measurement of the total energy of the EAS. The expected energy resolution is expected to be 10%-35%, depending upon the zenith angle of the primary. The Čerenkov light lateral distribution also possesses information about the depth of the shower maximum (X_{max}), and hence may provide information on the cosmic ray primary composition.

In this appendix we describe some of the capabilities of a 'strawman' design for an air Čerenkov detector for the Auger project. The detector can easily be added on to the water Čerenkov particle detector array, as the mechanical and power requirements of the solar panel station are minimal. From our Monte Carlo simulations of this strawman design, we demonstrate that a solar panel air Čerenkov detector can provide a substantial increase in the detection capability of the full Auger project.

It is impossible to describe fully the Čerenkov array concept and design considerations in this paper due to space limitations. Instead, we will focus on the the most pertinent factors in the design of this detector. A full description of the concept of observation of 100 EeV cosmic rays with Čerenkov light and solar panels has been described elsewhere [79]. A paper providing full details of the design considerations and event reconstruction for a stand-alone solar panel Čerenkov array is in preparation[80].

A.2 Key Design Considerations

A.2.1 Signal and Noise levels

The Signal-to-Noise (S/N) ratio is the key parameter in determining the precision of measurements of the cosmic ray direction, energy, and composition. Figure A.1 shows the S/N ratio divided by the energy of the Čerenkov signal as a function of zenith angle, energy, and various background sky light conditions. This plot assumes a proton primary, a 5 μs integration of a 0.8 m^2 solar panel, and a 1 km perpendicular distance from the shower axis at ground level. The figure uses the calculated Čerenkov light spectra, and the known solar and lunar light spectra multiplied by the wavelength-dependent quantum efficiency of the solar panel integrated between 300 and 1200 nm. A realistic atmospheric transmission model (wind-driven aerosol) is used in the calculation of the Čerenkov light spectrum.

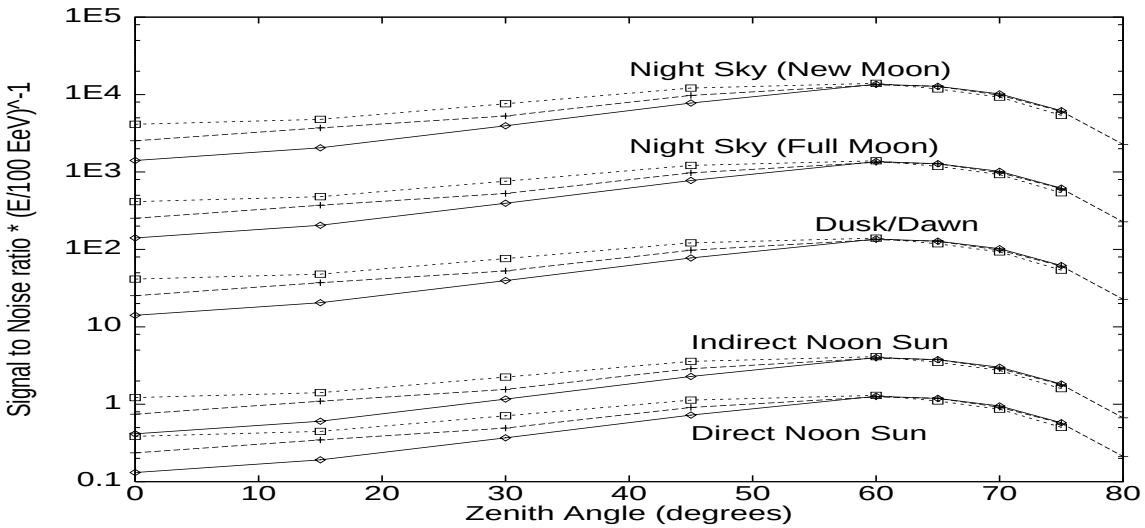

Figure A.1: Signal and Noise for Solar Panel detector at 1 km perpendicular distance from the shower axis as a function of zenith angle, primary energy, and various sky conditions. Primary Energies: Solid Lines with diamonds : 1000 EeV; Long Dash with Crosses: 100 EeV; Short Dashes with Boxes: 10 EeV. Horizontal Axis: Zenith angle (degrees); Vertical Axis: Energy scaled Signal-to-Noise ratio $S/N \times (\mathrm{E}/100\ \mathrm{EeV})^{-1}$.

For nearly vertical showers, S/N does not scale with energy. It rises more slowly than a linear increase with energy because at these energies vertical EAS strike the ground near their X_{max}, resulting in a loss of Čerenkov light from electrons which normally would radiate light at steeper zenith angles. Higher energy events have deeper X_{max}, and therefore as the energy increases a larger percentage of the shower energy is lost into the ground, resulting in a suppression of the available Čerenkov light.

Throughout the remainder of this appendix the above figure can be consulted to relate the S/N to the cosmic ray primary energy and sky conditions.

A.2.2 Rejection of Airplane and Lightning Backgrounds

An additional design constraint for optical cosmic ray detectors is the need to eliminate false triggers due to airplanes, lightning and other artificial sources of light pulses. These backgrounds have several features which distinguish them from cosmic ray generated Čerenkov light. Some of the characteristics which can be used include periodicity, pulse width, lateral distribution, and wavefront timing. These constraints provide sufficient redundant measurements to reject unambiguously these background events[79]. To exploit these constraints, the electronics data acquisition system needs to provide a waveform digitization of each pulse, with approximately 100 nsec time slice, and about 5 msec duration.

A.2.3 PMTs vs. Solar Panels

We believe there are two possible choices for the optical detector for the air Čerenkov array: photomultiplier tubes (PMTs) and solar cell panels. PMTs can be used if the gain of the PMT is reduced to 10-50 by disabling all but the first few dynodes. This has been successfully demonstrated[81]. Large (0.8 m^2) panels of single crystal CZ-Si solar panels are another possibility for the optical detection element. Initial tests with large solar panels have indicated the capability to detect 800 nsec wide pulses of $< 10^8$ photons. Theoretically, pulses of 10^6 photons with microsecond pulse widths should be easily detectable.

There is a trade-off between detector area and quantum efficiency with signal gain which makes solar panels advantageous in some situations, and PMTs advantageous in others. Consider the 'ratio of the S/N ratios' for silicon solar panels and PMTs. The S/N ratio for the solar panel is

$$(S/N)_{panel} \propto (\frac{A_{panel}}{\Delta t_{panel}})^{1/2} \frac{\int \frac{dN_{ch}(\lambda)}{d\lambda} qe_{panel}(\lambda) d\lambda}{\int \frac{dN_{sky}(\lambda)}{d\lambda} qe_{panel}(\lambda) d\lambda}$$

Here A_{panel} is the panel area, $qe_{panel}(\lambda)$ is the wavelength dependent quantum efficiency of the panel, Δt_{panel} is the optimal integration time for the photon pulse, $\frac{dN_{ch}(\lambda)}{d\lambda}$ is the Čerenkov photon flux, and $\frac{dN_{sky}(\lambda)}{d\lambda}$ is the sky background photon flux. For the PMT, the expressions will be similar, except the PMT has an area A_{pmt}, a quantum efficiency $qe_{pmt}(\lambda)$ and a different optimal integration time window Δt_{pmt}. The PMT also has a gain G which enters as a factor of G in the signal, and a factor of $\sqrt{G}$ in the noise.

The ratio of the solar panel S/N ratio to the PMT S/N ratio is therefore

$$\frac{(S/N)_{panel}}{(S/N)_{pmt}} = (\frac{A_{panel}\Delta t_{pmt}}{A_{pmt} G \Delta t_{panel}})^{1/2} \frac{\int \frac{dN_{ch}(\lambda)}{d\lambda} qe_{panel}(\lambda) d\lambda}{\int \frac{dN_{ch}(\lambda)}{d\lambda} qe_{pmt}(\lambda) d\lambda} \frac{\int \frac{dN_{sky}(\lambda)}{d\lambda} qe_{pmt}(\lambda) d\lambda}{\int \frac{dN_{sky}(\lambda)}{d\lambda} qe_{panel}(\lambda) d\lambda}$$

Typically, the average PMT quantum efficiency integrated over the background sky spectrum or the Čerenkov light spectrum is 10%, whereas the solar panel average quantum efficiency is about 60%. If $A_{panel} = 0.8m^2$ and we assume a 5 in diameter PMT ($A_{pmt} =$

$0.0126m^2$), the equation reduces to

$$\frac{(S/N)_{panel}}{(S/N)_{pmt}} = 19.5(\frac{\Delta t_{pmt}}{G\Delta t_{panel}})^{1/2}$$

For the solar panel , Δt_{panel} is dominated by the impulse response of the solar panel and its associated electronics. The typical optimal value is 5 μs. Since the PMT rise time is fast, Δt_{pmt} is determined by the width of the Čerenkov light wavefront. Table A.1 lists the optimal integration widths and also the ratio of ratios as functions of the radial distance from the shower axis.

Distance (km)	Δt_{panel} (nsec)	$\frac{(S/N)_{panel}}{(S/N)_{pmt}}$ $(1/G)^{1/2}$	Gain G
0.5	163	3.5	12
0.7	288	4.7	22
1.0	467	6.0	36
1.4	808	7.8	61
2.0	1484	10.6	112
2.8	3310	15.9	252

Table A.1: Ratio of S/N ratios for solar panel and PMT optical detectors. G is the necessary PMT gain for the PMT to have the same S/N ratio as the solar panel at the specified radius.

Since most of the stations which detect the Čerenkov light will be at a distance of 2-3 km, one would probably want to run the PMTs at a gain of 200-300 just to have the same S/N ratio as the solar panel. If one wanted to use the PMT gain to increase the S/N ratio substantially, one would need to run the PMT at a gain of 500-1000. This would require using more than just the first few dynodes of the PMT. Since other types of optimal detectors (PIN and avalanche photodiodes) have smaller areas and lower gains than this, one would not consider these devices to be useful for the air Čerenkov application.

A.3 Design and Performance

Based upon the considerations of the previous section we have designed amd simulated a strawman air Čerenkov detector. We have chosen solar panels as the baseline design because of their simplicity, their ability to record Čerenkov light from steep zenith angle showers, and the fact that the PMTs would probably have to be run at a gain of 1000 or more, which could lead to difficulties with linearity and long term stability. A PMT-based Čerenkov detector would operate in a similar manner, and would probably meet the solar panel performance.

A.3.1 Detector Station Description

Optimization of Solar Panel Quantity and Orientations

In order to keep the air Čerenkov detector costs to a minimum, we optimize the number of panels and their orientations to yield the best reconstruction of the Čerenkov light direction and amplitude at a given station.

Stations with 4, 5, 6, 7, and 8 panels were investigated with various panel orientations. The optimum minimal panel configuration consisted of six panels, with one panel horizontal and five detectors oriented at a 60° tilt to the vertical, spaced evenly in 72° increments. This is referred to as a (1+5) panel design with (0°, 60°) panel orientation.

Mechanical Attachment

The heavy mass of the water Čerenkov detector makes an ideal anchor for the solar panel detector (Figure A.2). We anticipate attaching the solar panels to the outside of the water Čerenkov tanks using lightweight steel supports.

Data Acquisition System

Figure A.3 illustrates the general design of the solar panel data acquisition system. The system consist of six solar panels, each of which feeds its own AC-coupled transformer system allowing pickoff of the pulsed signal without disturbing the DC current path for the panel. The output of the transformer is connected to a high gain charge-sensitive preamplifier. The output of each preamp feeds into a FADC data recording system,which records the AC pulse amplitude in 100 nsec bins. The FADC output feeds into a deep buffer ($> 64K$ deep) which allows the pulse shape to be recorded, for up to 6 msec.

A central processor continually reads the aligned buffer memory from each panel and forms a coincident sum. This summed waveform is then examined using a moving boxcar averager, and if the integrated area under the boxcar exceeds a dynamic threshold the event forms a trigger. The data from each of the six panels are then read into a secondary buffer. The time of the crossing over threshold is recorded for the summed data stream.

The trigger bit is sent to the water Čerenkov triggering system and communicated to the adjacent detectors to see if they have also been triggered by a light pulse. If several stations have triggered within a predefined time window, all triggering events are instructed to forward the data for the event back to the central station. We anticipate that the air Čerenkov system will trigger itself, or that it will be triggered by the water Čerenkov detector. In this manner, we expect that the air Čerenkov system will impose little burden on the water Čerenkov system.

Typical data sizes per event are expected to be about 100 bytes, and individual station alert rates should be on the order of 0.5 Hz (based upon laboratory studies of the panel noise

Figure A.2: Solar panel detector physical design. Individual solar panels are mounted on the water Čerenkov tank using rigid steel frames.

level in a dark box). A trigger requiring 3 nearest neighbors (in a 6-nearest-neighbor system) to trigger within 100 μs would give a station triggering rate of 0.0014 Hz, and an average data rate of 500 bytes per hour. This data rate is very small compared to the expected data rate for the water Čerenkov detector, and should easily be accommodated by the envisioned communications and triggering system for the water Čerenkov detector.

A.3.2 Expected Performance

We have simulated the performance of a large array of solar panel detectors to examine the angular, energy, and X_{max} resolutions as functions of primary energy and S/N ratio.

The simulated detector consists of 1089 stations arranged in a hexagonal close-packed

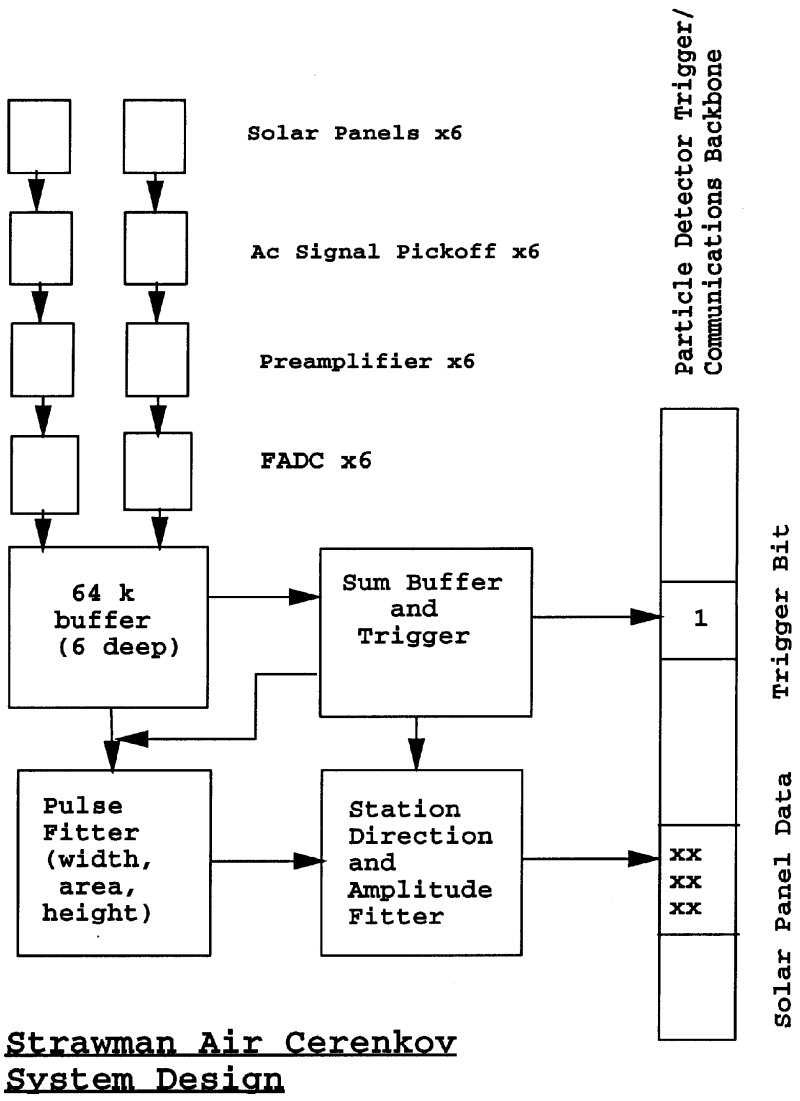

Figure A.3: Strawman Data Acquisition System

array on a flat plane. The detector is assumed to be located at an altitude of 50m above sea level (1030 g cm^{-2}), similar to the Woomera, Australia site altitude. The spacing between nearest neighbor detectors is 1.5 km. The full detector array is approximately 48 km in the east-west direction, and 42 km in the north-south direction (Figure A.4). Each detector contains the solar panel orientation and electronics systems described above.

Events are generated by simulating showers with MOCCA and calculating the light falling on the simulated array. Events are analyzed by reconstructing the local Čerenkov light direction at each station using a 'shadow fitting' algorithm. The impact location for the core of the shower is calculated from the mean station position, weighted by the fitted station amplitudes derived in the first stage of reconstruction. A second reconstruction is performed to determine the direction of the original cosmic ray from the individual station directions[80]. The lateral distribution of the Čerenkov photons is reconstructed using the fitted amplitudes, core position, and primary direction. The fitted lateral distribution function is used to

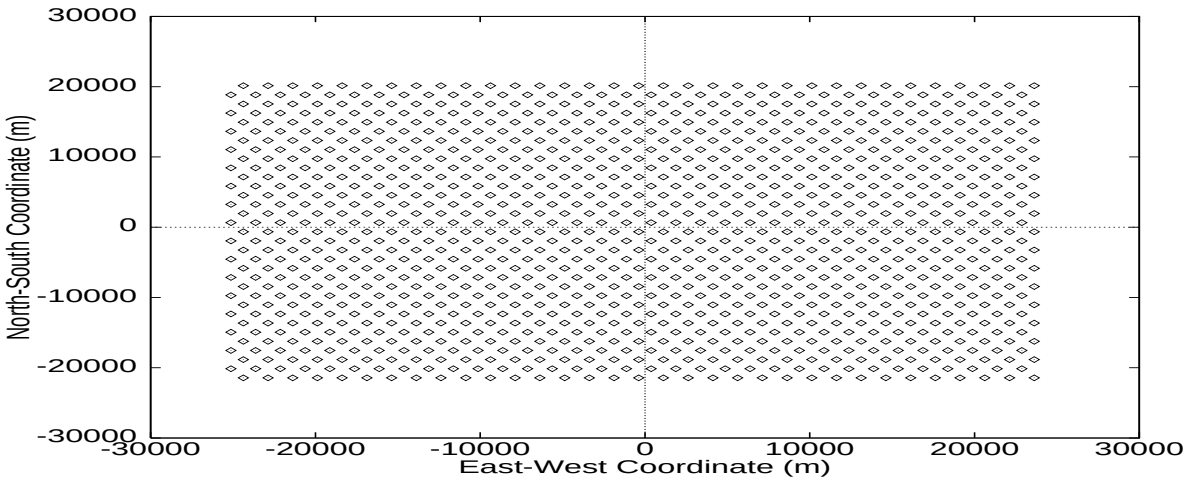

Figure A.4: Air Čerenkov station layout for performance simulation. Each diamond represents a single 6-panel detection station. Horizontal Axis: distance (m); Vertical Axis: distance(m).

calculate $\rho(1200)$, the Čerenkov photon density at a perpendicular distance of 1.2 km from the shower axis, and $\rho(500)/\rho(3000)$. This ratio $\rho(500)/\rho(3000)$ is a useful quantity because it is correlated with the shower X_{max}.

We present only results for S/N ratio of 100:1 due to space considerations.

A.3.3 Angular Resolution

Figure A.5 illustrates the expected angular resolution for the primary cosmic ray direction for a S/N ratio of 100. In general, one has an angular resolution of 1-2° for nearly vertical showers, and 0.3-0.5° for showers with a steep zenith angle.

The angular resolution expected is similar to, or perhaps better than, the resolution expected for the water Čerenkov particle detector array. It may however be possible to use the core from the latter to substantially improve the angular resolution of the Air Čerenkov detector.

A.3.4 Energy Resolution

Figure A.6 illustrates the expected energy resolution of the air Čerenkov detector as a function of zenith angle for a S/N ratio of 100. For vertical showers, the energy resolution is about 30-40%, and for steep zenith angles the resolution can be better than 10%. This is because $\rho(1200)$ is optimized for energy resolution at steep zenith angles, at near-vertical shower trajectories, when the optimal energy measurement distance is close to 100 m from the core. Since the array has 1.5 km spacing between detectors, it is unlikely that a station will be hit within 100 m from the core for a vertical shower. However, one may choose to

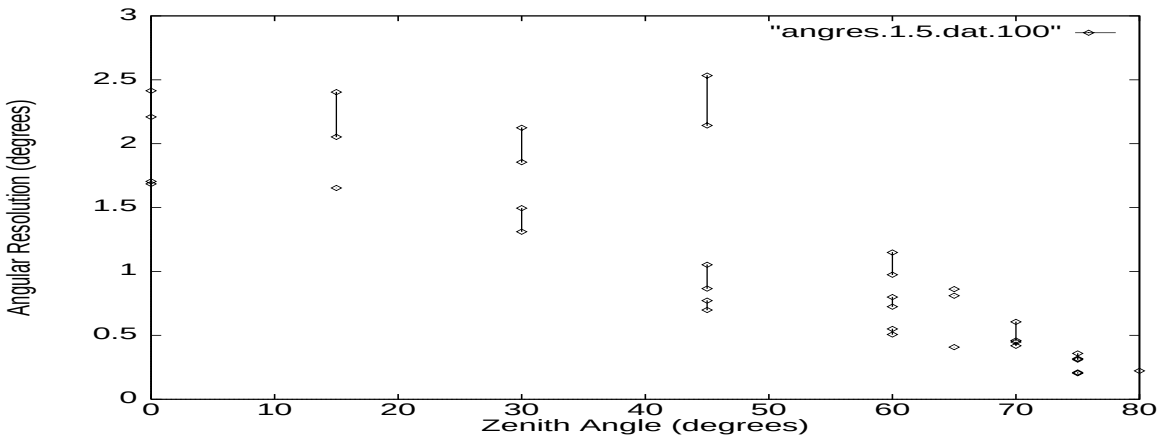

Figure A.5: Expected angular resolution of original primary direction as a function of zenith angle for various cosmic ray energies for fixed S/N ratio of 100. For each zenith angle, several points/bars are plotted. For angles with 3 distinct points/bars, the smallest error point is for 1 ZeV, next smallest error is for 100 EeV, largest error is for 10 EeV. When two points/bars are plotted, the smallest error is for 1 ZeV, and the second point is for 100 EeV. Horizontal axis: zenith angle (degrees); vertical axis: 1 σ angular resolution (degrees).

fit the small *subset* of showers which do have density measurements at this distance, and improve the energy measurement for these events. We have not studied this. It is unlikely that the vertical energy resolution will ever get much better than 40% at 1 ZeV, due to the fact that vertical EAS at these energies can have X_{max} approaching the ground level!

X_{max} Resolution

In Figure A.7 we show the correlation between the fitted $\rho(500)/\rho(3000)$ ratio and the X_{max} determined from a gaussian fit to the longitudinal development for S/N=100. A good correlation between the two parameters is observed, but there are a number of outlying exceptions. These are mostly due to bad geometric fits, and can probably be removed with tighter cuts on the geometric reconstruction quality. The typical width of the X_{max} distribution is 40-60 g cm^{-2} for S/N=100 or higher. With an improved core position one might be able to push the X_{max} resolution down to 30-50 g cm^{-2}.

Detector Angular Acceptance

The angular acceptance for the simulated detector is summarized in Table A.2. The results are presented in terms of acceptance (km^{2}sr of detection aperture per km^2 of ground area of the detector) so that the full aperture is easily calculated by multiplying the physical ground area of the detector by the angular acceptance. Note that the aperture at 10^{20} eV is approximately π steradians. This is similar to the angular acceptance of the surface array. The difference is that the air Čerenkov aperture is more heavily weighted towards large zenith angles than the water Čerenkov detector. The detection aperture can exceed π steradians,

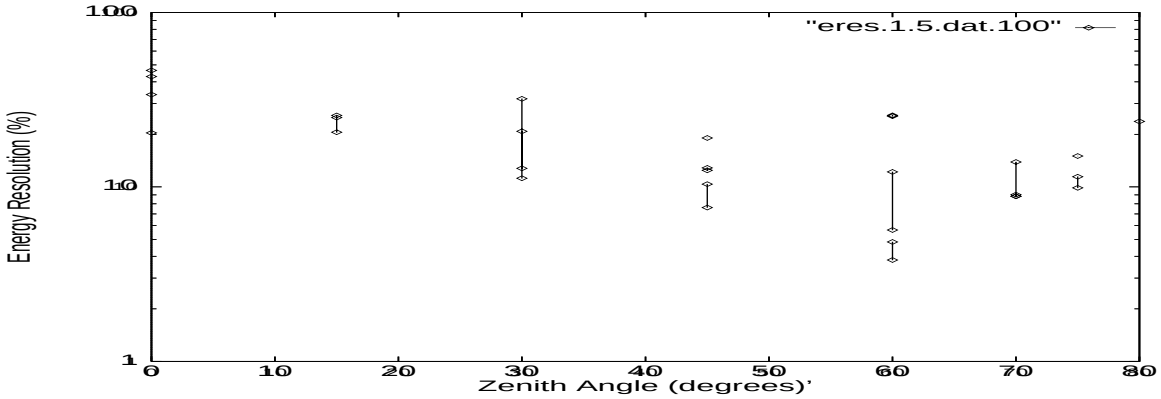

Figure A.6: Expected energy resolution as a function of zenith angle for various cosmic ray energies for fixed S/N ratio of 100. For each zenith angle, several points/bars are plotted. For angles with 3 distinct points/bars, the smallest error point is for 1 ZeV, next smallest error is for 100 EeV, largest error is for 10 EeV. When two points/bars are plotted, the smallest error is for 1 ZeV, and the second point is for 100 EeV. Horizontal axis: zenith angle (degrees); vertical axis: 1 σ energy resolution (%).

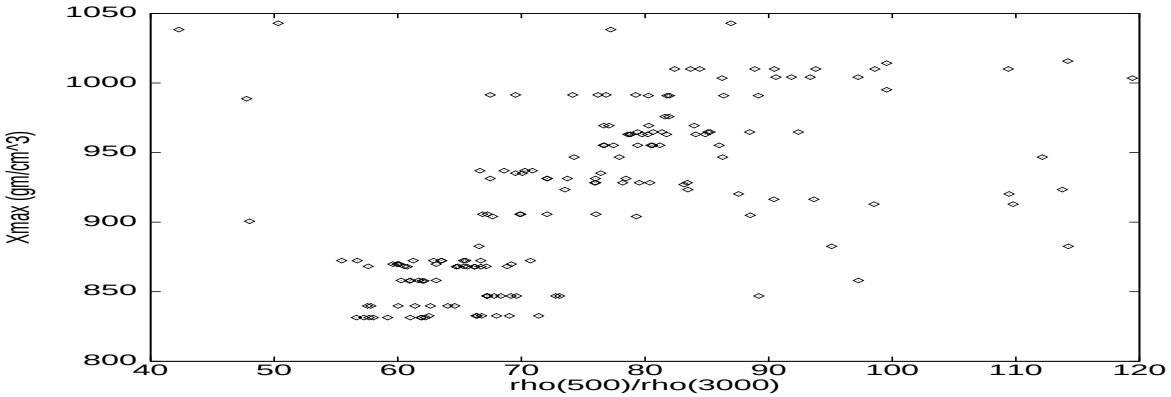

Figure A.7: Correlation between $\rho(500)/\rho(3000)$ and shower X_{max} for 0.01 to 1 ZeV cosmic ray showers with S/N =100. Horizontal Axis: $\rho(500)/\rho(3000)$; Vertical Axis: X_{max} (g cm^{-2})

because showers hitting outside the physical detector dimensions can also trigger the array, especially for large zenith angle trajectories.

Energy (EeV)	S/N ratio	Acceptance (sr)
10	10	1.36
10	100	1.36
100	10	3.13
100	100	3.23
100	1000	3.32
1000	10	1.72
1000	100	3.75
1000	1000	3.74

Table A.2: Detector Angular Acceptance as a function of primary energy and S/N ratio.

Appendix B

Radio Pulse Detectors

B.1 Motivation

As a result of work in the 1960s and 1970s [82], some of which has continued beyond then, it is recognized that air showers of energy 10^{17} eV are accompanied by radio-frequency pulses. Their polarization and frequency spectrum suggest that they are due mainly to the separation of positive and negative charges of the shower in the Earth's magnetic field. The most convincing data have been accumulated in the 50–100 MHz frequency range. Opinions have differed regarding the strength of the pulses, and atmospheric and ionospheric effects have led to irreproducibility of results. In particular, there may also be pulses associated with cosmic-ray-induced atmospheric discharges [83].

A study is being undertaken of the feasibility of equipping the Auger array with the ability to detect such pulses. The higher energy of the showers to which the array would be sensitive may change the detection parameters. However before a design for large-scale RF pulse detection can be produced, it is necessary to demonstrate conclusively the existence of the pulses for 10^{17} eV showers, controlling or monitoring some of the factors which led to their irreproducibility in the past.

In this appendix we describe the prototype activity at the CASA/MIA site, note related activities, and set forth some considerations regarding plans for the Auger project. More concrete plans for RF detection must await the outcome of prototype work at the CASA/MIA site.

B.2 CASA/MIA Prototype setup

To verify the claim [82] that 10^{17} eV showers are accompanied by RF pulses with significant energy in the 50–100 MHz range, a prototype detector is being set up at the CASA/MIA site in Dugway, Utah. This section describes the status of that effort.

B.2.1 Large-event trigger

A trigger based on the coincidence of several muon "patches" is being set up to select large showers with a rate of several per hour. The MIA Patch-Sum trigger is sent into a fan-in/fan-out from which the signal is put into a LeCroy 821 Discriminator. This produces a pulse of height -0.85 V (on 50 Ohm output) whose width can be adjusted as desired (typically it is set at 300 ns). The frequency of the output can be varied by adjusting the threshold on the discriminator.

The rate varies depending on the noise in any particular patch. The initial goal is to set up the electronics to deliver triggers at the rate of several per hour, corresponding to several times 10^{16} eV to 10^{17} eV on the basis of the rate at 10^{18} eV of $1/\mathrm{km}^2/\mathrm{day}/\mathrm{sr}$. It is notable that the rate of HiRes - MIA coincidences, for events above 10^{17} eV, is somewhat less than 1 per hour [84].

The performance of the "large-event" trigger was monitored during June, August, and October, 1995. In June and August, the trigger was used to key a transceiver which then broadcast a digitally recorded voice message which was picked up remotely. Times of receipt of the trigger message were measured to an accuracy of about 5 seconds. These times were matched with events in an off-line file of CASA events. Of 58 potential matches in the June runs, only 27 actual matches were found. Although this correlation appears higher than accidental, it is clear that many large-event triggers failed to match events in the actual data record. Consequently, more effort is being devoted to construction of an efficient large-event trigger. Studies of the pulse-summation setup were conducted in October of 1995 and are continuing.

B.2.2 Monitoring RF Noise

It was a concern that the RF noise of the local electronics and the presence of an extensive lightning-protection array might dictate the placement of one or more antennas outside the periphery of the array, or might make the site unsuitable altogether. The behavior of a single CASA board was investigated at the University of Chicago. The various clock signals were detected at short distances (< 1 m) from the board, but a much more intense set of harmonics of 78 kHz emanated from the switching power supplies. These harmonics persisted well above 100 MHz. At 144–148 MHz, they overlapped, leading to intense broad-band noise.

An initial survey of RF noise at the CASA site was performed. On the basis of the results, which indicated some RF noise within the array, it was decided to perform a follow-up survey just outside the array. The original log-periodic antenna used to detect RF pulses at Chacaltaya in the 1960s and 1970s was obtained, tested for bandwidth, taken out to Utah, and used in a follow-up study of RF noise in the 60–85 MHz frequency range. Sources of most strong RF signals in this range appeared to be due to either the receiver itself or to local TV stations. Spectrum analysis techniques may be suitable for removing such monochromatic

signals.

A subsequent survey involved mounting the log-periodic antenna near the CASA central trailer site, just above the lightning protection grid. The RF noise at this site was found to be unacceptably high, so that future studies will be conducted just outside the CASA array.

B.2.3 Near-term plans

RF noise will be monitored and pulses detected by mounting the log-periodic antenna just outside the CASA array in a trailer which will be set up for the purpose. A digital storage scope will be used to register several microseconds of RF data on a rolling basis. These data will then be captured and studied upon receipt of a large-event trigger.

The experiment will be repeated using successively greater amounts of amplification and a variety of band-pass filters. The preamplifiers and filters are being developed at the University of Chicago. Once the large-event trigger has been demonstrated to select events of 10^{17} eV and above, permanent digital recording of coincident pulses will be undertaken.

Later experiments will monitor RF pulses at lower frequencies and at greater distances from the array. These pulse strengths may be correlated with atmospheric electric fields, and we plan to monitor such fields with the help of a field mill.

A spectrum analyzer will be used to make a broader survey of the RF noise in various frequency ranges and may be of help in detecting potential sources of interference to RF communications in the Auger project.

B.3 Recent information on related activities

B.3.1 FORTE, BLACKBEARD, SNO, and other projects requiring digitizers

Discussions with John Wilkerson at the University of Washington have been very productive. Wilkerson was engaged in projects at Los Alamos with the acronyms FORTE and BLACKBEARD whose aim was the detection of electromagnetic pulses, including those produced by cosmic ray-induced electromagnetic discharges, with frequency ranges in the 30-100 MHz range. Many of the fast digitization and memory problems appear to be identical to those in the proposal for a prototype pulse detector at CASA/MIA. Time:frequency plots have been obtained by the BLACKBEARD project which are exactly those one would hope to generate in a survey at CASA/MIA.

Wilkerson has also encountered requirements similar to the present ones for digitization of SNO data. His estimate is that one can use Maxim MAX 100 A/D chips for less than \$1K per channel, but that feeding their output into memory may well amount to another

$1K per channel. Other references on digitizers have been obtained [85, 86]. Discussions with Wilkerson will continue, and further discussions with Dan Holden at Los Alamos are envisioned. Wilkerson is proposing to test his digitization system using a broad-band antenna with sensitivity in the 10 - 30 MHz range.

B.3.2 Status of GHz detection

David Wilkinson, who visited the University of Chicago during the spring of 1995, will study the power radiated at frequencies of several GHz, where new opportunities exist associated with the availability of low-noise receivers. RF noise in the range below 1 GHz will be surveyed outside the CASA site with the help of a commercial broad-band antenna directed toward the zenith.

B.3.3 Other options

Dispersion between arrival times of GPS signals on two different frequencies may serve as a useful monitor of air shower activity. The possibility of correlation of large showers with such dispersion events will be investigated.

It may be possible at the CASA/MIA site to monitor commercial broadcast signals to detect momentary enhancements associated with large showers, in the same sense that meteor showers produce such enhancements. Television Channels 3 and 6, for which no nearby stations exist, and the WWV transmitters in Fort Collins, Colorado, offer some possibilities.

B.4 Considerations for the Auger project

At present we can only present a rough sketch of criteria for detection in the 50-100 MHz range. Data would be digitized at 500 MHz at each station and stored in a rolling manner, with at least 10 microseconds of data in the pipeline at any moment. Upon receipt of a trigger signaling the presence of a large shower ($> 10^{17}$ eV), these data would be merged into the rest of the data stream at each station.

Per station, we estimate the following additional costs, in US dollars, for RF pulse detection:

Two antennas and impedance transformers:	200	(a)
Mounting hardware:	100	(b)
Cables and connectors:	200	(c)
Preamps and lightning protection:	100	(d)
Digitization and memory electronics:	2000	(e)
Total per station:	2600	(f)

The following are notes referred to in the table:

(a) Two commercial log-periodic TV antennas with commercial 4:1 baluns; crossed polarizations. Difference signal to be detected.

(b) Highly dependent on other installations at site. Antennas are to be pointed vertically but optimum elevation not yet determined.

(c) Antennas are mounted near central data acquisition site of each station.

(d) Commercial GaAsFET preamps and gas discharge tubes.

(e) Subject to prototype development experience. Power requirements not yet known.

(f) The number of stations equipped with RF detection will not exceed 2000 per array, but could be fewer, depending on prototype experience.

The above estimate assumes that one can power the preamps and DAQ electronics from the supply at each station without substantial added cost. It also assumes that the "large-event trigger" will be available at each station. A further assumption is that the difference signal suffices to characterize the pulse. Additional preamplification and DAQ electronics may be required if this is not so. A major consideration may be the acquisition of antennas robust enough to withstand extreme weather (particularly wind) conditions.

For detection at frequencies above or below 50–100 MHz, the criteria are not yet well enough developed to permit any cost estimate.

Appendix C

Surface Detector Alternatives

C.1 Introduction

In developing the concepts for the surface detector array, both water Čerenkov and sandwich detectors were considered. Once the water detector was determined to have cost advantages and to be comparable in performance, work on sandwich detectors was stopped. The concept of the sandwich detector, however, was well advanced and will serve as a back-up.

The sandwich detectors consist of two planes of particle detectors such as scintillators or resistive plate chambers (RPCs) separated by a layer of absorber. In addition to energy determination, the objective is to provide ground particle identification, and muon content in particular, to assist in determination of the primary composition. (See Figure C.1) Muons in showers have a typical energy of a GeV and penetrate the absorber, so they register in both top and bottom detectors. The electron spectrum in showers is soft, so they will typically penetrate the first counter and range out in the absorber, leaving no signal in the bottom detector. Most photons pass through undetected; about 3% will convert in the absorber and be detected only in the bottom counter. Monte Carlo calculations of the response of various detector configurations have been performed using the EGS-4 code. Table C.1 shows the results of such a calculation. By recording the individual detector time profiles during the event and noting coincidences, the muon content of the showers can be determined.

The chief source of potential misidentification of particles is punch-through of high energy electrons. We have performed trade-off studies between absorber candidates to minimize this misidentification while maintaining good efficiency for the detection of photons. In a comparison of lead and steel absorbers (which have approximately the same cost per radiation length) we found that steel significantly reduced punch-through because of its higher stopping power per radiation length. This also reduces photon efficiency slightly since conversion electrons are more likely to range out in the absorber undetected. Figure C.2 shows the EGS-4 results for a range of absorber thickness for lead, steel, and concrete absorbers. We find that a 2 X_0 steel or concrete absorber is close to an optimal choice.

While high energy showers are infrequent events, the instantaneous particle rate within

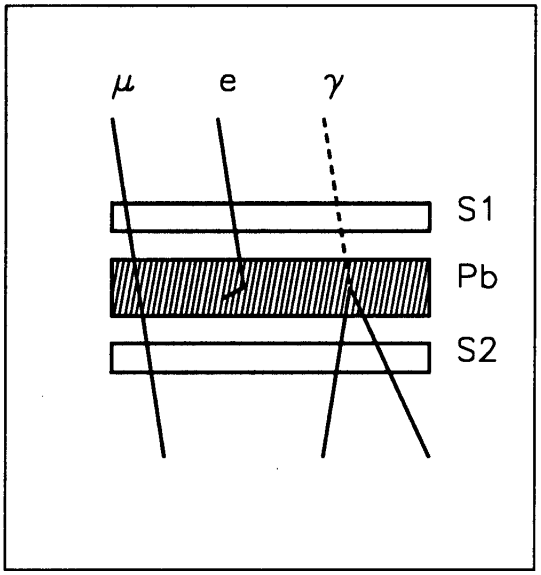

Figure C.1: An ideal sandwich counter: top only is an "electron", bottom only is a "photon" and top plus bottom is a "muon".

1.5 km of the core exceeds 10 MHz/m^2. In any high energy event, the nearest detector to the core will be saturated and will provide information only on the total particle flux, with no muon content information. Far from the core, rates are low and muons may be easily separated from the electromagnetic component. In the intermediate region, segmentation of the counter reduces accidental coincidences within the shower to an acceptable level and allows one to distinguish muons. For the scintillation counter, four segments is a reasonable choice; for the RPC option, the pad configuration can be adjusted to provide segments of varying sizes optimized for a range of shower impact parameters [107]

We have studied two technologies for the detection of shower particles above and below the absorber: RPCs and plastic scintillators. Resistive plate chambers detect particles in a digital mode and have excellent timing and scalability. Because the RPCs use commonly available materials, they can be built at lower cost than scintillator counters. RPCs, however, require periodic servicing to replenish the supply of chamber gas. Scintillation counters have been used in a number of ground array air shower detectors. Their design and performance are well understood.

Both resistive plate and scintillator-based sandwich detectors will be discussed in the sections that follow. A number of designs for the scintillator sandwich were studied. Three types of prototypes of scintillator-based detectors were built. The first was based on the CASA [108] detector "direct readout" design, where phototubes were glued to the face of cast plastic scintillator sheets. In the second, the light was read out by wavelength-shifting fibers embedded in sheets of scintillator. Finally, the response of a lead scintillator sandwich to high energy (10^{19} eV) showers was measured in the AGASA array at Akeno. The results of these studies are given below. Schemes using other approaches to plastic scintillator readout, or liquid scintillator, were only superficially studied and are not described.

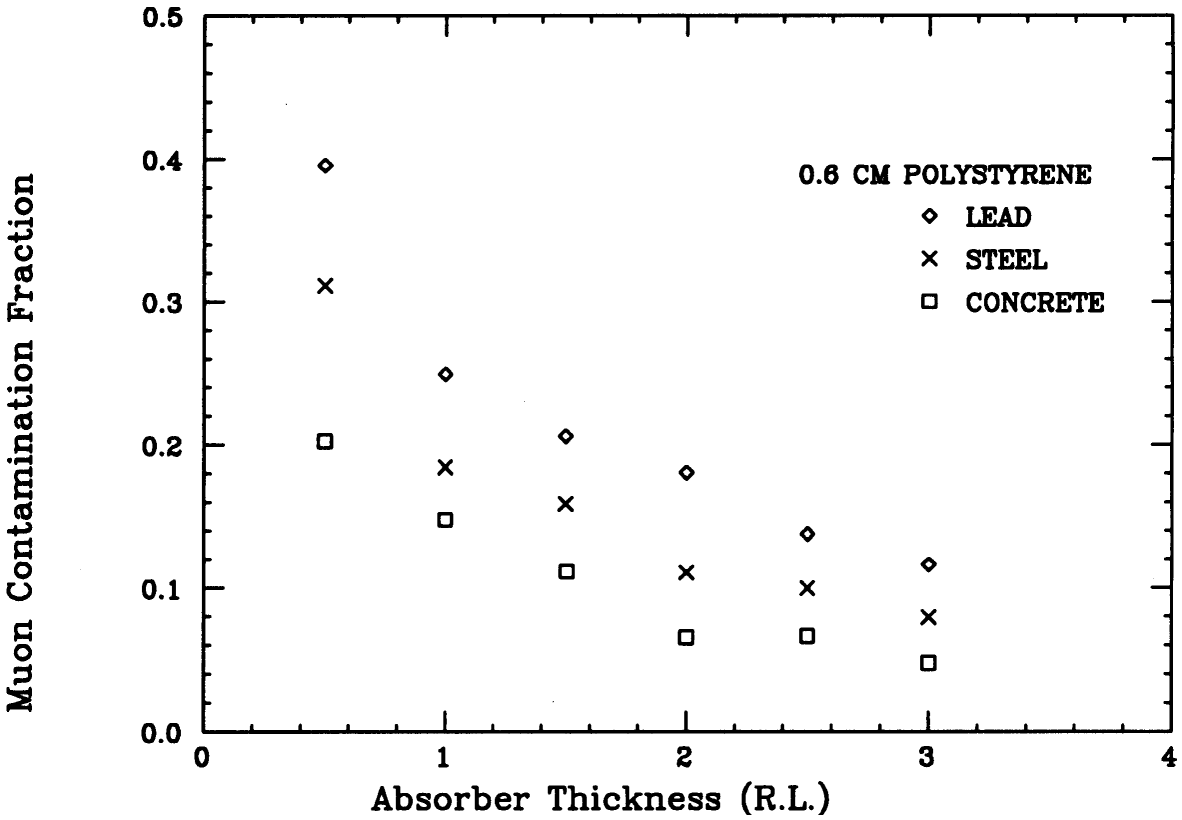

Figure C.2: The muon contamination fraction (fraction of muon signals faked by photons or electrons) vs. absorber thickness for various absorbers.

C.2 RPC Sandwich

C.2.1 RPC Sandwich Detectors

RPC sandwich detectors are, in principle, very similar to scintillator sandwich detectors: Two charged particle detectors are placed above and below a layer of electromagnetic converter in order to detect and identify muons, electrons, and photons from the air showers. The requirements for the converter, enclosures, mechanical supports, communications, and power are very similar to scintillation sandwich detectors and will not be dwelt upon here.

Resistive Plate Counters are particle detectors in which a gas-filled gap between two highly resistive plates is kept at a high electric field, about 4000V/mm. The passage of a charged particle causes a local discharge which is read out by conducting pads or strips. The output is digital, i.e., a pulse appears for each particle detected but the pulse height does not contain information about the primary ionization. RPCs have been used in both accelerator-based experiments and astrophysics experiments because of several compelling strengths: 1. Large signals directly read out, eliminating the need for expensive front-end electronics. Because the electronics is simple and no photomultiplier is required, fine segmentation of readout is available simply and for low cost; 2. Excellent time resolution, in some cases

	Both Detectors	Top Only	Bottom Only
Muon	0.875	0.070	0.056
Total Electromagnetic	0.001	0.038	0.021
Electron	0.030	0.870	0.005
Photon	0.000	0.007	0.021

Table C.1: Particle identification probabilities for a sandwich detector consisting of a 2 X_0 steel absorber between two sheets of 6 mm scintillator, for particles 1000 m from the core of a 10^{19} eV proton shower.

less than a nanosecond; 3. High detection efficiency, including multiparticle efficiency in extensive airshowers; 4. Because of the simplicity of the RPCs and use of very ordinary materials the cost per square meter can be kept very low. Ordinary glass or bakelite sheets are usually used for the resistive plates and the high voltage distribution is by drawing ink, or sprayed-on graphite-loaded paint, read out by aluminum foil taped to foam plastic sheets. Production costs are substantially less than for scintillator sandwich detectors and may even prove to be less than water Čerenkov detectors.

Because of the above advantages, the RPC sandwich detector is a reasonable candidate for use as the surface detector. There are several concerns to be addressed before a final selection of this detector could be made. These include:

1. Selection of a gas for good performance, low cost, and optimum ageing behavior so that the detectors will perform properly throughout the lifetime of the experiment, taken here as 20 years. Accelerator-based particle physics experiments have used RPCs for several years and the literature does not contain references to observed degradation of the RPCs with time, suggesting that the RPCs as operated at accelerators will perform properly for the Auger project. Selection of a gas which might be different from the gas mixtures used in the accelerator-based experiments would require some long term testing to verify that no adverse ageing will be introduced.

2. A gas system design has been studied which would operate for years in a remote location. The system consists of a propane-type tank of a standard capacity (1000 gallons or about 4000 liters), a pressure regulator, and a flow restrictor. At expected flow rates, the tank would be refilled every one to three years, and perhaps less frequently if new gas mixtures under study prove to be successful.

3. Operation for long times in the temperature extremes that might be encountered by the experiment should be addressed. RPCs have been tested successfully at Fermilab down to -10C for brief (few days) periods. The high temperature limits have not been explored.

4. Selection of the materials and fabrication techniques for the RPCs which will result in the lowest production costs with long gas and counter lifetimes needs to be made.

5. Preliminary design of the readout electronics suggests that the readout and calibration will be very straightforward and inexpensive, with a segmentation of 100 at each

station. Simulation and further engineering effort will be required to establish this design.

Production techniques for glass RPCs are being developed at Fermilab. These have produced successful RPCs with both glass and metal spacers. The graphite layer for high voltage distribution is applied consistently and is durable and stable, although the manufacturer of the ink used may not continue to supply this ink made to a consistent formula. Alternative brands are believed to be acceptable, so that we do not consider this a major problem. Production of large ($1 \times 2m^2$) glass RPCs has been done successfully at VPI [109] and production of glass RPCs with PVC housings has been done routinely in Italy where they are in use in experiments. Development of mass production technology for glass RPCs is being evaluated at Fermilab.

The gas used in the RPCs and, a related issue, the lifetime of the RPCs in operation, has been studied at Fermilab and elsewhere. A simple technique consists of stopping all gas flow and monitoring RPC performance over time. Tests have demonstrated that operation can continue for three to four days, depending on gas mixture, without loss of efficiency and with an acceptable increase in the noise rate. Workers at Osaka have RPCs operating over 10 weeks with zero gas flow, although efficiency has dropped to 93%[109], suggesting that less than one gas change per day will prove acceptable. Studies with bakelite RPCs[110] in which the gas flow was stopped for 180 hours, produced some encouraging preliminary results and demonstrated that the bakelite does not outgas in ways that cause gas poisoning. Plans at Fermilab call for further studies of gas mixtures in order to minimize flow requirements, maximize RPC lifetime, and eliminate R13B1, an ozone-damaging gas, perhaps substituting R116, which is ozone friendly, less expensive, and has been shown by preliminary tests to provide acceptable performance. The gas optimization is a long-term activity and should result in a reduction of gas flow requirements and hence in operating costs.

Although a provisional selection of the water Čerenkov technique has been made, the possibility of a future infill array consisting of RPC sandwich detectors remains. Because the infill array would consist of a set of detector stations located near the center of the main array, delivery of gas to each station even as often as annually would not present a difficult or expensive problem. As a result, the experiment may be able to take advantage of the very low fabrication costs and the excellent ability to measure high track densities with good particle identification.

C.3 Scintillator Sandwich with Direct Readout

Shortly after the scintillator sandwich idea was first proposed in 1993 [87], tests were conducted with the NEPAL accelerator station at Orsay on the behavior of low-energy electrons incident on such a sandwich. These were followed by the construction of a full-size (9 m^2) prototype station [88] [89] of which the basic detector element is a 2.25 m^2 square sheet of 12 mm-thick acrylic scintillator (2 m attenuation length, yield 21% of NE110). It is read out with a single 12 cm flat cathode, ten-stage EMI 9390 PMT simply glued to the center of the sheet using a transparent, flexible coupling compound 2 mm thick. Measurements

using cosmic ray muons had shown that with a high-gain voltage divider and an electronic threshold of 0.6 mA, close to the single photoelectron level, more than 99% efficiency could be achieved over the whole surface with this simple geometry.

Naturally, pulse-heights will be far from uniform over the detector surface. Thus, this design is intended to count particles individually, being sensitive in particular to the dominant (electromagnetic) shower component consisting of electrons, detected directly by the upper scintillator layer, and gamma-rays, detected by the lower layer after conversion in the lead plate.

The four two-layer modules provide sufficient segmentation of the detector surface to handle typical Auger particle densities in the 1 km distance range. This segmentation also makes possible a simple local hardware trigger; one can require, for example, a minimum of 4 counts in the 8 layers. Additional segmentation (more elements of smaller size) would improve performance since saturation in particle counting would be reached at higher particle densities. Muon identification (provided to first order by a tight top-bottom coincidence within a module) would also be facilitated. However, this would increase the cost due to the greater number of PMTs and readout channels and probably a more expensive mechanical structure. Reducing the number of modules would reduce particle counting performance, and in addition it is not clear that larger scintillator sheets could be read out efficiently with the simple optical coupling method used for the Orsay prototype. Production of scintillator sheets in greater widths might also be a problem.

In order to be able to trigger on and record times of particles spread over several microseconds, a special-purpose VME module was built which performs continuous storage of the eight discriminator output bits, after synchronization with a 32 MHz clock. The trigger is generated typically by requiring counts from at least 4 scintillators within 2 μs, and storage is halted 20 μs later. The memory contents are subsequently analyzed to determine the nature of the configuration of hits which triggered. Standard modular electronics were used for efficiency and other measurements and also served to verify and complement the results obtained with the VME module.

At Orsay (alt. 100 m), where all the tests have been conducted so far, the stand-alone characteristics of the station have been evaluated as it triggers on a combination of chance coincidences (involving noise counts, single muons and low-energy showers) and clearly identified low-energy shower events. Low-energy showers are characterized by a negligible time spread and an electromagnetic component which largely dominates the muons except far from the core. The parameters that have been varied are absorber thickness (1 and 2 radiation lengths) and module spacing. For these tests, the modules were located in a large assembly building whose light roof is not expected to influence the results significantly. However the trigger rates given below from low energy showers can be expected to increase significantly at higher elevations. Test runs had to be made when the 2 GeV Orsay electron linac was off. Otherwise, neutrons from a positron converter, although 200 m away, produced loose 4-fold coincidences from the upper scintillators.

C.3.1 Counting and Trigger Rates

The singles rate of an individual counter is typically 2000-3000 c/s, and the number of top-bottom coincidences is 300-400 c/s per module, mostly coming from single muons. With a trigger requirement of "any 4 out of 8" and the coincidence pulse width of 2 μs currently used, the rate for events identified as chance coincidences is in the 4-8 c/s range.

The rates for events identified as showers by their tight time structure were 6.8 c/s with $\sim$1 X_0 (6 mm) of lead and 4.5 c/s with 2 X_0 with the modules relatively closely spaced (mean distance of module centers from their center of gravity: 2.3 m). When the modules were moved farther apart to a 5.5 m mean distance, the above rates dropped to 2.7 and 2.1 c/s, respectively.

C.3.2 Shower Particle Configurations

In order to get an indication of the effect of increasing absorber thickness, the number of modules involved for events having a total of 4 counters hit has been examined. Experimentally, with 1 X_0 of lead, 2, 3 and 4-module events were observed 69%, 30% and $\sim$1.5% of the time, respectively, whereas with 2 X_0 these figures become 62%, 36% and $\sim$2.4%. These values do not change with module spacing. Without an absorber, such events would have almost entirely 2 modules only, since most charged particles would count in the two layers, and few γ-rays would convert. On the other hand, a very thick absorber would mean essentially top-layer, and thus 4-module, events only. These results can be interpreted by the tendency for a dominant hard-electron component to be attenuated when the absorber is increased.

C.3.3 Comparison with Shower Simulation Results

The MOCCA Monte-Carlo program followed by other Monte-Carlo calculations has been used to examine detection rates for four 2.25 m^2 scintillators, equivalent to just the upper layers of the prototype modules. Most of the events come from 30-100 TeV showers which fall less than about 30 m from the station. The detection rate for vertical showers decreases by 20% when the mean distance of the modules from their center of gravity goes from 2.8m to 5.6m. This is compatible with an experimental result obtained for this trigger configuration (although without the restriction on verticality). The stronger decrease (1 : 0.45) observed with the "any 4 out of 8" trigger condition (see Section C.3.1) with the full detector can be interpreted as coming from increased sensitivity to low-energy showers. With the two-layer modules this comes from penetrating electrons counting double and from gamma-rays converting in the lead and being counted in the lower layer. The effective sensitive area of a station for these additional showers is small (to be counted such showers must fall close to the station), and as the modules are separated, fewer of the showers contribute counts in more than one module, leading to a rapid rate decrease.

Another result of these simulations is that the secondary electron spectrum in this

primary energy range is considerably harder than that expected for high-energy showers as would typically be detected in the AUGER array[88]. For example, for 100 TeV showers at less than 30 m, the integrated flux above 13 MeV (the cutoff energy for 1 X_0 of lead) is only about 3 times that above 150 MeV (the cutoff for 3 X_0). This is consistent with the experimental indication of a dominant hard-electron component, but more detailed low-energy simulations and additional experimental work need to be done.

C.3.4 Chance Coincidences

A simple Monte-Carlo calculation was performed to determine the trigger rate due to chance coincidences, assuming a 350 Hz doubles rate per module due to single muons, combined with a per-counter singles rate varied from 1000 to 5000 Hz. The trigger requirements were taken to be 3 and 4 counts from the 8 scintillators occurring within 4 μs. With the 3-count threshold, the trigger rate already reaches the 20 Hz range for a singles level of 1500 Hz. For a threshold of 4 counts, the rates for singles levels of 2000, 3000 and 4000 c/s are 0.8, 3.9 and 11.4 Hz, respectively. These results are consistent with the experimental values (although, for various reasons, these are not strictly comparable). It can be seen that the PMT noise level is an important parameter affecting station alert rate; to reduce noise, the tubes should be operated at the lowest possible gain compatible with satisfactory single-particle efficiency. This can be expected to provide an alert rate quite compatible with the requirements for the surface array.

C.3.5 PMT After-pulsing

The phenomenon of after-pulsing in photomultiplier tubes is well known, but it can often be ignored when the events studied are characterized by time coincidences between the different detectors on the ns scale. For extremely high energy cosmic rays, the particles to be detected are spread over microseconds, and this is also the time scale for after-pulses, which can be expected to be a concern for any type of detector using PMTs. With the high PMT gain required with direct readout, the average after-pulse level integrated over several μs can reach 100% or more. This effect has several sources within the tube, some of them depending on total current in the final stages of amplification. Running with fewer multiplier stages and adding an amplifier to reach the same threshold level in terms of number of photoelectrons will lower current levels and is expected to reduce the phenomenon. Test results for an EMI-9390 tube are shown in Table C.2.

The tests were performed with light from a pulsed LED at levels comparable to the minimum levels produced by the scintillator, as well as three times higher. Without an amplifier, the anode output was sent over 50 Ω cable to a 100 MHz discriminator with a 30 mV threshold. With an amplifier, the 8th dynode, used as the output electrode, was connected directly to a video amplifier of gain 30 and input impedance 1 kΩ. The total capacitance at the input was about 10 pF. The amplifier output was then sent to the same discriminator. The VME module used for the tests described above was employed here for

Setup:	1100 V on a, no amp.		760 V on d_8 + amp.	
Light pulse level:	$\times 1$	$\times 3$	$\times 1$	$\times 3$
< 94 ns	3.3	20.9	3.7	2.2
$94 - 594$ ns	7.9	49.2	1.6	4.1
$625 - 3125$ ns	4.0	13.2	0.5	1.6

Table C.2: After-pulse levels (%) for different test conditions and time regions.

data acquisition. In the table, the after-pulse count (in %) is given for three time regions. For the first of these, detailed studies will be necessary to distinguish between tube behavior and electronics effects, for example amplifier under/over-shoot. For the 100 ns to 3 μs regions, in all cases use of the amplifier reduces afterpulsing by a factor ranging from 5 to 12. For the high light-level case, the total drops from 62% to 5.7%, which would correspond to a reduction from perhaps two or three afterpulses per event on the average for the 8-PMT station, to only one every few events. According to tests conducted by EMI [90], reducing the $k-d_1$ voltage further reduces afterpulsing, but at the expense of photocathode uniformity and overall sensitivity.

The tubes of the Orsay prototype are being equipped with low-noise hybrid preamplifiers developed at LAL for the H1 experiment at HERA. This design uses a fast common-base input transistor and provides somewhat more gain than the amplifier used for the tests described above. In preliminary measurements of afterpulse rate performed on one module using single muons, surprisingly, the two counters showed quite different behavior (as much as a factor of 7 in certain time regions). This may originate from inherently different tube performance (in spite of similar gain characteristics) or be due to operating-point differences bringing the afterpulses above threshold for only one of the two counters, although for both, efficiencies were high and the different counting rates comparable. As in the case of singles rates, it is no doubt important to use the lowest gain possible, compatible with satisfactory efficiency.

C.3.6 Conclusions

Diverse technical aspects of the direct scintillator readout method have been explored in considerable detail, and the performance of a full-size prototype scintillator-sandwich detector has been evaluated on low-energy showers. Although some additional studies are necessary, this simple, robust design can be seen generally to satisfy the requirements for the Auger project surface detector station.

C.4 Scintillator Sandwich with Wavelength Shifter Readout

C.4.1 Overview

Large area plastic scintillation counters have been used for many years in cosmic ray air shower detector arrays. The 2.2 m^2 detectors, for example, used in the AGASA array in Japan use 5 cm thick scintillator viewed by a photomultiplier tube through air light pipes. The Yakutsk array uses similar detectors. The CASA array[108] in Utah has 1 m^2 counters of 0.5" scintillator with a 5" photomultiplier glued to the center of the counter. Large area counters used in high energy physics experiments have used wavelength shifter bars along the counter edges coupled to photomultiplier tubes at opposite corners. Such large area counters are difficult to read out with high efficiency and uniformity while keeping the cost reasonable.

A technique has been developed to read out scintillator tiles in sampling calorimeters in high energy physics experiments using optical fibers[111]. Calorimeters using large scintillator arrays designed for the SDC detector for the SSC[112], the new endplug calorimeters for the CDF detector at Fermilab[113], and for detectors being planned for use at the Large Hadron Collider at CERN use optical fiber readout. Wavelength shifting (WLS) optical fibers embedded in grooves in the scintillator collect the light for transmission via clear optical fibers to photomultiplier tubes outside the calorimeter. This method allowed the construction of highly efficient, segmented, and yet hermetic calorimeters.

The largest tiles with fiber readout typically used in calorimetry are about 50 $\times$ 50 cm^2. Wavelength shifter fiber readout can also be used to advantage for scintillation counters of much larger area. As will be shown, counters of 3m^2 can be effectively read out by a single 38 mm diameter photomultiplier with good uniformity and efficiency.

C.4.2 Detector Requirements

The candidate lead/scintillator or iron/scintillator sandwich detector is segmented into four parts to reduce the counting rate. Each detector segment is nominally 2.5m^2. The detector needs to be efficient ($> 95\%$) for a single minimum ionizing particle (MIP). The energy of the air shower is inferred from the density of particles measured in the surface detectors. The uniformity of the counter is, therefore, an important contributor to the determination of the shower energy. Also of crucial importance is the unit cost of the detectors in large scale production. Scintillating plastic is the single most costly item in the array detector module. It is important, therefore, that the scintillator be as thin as possible consistent with good efficiency and uniformity.

C.4.3 Fiber read-out counter development

An intensive effort went into the development of scintillating tile/fiber calorimetry for the SSC/SDC detector and Fermilab CDF detector end plug upgrade[114] [115]. This experience makes the design of a large area counter fairly straightforward. The design starts with the determination of the number of fibers, spacing, and groove geometry necessary to ensure adequate light collection.

Studies were carried out on small test counters to choose these parameters[116]. The results suggest that the optimum fiber/scintillator configuration is to have grooves machined in the plastic 3 or 4 mm deep using slitting saws. The light yield of this style of counter is fairly insensitive to both groove depth and to the depth of the fiber in the groove[117]. One millimeter thick wavelength shifter fibers are a reasonable choice for the largest diameter consistent with the necessary flexibility. A fiber spacing of 5 cm was chosen. Since the volume of scintillating plastic drives the cost of the detector the thinnest possible scintillator should be used. It was found that 6 mm thick Kurary SCSN38[1] would give a light yield of greater than 10 photoelectrons per MIP in a three square meter counter. SCSN38 is a polystyrene-based scintillator. Large area scintillators are normally made with acrylic based scintillator for reasons of lower cost. Grooves in styrene-based scintillator, however, can be machined at twice the speed as grooves in acrylic. A study of cost, specific light output, and machineability favors styrene scintillator for this application.

C.4.4 Large Area Test Counter

The configuration of the 3 m^2 test counter was based on the results from studies with small models. It was made with available 2.5 m x 1.2 m x 25 mm acrylic scintillator grooved with a 1.2 mm slitting saw on CNC horizontal mill. The material was uneven, varying in thickness by about 25% and in flatness by about 5 mm. The resulting groove depth consequently varied from 5 to 10 mm. As indicated above, this variation in groove depth does not affect light gathering performance. The grooves were spaced every 5 cm parallel to the short edge as shown in Figure C.3. Two extra grooves were placed at each edge to enhance light levels in order to extend the light yield uniformity to the edge of the counter. The edges of the counters were painted with Bicron BC620[2] white reflective paint. The readout fibers consisted of 3 m of WLS fiber with 1.5 m of clear fiber 1 mm diameter (Kurary double clad 200ppm) spliced to each end. The clear fiber was used to decrease attenuation between the counter and the photomultiplier. The splices were made by diamond-cutting the ends and fusing the plastic[118]. Although the transmission of these splices was not measured, similar splices exhibit a 90% transmission with a few percent variation[119]. The fibers are looped back into every second groove. The use of the looped fiber results in uniform light yield in the detector parallel to the fibers. Three fibers were placed in each groove to ensure adequate light collection. The fibers were collected, glued into a plastic "cookie," and the assembly

[1]Kurary International Corp., 200 Park Ave., New York, NY 10166.
[2]Bicron, Inc., 12345 Kinsman Rd, Newbury, Ohio 44065-0677.

was polished using a diamond cutter. The "cookie" was connected via a simple light mixer bar to an EMI-9902KB 38 mm photomultiplier tube. The counter was wrapped in Dupont Tyvek and enclosed in a shallow light-tight plywood box for testing.

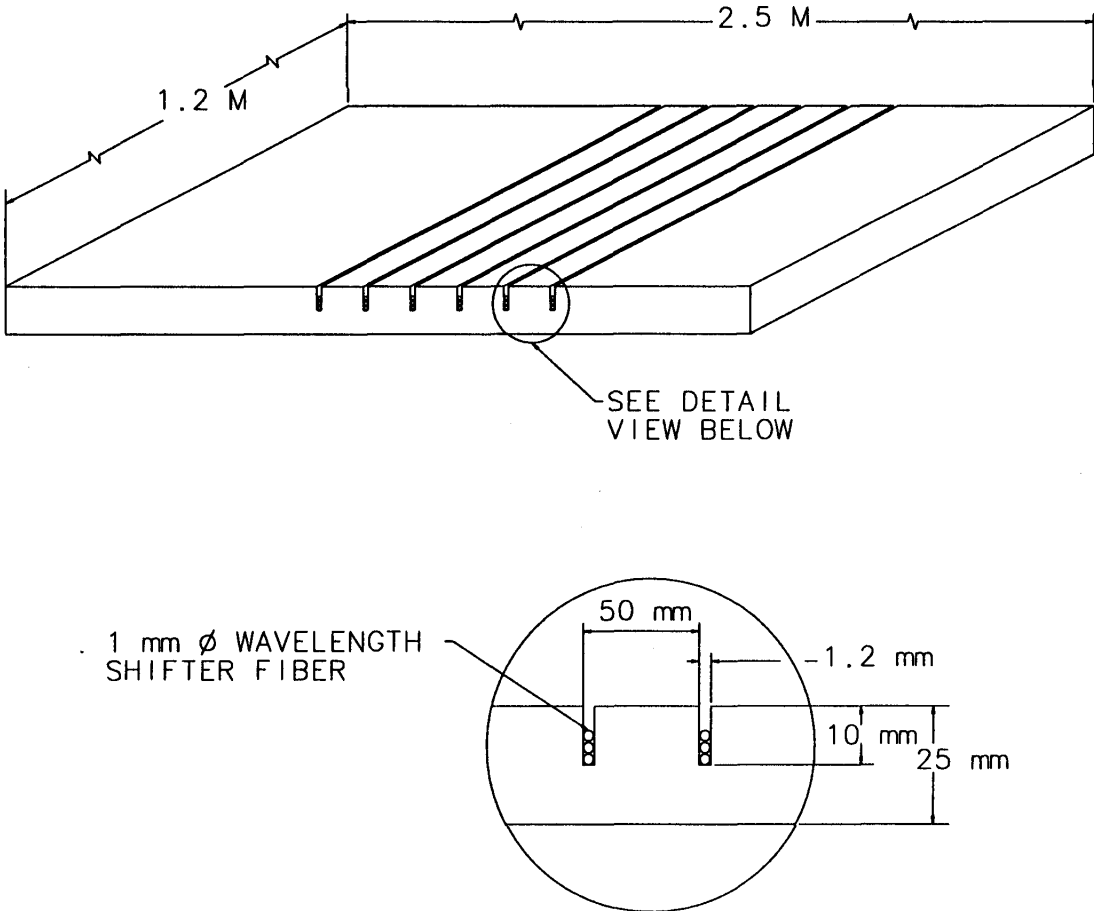

Figure C.3: Detail of the grooves and fibers in the scintillator.

C.4.5 Test Results

Two paddle counters of 4 x 4 in^2, used to gate the ADC, accepted cosmic rays in a cone of roughly 13° about the vertical. A 21 mm thick steel plate was placed between the test counter and bottom paddle. Figure C.4 shows a pulse height spectrum at the center of the counter. The mean pulse height at that position corresponds to about 10 photoelectrons. The uniformity was measured over the surface of the counter. Scans were made perpendicular and parallel to the fiber directions. In the longitudinal scan and transverse scans, shown in Figure C.5 and Figure C.6, the light yield is minimum at the center of the counter and increases by about 30% at the two ends. This non-uniformity is due almost entirely to the fact that the scintillator is 25% thicker at the edges than in the center. This thickness variation is typical for large sheets of acrylic scintillator. A second reason for the additional light near the edges is the extra grooves and fibers placed there. The experience of Beretvas et al. [128] showed that with uniformly spaced grooves, the light dropped off by 20% at the edges of the counter. By adding two extra grooves at each end, we apparently over-compensated for light loss at the edges. Were the material of consistent thickness, the light yield would be uniform to a few percent.

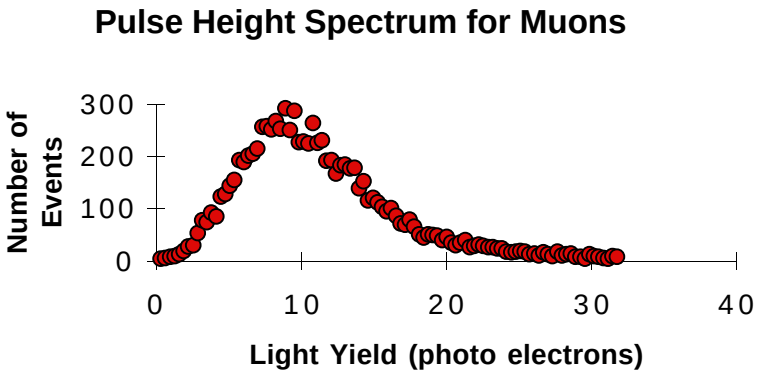

Figure C.4: Pulse height spectrum for through-going muons.

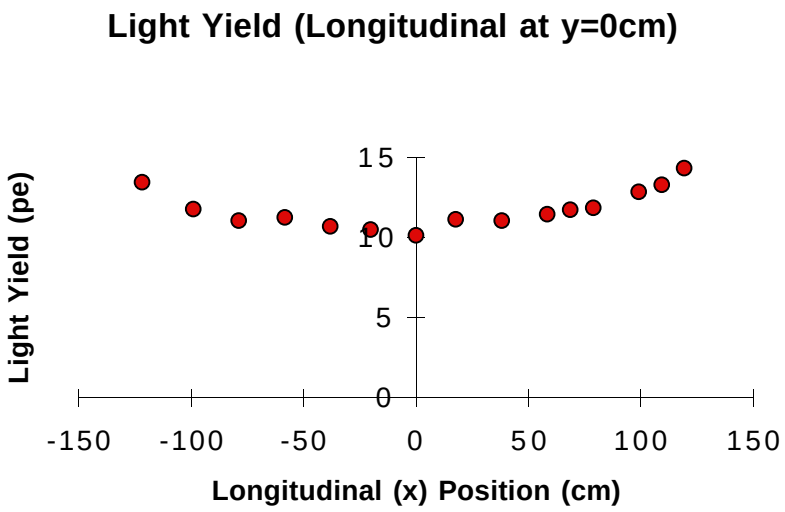

Figure C.5: Longitudinal uniformity. Note that the rise in the light yield toward the ends is due to the fact that the scintillator gets thicker at the ends by about 25%.

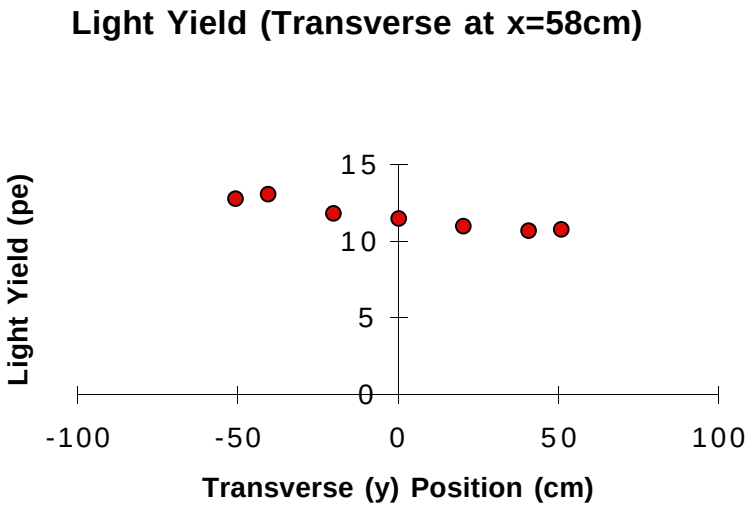

Figure C.6: Transverse uniformity. Fiber readout is at negative y end.

Scintillator Sandwich Prototype

A second 3 m^2 counter identical to the one described above was built. The second scintillator counter was placed below the 21 mm steel plate to form a prototype sandwich counter[120]. Figure C.7 shows the pulse height distribution of the upper counter self triggering i.e., no coincidence. Figure C.8 shows the pulse height distribution of the upper counter when the ADC was gated by coincidences of the upper and lower counters. It is clear in Figure C.7 that the counter is sufficiently uniform that a single particle peak is clearly separable from the noise even without requiring a coincidence. As shown in Figure C.9, the singles rates corresponding to 95% efficiency are found to be 800 and 1100 per second for the upper and lower counters respectively. (The phototube on the lower counter is slightly noisier.) The time resolution for coincidences of the two counters was measured with a TDC. The time fluctuation between top and bottom counter signals is shown in Figure C.10. The coincidence window necessary to register 98% of real top-bottom coincidences is 28 ns, well within the requirements for the Auger surface detector.

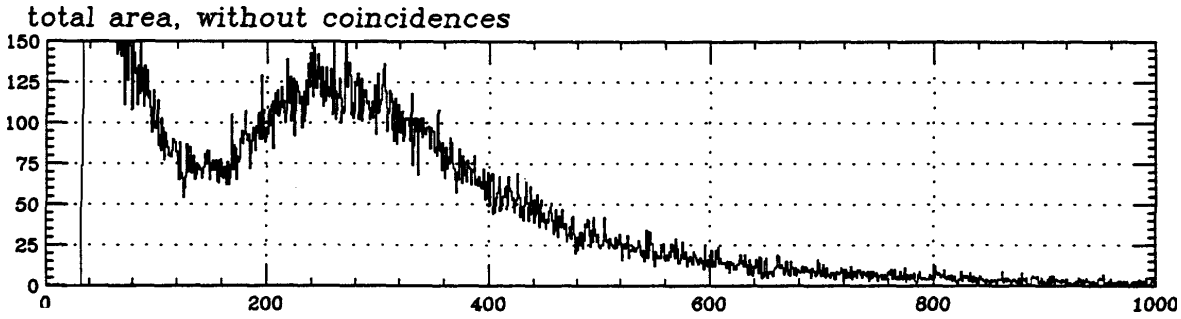

Figure C.7: Pulse height spectrum for large test counter self triggered.

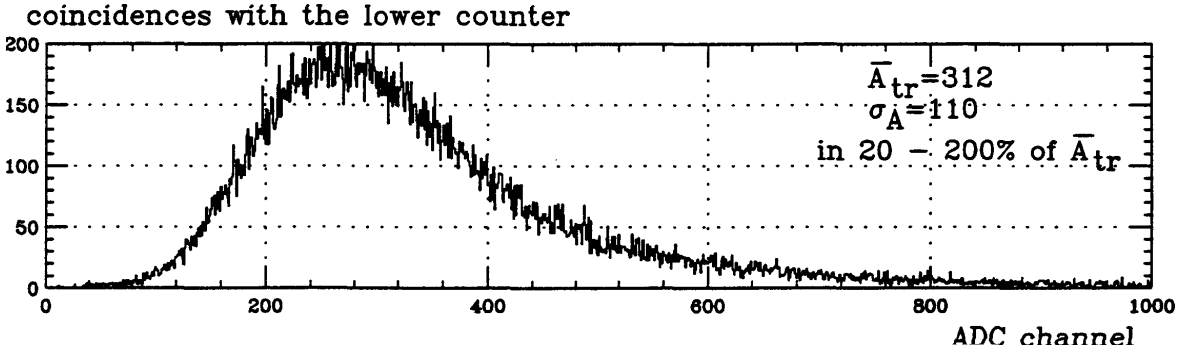

Figure C.8: Pulse height spectrum for upper counter with upper and lower counters in coincidence.

Figure C.9: Upper and lower counter efficiency as a function of discrimination threshold.

Figure C.10: Coincidence time resolution of upper and lower sandwich counters.

Conclusions

Optical wavelength shifting fibers have been demonstrated to effectively and uniformly read out the large area (2.5 m^2) scintillation counters proposed for the Auger surface detector array.

On the basis of these tests, a counter configuration for the detector surface can be designed. The details of the design are driven by cost. Given the large quantities of scintillator, about 60,000 m^2, the mass of the constituent plastic material will determine the cost. This fact, together with the insensitivity to light attenuation in the scintillator when using WLS fiber readout, leads to the use of the thinnest possible scintillator. Polystyrene based scintillator with a brightness over three times that of the acrylic is the material of choice as shown above. Even with this optimization, however, the cost of the cast scintillator, the cost of machining the grooves, and the labor of installing the fibers makes the fiber readout design more costly than other readout methods.

There are some possible ways to reduce costs but still retain the advantages of fiber readout counters. Because of lower labor costs, extruded scintillators can be produced at significantly lower cost than cast sheet. It is also possible to cast in grooves or holes for the wave shifter fiber eliminating the machining cost. In this way it may be possible to reduce the scintillator cost by two thirds, thereby making fiber readout cost competitive with other scintillator based designs.

Scintillator sandwich counters using fiber readout have been shown to be an efficient and uniform alternative to water Čerenkov detectors. Further refinement of the design could drive costs down to an acceptable level should further study reveal a performance advantage of the sandwich detector over the water detector.

C.5 Performance Test of a Lead Sandwich Detector

C.5.1 Introduction

The design of a detector that can not only measure energy, but separate muons from photons and electrons is being extensively studied, based on the results of shower simulations by Cronin [92] using the MOCCA program developed by Hillas [93]. According to their simulation, the electromagnetic components, namely the photons and electrons, are very soft at large distances from the core ($r > 1000$ m), while the muonic component has a mean energy of around 1 GeV. Therefore the muons may be separated from the electromagnetic components in air showers using two thin scintillators between which a lead layer of thickness of a few radiation lengths has been placed [92], the so-called "leadburger". Since the muons arrive early while the soft electromagnetic components are spread over a few μsec, the arrival time measurement for each particle may also be helpful in separating the muon component from the electromagnetic.

Before assessing the usefulness of a detector which distinguishes muons from electromagnetic components, it is essential to examine the validity of the simulations in reproducing the observed features of low energy particles at great distances from the extensive air shower core.

C.5.2 Experiment

A prototype of a leadburger has been built at the Akeno Giant Air Shower Array (AGASA) [94] using available detectors at Akeno. The AGASA consists of 111 scintillation detectors of $2.2m^2$ area deployed over 100 km^2 area. The sandwich detector is triggered by the AGASA. The detector, covering an area of $12m^2$ is segmented into 2×12 plastic scintillation counters, each with an area of $1m^2$. The lead layer has a thickness of 1cm corresponding to about 1.8 radiation lengths.

Each scintillation counter is equipped with a photomultiplier, preamplifier and main amplifier. The 7th dynode signal is shaped to be exponential with an average decay constant of 11 μs. The signal is fed to the main amplifier and is discriminated to give a square pulse, the width of which is proportional to the logarithm of the number of particles incident over the detector. From January 1995 onwards, the anode signals from phototubes of each layer have been summed up and the shape of the sum pulse for each layer is recorded using a digital recorder with 20ns resolution.

The distribution of arrival times for the incident particles over $12m^2$ area of the top and the bottom counters are recorded in each shower. Full width at half maximum distributions for top-bottom coincidence, which recorded a signal in both top and bottom counters (referred to hereafter as a coincidence signal), top-only and bottom-only signals are about 85ns. The median values of integral pulse shape, defined as the summation of amplitudes (A_i) for n successive bins (in each 20ns) exceeding 3mV ($\sum_{i=1}^{n(>3mV)} A_i$), are used for the definition of one particle and are about 30mV.

C.5.3 Results

The experiment started on September 24th 1994 and the data for eight months have been analyzed. Data from the waveform recorder are available from January 24th 1995. From all recorded data, only showers with energies larger than 10^{18}eV, zenith angles smaller than 45° and hitting well inside the boundary of the Akeno branch of the AGASA are used for the present analysis.

In Figure C.11 the densities of top-only, bottom-only and coincidence signals are plotted as functions of core distance, after reducing the background counts. Here (i) only signals whose energy deposits are less than 50 MeV per counter are used and (ii) every signal (<50 MeV) is assumed to be one particle, irrespective of its energy loss. Since we took all signals to be one particle and some top-only or bottom-only signals may be included in coincidence signals, the plotted frequency may be lower than the real one.

The expected densities of coincidence, top-only and bottom-only signals are estimated from the results which were simulated using the MOCCA program. Here the converted electrons from photons in top only, bottom only and coincidence signals are taken into account. The results for incident showers of primary proton with energy 10^{19}eV at a zenith angle of 0° are used.

For experimental plots, the median energy of the primary particles is $10^{18.2}$eV. To normalize the simulation results of 10^{19}eV to those of $10^{18.2}$eV, electromagnetic components are reduced linearly with energy, however muons are reduced by assuming a relation $\rho_\mu \sim E^{0.82}$ irrespective of core distance, from the experimental relation $N_\mu \sim E^{0.82}$ obtained at Akeno [95]. Error bars are statistical only, and if we consider the uncertainties in both experiment and simulation, the difference between them may be less than a factor of 2.

So far we have discussed the identification of coincidence, top-only and bottom-only signals for showers of $10^{18.0} \sim 10^{18.5}$eV, between 1000m and 1500m from the core, where the densities are less than 1 particle per m^2. In this project, showers of energies above 10^{19}eV will be intensively studied and hence the densities will be ten times higher than in the above examples. In Figure C.12 an example of leadburger data from a shower of $10^{19.4}$eV, whose core distance is about 1500m, is shown. The energy losses recorded in each counter are listed in the table in units of 10 MeV.

There are three clear signals delayed by more than 3μs. A big signal showing a large energy loss is sometimes observed in a top scintillator or a bottom scintillator. Most of these particles are delayed by more than a few μsec and are likely to be slow neutrons.

By comparing the table and the arrival time distribution, it is found that the top counters of segments 4 and 6 show extraordinary values. This can be understood if these counters are hit by two particles separated in time by 4 to 5 μs, respectively. Overestimation occurs when a delayed signal is added to the tail of an exponentially decaying pulse. Assuming energy losses of the top-bottom coincidence signals in each segment 4 and 6 are the same, the energy losses of 3.0 and 6.5 for the delayed signal do not contradict the observed values of 7.5 and 14.1.

Since there is only one candidate in segment 9 for a delayed bottom-only signal, the energy deposit of the top-counter of segment 9 may be top-only. The separation only by segmentation of the detector is not satisfactory for average densities above 1/m^2. Even if we use both segmented density data and arrival time information, a few top-only or bottom-only signals can not be resolved with the present resolution in space and time.

If an Auger detector is segmented into four, this event may be a good example of one of four detectors at 1500m from the core of a 10^{20}eV shower (or at 1200m from the core of a 10^{19}eV shower), though the time scale of the figure shown may be somewhat reduced at 1200m.

C.5.4 Conclusions

The eight-month run of the leadburger detector triggered by the AGASA has been analyzed and it provided important information on electrons, photons and muons at around 1000m $\sim$ 2500m from the core for showers of energies larger than 10^{18}eV. Although the statistics are still low, the present lateral distributions of electrons, photons and muons agree with simulation results by the MOCCA program within a factor 2. Their arrival time distribution is still under analysis. Considering that a sandwich detector works according to expectations rather well, estimation from the MOCCA program may be a powerful tool for the development of the water Čerenkov detector which will be used in the Auger array.

A sandwich detector with a 1.8 X_0 lead plate and with 1m^2 area segmentation, may serve as a good separator between muonic and electromagnetic components of an air shower at energies below $10^{18.5}$eV above 1000m from the core.

For higher energy showers, however, more study is necessary to find a good algorithm for separating muons from electrons and photons.

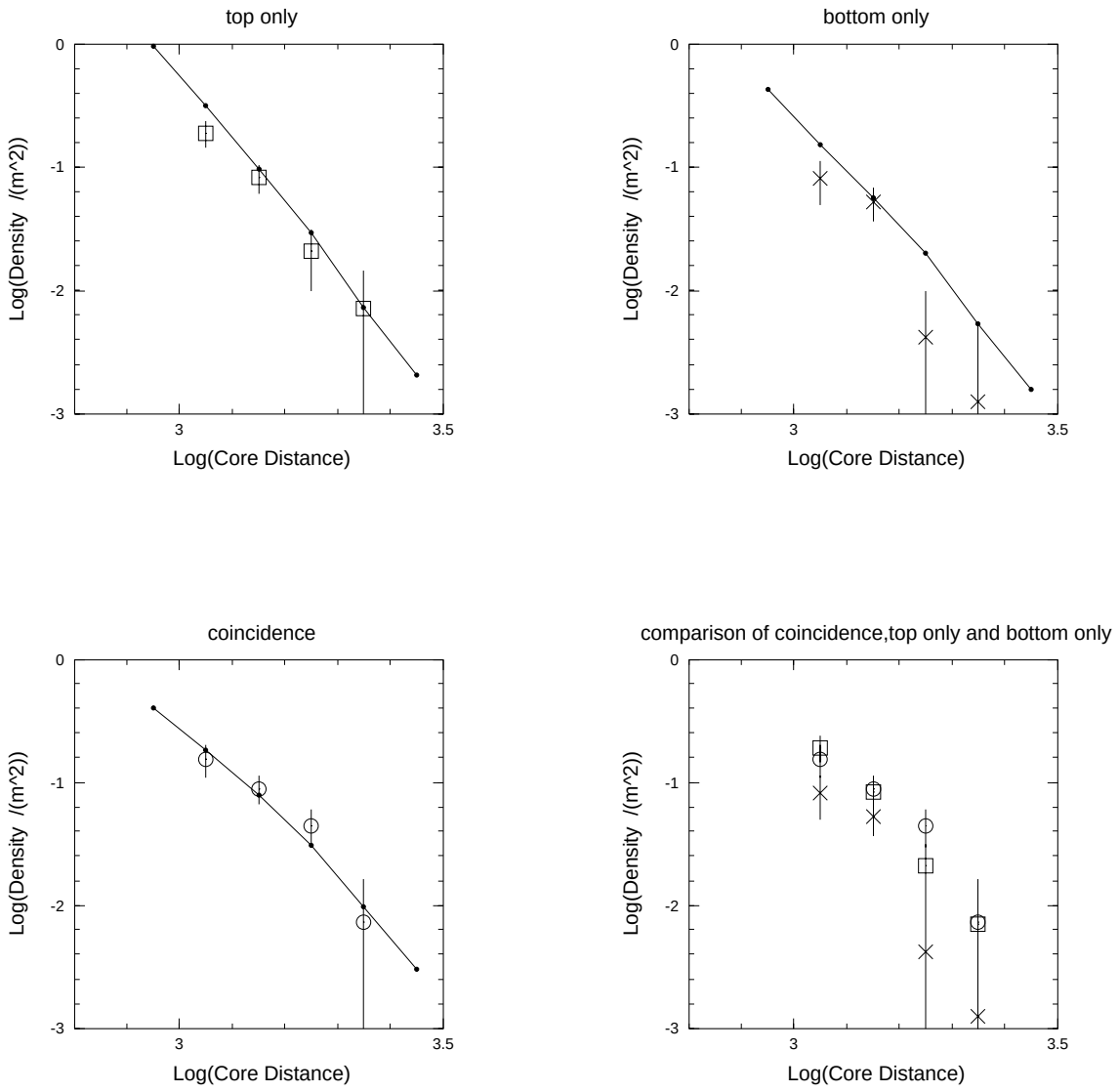

Figure C.11: Lateral distributions of top and bottom only signals, as well as coincidence events. Closed circles connected by lines represent the simulation results estimated from simulation results (normalized to $10^{18.2}$eV).

segment No.	1	2	3	4	5	6	7	8	9	10	11	12
top	2.3	1.7	1.5	7.5	0.69	14.1	4.6	3.0	4.1	1.0	2.6	0.76
bottom	1.2	2.1	1.4	1.2	1.3	1.4	1.4	0.0	4.6	1.1	1.2	0.0

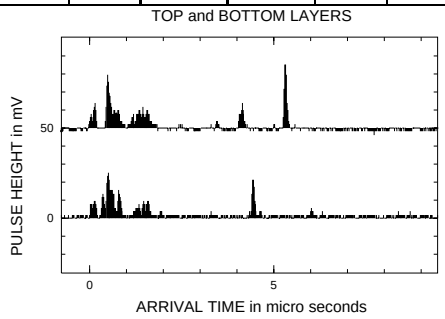

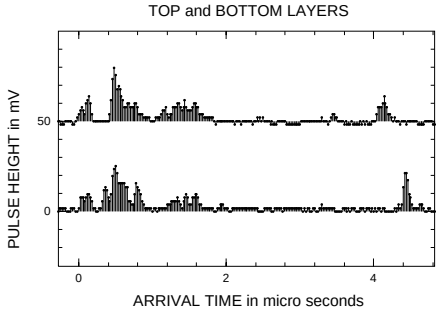

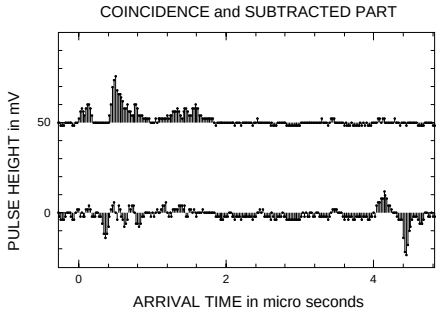

Figure C.12: An example of arrival time distributions of the top (T) and the bottom (B) layers of the leadburger at 1500m from the core is shown with two different time scales, 10.24μs (top figure) and 5.12μs (middle and bottom). The primary energy is 25 EeV and zenith angle is 34.5°. C is the coincident part of the distributions of top and bottom layers and S is the subtracted one of the bottom layer from that of top layer.

Appendix D

List of Contributors

Argentina

Laboratorio Tandar - CNEA
Alberto Filevich
Alberto Etchegoyen

Comision Nacional de Actividades Espaciales
Fernando R. Colomb

Instituto de Astronomia y Fisica del Espacio, B.A.
Adrian C. Rovero

Armenia

Yerevan Physics Institute
Edouard Mnatsakanian
Ashot Chilingarian

Australia

University of Adelaide
David J. Bird
Roger W. Clay
Bruce R. Dawson
R. J. Protheroe

Telstra Applied Technologies
Geoff Kelly

Bolivia

National Academy of Sciences
Carlos Aguirre

Brazil

LAFEX/CBPF
Alberto Santoro

Bulgaria

Institute for Nuclear Research
L. Popova

Peoples Republic of China

Institute of High Energy Physics
Ding Linkai
Jian-Zhong Wang

France

Ecole Nationale Superieure des Telecommunications
Nicolas Demassieux
Denis Roux

Laboratoire de Physique Corpusculaire - College de France
Jean-Michel Brunet
Jean-Noël Capdevielle
Laurent Guglielmi
Gerard Tristam

Laboratoire de Physique Nucleaire et de Hautes Energies - Universites Paris 6 and 7
Murat Boratav
Antoine Letessier-Selvon
Zacharia Strachman

Laboratoire de l'Accelerateur Lineaire - Orsay
Boris Dudelzak
Paul Eschstruth
Bernard Merkel
Philippe Roy
Vardan Sahakian (permanent address: Yerevan Physics Institute)

Observatoire de Besançon:
François Meyer
François Vernotte
Alain Vincent
Michel Vincent

LURE - Orsay
Roger Bosshard

Germany

Gottingen
K. Mannheim

University of Heidelberg
T. Kutter

M-P-I fur Kernphysik, Heidelberg
F. A. Aharonian

M-P-I fur Fysik, München
Eckhart Lorenz

M-P-I fur Radioastronomie, Bonn
P. L. Biermann

India

Tata Institute of Fundamental Research, Bombay
B. V. Sreekantan

Italy

INFN, laboratory Nazionali del Gran Sasso
V. S. Berezinsky

University of Rome
Paolo Lipari

University of Torino
Gianni Navarra

Japan

Nagoya University
Y. Matsubara

Yamanashi University
K. Hashimoto
K. Honda
N. Kawasumi
I. Tsushima

University of Tokyo
Institute for Cosmic Ray Research
Motohiko Nagano
Masahiro Teshima
S. Yoshida

Mexico

CINVESTAV
Arnulto Zapata

Netherlands

Philips Photonics
Esso Flyckt
Wayne Seemungal

Russia

Inst. of Terrestrian Magnetism, Ionosphere and Propagation of Radio Waves
V. Ptuskin

Moscow State University
Boris Khrenov
G. B. Khristiansen
Vyacheslov Vashkevich

South Africa

Space Research Unit, Potchefstroom
B. Christo Raubenheimer

Spain

Univ. of Santiago Complutense
Enrique Zas

Sweden

Uppsala University
Hector Rubinstein

United Kingdom

University of Leeds
Jeremy Lloyd-Evans
M. Gallagher
A.M. Hillas
C. L. Pryke
Alan A. Watson

United States

Columbia University
John H. Boyer
Eric J. Mannel

Fermilab
Michael Albrow
Thomas Droege
Thomas Groves
Hans Kautzky
Rocky Kolb
Paul Mantsch
Peter O. Mazur
Andrew Shih
Louis Voyvodic
Merle M. Watson

University of Hawaii
Mary Anne Cummings

Johns Hopkins University
R. Fletcher
Colin Norman

Los Alamos National Laboratory
Stirling Colgate

Moorhead State University
Joseph Gress

NASA, Goddard Space Flight Center
Floyd Stecker

Institute for Advanced Study, Princeton
Eli Waxman

Texas A&M University - Kingsville
Daniel J. Suson

University of Arizona
J. R. Jokipii

University of California, Irvine
Gaurang Yodh

University of Chicago
Fausto Cattaneo
James Cronin
Brian Fick
Kenneth Gibbs
Angela Olinto
Rene Ong
Jonathon Rosner
G. Sigl

University of Michigan
Lawrence W. Jones
John Mann
Jim Matthews
Colleen Murphy
David Nitz
Wayne Stark

University of Utah
J. Ball
Hongyue Dai
David Kieda
Eugene C. Loh
A. Pantziris
Paul Sommers

University of Wisconsin
Lori A. Gray
Francis Halzen

Pennsylvania State University
James Beatty

University of Delaware
T. K. Gaisser
T. Stanev

Vietnam

Dalat Nuclear Research Institute
Phuong Dong Huynh

newpage

Bibliography

[1] P. Auger et al., Comptes Rendus **206**, 1721 (1938), P. Auger, Rev. Mod. Phys. **11**, 288 (1939)

[2] A.A. Penzias and R.W. Wilson, Ap.J. **142**, 419 (1965).

[3] K. Greisen, Phys. Rev. Letters **16**, 748 (1966).

[4] G.T. Zatsepin and V.A. Kuz'min, JETP Letters **4**, 78 (1966).

[5] M. Nagano et al., J. Phys. **G18**, 423 (1992) and S. Yoshida et al., Astroparticle Physics **3**, 105 (1995).

[6] D.J. Bird et al., Phys. Rev. Lett. **71**, 3401 (1993).

[7] N. Hayashida et al., Phys. Rev. Letters **73**, 3491 (1994).

[8] P.O. Lagage and C. Cesarsky, Astron. Astrophys. **118**, 223 (1983).

[9] J.R. Jokipii, Ap. J. **313**, 842 (1987).

[10] A.M. Hillas, Ann. Revs. Astron. Astrophys. **22**, 425 (1984).

[11] Stirling Colgate, talk at the opening workshop of the Auger Study, Fermilab, January 31, 1995. There is a discussion of related mechanisms in Ref. [12] based on the work of R.V.E. Lovelace, Nature, **262**, 649 (1976) and R.D. Blandford, Mon. Not. R. Astron. Soc. **176**, 465 (1976) and **179**, 433 (1977).

[12] Astrophysics of Cosmic Rays, Chapter IV, V.S. Berezinsky et al., North-Holland (1990).

[13] J.L. Puget, F.W. Stecker and J.H. Bredekamp, Ap. J. **205**, 638 (1976).

[14] F.A. Aharonian and J.W. Cronin, Phys. Rev. **D50**, 1892 (1994).

[15] S. Yoshida and M. Teshima, Prog. Theor. Phys. **89**, 833 (1993).

[16] P. P. Kronberg, Rep. Prog. Phys. **57**, 325 (1994).

[17] S. Lee, G. Sigl, and A. Olinto, in preparation (1995).

[18] G. Cocconi, Nuovo Cimento **3**, 1433 (1956).

[19] J. H. Cronin, Nucl. Phys. B (Proc. Suppl.) 28B, 213 (1992).

[20] C. A. Norman, D. B. Melrose and A. Achterberg, Ap. J. (to be published, 1995).

[21] H. Kang, D. Ryu and T.W. Jones, Ap.J. to be published (1996).

[22] C. Cesarky and V. Ptuskin, Proc. 23rd Int. Cosmic Ray Conf. (Calgary) **2**, 341 (1993).

[23] P.L. Biermann and P.A. Strittmatter, Ap.J. **322**, 643 (1987).

[24] D. Fichtel et al., Ap. J. (Suppl.) **94**, 551 (1994).

[25] M. Punch et al. Nature **358**, 477 (1992), J. Quinn et al., (Whipple Collabn.) IAU Circular 6178 (1995).

[26] K. Meisenheimer et al., Astron. Astrophys. **219**, 63 (1989).

[27] J. Rachen and P.L. Biermann, Astron. Astrophys. **272**, 161 (1993).

[28] J. Rachen, Todor Stanev and P.L. Biermann, Astron. Astrophys. **273**, 377 (1993).

[29] T. Stanev et al., Phys. Rev. Lett (in press).

[30] E. Waxman, Phys. Rev. Lett. **75**, 386 (1995).

[31] M. Vietri, Astrophys. J. to be published (1995).

[32] M. Milgrom and V. Usov, Astrophys. J. to be published (1995).

[33] C. A. Meegan et al., Nature **355**, 143 (1992); B. Paczyński, Nature **355**, 521 (1992); T. Piran, Astrophys. J. **389**, L45 (1992); J. P. Norris et al., Astrophys. J. **423**, 432 (1994).

[34] P. Meészáros and M. Rees, Mon. Notes Roy. Astron. Soc. **269**, 41P (1994).

[35] P.Bhattacharjee, C.T.Hill, D.N.Schramm, Phys.Rev.Lett. **69**, 567 (1992).

[36] G. Sigl, K. Jedamzik, D.N. Schramm and V.S. Berezinsky, FERMILAB-Pub-95/051-A and G. Sigl, to appear in Space Science Reviews.

[37] L. D. Landau and I. J. Pomeranchuk, Dokl. Akad. Nauk. SSSR **92**, 535 (1953), and Dokl. Akad. Nauk SSSR **92**, 735 (1953). These papers are translated into English in L. D. Landau, Collected Papers, Pergamon Press (1965). A. B. Migdal, Phys. Rev. **103** 1811 (1956).

[38] R.J. Protheroe and P.A. Johnson, ADP-AT-95-5, astro-ph/9506119, to appear in Astroparticle Physics.

[39] G.Sigl, S.Lee, D.N.Schramm, P.Bhattacharjee, FERMILAB-Pub-95/148-A, astro-ph/9506118.

[40] S.M. Astley et al., Proc. ICRC 17 **2**, 156 (Paris, 1981).

[41] N.N. Efimov et al., Proc. ICRC 18 **2**, 149 (Bangalore, 1983).

[42] P.V.J. Eames et al., Proc. ICRC 19 **2**, 254 (LaJolla, 1985)].

[43] A.W. Wolfendale and J. Wdowczyk, J. Phys. G. **10**, 1453 (1984).

[44] J. Linsley and L. Scarri, Phys. Rev. **128**, 485 (1962).

[45] D. J. Bird et al., Ap. J. 424, 491 (1994).

[46] A. A. Watson, Nucl. Phys. B (Proc. Supp.) **22B**, 116 (1991).

[47] R. Kulsrud, talk given at the May 13-15 Workshop of the Giant Air Shower Design Group.

[48] F. Halzen et al., Astroparticle Physics **3**, 151 (1995).

[49] F. Aharonian and J.W. Cronin, Phys. Rev. **D50**, 1892 (1994).

[50] D.J. Bird et al., Phys. Rev. Lett. **71**, 3401 (1993).

[51] J. Engel et al., Phys. Rev. **D46**, 5013 (1992). Further discussion on the validity of the assumptions underlying the superposition model can be found in T.K. Gaisser et al., Phys. Rev. **D47**, 1919 (1993)

[52] A.M. Hillas, Proc. 19th ICRC (La Jolla) **1**, 155 (1985).

[53] R.S. Fletcher et al., Phys. Rev. **D50**, 5710 (1994).

[54] T.K. Gaisser, "Cosmic Rays and Particle Physics", (Cambridge: Cambridge Univ. Press, 1990), Chapter 17.

[55] S. Yoshida et al., J. Phys. **G20**, 651 (1994).

[56] Y. Mizumoto, Proc. Tokyo Workshop on Techniques for the Study of Extremely High Energy Cosmic Rays, ed: M. Nagano, 194 (1993).

[57] P. Sommers, Astroparticle Physics **3**, 349 (1995).

[58] M. S. Longair, High Energy Astrophysics, 2nd Edition, Cambridge Univ. Press 1992.

[59] T. K. Gaisser and A. M. Hillas, Proc. 15th Int. Cosmic Ray Conf. (Plovdiv), **8**, 353 (1977).

[60] W. H. Press et al., Numerical Recipes, Cambridge University Press (1986).

[61] P. Sokolsky, Proc. Tokyo Workshop on Techniques for the Study of Extremely High Energy Cosmic Rays, ed: M. Nagano, p.280 (1993).

[62] J. Boyer et al., "A Flash ADC Electronics System for the HiRes Detector," Proc. 24th Int. Cosmic Ray Conf. (Rome) **3**, 750 (1995).

[63] T.K.Gaisser et al. Phys. Rev. D **47**, 1919 (1993)

[64] R.M. Baltrusaitis et al. Proc. 19th ICRC, La Jolla **7**, 159 (1985)

[65] T.K.Gaisser and A.M. Hillas, Proc. 15th ICRC, Plovdiv **8**, 353 (1977).

[66] S.Yoshida et al. Astroparticle Physics **3**, 105 (1995).

[67] R.M. Baltrusaitis et al Nucl. Inst. Methods **A240**, 410 (1985).

[68] H.Y. Dai, in "Tokyo Workshop on Techniques for the Study of Extremely High Energy Cosmic Rays", 133, ICRC Tokyo (1993).

[69] J.W. Elbert, in "Tokyo Workshop on Techniques for the Study of Extremely High Energy Cosmic Rays", 158, ICRC Tokyo (1993).

[70] Proceedings of the International Workshop on Techniques to Study Cosmic Rays with Energies Greater than 10^{19}eV, Nucl. Phys. B, Proc. Supp. **28B**, 1992

[71] This volume.

[72] Auger Project Technical Note GAP-95-025 (1995)

[73] DE6003 Digital Radio Tranceiver, GEC Plessey Application Note DS3506-6.3 (1994)

[74] R.J. Yarema et al., IEEE Nucl. Sci. Symposium **1**, 381 (1992)

[75] R.J. Yarema et al., Proc. 2nd Int. Conf. Electronics for Future Colliders, 131 (1992)

[76] C. Pryke et al., Nucl. Inst. Methods **A354** 560 (1995)

[77] Code of Federal Regulations, Title 47, Parts 0-19, Office of Federal Register, National Archives and Record Admin. (1994)

[78] Donald E. Kerr, Propagation of Short Radio Waves, Dover Publ. (1951)

[79] D. B. Kieda, "A New Detection Technique for EeV/ZeV Cosmic Rays", Astroparticle Physics, to be published.

[80] D. B. Kieda and D. J. Suson, "Design Considerations for a Čerenkov array detector for EeV/ZeV energy Cosmic Rays", to be submitted to Astroparticle Physics.

[81] G. K Garipov, B.A. Khrenov, and V.V. Prosin, "EAS Čerenkov Radiation Detector for Operation in the Presence of High Light Noise"

[82] H. R. Allan, in "Progress in Elementary Particles and Cosmic Ray Physics," v. 10, edited by J. G. Wilson and S. G. Wouthuysen (North-Holland, Amsterdam, 1971), p. 171; V. B. Atrashkevich et al., Yad. Fiz. **28**, 366 (1978).

[83] R. A. Roussel-Dupre et al., Los Alamos National Laboratory report LA-12601-MS, November, 1993.

[84] D. J. Bird et al., "Multi-Component Observation of 10^{17} eV EAS with the CASA-MIA and HiRes Detectors," contributed to session OG 6, 24th International Conference on Cosmic Rays, Rome, Italy, August, 1995.

[85] M. S. Atiya et al., Nucl. Inst. Meth. A **279**, 180 (1989).

[86] D. Bryman et al., IEEE Trans. **NS-38**, 295 (1991).

[87] Clay R.W. and Dawson B.R., Eds., Adelaide Design Workshop, Final Report, Univ. of Adelaide (1995) 66.

[88] Dudelzak B. et al., LAL Orsay, Report 95-01 (1995).

[89] Boratav M. et al., contributed paper, 24th ICRC (Rome 1995).

[90] Stubberfield R., Thorn EMI Electron Tubes, Ruislip, U.K., private communication.

[91] J.W.Cronin, University of Chicago preprint, EFI92-8 (1992).

[92] J.W.Cronin, 1994, preprint, Contribution to Snowmass Report on Cosmic Rays.

[93] A.M.Hillas, Proc. 12th ICRC, Hobart, **3**, 1001 (1971).

[94] N.Chiba et al., Nucl. Instr. and Methods, **A311**, 338 (1992).

[95] N.Hayashida et al., J. Phys. **G21**, 1101 (1994).

[96] S.Yoshida et al., J. Phys. **G20**, 651 (1994).

[97] K.Honda et al., Prof. 23rd ICRC, Calgary, **4**, 311 (1993).

[98] R. M. Tennant, Proc. Roy. Soc. **92**, 622 (1967)

[99] E. W. Kellermann and L. Towers, J. Phys. **A3**, 284 (1970)

[100] M. A. Lawrence, R. J. O. Reid and A. A. Watson, J. Phys. **G17**, 733 (1991)

[101] R. Walker and A. A. Watson, J. Phys. **G7**, 1297 (1981)

[102] A. M. Hillas, Nucl. Phys. B **28B**, 67 (1992)

[103] N. Hayashida et al., J. Phys. **G21**, 1101 (1995)

[104] R. C. Smith and K. S. Baker, Appl. Optics **20**, 177 (1981)

[105] M. Takiue, H. Fujii and H. Ishikawa, Nucl. Inst. Meth. **227**, 571 (1984)

[106] N. A. Porter, Il Nuovo Cim. **5**, 526 (1957)

[107] J.W. Cronin, Auger Technical Note GAP-94-002 (Apr 1994)

[108] A. Borione et al., Nucl.Instr.Methods **A346**, 329 (1994)

[109] N. Morgan, private communication.

[110] M. Ambrosio, private communication.

[111] M.G. Albrow et al.,Nucl.Instr.Methods **A256**, 23 (1987)

[112] Solenoidal Detector Collaboration Technical Design Report, SSCL-SR-1215 (1992)

[113] G. Apollinari et al., Proc. 4th Int. Conf. in Calorimetry, LaBiodalas (1993)

[114] G.W. Foster et al., Nucl. Phys. B **23A**, 92 (1991)

[115] P. de Barbaro et al., Nucl. Instrum. Methods **A315**, 317 (1992)

[116] P. Mantsch et al., Auger Note GAP 95-008 (1995)

[117] P. de Barbaro et al., SDC-93-407 (1993)

[118] G. Apollinari et al., Nucl. Instrum. Methods **A311** 520 (1992)

[119] P. de Barbaro, CDF/DOC/PLUG-UPGR/CDF-2545 (July 1994)

[120] V. Vaskevich, Auger Note GAP-95-014 (May, 1995)

[121] Catalogue of highest energy cosmic rays No.1 (Volcano Ranch and Haverah Park), World Data Center C2 for Cosmic Rays, Tokyo (1980)

[122] J. Linsley, Phys. Rev. Lett. **10**, 146 (1963)

[123] M.A Lawrence et al., J. Phys. G **17**, 733 (1991)

[124] N.N. Efimov et. al. Proc. of Int. Workshop on Astrophysical Aspects of Most Energetic Cosmic Rays, Editors: M. Nagano & F. Takahara, p20. (1990)

[125] K. Greisen, Proc. 9^{th} Int. Conf. Cosmic Rays. London, **2**, 609 (1965)

[126] G. Cavallo, Astron. Astrophys., **65**, 415 (1978)

[127] C.J. Cesarsky, Nuclear Physics B (Proc. Suppl.), **28B**, 51 (1992)

[128] A. Beretvas et al., Nucl. Inst. Methods A329, 50 (1993).